NATURAL CONVECTION IN ELECTROCHEMICAL SYSTEMS



Yavor Kirilov Novev

Trinity College

University of Oxford

A thesis submitted for the degree *Doctor of Philosophy in Physical and Theoretical Chemistry*

Supervisor: Prof. Richard G. Compton

Trinity Term, 2018

Natural Convection in Electrochemical Systems

Yavor Kirilov Novev

Trinity College

A thesis submitted for the degree *Doctor of Philosophy in Physical and Theoretical Chemistry*

Trinity Term, 2018

Abstract

This thesis is concerned with modelling natural convective flows and specifically with their role in electrochemistry. The studies described here demonstrate that many electroanalytical techniques are prone to non-negligible natural convective effects, thus making the standard assumption for purely diffusional mass transport inapplicable. The chosen approach focusses on investigating idealized systems and establishing orders of magnitude for the quantities of interest. The complexity of the observed natural convective flows and their strong dependence on factors such as container geometry serve as compelling arguments for rigorously excluding natural convection in experimental measurements.

The text is structured as follows. Chapter 1 introduces the theoretical framework used in the rest of the text and gives an outline of the electrochemical techniques to which the results in later chapters apply. Chapter 2 surveys the literature on natural convection in electrochemistry and emphasizes recent developments. Chapter 3 studies the natural convection induced by the intrinsic heat of an electrochemical reaction, specifically its effect on mass transport in chronoamperometry and cyclic voltammetry. Chapters 4-6 deal exclusively with coupled heat and momentum transport. Chapter 4 considers the thermal convective flows that arise in an idealized cell for scanning electrochemical microscopy (SECM) and the surrounding air under conditions of imperfect thermostating. Chapter 5 is dedicated to thermal convection in an SECM cell that is being thermostated from below through a solid substrate. This chapter demonstrates the influence of the spatial distribution of substrate thermal conductivity on the observed flows and

highlights this effect by using a simpler model of the SECM cell than Chapter 4. Chapter 6 investigates the thermal convection in a novel thermostated cell for electrochemical measurements. Chapter 7 contains the main conclusions from the studies described in the thesis. Appendices A, B and C provide additional data for Chapters 3, 5 and 6, respectively.

Acknowledgements

Thanks are due to the following people for help with the research forming specific parts of this thesis.

- Dr Enno Kätelhön from the University of Oxford for discussions of the material forming the basis of Chapter 3.
- Prof. Krassimir Danov from the University of Sofia, Dr Andrew J. Wain from the National Physical Laboratory (UK) and Dr Giorgia Zampardi from the University of Oxford for helpful discussions related to the work described in Chapter 4.
- Prof. Ian Hewitt, Prof. Philip Maini and Dr Thomas Woolley, all of them from the Mathematical Institute of the University of Oxford, for very helpful discussions and valuable suggestions with respect to the work described in Chapter 5.
- Dr Xiuting Li, Dr Christopher Batchelor-McAuley and Prof. Richard G. Compton (University of Oxford) for designing the home-made thermostated cell discussed in Chapter 6; Dr X. Li and Dr C. Batchelor-McAuley for obtaining the experimental data presented there.

More generally, I thank Professor Richard G. Compton for supervising me over the course of my DPhil studies.

I thank the Clarendon Fund and Trinity College of the University of Oxford for a Clarendon-Titley Scholarship that allowed me to study at Oxford; thanks also go to Trinity College for awarding me a graduate scholarship.

I am deeply indebted to my mother (Anastassia), father (Kiril) and brother (Martin) for their support throughout this degree and in general!

I owe many thanks to all my friends in Oxford, Sofia and other places around the world for their companionship, help and support.

Publications

This thesis is based in part on five papers that have appeared in peer-reviewed journals during the course of my DPhil studies. Full bibliographic information about these papers is given below.

1. J.K. Novev, R.G. Compton, Natural convection effects in electrochemical systems, Curr. Opin. Electrochem. 7 (2018) 118-129.
2. J.K. Novev, S. Eloul, R.G. Compton, Influence of Reaction-Induced Thermal Convection on the Electrical Currents Measured in Chronoamperometry and Cyclic Voltammetry, J. Phys. Chem. C 120 (2016) 13549-13562.
3. J.K. Novev, R.G. Compton, Convective Heat Transfer in a Measurement Cell for Scanning Electrochemical Microscopy, Phys. Chem. Chem. Phys. 18 (2016) 29836-29846.
4. J.K. Novev, R.G. Compton, Thermal Convection in Electrochemical Cells. Boundaries with Heterogeneous Thermal Conductivity and Implications for Scanning Electrochemical Microscopy, Phys. Chem. Chem. Phys. 19 (2017) 12759-12775.
5. X. Li[+], C. Batchelor-McAuley[+], J.K. Novev[+], R.G. Compton, A Thermostated Cell for Electrochemistry: Minimising Natural Convection and Investigating the Role of Evaporation and Radiation, Phys. Chem. Chem. Phys., 20 (2018) 11794-11804.

   [+]Equal contributors.

Chapter 2 adapts sections of paper No. 1. Chapter 3 is adapted with permission from paper No. 2; Chapter 8 is adapted from the Supporting Information of the same paper. Copyright (2016), American Chemical Society. Material in Chapters 4-6 is adapted from papers No. 3-5 by permission of the PCCP Owner Societies. Material in Chapters 9 and 10 is adapted from the Supplementary Information to papers 4 and 5 by permission of the PCCP Owner Societies.

Table of Contents

Abstract ..... **I**

Acknowledgments ..... **III**

Publications ..... **IV**

Table of Contents ..... **V**

Epigraph ..... **IX**

1. Introduction **1**

1.1. Theoretical framework for modelling natural convection 1

1.2. Basics of the finite element method 5

1.3. Examples of natural convective flows 10

1.4. Electrode potentials 13

1.5. Nernstian boundary condition 16

1.6. Electrochemical current 17

1.7. Chronoamperometry 17

1.8. Cyclic voltammetry 19

1.9. Scanning electrochemical microscopy 21

1.10. References 22

2. Survey of the Literature on Natural Convection in Electrochemical Systems **26**

2.1. Solute-driven natural convection 26

2.2. Temperature-driven natural convection 31

2.3. Temperature and solute-driven natural convection 33

2.4. Experimental approaches for minimizing free convection 34

2.5. Electrochemical sensors that make use of natural convection 35

2.6. Natural convection in fuel and thermogalvanic cells 36

2.7. Bubble-induced convection 37

2.8. Studies with an additional external force 38

2.9. Studies that utilize the analogy between heat and mass transfer 39
2.10. Spontaneous convection? 40
2.11. Conclusions 45
2.12. References 45

3. The Influence of Reaction-Induced Thermal Convection on the Electrical Currents Measured in Chronoamperometry and Cyclic Voltammetry 53

3.1. Introduction 53
3.2. Theory 55
3.2.1. Model 56
3.2.1.A Mass transfer 56
3.2.1.B Heat transfer 60
3.2.1.C Hydrodynamics 62
3.2.2. Simulations 67
3.3. Results and discussion 70
3.3.1. Chronoamperometry 71
3.3.2. Cyclic voltammetry 80
3.4. Conclusions 82
3.5. References 84

4. Convective Heat Transfer in a Measurement Cell for Scanning Electrochemical Microscopy 87

4.1. Introduction 88
4.2. Model 90
4.2.1. Theory 90
42.1.A Heat transfer 90
42.1.B Momentum transfer 94
4.2.2. Simulations 98
4.3. Results and discussion 100
4.4. Conclusions 107
4.5. References 108

5. Thermal Convection in Electrochemical Cells. Boundaries with Heterogeneous Thermal Conductivity and Implications for Scanning Electrochemical Microscopy 112

5.1. Introduction 113

5.2. Theoretical model 115

5.3. Simulations 123

5.4. Results and discussion 125

5.4.1. Simulations for r_{cell} = 3 mm 126

5.4.1.A Solution colder than substrate at t = 0 ($\Delta T > 0$) 127

5.4.1.B Solution warmer than substrate at t = 0 ($\Delta T < 0$) 137

5.4.2. Simulations for r_{cell} = 8 mm 140

5.4.2.A Solution colder than substrate at t = 0 ($\Delta T > 0$) 140

5.4.2.B Solution warmer than substrate at t = 0 ($\Delta T < 0$) 146

5.5. Conclusions 148

5.6. References 151

6. A Thermostated Cell for Electrochemistry: Minimising Natural Convection and Investigating the Role of Evaporation and Radiation 155

6.1. Introduction 155

6.2. Theoretical model 160

6.3. Results 165

6.3.1. Thermostating a closed cell 166

6.3.2. Thermostating an open cell 173

6.3.3. Thermostating insights and design criteria 175

6.4. Conclusions 176

6.4. References 178

7. Conclusions 181

A. Appendix A: Additional Data for Chapter 3 183

A.1. Concentration, temperature and velocity profiles for simulations of chronoamperometry 183

A.2. Concentration, temperature and velocity profiles for simulations of cyclic voltammetry 191
A.3. Reference 200

B. Appendix B: Additional Data for Chapter 5 201

B.1. Details on the simulations discussed in Chapter 5 and stability tests 201
B.1.1. Simulations for r_{cell} = 3 mm 202
B.1.1.A Solution colder than substrate at t = 0 (ΔT > 0) 202
B.1.1.B Solution warmer than substrate at t = 0 (ΔT < 0) 225
B.1.2. Simulations for r_{cell} = 8 mm 241
B.1.2.A Solution colder than substrate at t = 0 (ΔT > 0) 241
B.1.2.B Solution warmer than substrate at t = 0 (ΔT < 0) 248
B.2. Meshing 251

C. Appendix C: Additional Data for Chapter 6 252

C.1. Details of the simulation procedure 252
C.2. Assessment of the experimental significance of the perturbations in ΔT_{probe} at short times 253
C.3. Data for simulations and experiments at ΔT = 1.8 K 255
C.4. Additional data simulations and experiments under open-cell conditions at ΔT = 2.3 K 258
C.5. Data on ΔT_{probe} for a cell immersed deeper in the water bath 259
C.6. Volume-averaged velocities of the observed flows 261
C.7. Comparison of thermostating systems 263
C.8. References 264

D. Appendix D: List of symbols and dimensionless criteria 266

D.1. List of symbols 266
D.2. List of dimensionless criteria 267

Epigraph

Science is magic that works.

. . .

Tiger got to hunt,

Bird got to fly;

Man got to sit and wonder, "Why, why, why?"

Tiger got to sleep,

Bird got to land;

Man got to tell himself he understand.

Cat's Cradle, Kurt Vonnegut

1. Introduction

This thesis is dedicated to the study of natural convective flows and their importance to various areas of electrochemistry. Natural (free) convective flows are driven by the buoyancy forces that arise in fluids of spatially inhomogeneous density subjected to the action of gravity [1, 2] in the absence of stirring (forced convection). Modelling systems that exhibit free convection is challenging as the transport processes in them are strongly coupled – transport of momentum, i.e., flow, is strongly interlinked with that of heat and mass. In electroanalytical experiments, it is typically assumed that such flows do not contribute to the mass transport and that the latter is purely diffusional. However, as this work demonstrates, various factors such as imperfect thermostating and the occurrence of electrochemical reactions can generate substantial free convective flows, making this assumption inapplicable to many systems. The importance of electrochemical natural convection goes beyond the scope of just electroanalytical chemistry – many industrial processes involve electrochemical currents that feature a free convective contribution, and a substantial amount of research has been conducted in that area, as the literature survey in the next chapter shows.

The structure of the present chapter is as follows: in Sections 1.1-1.2 we give brief outlines of the theory that is used for modelling natural convection and the numerical method underlying the simulations described in this thesis; in Section 1.3 we discuss some classical natural convective problems; in Sections 1.4-1.6, we define basic electrochemical concepts necessary for the later chapters, and in Sections 1.7-1.9, we briefly describe the experimental techniques to which the studies in the later chapters are relevant.

1.1. Theoretical framework for modelling natural convection

The experimental methods with which we are concerned measure the currents generated by electrochemical reactions. Modelling these currents requires the

determination of the concentration profiles C_i of the species in solution through the mass-conservation relation [1]

$$\partial_t C_\mathrm{i} = -\nabla \cdot \boldsymbol{J}_\mathrm{i}, \tag{1.1}$$

where $\boldsymbol{J}_\mathrm{i}$ is the total flux of solute 'i' and t is time. Note that in the presence of bulk sources or sinks of chemical species, e.g. homogeneous chemical reactions, there would be an additional term on the right-hand side of Eq. (1.1). In general, $\boldsymbol{J}_\mathrm{i}$ is determined by diffusion, convection and migration and obeys the Nernst-Planck equation [1, 2]

$$\boldsymbol{J}_\mathrm{i} = -D_\mathrm{i}\nabla C_\mathrm{i} - \frac{D_\mathrm{i} C_\mathrm{i} z_\mathrm{i} F}{RT}\nabla\phi + C_\mathrm{i}\boldsymbol{v}, \tag{1.2}$$

in which $\boldsymbol{v}$ is the fluid velocity, D_i is the diffusivity of the species, z_i – its charge normalized by the elementary one, ϕ is the electrical potential in the solution, and R and F are the gas and Faraday constants. The form (1.2) contains the approximation that the activity coefficient of species 'i' is unity and is thus valid for dilute solutions.

The first term in Eq. (1.2) reflects the transport of solute via diffusion, the second one – that under the influence of an electrical field and the last one – transport due to the flow of the medium [2]. In electrochemical studies, the migration term is typically suppressed by the addition of a nonelectroactive *supporting electrolyte* in a large excess with respect to the species under study [1, 2]. The high concentration of electrolyte compresses the characteristic length over which the density of free charge is non-zero, i.e. the Debye length [1], $L_\mathrm{D} = \sqrt{(\varepsilon RT)/(F^2 \sum_{\forall\,\mathrm{i}} z_\mathrm{i}^2 C_\mathrm{i})}$, where ε is the absolute dielectric permittivity of the medium. Migration is important at distances of the order of L_D from the electrode, and as under typical conditions[1] $L_\mathrm{D} \sim 1$ nm, its effect is negligible for electrodes of macroscopic dimensions [3]. This is due to the high electrical conductivity of solutions containing an excess of supporting electrolyte, which minimizes the ohmic drop and makes the electric field within the solution negligible [1]; neglecting the electric field in the cases considered here is further justified by the low magnitude of the currents involved.

[1] For example, an aqueous solution of 100 mM 1:1 electrolyte at 298.15 K for which $\varepsilon \sim 78 \times 8.85 \times 10^{-12}$ F · m^{-1}.

In all cases considered here, the motion of the fluid is generated by buoyancy forces within it, in contrast with *forced* convective flows in which there is an external driving force [4]. We determine the fluid velocity by solving the Navier-Stokes and continuity equations [1, 5]

$$\rho(\partial_t \boldsymbol{v} + \boldsymbol{v} \cdot \nabla \boldsymbol{v}) = -\nabla p + \eta \nabla^2 \boldsymbol{v} + \rho \boldsymbol{g}, \tag{1.3}$$

$$\nabla \cdot \boldsymbol{v} = 0; \tag{1.4}$$

above, p is the pressure in the solution, η – its viscosity, ρ – its density, and $\boldsymbol{g}$ is the gravitational acceleration. Equations (1.3)-(1.4) treat the fluid as incompressible, which is a good approximation as compressibility effects are negligible for the low velocities ($\ll 1$ m·s^{-1}) under consideration here [5].

For systems that are not in thermal equilibrium, the transport of mass and momentum is also coupled with that of heat. The latter obeys the heat equation

$$\partial_t T + \boldsymbol{v} \cdot \nabla T = \chi \nabla^2 T, \tag{1.5}$$

in which T is the temperature of the medium and χ is its thermal diffusivity. In principle, the temperature distribution in the fluid is also affected by viscous dissipation, which is described by adding the term $\eta\Phi/(2\rho C_p)$ to the right-hand side of Eq. (1.5), with C_p being the constant-pressure specific heat capacity of the fluid [J·kg^{-1}·K^{-1}] and $\Phi = \sum_{\forall \mathrm{j,k}} \left(\partial v_\mathrm{j}/\partial x_\mathrm{k} + \partial v_\mathrm{k}/\partial x_\mathrm{j}\right)^2$ [5]. The importance of viscous dissipation relative to that of heat conduction is characterized by the Brinkman number, $Br = \eta v_0^2/(\kappa \Delta T)$ [4], in which v_0 is the characteristic velocity magnitude of the flow, ΔT – the characteristic temperature difference, and $\kappa = \rho \cdot C_\mathrm{p} \cdot \chi$ is the thermal conductivity of the medium. For all systems considered here, $Br \ll 1$ – for example, for water and $\Delta T \sim 1$ K, v_0 has to be of the order of 1 m·s^{-1} to warrant a Brinkman number of just $\sim 10^{-3}$. Therefore, we neglect viscous heat dissipation throughout the text.

In general, the parameters D_i, η, ρ and χ that appear in Eqs. (1.1)-(1.2), (1.3) and (1.5) are dependent upon both solute concentration and temperature, making the system strongly coupled. However, we are only concerned with dilute solutions and small deviations from the ambient temperature, and we therefore regard these parameters as constants. As ignoring the variability of the fluid density ρ would

yield no natural convective flow, we instead expand it in a Taylor series about a reference state and truncate the series to the linear terms,

$$\rho - \rho_0 = \Delta\rho \approx \rho_0 \left[\sum_{\forall\, \mathrm{i}} \frac{1}{\rho_0} \frac{\partial \rho}{\partial C_\mathrm{i}} (C_\mathrm{i} - C_{\mathrm{i\,ref}}) + \frac{1}{\rho_0} \frac{\partial \rho}{\partial T} (T - T_\mathrm{ref}) \right], \tag{1.6}$$

where ρ_0 is the unperturbed density.

Thus, we obtain the following system for C_i, T and $\boldsymbol{v}$:

$$\partial_t C_\mathrm{i} + C_\mathrm{i} \nabla \cdot \boldsymbol{v} \approx D_{\mathrm{i}0} \nabla^2 C_\mathrm{i}; \tag{1.7}$$

$$\partial_t T + \boldsymbol{v} \cdot \nabla T \approx \chi_0 \nabla^2 T; \tag{1.8}$$

$$\rho_0 (\partial_t \boldsymbol{v} + \boldsymbol{v} \cdot \nabla \boldsymbol{v}) \approx -\nabla \Delta p + \eta_0 \nabla^2 \boldsymbol{v} + \Delta\rho \boldsymbol{g}; \tag{1.9}$$

$$\nabla \cdot \boldsymbol{v} \approx 0, \tag{1.10}$$

where quantities subscripted with '0' refer to the unperturbed state. In Eq. (1.9), the fluid pressure is offset by the hydrostatic pressure of the unperturbed state, $\Delta p = p - p_\mathrm{ref} + \rho_0 \, |\boldsymbol{g}| z$, where p_ref is a reference pressure and z is the normal coordinate, defined to have a direction contrary to that of $\boldsymbol{g}$. The Boussinesq approximation describes natural convection accurately provided that $\Delta\rho/\rho_0 \ll 1$; detailed discussions of the limits of its validity for thermal convection, i.e., when Eq. (1.7) is trivially fulfilled, can be found in Refs. [6, 7].

The linearization of ρ in the buoyancy term combined with treating the other properties of the fluid as constant is known as the *Boussinesq approximation* [4] and is standard in modelling natural convective systems. The free convective flows governed by Eqs. (1.7)-(1.10) are driven by both solutal and thermal effects; later in the thesis we consider some scenarios in which temperature variations are the sole driving force. The studies described in this thesis focus on modelling particular problems relevant to electrochemistry by finding numerical solutions of equations (1.7)-(1.10) under appropriate initial and boundary conditions.

In this work, we solve the governing equations via the finite-element method in the commercial modelling software COMSOL Multiphysics [8]. We will not discuss the specific implementation of the numerical method, but we give a short outline of the finite element method and its application to a specific equation in the next section.

1.2. Basics of the finite element method

The system (1.7)-(1.10) that governs the natural convective flows we consider is challenging to solve – it is a set of coupled time-dependent equations that includes the nonlinear Navier-Stokes equation. The studies in this thesis focus on the interpretation of the numerical solutions of this system, rather than the algorithms for obtaining them; thus, we solve the problems of interest in the commercial finite-element software package COMSOL Multiphysics. The latter is a standard tool for modelling problems that involve coupled physical phenomena – see for example Ref. [9] for a discussion of its applicability to electrochemistry. To make the text self-sufficient, this section gives a very brief outline of the finite element method for a specific problem; the exposition here closely follows the core sections of Chapter 1 of Ref. [10].

We consider the two-dimensional Poisson equation,

$$\nabla^2 u = -f, \tag{1.11}$$

in which f is a bulk source term and u is a real-valued function, which we seek to determine in the real domain Ω with boundary $\partial\Omega$. Eq. (1.8) describes many physical phenomena – for example, as Eqs. (1.7)-(1.8) suggest, u can represent the stationary concentration or temperature distributions in a solid phase in the presence of a source of mass or heat, respectively.

Let us consider a problem that involves Dirichlet boundary conditions on a part of the domain boundary, $\partial\Omega_{\mathrm{D}}$,

$$u|_{\partial\Omega_{\mathrm{D}}} = g_{\mathrm{D}}\,, \tag{1.12}$$

and Neumann boundary conditions on the rest of it, $\partial\Omega_{\mathrm{N}}$,

$$\mathbf{n}\cdot\nabla u|_{\partial\Omega_{\mathrm{N}}} = g_{\mathrm{N}}, \tag{1.13}$$

where $\mathbf{n}$ is the unit vector normal to $\partial\Omega$. The finite element method does not solve the equation (1.11) in its classical form; instead, it deals with a form of the equation that facilitates the determination of an approximate solution, the *weak form*. To obtain the weak form, we multiply Eq. (1.11) by a *test function v,* integrate over Ω and use the rule for the derivative of a product to rearrange the term $v\nabla^2 u$, reaching

$$\int_{\Omega} \nabla \cdot (v\nabla u) - \int_{\Omega} \nabla v \cdot \nabla u + \int_{\Omega} vf = 0. \tag{1.14}$$

For a Neumann problem ($\partial\Omega_{\mathrm{N}} \equiv \partial\Omega$), applying the divergence theorem to Eq. (1.14) and using (1.13), we obtain

$$\int_{\Omega} \nabla v \cdot \nabla u = \int_{\partial\Omega_{\mathrm{N}}} v g_{\mathrm{N}} + \int_{\Omega} vf. \tag{1.15}$$

Importantly, the form (1.15) describes a broader class of problems than (1.11) as it imposes less strict smoothness requirements on u than Eq. (1.11) does – a classical solution must be continuous and have continuous *second* derivatives, but functions that do not fulfil that condition can be solutions to the weak formulation (1.15). The latter exists if the integrals appearing in it are well-defined and thus, the smoothness requirement is that u and its *first* derivatives are square-integrable in Ω; i.e., that u belongs to the Sobolev space $H^1(\Omega)$ [10]. Similarly, the test function v belongs to $H^1(\Omega)$, f has to be square-integrable in Ω, and v and g_{N} need to be square-integrable in $\partial\Omega$ [10]. For the case of Dirichlet boundary conditions in (1.15), further restrictions on u and v, are required, namely that they belong to the respective Sobolev spaces $H_E^1(\Omega) \coloneqq \{u \in H^1(\Omega), u|_{\partial\Omega_{\mathrm{D}}} = g_{\mathrm{D}}\}$ and $H_{E_0}^1(\Omega) \coloneqq \{v \in H^1(\Omega), v|_{\partial\Omega_{\mathrm{D}}} = 0\}$ [10].

The approximation to the solution u and the test functions v can be chosen in a variety of ways. In the commonly encountered Galerkin finite element method, the solution is expanded in terms of an n-dimensional set of basis functions $\{\phi_1, \ldots, \phi_n\}$ that is contained in $H_{E_0}^1(\Omega)$; these functions are known as *shape* or *trial* functions [10]. In the case of Dirichlet boundary conditions, this basis is extended to include additional functions and the coefficients u_{j} multiplying them in the expansion of u are chosen so that the approximate solution corresponds to the boundary data g_{D}. Thus, the finite-element approximation is

$$u_h = \sum_{\mathrm{i}=1}^{n} u_{\mathrm{i}}\phi_{\mathrm{i}} + \sum_{\mathrm{i}=n+1}^{n+n_{\mathrm{D}}} u_{\mathrm{i}}\phi_{\mathrm{i}}. \tag{1.16}$$

Substituting the Galerkin approximation (1.16) in the weak form (1.15), we require that for every basis function ϕ_{j}

$$\sum_{\mathrm{i}=1}^{n} u_{\mathrm{i}} \int_{\Omega} \nabla\phi_{\mathrm{j}} \cdot \nabla\phi_{\mathrm{i}} = \int_{\partial\Omega_{\mathrm{N}}} \phi_{\mathrm{j}} g_{\mathrm{N}} + \int_{\Omega} \phi_{\mathrm{j}} f - \sum_{\mathrm{i}=n+1}^{n+n_{\mathrm{D}}} \int_{\Omega} u_{\mathrm{i}} \nabla\phi_{\mathrm{j}} \cdot \nabla\phi_{\mathrm{i}}. \tag{1.17}$$

Thus, to solve the problem, we need to determine the coefficients u_{i} with 'i' ranging from 1 to n. In matrix form, this is

$$A\boldsymbol{u} = \boldsymbol{f}, \tag{1.18}$$

where A is known as the *stiffness matrix* and its elements are $A_{\mathrm{ij}} = \int_{\Omega} \nabla\phi_{\mathrm{j}} \cdot \nabla\phi_{\mathrm{i}}$; $\boldsymbol{f}$ is the *load vector*, whose components are $f_{\mathrm{j}} = \int_{\partial\Omega_{\mathrm{N}}} \phi_{\mathrm{j}} g_{\mathrm{N}} + \int_{\Omega} \phi_{\mathrm{j}} f - \sum_{\mathrm{i}=n+1}^{n+n_{\mathrm{D}}} \int_{\Omega} u_{\mathrm{i}} \nabla\phi_{\mathrm{j}} \cdot \nabla\phi_{\mathrm{i}}$. For Dirichlet boundary conditions, the choice of basis $\{\phi_1, \ldots, \phi_n\} \in H^1_{E_0}(\Omega)$ guarantees that A is positive-definite [10] and therefore invertible. For Neumann boundary conditions, the basis functions need to be selected so that they satisfy the condition

$$\sum_{\mathrm{i}=1}^{n} \phi_{\mathrm{i}} = 1. \tag{1.19}$$

In the finite element method, the basis functions $\{\phi_1, \ldots, \phi_n\}$ are chosen to be continuous piecewise polynomials. In particular, each of them is defined to be non-zero only in the vicinity of a specific element, i.e., a geometric entity that occupies part of the domain Ω [10]. In two spatial dimensions, the domain Ω is typically tiled (tessellated) with a set of triangular or quadrilateral elements; the former case is known as triangulation. Given a polygonal domain Ω, the triangulation is chosen so that no there is no overlap between the individual elements and the union of the closures of all triangles Δ_{k}, k = 1, . . . , K coincides with the closure of Ω, $\Omega \cup \partial\Omega$. The points where the vertices of multiple triangles coincide are known as nodes; for each node bearing index 'j' $= 1, \ldots, n$, there is a basis function ϕ_{j} that is only non-zero on the triangles for which this node is a vertex. In the simplest case (P_1), ϕ_{j} is a piecewise linear basis function that is 1 at the node 'j' and 0 at all others. This choice of basis functions leads to a sparse structure of the stiffness matrix, whose elements A_{ij} are only non-zero if the nodes 'i' and 'j' are on the same edge of an element; thus, a variety of numerical methods can be used for inverting A [10]. It is also possible to use a basis consisting of higher-order polynomials, for example quadratic (P_2);

when triangular P_2 elements are used, an additional node is introduced at the midpoint of each edge [10].

As for calculating A, the finite element method makes use of the triangulation of the domain Ω, presenting Eq. (1.17) as a sum of contributions from the individual elements,

$$\sum_{\mathrm{i}=1}^{n} u_{\mathrm{i}} \sum_{\mathrm{k}=1}^{K} \int_{\Delta_{\mathrm{k}}} \nabla\phi_{\mathrm{j}} \cdot \nabla\phi_{\mathrm{i}} =$$

$$\sum_{\mathrm{k}=1}^{K} \int_{\partial\Omega_{\mathrm{N}} \cap \partial\Delta_{\mathrm{k}}} \phi_{\mathrm{j}} g_{\mathrm{N}} + \sum_{\mathrm{k}=1}^{K} \int_{\Delta_{\mathrm{k}}} \phi_{\mathrm{j}} f - \sum_{\mathrm{k}=1}^{K} \sum_{\mathrm{i}=n+1}^{n+n_{\mathrm{D}}} \int_{\Delta_{\mathrm{k}}} u_{\mathrm{i}} \nabla\phi_{\mathrm{j}} \cdot \nabla\phi_{\mathrm{i}}. \tag{1.20}$$

For the case of P_1 triangles, only three of the *global* basis functions $\{\phi_1, \ldots, \phi_n\}$ are non-zero on the arbitrary element Δ_{k}. Restricting these three functions to zero outside Δ_{k} yields the element basis set $\{\psi_{\mathrm{k},1}, \psi_{\mathrm{k},2}, \psi_{\mathrm{k},3}\}$. Using that, the solution within this element can be written as

$$u^{(\mathrm{k})} = \sum_{\mathrm{j}=1}^{3} u_{\mathrm{j}}^{(\mathrm{k})} \psi_{\mathrm{k,j}}. \tag{1.21}$$

The contribution of each element to the stiffness matrix is a 3x3 *element stiffness matrix*,

$$A_{\mathrm{ij}}^{(\mathrm{k})} = \int_{\Delta_{\mathrm{k}}} \nabla\psi_{\mathrm{k,j}} \cdot \nabla\psi_{\mathrm{k,i}}, \tag{1.22}$$

and a 3-dimensional element load vector is defined similarly,

$$f_{\mathrm{j}}^{(\mathrm{k})} = \int_{\partial\Omega_{\mathrm{N}} \cap \partial\Delta_{\mathrm{k}}} \psi_{\mathrm{k,j}} g_{\mathrm{N}} + \int_{\Delta_{\mathrm{k}}} \psi_{\mathrm{k,j}} f\,; \tag{1.23}$$

The definition (1.23) of $f_{\mathrm{j}}^{(\mathrm{k})}$ that only contains contributions from Neumann boundary conditions is typically used, and Dirichlet boundary conditions are imposed after the assembly of the global stiffness matrix. The calculation of $A_{\mathrm{ij}}^{(\mathrm{k})}$ and $f_{\mathrm{j}}^{(\mathrm{k})}$ is simplified by utilizing a change of coordinates that maps every triangle to the reference isosceles right triangle with vertices at (0, 0), (0, 1) and (1, 1). As the basis functions $\{\psi_{*,1}, \psi_{*,2}, \psi_{*,3}\}$, for this reference element are particularly simple, the calculation of the integrals in (1.22)-(1.23) becomes trivial; see Ref. [10] for more details.

When the stiffness matrices $A_{ij}^{(k)}$ and load vectors $f_j^{(k)}$ have been calculated for all elements in the domain Ω, it is necessary to assemble the global quantities A_{ij} and f_j. A key step towards this is the definition of the *connectivity matrix*. The latter is an n x 3 matrix whose element P_{kj} = i gives the global index 'i' of the node that is labelled 'j' within triangle 'k' [10]. The global stiffness matrix can then be initiated to zero and its components computed by cycling through the recursive relation

$$A_{P_{ki}P_{kj}} = A_{P_{ki}P_{kj}} + A_{ij}^{(k)}, \tag{1.24}$$

where 'i', 'j' go from 1 to 3 for every 'k' from 1 to the number of triangles, K. Similarly, the global load vector is obtained from the recursive formula

$$f_{P_{kj}} = f_{P_{kj}} + f_j^{(k)}, \tag{1.25}$$

where 'j' goes from 1 to 3 for every value of 'k'. Dirichlet boundary conditions can be imposed on the system in various ways, for example by first computing A_{ij} and f_j from Eqs. (1.24)-(1.25) for 'i', and 'j' from 1 to $n + n_D$. In this case, the diagonal elements A_{pp} are then set to 1 for all vertices 'p' on the boundary with Dirichlet data, the off-diagonal elements are set to 0, and the corresponding component of the load vector $\boldsymbol{f}$ are set to the value u_p required by the Dirichlet data.

Overall, the finite element solution of a problem of the type (1.11) with specified boundary conditions that make it well-posed is obtained in the following steps [10] – 1) tessellation of the solution domain Ω; 2) construction of the discrete Galerkin system; 3) solution of the latter; 4) a posteriori error estimation. In case the estimated error is higher than desired, the approximation can be improved by using a finer mesh or increasing the order of the shape functions and repeating stages 2)-4); this iterative process is then repeated until a solution of the desired accuracy is obtained. Time-dependent equations are typically solved via the method of lines, which applies the finite element method with respect to spatial variables, thus obtaining a system of ordinary differential equations in time that can then be solved numerically via finite differences.

As the exposition in this section suggests, the application of the finite element method to the system (1.7)-(1.10) requires multiple non-trivial steps, and for that reason we perform it in the commercial software package COMSOL Multiphysics

rather than in a custom implementation. Steps 1)-4) as detailed above can be performed in COMSOL; the latter enables the user to work with mesh elements of various types, and contains solvers that are both appropriate for a broad spectrum of problems and subject to user configuration [9]. These features make COMSOL suitable for the equations we encounter in this text and allow for precise control over their numerical solution. Making use of this software package enables us to focus on modelling physically relevant systems rather than on implementing numerical algorithms.

1.3. Examples of natural convective flows

This section gives a non-exhaustive overview of some commonly encountered natural convective flows and thus provides a broader context for the studies described in the later chapters of the thesis.

Natural convective phenomena have been extensively investigated in the literature, and a particularly large number of studies have been dedicated to the Rayleigh–Bénard problem for flow of a pure liquid between two horizontal solid plates held at different temperatures [11]. In the classic formulation of the problem, one plate is situated at $z = 0$ and the other at $z = L$, with the z-axis aligned opposite to the vector of gravity $\boldsymbol{g}$. The temperature of the lower one (T_{bottom}) is set to a higher value than that of the top (T_{top}); as the plates are solid, there is no relative motion between them and the fluid, i.e., $\boldsymbol{v} = 0$ at $z = 0$ and $z = L$. The latter requirement is known as a no-slip condition in the literature, see e.g. Ref. [12]. As this problem concerns a single-component fluid, the diffusion equation (1.7) is trivially fulfilled and the system is governed by the following set:

$$\partial_t T + \boldsymbol{v} \cdot \nabla T = \chi_0 \nabla^2 T; \tag{1.26}$$

$$\rho_0(\partial_t \boldsymbol{v} + \boldsymbol{v} \cdot \nabla \boldsymbol{v}) = -\nabla \Delta p + \eta_0 \nabla^2 \boldsymbol{v} - \rho_0 \alpha (T - T_{\text{bottom}}) \boldsymbol{g}; \tag{1.27}$$

$$\nabla \cdot \boldsymbol{v} = 0, \tag{1.28}$$

with $\alpha = (\rho_0)^{-1} \partial \rho / \partial T$ signifying the volumetric thermal expansion coefficient of the liquid. The system (1.26)-(1.28) permits a stationary solution with no flow in

which the temperature only depends on the normal coordinate, and the buoyancy force in the Navier-Stokes equation is compensated by a vertical pressure gradient,

$$\bar{T} = T_{\text{bottom}} + \frac{\left(T_{\text{top}} - T_{\text{bottom}}\right)z}{L} = T_{\text{bottom}} - z\Delta T/L; \tag{1.29}$$

$$\mathrm{d}\Delta\bar{p}/\mathrm{d}z = -\rho_0 \alpha z|\boldsymbol{g}|\Delta T/L; \tag{1.30}$$

$$\bar{\boldsymbol{v}} = \mathbf{0}. \tag{1.31}$$

However, under sufficiently large $\Delta T = T_{\text{bottom}} - T_{\text{top}}$, the solution (1.29)-(1.31) is unstable with respect to infinitesimal perturbations and transitions to a state with convective flow [5, 7]. Taking the perturbed state

$$T = \bar{T} + T'; \tag{1.32}$$

$$\Delta p = \Delta\bar{p} + \Delta p'; \tag{1.33}$$

$$\boldsymbol{v} = \boldsymbol{v}', \tag{1.34}$$

substituting in (1.26)-(1.27) and only taking the terms that are linear with respect to the perturbations, we arrive at

$$\partial_t T' - (\Delta T/L)v_z' = \chi_0 \nabla^2 T'; \tag{1.35}$$

$$\rho_0\, \partial_t \boldsymbol{v}' = -\nabla\Delta p' + \eta_0 \nabla^2 \boldsymbol{v}' - \rho_0 \alpha T' \boldsymbol{g}; \tag{1.36}$$

it follows from (1.34) that the continuity equation retains the form (1.28).

Nondimensionalizing the variables according to

$$\tilde{x}_{\mathrm{i}} = \frac{1}{L} x_{\mathrm{i}};\ \tilde{v}_{\mathrm{i}} = \frac{\rho_0 L}{\eta_0} v_{\mathrm{i}}';\ \tilde{p} = \frac{\rho_0 L^2}{\eta_0^2} p';\ \tilde{t} = \frac{\eta_0}{\rho_0 L^2} t;\ \tilde{T} = \frac{\rho_0 \chi_0}{\eta_0 \Delta T} T' \tag{1.37}$$

leads to the following form of the equations [5],

$$Pr\, \partial_{\tilde{t}} \tilde{T} = \tilde{\nabla}^2 \tilde{T} + \tilde{v}_z; \tag{1.38}$$

$$\partial_{\tilde{t}} \tilde{\boldsymbol{v}} = -\tilde{\nabla}\Delta\tilde{p} + \tilde{\nabla}^2 \tilde{\boldsymbol{v}} + Ra\tilde{T}\mathbf{e}_z, \tag{1.39}$$

$$\tilde{\nabla} \cdot \tilde{\boldsymbol{v}} = 0 \tag{1.40}$$

where we have introduced the Prandtl and Rayleigh numbers, $Pr = \eta_0/(\rho_0\chi_0)$ and $Ra = \alpha\rho_0 L^3|\boldsymbol{g}|\Delta T/(\eta_0\, \chi_0)$; it is evident from Eqs. (1.38)-(1.40) that the behaviour of the system is controlled by these two parameters. Assuming an oscillatory form for the perturbations and solving the corresponding eigenvalue problem yields the result that the solution with purely conductive heat transfer (1.29)-(1.31) becomes unstable if the Rayleigh number is increased beyond a critical value, Ra_{cr}. Ra_{cr} itself depends on the type of boundary conditions for the velocity at $z = 0$ and $z = L$, having the value of 1708 for two no-slip surfaces, 1101 for the combination of a no-

slip and a free boundary, and 658 for two free surfaces – see e.g. Ref. [13] for the full analysis. In general, the flows in the case with a free surface are driven by both buoyancy and surface tension effects; this is known as Bénard-Marangoni convection, see for example Ref. [14].

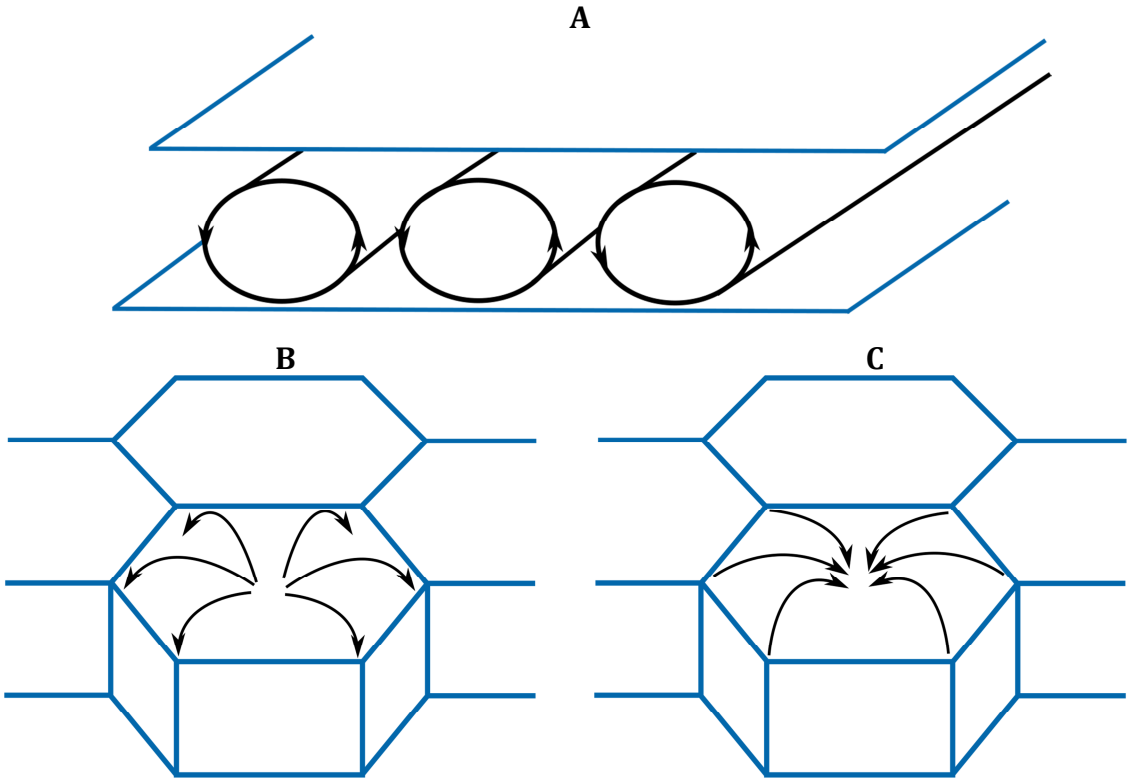


Figure 1.1. Sketches of some of the possible flow patterns in the Rayleigh-Bénard problem. **A** – rolls; **B** and **C** – hexagonal convection cells with upflow and downflow at the symmetry axis. Both roll and hexagonal roll flow patterns have been observed experimentally [12].

The case of thermal convection between two solid surfaces, i.e., Rayleigh–Bénard convection, is especially well-covered in the scientific literature. The convective instability that arises at $Ra > Ra_{cr}$ can bring about various flow patterns with internal circulation such as rolls that extend to infinity in one spatial direction, as well as hexagonal convective cells with upflow or downflow at the symmetry axis [15] – see Figure 1.1 for a schematic illustration. As the equations governing convection are non-linear, it is possible for a problem of the Rayleigh–Bénard type to have multiple solutions, and it is a non-trivial task to analyse the stability of

possible flows and determine which of them can be observed in practice [12]. A further complication is that solutions that appear equivalent in stability under the Boussinesq approximation (1.26)-(1.28) may in fact be distinguishable due to significant variation of the liquid properties with temperature [12]. For example, the dependence of viscosity on temperature causes the hexagonal flows with upward motion at the axis (Figure 1.1B) to be more common in liquids and those with downward flow at the axis (Figure 1.1C) – in gases [12].

In most of the following chapters of this thesis, we will not be concerned with the stability of the flows that our simulations predict. However, as some of the simulations in Chapter 5 yield different flow patterns depending on the discretisation used, we perform a qualitative stability analysis there. All results chapters of the thesis (3-6), which deal with different problems relevant to electrochemistry, contain examples of the complicated flow patterns that natural convection can generate. These flow patterns belong to a wider family that has been extensively studied via theory, simulation and experiment, see e.g. Refs. [15, 16] for more on this subject.

Natural convective flows are important in a much broader range of problems than the one we consider here – to give but a few examples, they are relevant in the study of the earth's atmosphere [12] and mantle [17], the heat transport in stars [12], industrial applications [12]; mixing due to natural convection can also be utilized in conducting chemical reactions at a laboratory scale, for example PCR [18]. In Chapter 2, we elaborate on the discussion of the relevance of natural convective flows in the specific context of this thesis, i.e., in the field of electrochemistry.

1.4. Electrode potentials

The next several sections (1.3-1.6) introduce key electrochemical concepts necessary for the later chapters of the thesis. We begin by discussing the definition of electrode potentials.

Electrochemical measurements are conducted in electrochemical cells; such a cell must generally include a minimum of two electrodes (electronic conductors) separated by at least one electrolyte phase (ionic conductor) [2]. In electrolytic cells, with which this thesis is concerned, an external potential difference applied between the electrodes drives a chemical reaction [2]. In principle, the cell potential, i.e., the voltage between the two electrodes in an electrochemical cell is defined as the difference between their Galvani potentials [19],

$$E_{\mathrm{cell}} = \phi_2 - \phi_1. \tag{1.41}$$

The Galvani, or inner potential of phase 'i' (ϕ_i) is defined through the electrical energy $e{\cdot}\phi_\mathrm{i}$ required for transporting a test charge from infinity to the interior of the phase [19]. Since the Galvani potential of an isolated phase cannot be determined, electrode potentials are measured relative to that of the standard hydrogen electrode (SHE), which by convention is taken to be zero [19]. The standard hydrogen electrode consists in a sheet of platinized platinum immersed in an acid solution which is subjected to bubbling with hydrogen with a pressure of 1 atm and has an activity of hydrogen cations of $a_{\mathrm{H^+}} = 1$[20].

We consider an electrochemical cell that consists of a working electrode at which the general oxidation reaction

$$\sum_{\mathrm{i}=1}^{n_\mathrm{R}} \nu_{\mathrm{R_i}} \mathrm{R_i} - n\mathrm{e}^- \rightleftarrows \sum_{\mathrm{i}=1}^{n_\mathrm{P}} \nu_{\mathrm{P_i}} \mathrm{P_i}, \tag{1.42}$$

occurs, with n_R being the number of reacting species and n_P – that of products; in this case, both $\mathrm{R_i}$ and $\mathrm{P_i}$ are in solution. This electrode is connected to a standard hydrogen electrode at which the reaction

$$n\mathrm{H}^+ + n\mathrm{e}^- \rightleftarrows n/2 \cdot \mathrm{H_2} \tag{1.43}$$

takes place. The cell potential for the overall reaction, given by the sum of Eqs. (1.42) and (1.43), is related to the molar Gibbs energy of the reaction as $E_{\mathrm{cell}} = \Delta G_{\mathrm{reaction}}/(nF)$, where $\Delta G_{\mathrm{reaction}}$ excludes electrostatic contributions, see Ref. [19]; note that $\Delta G_{\mathrm{reaction}}$ refers to the *oxidation* of the reactants $\mathrm{R_i}$ to the products $\mathrm{P_i}$. $\Delta G_{\mathrm{reaction}}$ is the sum of the chemical potentials μ_i of the species participating in the reaction. Thus, we obtain the expression

$$E_{\text{cell}} = \frac{1}{F}\left[\frac{1}{n}\left(\sum_{\text{i}=1}^{n_{\text{P}}} \nu_{\text{P}_\text{i}}\mu_{\text{i}} - \sum_{\text{i}=1}^{n_{\text{R}}} \nu_{\text{R}_\text{i}}\mu_{\text{i}}\right) + \frac{1}{2}\mu_{\text{H}_2} - \mu_{\text{H}^+}\right]. \tag{1.44}$$

The chemical potential of a species in solution is

$$\mu_{\text{i}} = \mu_{0\text{i}} + RT\ln a_{\text{i}}, \tag{1.45}$$

where $\mu_{0\text{i}}$ is its standard chemical potential and a_{i} is its activity, given by the product of its concentration (C_{i}) and activity coefficient (γ_{i})

$$a_{\text{i}} = \gamma_{\text{i}} C_{\text{i}}. \tag{1.46}$$

Using Eqs. (1.44)-(1.46) and noting that under the conditions of interest the chemical potentials of H_2 and H^+ are at their standard values, we obtain the Nernst equation for E_{cell}:

$$\begin{aligned} E_{\text{cell}} &= \frac{1}{F}\left[\frac{1}{n}\left(\sum_{\text{i}=1}^{n_{\text{P}}} \nu_{\text{P}_\text{i}}\mu_{0\,\text{i}} - \sum_{\text{i}=1}^{n_{\text{R}}} \nu_{\text{R}_\text{i}}\mu_{0\,\text{i}}\right) + \frac{1}{2}\mu_{0\,\text{H}_2} - \mu_{0\,\text{H}^+}\right] \\ &\quad + \frac{RT}{nF}\left(\ln\frac{\prod_{\text{i}=1}^{n_{\text{P}}}\gamma_{\text{i}}^{\nu_{\text{P}_\text{i}}}}{\prod_{\text{i}=1}^{n_{\text{R}}}\gamma_{\text{i}}^{\nu_{\text{R}_\text{i}}}} + \ln\frac{\prod_{\text{i}=1}^{n_{\text{P}}} C_{\text{i}}^{\nu_{\text{P}_\text{i}}}}{\prod_{\text{i}=1}^{n_{\text{R}}} C_{\text{i}}^{\nu_{\text{R}_\text{i}}}}\right) \\ &= E_{0\,\text{cell}} + \frac{RT}{nF}\left(\ln\frac{\prod_{\text{i}=1}^{n_{\text{P}}}\gamma_{\text{i}}^{\nu_{\text{P}_\text{i}}}}{\prod_{\text{i}=1}^{n_{\text{R}}}\gamma_{\text{i}}^{\nu_{\text{R}_\text{i}}}} + \ln\frac{\prod_{\text{i}=1}^{n_{\text{P}}} C_{\text{i}}^{\nu_{\text{P}_\text{i}}}}{\prod_{\text{i}=1}^{n_{\text{R}}} C_{\text{i}}^{\nu_{\text{R}_\text{i}}}}\right), \end{aligned} \tag{1.47}$$

where $E_{0\ \text{cell}}$ is the standard potential of the cell. As it is simpler to work with concentrations rather than activities, $E_{0\ \text{cell}}$ and the activity coefficient term in Eq. (1.47) are often combined in the formal potential E_{formal} so that

$$E_{\text{cell}} = E_{\text{formal}} + \frac{RT}{nF}\ln\frac{\prod_{\text{i}=1}^{n_{\text{P}}} C_{\text{i}}^{\nu_{\text{P}_\text{i}}}}{\prod_{\text{i}=1}^{n_{\text{R}}} C_{\text{i}}^{\nu_{\text{R}_\text{i}}}}. \tag{1.48}$$

Since only the reaction occurring at one of the electrodes is of interest in most electrochemical studies, it is also useful to define the half-cell potential E [2]. For reaction (1.42), the difference between this potential and that of the standard hydrogen electrode is also given by Eq. (1.48). In electrochemical experiments, the potential of the working electrode, i.e., the electrode at which the half-reaction of interest occurs, is typically measured and controlled with respect to a reference electrode. In most cases, the other half-reaction occurs at a counter electrode; this setup ensures that only a negligible current passes through the reference electrode and its potential can be treated as constant [2]. However, here we will exclusively consider the reaction occurring at the working electrode.

1.5. Nernstian boundary condition

The parts of this thesis dedicated to solving electrochemical mass-transport problems deal with one-electron oxidation reactions of the type

$$\text{Red} - \text{e}^- \rightleftarrows \text{Ox}. \tag{1.49}$$

The reaction (1.49) occurs at the interface between an electrode whose potential is set to E with respect to the standard hydrogen electrode and a solution containing a large excess of supporting electrolyte. We consider scenarios in which only the reduced form is present at $t = 0$ and its concentration is C_{bulk}; moreover, we neglect the difference in diffusion coefficients between the two species, adopting $D_{\text{Ox}} \approx D_{\text{Red}}$. The reaction occurs in a container with no-slip inner boundaries. This container has sufficiently large dimensions that the bulk of the solution remains unaffected over the duration of the experiment; for the specific cases studied here, this is equivalent to having no-flux mass transport boundary conditions everywhere on the inner walls of the container except on the electrode surface [3]. Under the specified conditions, the sum of the concentrations of Red and Ox remains equal to C_{bulk} at all times regardless of position [21],

$$C_{\text{Red}} + C_{\text{Ox}} = C_{\text{bulk}}. \tag{1.50}$$

Eq. (1.50) means that C_{Red} completely determines C_{Ox} and that it is only necessary to solve the diffusion equation for one of the species.

We assume that there is local equilibrium between Red and Ox, i.e., that the half-reaction reaction (1.49) is *electrochemically reversible*; therefore, at any moment in time, the concentrations C_{Red} and C_{Ox} are related through the Nernst equation. Thus, making use of the mass balance (1.50), we obtain the boundary condition

$$C_{\text{Red}}\big|_{\text{electrode}} = \frac{C_{\text{bulk}}}{1 + \exp\left[\dfrac{F(E - E_{\text{formal}})}{RT}\right]}. \tag{1.51}$$

Eq. (1.51) suggests that the quantity $\theta = F{\cdot}(E - E_{\text{formal}})/(R{\cdot}T)$ is a convenient nondimensionalization of the electrode potential.

1.6. Electrochemical current

The density of the electrochemical current generated by the electrochemical reaction from Section 1.5 is proportional to the diffusional mass flux at the electrode, and is given by the expression

$$i = FD_{\mathrm{Red}}\mathbf{n} \cdot \nabla C_{\mathrm{Red}}|_{\mathrm{electrode}}, \tag{1.52}$$

where **n** is the unit outward normal to the electrode surface. The sign in Eq. (1.52) is chosen so that the expression yields a positive oxidative current, as per the IUPAC sign convention for electrochemistry [3, 22]. The total current I is obtained by integrating i over the electrode surface S,

$$I = \int_S i \mathrm{d}S. \tag{1.53}$$

As we assume that all reactions studied here are reversible, the current (1.53) is limited by mass transport. Furthermore, by adopting eq. (1.52), we consider only the current due to the electrochemical reaction (the faradaic current), neglecting capacitive contributions.

1.7. Chronoamperometry

In this section and the ones following it (1.7-1.9), we briefly describe the electroanalytical techniques with which the later chapters of the thesis are concerned, beginning with chronoamperometry.

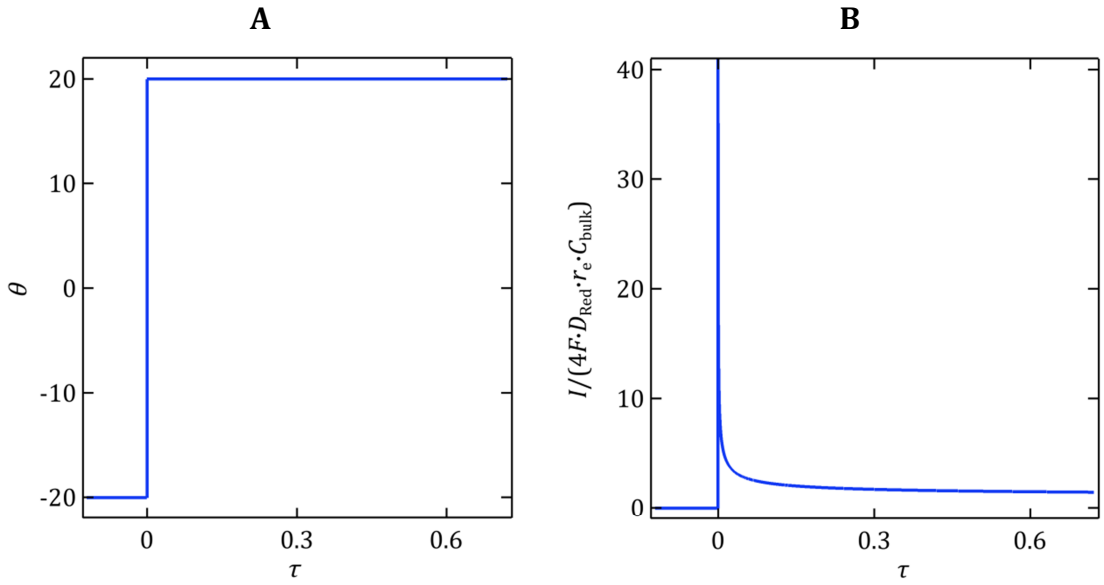


Figure 1.2. **A**. Dimensionless potential vs. time for the chronoamperometric studies in this thesis. **B**. Electrical current resulting from the potential step in **A** as a function of time as predicted by the Shoup-Szabo equation, (1.54). I is nondimensionalized with the steady-state value $4F{\cdot}D_{\mathrm{Red}}{\cdot}r_{\mathrm{e}}{\cdot}C_{\mathrm{bulk}}$ and t – with the diffusional time scale $r_{\mathrm{e}}^2/D_{\mathrm{Red}}$. The plots correspond to r_{e} = 250 µm, D_{Red} = 7.53×10^{-10} m^2·s^{-1} and T = 298.15 K.

Broadly speaking, chronoamperometric techniques consist in applying a potential to the studied solution and recording the resulting current as a function of time. Here, we will be concerned with the application of a single potential step to the system described in Section 1.5. The initial value of the electrode potential is chosen so that no electrochemical reaction occurs ($\theta \ll 1$), whereas at the step, the analyte is consumed by a strongly driven electrochemical redox reaction ($\theta \gg 1$) according to Eq. (1.49), i.e., we consider chronoamperometry (CA) performed under limiting current conditions [3]. The applied potential step and the resulting electrochemical current for this case are illustrated in Figure 1.2.

Specifically, we deal with a chronoamperometric oxidation occurring at a finite-sized disc-shaped electrode of radius r_{e}; the disc is embedded in an infinite insulating plane. Under purely diffusional mass transport, the total electrochemical

current for this case at $\theta \to \infty$ is approximated well by the Shoup-Szabo equation [23],

$$I = 4FD_{\mathrm{Red}}r_{\mathrm{e}}C_{\mathrm{bulk}}\left[0.7854 + 0.4431\frac{r_{\mathrm{e}}}{\sqrt{D_{\mathrm{Red}}t}} + 0.2146 \cdot \exp\left(-0.7823\frac{r_{\mathrm{e}}}{2\sqrt{D_{\mathrm{Red}}t}}\right)\right]$$
$$= 4FD_{\mathrm{Red}}r_{\mathrm{e}}C_{\mathrm{bulk}}\left[0.7854 + \frac{0.4431}{\sqrt{\tau}} + 0.2146 \cdot \exp\left(-\frac{0.7823}{2\sqrt{\tau}}\right)\right], \quad (1.54)$$

with $\tau = D_{\mathrm{Red}}t/r_{\mathrm{e}}^2$ being the dimensionless time for the problem. The numerical coefficients in Eq. (1.54) are chosen so that it gives the exact asymptote to the current at long time scales and fits data from simulations at all times. Note that the current diverges at t = 0 due to the infinitely high applied potential. In Chapter 3, we compare the results of simulations involving natural convection to the purely diffusive flux (1.54).

1.8. Cyclic voltammetry

In cyclic voltammetry (CV), the potential E of the working electrode in contact with the studied solution is varied over time. Information about the analyte is then extracted from the dependence of the measured electrochemical current on E. For all cases considered here, the potential is varied linearly from a value at which no reaction occurs (E_{i}) to one at which the reaction is strongly driven (E_{v}) and back. The dependence of electrode potential on time has the shape of a triangular wave

$$E = \begin{cases} E_{\mathrm{i}} + vt, t < t_{\max}/2; \\ 2E_{\mathrm{v}} - E_{\mathrm{i}} - vt, t \geq t_{\max}/2. \end{cases} \quad (1.55)$$

Here $t_{\max}$ is the duration of the potential scan, the potentials E_{i} and E_{v} are chosen so that they correspond to $\theta \ll 1$ and $\theta \gg 1$, respectively and $v = 2(E_{\mathrm{v}} - E_{\mathrm{i}})/t_{\max}$ is the scan rate.

Under the conditions with which this thesis is concerned, the dependence of current on potential in cyclic voltammetry has a characteristic double-peaked form, as shown in Figure 1.3. The peaks arise due to the competition between two effects – the change in the driving force of the reaction (θ) and the depletion of the reacting species in the region surrounding the electrode.

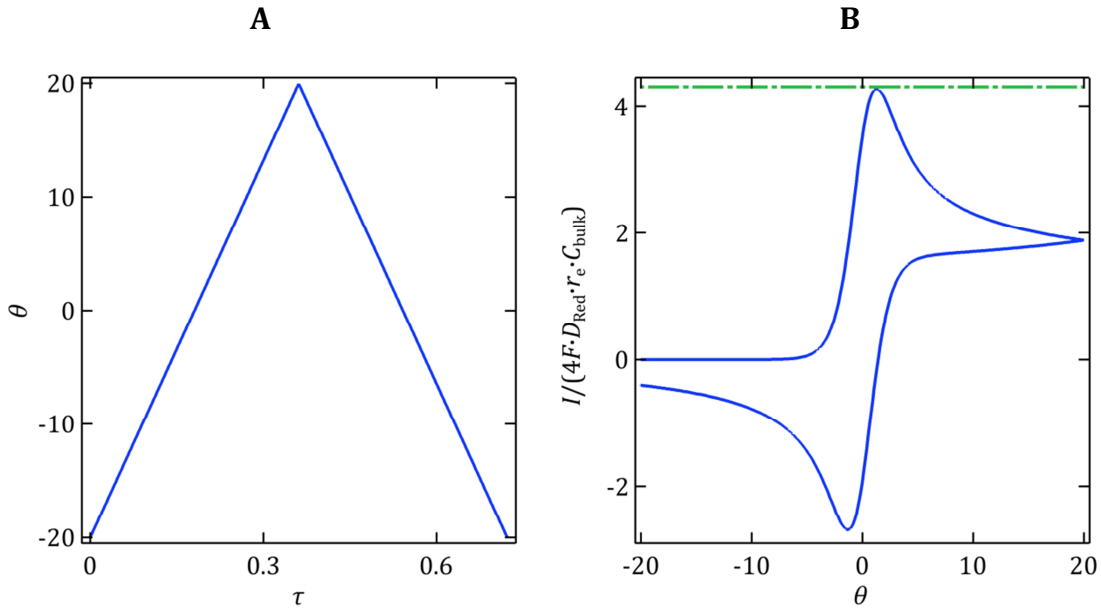


Figure 1.3. **A.** Dimensionless potential, $\theta = F(E_{\text{cell}} - E_{\text{formal}})/(R{\cdot}T)$, vs. dimensionless time $\tau = D_{\text{Red}}t/r_{\text{e}}^2$, corresponding to Eq. (1.55). **B**. Simulated current as predicted by a simulation that only involves diffusional mass transport (solid line); peak current (dashed line) as per Eq. (1.56). The plots correspond to r_{e} = 250 μm, D_{Red} = 7.53×10^{-10} $\text{m}^2{\cdot}\text{s}^{-1}$, v = 33.68 $\text{mV}{\cdot}\text{s}^{-1}$ and T = 298.15 K.

For the conditions under study, the height of the forward peak is approximated accurately by the empirical equation [3]

$$I_{\text{max}} = 4FD_{\text{Red}}r_{\text{e}}C_{\text{bulk}}\left(0.34\text{e}^{-0.66\sqrt{\sigma}} + 0.66 - 0.13\text{e}^{-\frac{11}{\sqrt{\sigma}}} + 0.351\sqrt{\sigma}\right), \quad (1.56)$$

where $\sigma = Fr_{\text{e}}^2v/(RTD_{\text{Red}})$ is the dimensionless scan rate.

Additionally, simple expressions exist for the peak-to-peak separation ΔE_{pp} and the midpoint potential E_{mid} for CV performed at electrodes sufficiently large in comparison with the maximum extent of the diffusion layer that edge effects are negligible. The peak-to-peak separation is then [3]

$$\Delta E_{\text{pp}} = 2.218RT/F. \quad (1.57)$$

The midpoint potential, which is halfway between that of the two peaks, is equal to the formal potential [24],

$$E_{\text{mid}} = \frac{E(I_{\text{max}})+E(I_{\text{min}})}{2} = E_{\text{formal}}. \quad (1.58)$$

In Chapter 3, we use the expressions given above to quantify the effect of natural convective flows on cyclic voltammetry.

1.9. Scanning electrochemical microscopy

Scanning electrochemical microscopy (SECM) is another common experimental method in electrochemistry. In it, the surface properties of a substrate are studied by way of rastering an electrode (tip) of micro- or nanometric dimensions in a plane above the said substrate [25]. Information is also extracted from measurements of the current passing through the electrode as a function of the vertical separation between it and the substrate; in certain variations of the technique, the current passing through the substrate is monitored as well [25]. The electrode is immersed in an electroactive solution and given a potential that drives a redox reaction; both voltammetric and chronoamperometric experiments can be performed [25]. The electrical properties and topographical features of the underlying substrate are determined through analysis of the current passing through the tip. Figure 1.3 schematically illustrates the setup of the technique.

Typically, only the current at the tip is measured; this is known as *feedback mode*. The current increases in magnitude as the tip approaches an electrically conducting substrate, which can act as an electrode. If the potential of the conducting substrate is set to an appropriate value, the reacting species may be regenerated at its surface (*positive feedback*) [25]. In contrast, the current decreases with tip-substrate separation for an insulating substrate (*negative feedback*) due to local depletion of the reactant [25]. Feedback mode is commonly applied to measuring the stationary current at the tip as a function of the normal separation between it and the substrate. The plot of this dependence is known as an *approach curve*; approach curves have been calculated for many experimentally encountered cases and it is thus possible to extract information about the geometry of the tip and reaction kinetics from such measurements [25].

Although steady-state SECM measurements are most common, it is also possible to apply transient approaches, such as chronoamperometry and cyclic voltammetry [25]. Moreover, SECM can be used for a broad range of purposes, such as characterization of solid|liquid and liquid|liquid interfaces, chemical modification of

surfaces, shape characterization of microelectrodes, kinetic studies of both heterogeneous and homogeneous reactions, and many others. The various implementations and applications of SECM have been exhaustively studied in the literature and reviewed many times, e.g. in Refs. [25-28].

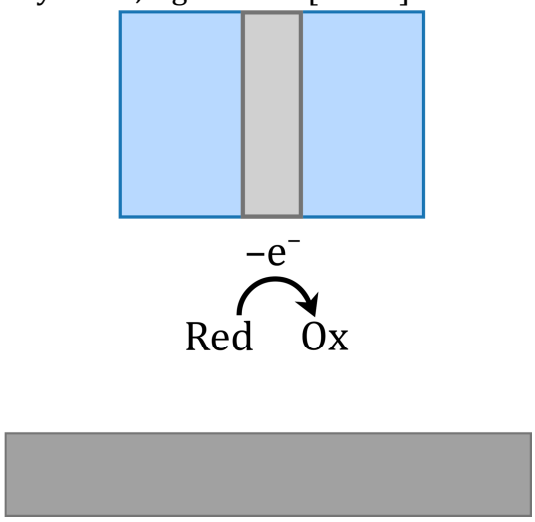


Figure 1.4. Schematic representation of an SECM experiment. The electrode (top) is typically disc-shaped and embedded in an insulating cylinder. Analysis of the current generated by the electrochemical reaction yields information about the properties of the substrate (bottom).

Explicitly modelling SECM is not within the aims of this thesis, but in Chapters 4-5, we will discuss two thermal convection problems relevant to this technique. Therein, we simulate a system based on a typical measurement cell for SECM and demonstrate that imperfect thermostating can generate significant natural convective flows. As special effort is rarely made to thermostat SECM experiments and the mass transport is typically assumed purely diffusional, these flows can potentially compromise experimental data from this technique.

1.10. References

[1] V.G. Levich, Physicochemical Hydrodynamics, Prentice-Hall, Inc., Englewood Cliffs, N.J., 1962.

[2] A.J. Bard, L.R. Faulkner, Electrochemical Methods: Fundamentals and Applications, Second ed., John Wiley & Sons, Inc., New York, 2001.

[3] R.G. Compton, E. Laborda, K.R. Ward, Understanding Voltammetry: Simulation of Electrode Processes, Imperial College Press, 2014.

[4] R.B. Bird, W.E. Stewart, E.N. Lightfoot, Transport Phenomena, Second ed., John Wiley & Sons, New York, 2002.

[5] L.D. Landau, E.M. Lifshitz, Fluid Mechanics, Second ed., Pergamon Press, Oxford, 1987.

[6] D.D. Gray, A. Giorgini, The Validity of the Boussinesq Approximation for Liquids and Gases, Int. J. Heat Mass Transfer, 19 (1976) 545-551.

[7] P.K. Kundu, I.M. Cohen, Fluid Mechanics, Second ed., Academic Press, San Diego, California, 2002.

[8] COMSOL Multiphysics, COMSOL AB, www.comsol.com.

[9] E.J.F. Dickinson, H. Ekström, E. Fontes, Comsol Multiphysics®: Finite Element Software for Electrochemical Analysis. A Mini-Review, Electrochem. Commun., 40 (2014) 71-74.

[10] H. Elman, D. Silvester, A. Wathen, Finite Elements and Fast Iterative Solvers, Oxford University Press, 2014.

[11] P. Bergé, M. Dubois, Rayleigh-Bénard Convection, Contemp. Phys., 25 (1984) 535-582.

[12] S. Richardson, On the No-Slip Boundary Condition, J. Fluid Mech., 59 (1973) 707.

[13] S. Chandrasekhar, Hydrodynamic and Hydromagnetic Stability, Clarendon Press, Oxford, 1961.

[14] C. Pérez-García, G. Carneiro, Linear Stability Analysis of Bénard–Marangoni Convection in Fluids with a Deformable Free Surface, Phys. Fluids A Fluid Dyn., 3 (1991) 292-298.

[15] F.H. Busse, Non-Linear Properties of Thermal Convection, Rep. Prog. Phys., 41 (1978) 1929-1967.

[16] E. Bodenschatz, W. Pesch, G. Ahlers, Recent Developments in Rayleigh-Bénard Convection, Annu. Rev. Fluid Mech., 32 (2000) 709-778.

[17] A. Fowler, Chapter 8: Mantle Convection, in: Mathematical Geoscience, vol. 36, Springer London, London, 2011, pp. 463-538.

[18] M. Krishnan, V.M. Ugaz, M.A. Burns, PCR in a Rayleigh-Bénard Convection Cell, Science, 298 (2002) 793-793.

[19] K.J. Vetter, Electrochemical Kinetics: Theoretical and Experimental Aspects, Academic Press, New York, 1967.

[20] E.R. Cohen, T. Cvitaš, J.G. Frey, B. Holmström, K. Kuchitsu, R. Marquardt, I. Mills, F. Pavese, M. Quack, J. Stohner, H.L. Strauss, M. Takami, A.J. Thor, IUPAC Green Book – Quantities, Units and Symbols in Physical Chemistry, 3rd Edition, 2nd Printing, IUPAC & RSC Publishing, Cambridge, UK, 2008.

[21] K.B. Oldham, S.W. Feldberg, Principle of Unchanging Total Concentration and Its Implications for Modeling Unsupported Transient Voltammetry, J. Phys. Chem. B, 103 (1999) 1699-1704.

[22] Analytical Chemistry Division Commission on Electroanalytical Chemistry Recommendations for Sign Conventions and Plotting of Electrochemical Data, Pure Appl. Chem., 45 (1976) 131-134.

[23] D. Shoup, A. Szabo, Chronoamperometric Current at Finite Disk Electrodes, J. Electroanal. Chem., 140 (1982) 237-245.

[24] R.G. Compton, C.E. Banks, Understanding Voltammetry, Second ed., Imperial College Press, London, 2011.

[25] A.J. Bard, M.V. Mirkin (Eds.), Scanning Electrochemical Microscopy, Second ed., CRC Press, Boca Raton, FL, 2012.

[26] P. Sun, F.O. Laforge, M.V. Mirkin, Scanning Electrochemical Microscopy in the 21st Century, Phys. Chem. Chem. Phys., 9 (2007) 802-823.

[27] M.V. Mirkin, W. Nogala, J. Velmurugan, Y. Wang, Scanning Electrochemical Microscopy in the 21st Century. Update 1: Five Years After, Phys. Chem. Chem. Phys., 13 (2011) 21196-21212.

[28] C.G. Zoski, Review—Advances in Scanning Electrochemical Microscopy (SECM), J. Electrochem. Soc., 163 (2016) H3088-H3100.

2. Survey of the Literature on Natural Convection in Electrochemical Systems

Here, we summarize some important studies related to natural convection in electrochemistry, placing a particular emphasis on recent papers concerned with modelling this phenomenon.

2.1. Solute-driven natural convection

Solute-driven convection arises when the temperature of the solution is homogeneous or can be approximated as such, but non-negligible density variations due to concentration gradients are present, making the first term in Eq. (1.6) significant. Electrochemical natural convective flows are difficult to avoid in solvents of comparatively low viscosity such as water [1] and although it is recognized that they can contribute to the measured currents [1], particularly at long times [2], they have not been thoroughly studied in the literature due to the modelling difficulties they pose.

Nevertheless, some specific cases are well-studied, notably the electrodeposition of metals under limiting current conditions. A simple model that can be applied to this case is that for steady natural convection next to a vertical plate at whose surface the reacting species is completely depleted by a mass-transport controlled chemical reaction. In contrast with the Rayleigh–Bénard problem (see Section 1.3), natural convection sets in without a stability threshold at vertical electrodes [3]. The latter case has been treated by Levich [1], who solved the steady Boussinesq equations (1.7) and (1.9)-(1.10) in the boundary-layer approximation. Working under the assumption that the boundary layers for mass and momentum transfer coincide, he derived the following expression for the total mass flux through the plate:

$$J = 0.9 \cdot \left(\frac{\eta_0}{\rho_0 D}\right)^{1/4} \left[\frac{g\rho_0}{4\eta_0^2} C_0 \left(\frac{\partial \rho}{\partial C}\right)_{C=C_0}\right]^{1/4} W h^{3/4} C_0 D \,, \tag{2.1}$$

with C_0 signifying the bulk concentration of the reacting substance, D – its diffusion coefficient, W – the width of the plate and h – its height. It is convenient to work with J in dimensionless form, i.e., with the Sherwood number,

$$Sh = \frac{J}{WDC_0} = \frac{0.9}{\sqrt{2}} \cdot \left(\frac{\eta_0}{\rho_0 D}\right)^{1/4} \left[\frac{g\rho_0}{\eta_0^2} C_0 \left(\frac{\partial \rho}{\partial C}\right)_{C=C_0} h^3\right]^{1/4} = 0.64(Sc \cdot Gr)^{1/4}, \qquad (2.2)$$

where we have introduced the Schmidt number, $Sc = \eta_0/(\rho_0 D)$ and the Grashof number, $Gr = g\rho_0\ h^3 C_0(\partial\rho/\partial C)_{C=C_0}/\eta_0^2$ [4]. Expressions of the type (2.2) have been determined through analytical methods, as well as through fitting data from experiments or simulations. Analogous correlations exist for both the laminar and turbulent regime of other mass transport problems under limiting current conditions, such as the case of horizontal plate – see e.g. Ref. [5] for more on the subject.

The combined effect of natural convection and migration has also been studied, for example by Selman and Newman [6] who dealt with the electrodeposition of Cu^{2+} and the reduction of hexacyanoferrate (III) to hexacyanoferrate (II). They sought numerical solutions to the steady-state boundary-layer equations for the case of a vertical working electrode and found that at low support, the non-uniformity of the supporting electrolyte concentration can lead to a natural convective velocity profile substantially different from that for no support [6].

The natural convective mass and momentum transfer in the vicinity of vertical electrodes in the electrolysis of $CuSO_4$ have also been probed directly by methods such as holographic interferometry, e.g. by Awakura and Kondo [7]. The latter authors solved the boundary-layer transport equations and found good agreement between experiment and theory for currents much lower than the limiting value. Later, Fukunaka and Kondo [8] studied the same system, measuring the transient local concentration profiles via holographic interferometry and imaged the velocity field via suspending fine colophonium particles in the solution.

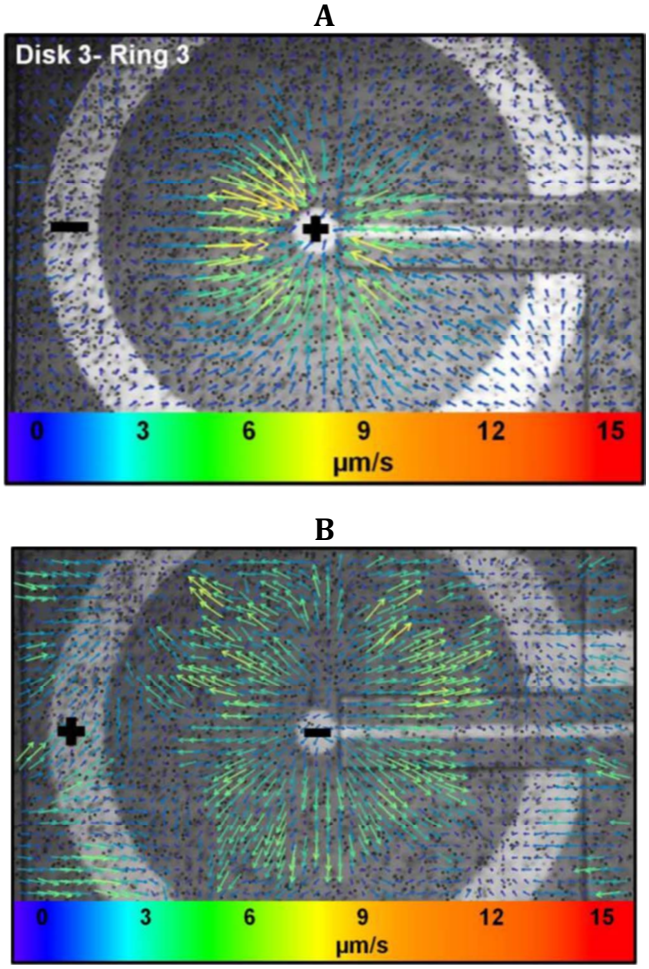


Figure 2.1. 'Snapshots' of the velocity distribution as visualized via PIV by Sahore et al. [9] in a ring-disc electrode setup. The solution under study contains 0.095 M $K_3[Fe(CN)_6]$ and 0.095 M $K_4[Fe(CN)_6]$ in 0.095 M KCl as the supporting electrolyte. $K_4[Fe(CN)_6]$ is oxidized at the anode, generating an upward buoyancy force, and $K_3[Fe(CN)_6]$ is reduced at the cathode. At a fixed vertical distance from the electrodes, the flow direction changes depending on whether the disc serves as the anode (**A**) or the cathode (**B**), indicating that the fluid motion is induced by the electrochemical reaction. The radius of the disc is 78 μm; the inner and outer radii of the ring are 800 and 1000 μm, respectively; the velocity is probed at a height of 320 μm above the plane of the electrodes; the label 'Disk 3 – Ring 3' reflects that the same experiment was conducted with ring-disc electrodes of various sizes. The figure is reprinted from Ref. [9] and licensed under the terms of the Creative Commons Attribution Non-Commercial No Derivatives 4.0 License (CC BY-NC-ND, http://creativecommons.org/licenses/by-nc-nd/4.0/).

Mühlenhoff et al. [3] used interferometry and shadowgraph imaging to investigate respectively the concentration and velocity profiles next to horizontal electrodes in a copper electrolysis cell. They showed that the presence of an electrochemically induced stable density gradient in the beginning of the electrolysis increased the time required for the onset of convection and constrained the emerging convective plumes [3].

Various other techniques have been used for the characterization of the flows arising due to natural convection, such as Schlieren imaging in the work of Patrick and Wragg [10]. They imaged the natural convective flow arising due to the chronoamperometric electrodeposition of copper at horizontal macrodisc electrodes at varying Rayleigh numbers. Patrick and Wragg observed flows consisting of a single plume with axial symmetry at $Ra \sim 10^5$ and complex three-dimensional multi-column flows above $Ra \sim 10^9$; the measured chronoamperometric current-time dependence in their experiments exhibited multiple extrema [10]. In a later paper, Wragg [11] summarized work on Schlieren imaging of natural convection for various electrode geometries.

More recently, velocity distributions in solute-driven natural convection have been characterized experimentally through particle image velocimetry methods [9, 12]. Sahore et al. [9] conducted experiments in solutions containing $[Fe(CN)_6]^{4-}$ and $[Fe(CN)_6]^{3-}$ over concentric ring-disc electrode systems of varying sizes. They observed circulatory flow patterns with maximum velocities of $\sim 10^{-5}$ m·s^{-1}, the direction of the former in a fixed horizontal plane above the electrodes being dependent on which electrode served as an anode and which as a cathode, as illustrated in Figure 2.1. Urban et al. [12] studied the enzymatic oxidation of O_2 at a vertical electrode in the absence of forced convection and obtained a peak current magnitude that exceeded the diffusion limit. Using particle image velocimetry (PIV), they determined that the local natural convective velocity in the solution had a maximum value of $\sim 10^{-4}$ m·s^{-1}. They conducted simulations with an added volume force corresponding to a velocity distribution similar to the measured one and

obtained improved correspondence with the experimental voltammograms in comparison with diffusion-only simulations [12].

Volgin and Davydov [13] summarized much of the important literature on natural convection between horizontal electrodes; their article points out the similarities and differences between electrochemical free convection and the classic Rayleigh–Bénard problem that we discussed in Section 1.3. The latter authors have been involved in other studies on this subject – notably, Bograchev and Davydov [14] considered the problem of solute-driven convection with full account for the dependence of the solution density on concentration and found that this more rigorous approach yielded a critical Rayleigh number that was higher by up to $\sim 10\%$ than the value predicted by the Boussinesq approximation.

More recently, Ehrl et al. [15] proposed a computational approach for the case of mass transport by diffusion, solutal convection and migration based on the finite element (FE) method and compared it against experimental data, as well as other models from the literature. The model in Ref. [15] was an extension of an earlier one that considered only forced convection and was proposed by the same group [16].

In another study, Nilson and Griffiths [17] considered the problem of natural convection in trenches subjected to filling by electrodeposition, a system relevant to industrial applications such as the LIGA (lithography, electroplating and molding) process for manufacturing microstructures. Through numerical simulations, they showed that solute-driven convection can substantially intensify the mass transport in such trenches [17]. Moreover, Nilson and Griffiths demonstrated that natural convective flow patterns with a single cell occupying the whole trench are more efficient at enhancing mass transport than multi-cellular patterns, and that the formation of the latter can be prevented by tilting the substrate containing the trench [17].

Solute-driven natural convection has been studied previously within the Compton group. Ngamchuea et al. [18] dealt with the effect of natural convection on fully supported chronoamperometry at horizontal disc-shaped electrodes of radius ~ 1 mm using Eqs. (1.7), (1.9)-(1.10) and a form of Eq. (1.6) that only accounted for

the electroactive species. They simulated the chronoamperometric oxidation of a dilute (9.5 mM) solution of $[Fe(CN)_6]^{4-}$ and showed that at a time scale of 1 min, natural convection could account for a significant contribution to the total current (17-38%), if the electrode was positioned so that a less dense species was generated at the bottom of the electrochemical cell [18]. The predicted effect of orientation on the importance of natural convection was in qualitative agreement with earlier experimental studies, such as the one on cyclic voltammetry by Gao et al. [19]. Ngamchuea et al. [18] were mainly concerned with the order of magnitude of the effect and did not consider the difference in diffusivity between the reduced and oxidized form or the influence of the supporting electrolyte on the density profile. The latter has been treated in some detail in a recent paper by Feldberg and Lewis [20], who analysed the density differences arising due to electrochemical reactions under the assumption that the diffusivities of all present species are equal.

2.2. Temperature-driven natural convection

As Eq. (1.6) implies, local variations in temperature can also drive natural convective flows; this is known as thermal convection. This type of free convection has been extensively studied in the literature, see for instance Sections 4 and 5 in Ref. [21] for an overview of important results on the subject.

In a recent study on temperature-driven natural convection, Amaya-Ventura and Rodríguez-Romo [22] demonstrated the applicability of the lattice Boltzmann method to an enzymatic reaction occurring at the membrane interface between an immobilized enzyme and a solution. They monitored the response of the simulated system through electrodes at the bottom of the porous enclosure containing the enzyme. Due to the large imposed temperature difference between the electrodes and the environment ($\Delta T \sim 30$ K), the authors neglected the influence of the reaction on ρ in Eq. (1.6), thus decoupling the governing equations for the species concentrations from those for momentum and temperature.

Ribeiro et al. [23] performed cyclic voltammetry under conditions of temperature-driven natural convection. In their experiments, the measurement cell was initially heated via a thermal bath and cooled down to the desired working temperature under ambient conditions. Thereafter, voltammetric experiments were performed; the currents recorded in them exhibited oscillations. Ribeiro et al. [23] modelled this oscillatory behaviour by solving the one-dimensional convection-diffusion equation with a coordinate-independent fluctuating convective velocity whose average was zero. Their expression for the amplitude of the velocity fluctuation depended exponentially on the solution temperature and led to good agreement with the experimental data; the oscillations in the simulated current were similar in magnitude to the measured ones [23].

In another work on thermal convection, Huang and Chao [24] performed finite-element simulations of the flow patterns generated by local heating from two wires situated at the bottom of a liquid layer. They analysed the behaviour of the system as a function of the relevant dimensionless numbers for the problem and constructed a stability map of the possible flow regimes. From their simulations, they determined the pattern resolution, defined through the minimum separation between the wires at which the flows generated by them were distinguishable, and obtained good agreement with experimental data. Furthermore, they showed that, if the dimensionless numbers characterizing the flow were in a particular region, the flow resolution could be tuned by varying the Prandtl and Grashof numbers of the system.

Temperature-induced free convection is the subject of Chapters 4-6 of this text. Chapters 4 and 5 deal with studies of thermal convection due to imperfect thermostating in a measurement cell for scanning electrochemical microscopy. In Chapter 6, we study the convective heat transfer in a thermostated cell for electrochemical measurements.

2.3. Temperature and solute-driven natural convection

Although considerably more scarce than that on purely thermal and purely solute-driven natural convection, there is a body of literature on convection driven by both temperature and concentration gradients (also known as thermosolutal or double diffusive convection [25]). An important study in this field is that of Gebhart and Pera [26], who considered thermosolutal convection at vertical electrodes via solving the steady Boussinesq equations in the boundary-layer approximation.

Thermosolutal convection has been investigated experimentally in an electrochemical context, e.g. by Kamotani et al. [25] who studied the natural convective flows arising in a rectangular enclosure with vertical electrodes. They imposed horizontal concentration and temperature gradients by controlling the potential and temperature of the electrodes, respectively. Kamotani and co-authors considered the cases of both opposing and cooperating driving forces for thermal and solutal convection, and reported that a multicellular flow pattern emerged when concentration-driven density variations were much larger than those due to temperature; unicellular flows occurred otherwise. For the opposing case, they observed that, as solute-driven convection was always dominant in their measurements, thermal convection did not affect mass transport significantly, i.e., that the Sherwood number *Sh* was a weak function of the thermal Grashof number Gr_T, the latter defined analogously to *Gr* for solutal convection [25]. For the cooperating case, *Sh* closely followed a correlation of type (2.2), but with *Gr* replaced by a generalized Grashof number accounting for both types of natural convection.

Combined thermal and solutal convection has also been studied in other configurations, see the work of Saraç et al. [27] and the references therein. In this paper, Saraç et al. [27] probed the natural convective flow past a horizontal cylinder electrode at which hexacyanoferrate (III) was reduced to hexacyanoferrate (II). The surface temperature of the cylinder was controlled and chosen so as to drive thermal convective flows in opposition to the ones caused by the electrochemical

reaction. Saraç et al. [27] observed the interplay between the flow patterns induced by the two types of natural convection via Schlieren imaging and correlated the Sherwood number for their system with a generalized Grashof number.

Recently, Pismensky et al. [28] examined the effect of combined natural and forced convection on the mass transport in electromembrane cells for desalination working under chronoamperometric and chronopotentiometric conditions. Following Taylor and Sharman [29], they expressed the electric current in their simulations of chronopotentiometry through a stream function, by analogy with incompressible fluid flow. They derived an expression relating the current and the concentration for a binary electrolyte under the electroneutrality approximation; their approach was clarified in a later paper [30]. In their model, the desalination and Joule heating at the membrane electrodes reduce the local solution density and generates a buoyancy force. Pismensky et al. [28] varied the intensity of the forced flow in the cell and estimated the conditions for the onset of natural convective flows; their simulated chronopotentiograms showed satisfactory agreement with experimental data.

We return to the problem of natural convective flows driven by gradients in both temperature and concentration in Chapter 3. There, we focus on the effect of the intrinsic enthalpy change of the studied electrochemical reaction on the currents measured in chronoamperometry and cyclic voltammetry.

2.4. Experimental approaches for minimizing free convection

A way of minimizing the contribution of natural convection to electrochemical measurements is to conduct them in highly viscous media [1]. Taking advantage of this, Aoki and co-workers [31, 32] performed voltammetric studies in solutions with added sodium alginate and demonstrated that convective currents were suppressed. They measured the voltammetric peak current, the solution electrical conductivity and viscosity as a function of the polymer concentration and found that the former two were approximately constant, while the latter increased greatly.

Aoki et al. [32] attributed these observations to the fact that the pores in the polymer network were much larger than the diffusing species and thus hardly affected their diffusion. Kang and Hwang [33] conducted cyclic voltammetry in agarose gels and also concluded that the polymer reduced free convection without affecting the diffusion coefficient of the species under study.

Park et al. [34] used a different approach for minimizing convection - they performed CV under conditions of reduced vibrations, thus obtaining better reproducibility of the measured current at low scan rates; they ascribed this improvement to reduced natural convection.

Ikeuchi et al. [35] reduced the effect of thermal convection in chronoamperometry at disc-shaped electrodes by using a temperature bath that maintained the temperature in their measurement cell homogeneous within ±3 mK. They determined the diffusion coefficient of ferrocene via a fit of the measured current to the Shoup-Szabo equation (1.54) at $t \leq 10$ s both under normal gravity and in microgravity. The agreement between the two sets of results led them to conclude that both temperature- and solute-driven convection had been eliminated in their experimental setup [35].

2.5. Electrochemical sensors that make use of natural convection

Electrochemical sensors utilizing natural convection have been developed in recent years. Sun and Agafonov [36] analysed the effects of solutal natural convection, diffusion and migration in a 4-electrode electrochemical accelerometer via FE simulations and compared the results obtained with the Boussinesq approximation to those for compressible flow. They came to the conclusion that the former was adequate for calculating the current at a single electrode, but not the difference between the currents at the two cathodes, which is used in measuring external accelerations [36].

Contento and Semancik [37] constructed a sensor consisting in a disc-shaped electrode of radius ~ 25 μm and an underlying microheater. These authors

performed CV at elevated temperatures and observed that upon raising the temperature from ≈ 293 to ≈ 353 K, the peak voltammetric current sees a threefold increase. Contento and Semancik compared the voltammetric currents obtained under these conditions against two types of finite-element simulations – a diffusion-only model and one that includes thermal convection, the latter giving currents closer to the experimental [37].

Boika and Zhao [38] constructed a heated SECM tip and reported that tip-substrate approach curves varied substantially with substrate conductivity at small separations.

2.6. Natural convection in fuel and thermogalvanic cells

Natural convective effects have been considered in electrochemical fuel cells. Antunes and Skrzypkiewicz [39] recently recorded current-versus-time curves for the chronoamperometric oxidation of CO at the anode of a direct carbon bed solid oxide fuel cell and fit them to a model expression derived under the assumption that CO is transported by diffusion and undergoes irreversible oxidation, obtaining a best-fit effective diffusion coefficient is of the order of 10^{-2} $m^2 \cdot s^{-1}$. They proposed that this high apparent value is due to a pressure gradient and a corresponding natural convective flow induced by the reverse Boudouard reaction occurring at the anode, $C + CO_2 \rightarrow 2CO$. The authors used a simple one-dimensional mass transfer model based on the assumption that convection is the predominant mode of transport and modelled the convective velocity via Darcy's law, as their study was concerned with flow through a porous medium [39].

Sikovsky et al. [40] simulated the heat transfer in an aluminium-air fuel cell, taking into account Joule heating and the heat flux due to the electrochemical reaction. They observed that thermal convection leads to fluctuations in the cell voltage, which were qualitatively confirmed by experimental data.

The thermogalvanic cell is another type of energy conversion device to which natural convection is relevant. Thermogalvanic cells convert heat into electrical

power and can be used to harvest waste heat [41, 42], the downside being their typical efficiency of well below 1% [41]. In devices of this type, a temperature difference between two electrodes generates a potential difference which in turn generates an electrical current. Recent simulations of such cells and demonstrated that natural convection can improve their efficiency several times [41, 42]. Salazar et al. [41] modelled the stationary mass, heat and momentum transport in a thermogalvanic cells, taking into account only thermal convection due to the large temperature difference between the two electrodes (60 K). Their simulations, which showed a five-fold increase in cell efficiency upon inclusion of natural convection in the model, compared favourably to literature experimental data. Gunawan et al. [42] observed that the maximum power output of a thermogalvanic cell depended strongly on its configuration, again attributing this to natural convection.

2.7. Bubble-induced convection

A problem of importance to many industrial processes is the bubble-induced convection in electrochemical systems [43]. Electrogenerated bubbles can affect the efficiency of such processes by inducing mixing, but also by altering the local electrical conductivity of the medium [43]. However, we should note that the description of such two-phase flows requires more involved equations than (1.6)-(1.10), see for instance Ref. [44].

Experimental and computational results pertaining to the common case of bubble convection at vertical electrodes were recently reviewed by Hreiz et al. [43], who highlighted the many difficulties of investigating such systems. Schillings et al. [45] recently simulated the bubble-induced flow in water electrolysis under conditions of both forced and natural convection and obtained adequate agreement with experimental results.

Interestingly, a number of recent studies have eliminated the contribution of bubble-induced convection by performing experiments in reduced gravity [46-48]. Mandin and co-authors have applied this technique to the electrolysis of water [46]

and $CuSO_4$ [47], and Sakuma et al. [48] minimized convection in this manner in order to focus on the effect of electrode wettability.

2.8. Studies with an additional external force

Several recent articles have investigated convection driven by both the buoyancy force considered in Eq. (1.9) and an additional force, $\boldsymbol{F}_{\text{ext}}$. Strictly speaking, this case falls under the label of mixed convection, as it contains contributions from both natural and forced flows.

Wang and co-workers [49] observed improved rate of electrodeposition of copper and nickel under centrifugal acceleration aligned with the electric field. They also recently published a review on the subject of electrochemistry in centrifugal fields [50].

Natural convection is of particular importance for the key industrial processes of electrowinning and electrorefining, e.g. of copper. Free convective flows, typically combined with forced ones, not only affect the transport of metal ions, but also play a role in the transport of anode slime particles, which are a major source of contamination of the purified metal in electrorefining [51, 52].

Zeng et al. [51, 52] have recently performed detailed simulations of both of these processes on a laboratory scale. In Ref. [51], they used the finite-element method to simulate the transport of Cu^{2+} by convection, diffusion and migration in the presence of a vertical temperature gradient, as well as the transport of anode slime particles in a pilot-scale cell for copper electrorefining. Their cell had an inlet at its bottom and an outlet at its top [51], as is conventional in electrorefining [52]. The simulated velocity profiles showed good agreement with the experimental ones, which were probed at a discrete set of points [51]. Zeng et al. also modelled the transport of slime particles in the solution and showed that the frequency of their appearance near the cathode correlates with the experimentally measured concentration of impurities in it [51].

Zeng et al. [52] also conducted simulations in order to compare conventional electrorefining cells with an inlet at the bottom and an outlet at the top, and ones with the reverse configuration. They showed that the latter design reduces the likelihood of slime particles reaching the cathode and warrants a more uniform distribution of Cu^{2+} in the solution, thereby allowing the electrodeposition process to be run at higher current densities and lower Cu^{2+} concentrations [52].

In another paper related to the purification of copper, Najminoori et al. [53] examined the free convective flow driven by concentration gradients and gas bubbles in a copper electrowinning cell via simulations and experiments.

An interesting area of research is the study of electrochemical systems subjected to magnetic fields. Electrochemical studies most often consider only the Lorentz force, $\boldsymbol{F}_{\text{Lorentz}} = \boldsymbol{J}\times\boldsymbol{B}$, where $\boldsymbol{J}$ is the electrical current density and $\boldsymbol{B}$ is the magnetic induction. Work concerning Lorentz force effects has been summarized by Monzon and Coey [54]; in another paper [55], they reviewed the effect of magnetic field gradients in electrochemistry. More recently, the effect of combined natural and magnetohydrodynamic convection on the electrodeposition of various materials has been studied, e.g. for Zn-Ni alloys [56] and copper [57, 58]. In particular, Refs. [57, 58] treated various magnetoelectrolysis problems by way of simulations and experiments, examining different orientations of the Lorentz force with respect to the buoyancy force. Baczyzmalski and co-authors dealt with Lorentz-force effects in bubble-driven convection at gas-evolving electrodes [59, 60]. In an experimental study, they showed that applying a magnetic field to a cell for water electrolysis can improve its efficiency by enhancing bubble detachment [59]. In another paper [60], they examined the effect of buoyancy and Lorentz forces on the evolution of a single H_2 bubble via both simulations and experiments.

2.9. Studies that utilize the analogy between heat and mass transfer

Under full support and appropriate boundary conditions mass and heat transfer are governed by equations of the same form. It is therefore possible to gain insight into

one process by probing the other. It is particularly useful that, if non-dimensionalized appropriately, the heat and mass fluxes obey analogous functional dependences [4]; for a discussion of the limitations of this analogy, see Section 22.3 in Ref. [4]. Electrochemical experiments enable the study in reduced scale of systems that are otherwise difficult to investigate – for example, Lim and Chung [61] have used an electrochemical cell with a rod electrode to model the heat transfer in a chimney. Moon and Chung [62] studied the solutal time-dependent Rayleigh-Bénard flow in a copper electroplating experiment as a model for the cooling of the molten core of a nuclear reactor during an accident. In another paper, the same group [63] modelled the natural convective heat transfer past two staggered cylinders through an electrochemical experiment. In another recent study, Vogt [64] used the same analogy to derive expressions for the dimensionless mass flux under various conditions from correlations formulated for the heat flux.

2.10. Spontaneous convection?

In a paper from 2001, Amatore et al. [65] introduced the term 'spontaneous convection', which they defined as a mode of mass transport due to 'microscopic chaotic motion' in macroscopically still solutions, underlining that it is distinct from forced or natural convection. The concept has since been invoked in numerous recent papers, e.g. Refs. [33, 66-73]. The model for spontaneous convection in [65] '. . . is based on a seminal idea introduced by Levich, and shows that in macroscopically still solutions microscopic chaotic motion has the same effect as an apparent [distance-dependent] diffusion coefficient . . .'. The model references Levich's monograph [1] and utilizes equations appearing in Chapter III of that book. However, Levich's equations cited in Ref. [65] relate to the case of a macroscopic *turbulent* flow past a solid wall; the author of the present thesis was unable to find any discussion of this type of microscopic chaotic motion in *stagnant* solutions in

Ref. [1][2]. Of course, chaotic motion on the molecular scale does occur in stagnant solutions and underpins diffusional processes (see for example Ref. [75]), but it is accounted for through the molecular diffusion coefficient of the species. Below, we compare Levich's model and that of [65], highlighting apparent contradictions in the latter.

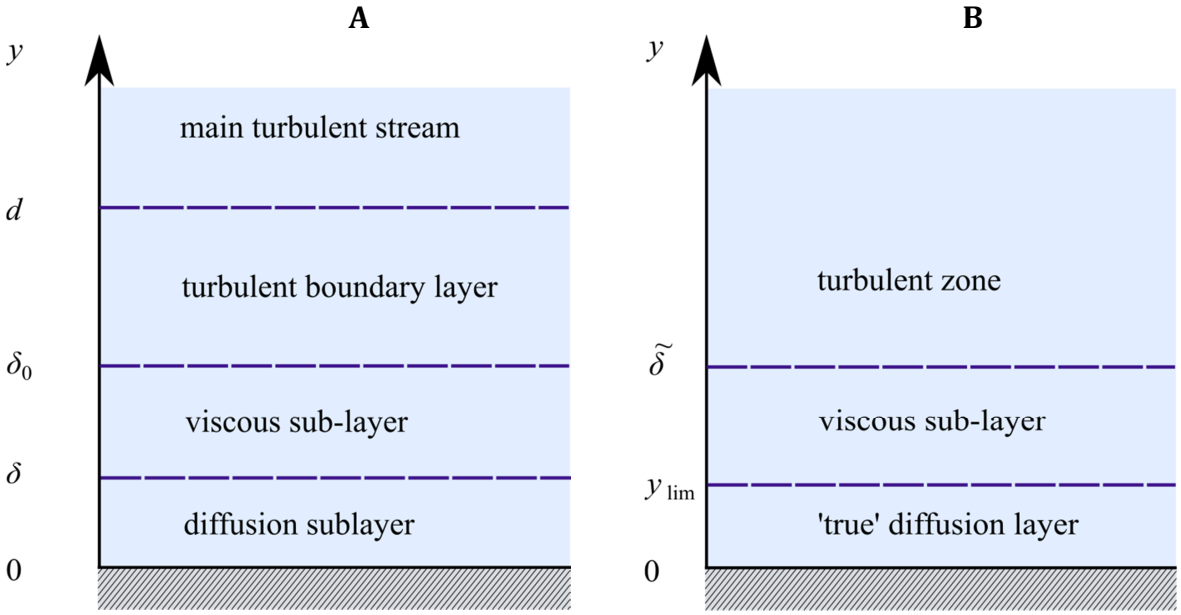


Figure 2.2. Layered structure of the concentration profile next to a flat wall. **A** – for turbulent flow, as given in Levich's monograph [1]. **B** – visual representation of the structure of the concentration profile for the model of Amatore et al. [65]. Both the scheme and the symbol $\tilde{\delta}$ in **B** are introduced by the author of this thesis based on the model from Ref. [65].

Levich's model, which Amatore and co-authors adopt, posits a four-layer structure of the concentration profile under conditions of turbulent flow next to an infinite solid flat plane, as illustrated schematically in Figure 2.2A. Large normal distances from the wall ($y > d$) correspond to the region of *developed turbulence*, where the solution is well-mixed and the concentration is homogeneous. Closer to the wall ($d > y > \delta_0$), there is a *turbulent boundary layer* in which both mass and

[2] Both the English translation of the book [1] and the second edition in Russian on which it is based [74] were consulted.

momentum transport occur mainly via turbulent eddies with a characteristic length scale of y. The mass flux j can be written as $j \propto D_{\text{turb}} \partial C/\partial y$, where D_{turb} is an effective diffusion coefficient that takes into account turbulent mass transport; for this region, $D_{\text{turb}} \propto y$. At still smaller y ($\delta_0 > y > \delta$), in the *viscous sub-layer*, momentum transport occurs predominantly via molecular viscosity, but mass transport is still mostly through turbulent eddies, whose characteristic scale is $\propto y^2$; within this sub-layer, $D_{\text{turb}} \propto y^4$. In this view of turbulence, the retarding effect of the solid wall is strong enough to make molecular diffusion the dominant mode of mass transport only in the *diffusion sub-layer* of thickness δ, $\delta < \delta_0$. For a detailed discussion of the subject, see Sections 4 and 24-25 of Levich's book [1].

Citing Levich [1], Ref. [65] explains discrepancies between data from electrochemical experiments and a simple diffusion-only mass transport model by postulating that macroscopically still solutions exhibit 'microscopic turbulence'. The latter is assumed to give rise to viscous and 'true' diffusion sub-layers next to the surface of a flat macroelectrode, with boundaries at normal distances of $y = \tilde{\delta}$ and $y = y_{\text{lim}}$, respectively (Figure 2.2B). Amatore et al. suppose that for the cases of interest the concentration reaches its bulk value within a distance $\tilde{\delta}$ (our notation) from the surface and exclusively consider $y < \tilde{\delta}$. For the viscous sub-layer, they assert that there is a convective contribution to the diffusion coefficient, $D_{\text{app}} = D + D_{\text{conv}}$, and that $D_{\text{conv}} \propto (y/y_{\text{lim}})^4$. However, as pointed out above, this functional dependence on distance is for the case of turbulent flows at *large Reynolds* numbers (typically, at $Re \gtrsim 1500$ [1]), namely, flows that involve intense macroscopic fluid motion. Applying the equation in question to a macroscopically still solution, for which the Reynolds number is zero, represents a major leap from the model in Ref. [1]. We next discuss the problematic points which arise as a consequence of that jump.

As we see from the comparison between the models in [1] and [65], the role of y_{lim} is equivalent to that of δ, i.e., both give the thickness of the layer in which diffusion is the predominant mode of mass transport. Thus, we can take the value of $y_{\text{lim}} = 2.3\times10^{-4}/1.108 = 2.08\times10^{-4}$ m from [65] and use Levich's equation 25.16,

$\delta = (10^3 D\nu^3/\gamma)^{1/4}/v_0$, to determine the velocity of the turbulent eddies characteristic of the flow in Levich's model, v_0; here, ν is the kinematic viscosity of the medium, and γ is a numerical constant 'not greatly different from unity' [1]. Specifically, as comparison between Eq. 25.11 in Ref. [1] and Eq. 9 in Ref. [65] shows, Amatore et al. implicitly set $\gamma = 1$. In this way, we obtain that for the system in question, the *turbulent eddies* in a *macroscopically still solution* postulated in [65] would have to have a characteristic velocity v_0 of the order of 10^{-3} m·s^{-1}! Moreover, accepting the analogy with Levich's model, we see that in the presumed turbulent zone, $y > \tilde{\delta}$, there are eddies of characteristic size $l \sim y$. $\tilde{\delta}$ itself is defined to be the distance from the surface at which the local Reynolds number for the eddies is of the order of 1, $Re = v_0 l(y)/\nu = v_0\tilde{\delta}/\nu \sim 1$. It follows that $\tilde{\delta} = a\nu/v_0$, where $a \sim 10$ [1], and for the case of Amatore et al. [65], $\tilde{\delta} \sim 10\times10^{-6}/10^{-3} \sim 10^{-2}$ m, which means that the smallest eddies in the turbulent sublayer have a characteristic size of the order of 1 cm and a characteristic velocity of the order of 10^{-3} m·s^{-1}! Such large-scale motion is incompatible with the core model assumption that the solution is *macroscopically still*, and eddies of this size and velocity could be observed by standard techniques for flow characterization, e.g., PIV, as seen for example in Ref. [76]. In Ref. [65], the authors appear to have adopted the Levich model [1] for eddy mass transport without taking into account that the eddies in question are caused by the bulk turbulent flow[3], and are therefore not present in a stagnant solution.

It is worth pointing out that the concept of an effective diffusion coefficient that contains convective contributions is not exclusively applicable to the turbulent regime. Such an approach been utilized for laminar flows, as in the Taylor dispersion problem for convective diffusion in Poiseuille flow (see Section 21 in Ref. [1]). However, this type of treatment is unsuitable to natural convective problems of

[3] Consult [1], page 22: "Together with these large scale eddies, turbulent flow also includes eddies of smaller scale λ, with lesser velocities v_λ. . . . The superposition of large scale eddies on each other creates small scale eddies, for which the Reynolds numbers rapidly decrease with decreasing λ.".

the type we study in this text, as the apparent diffusion coefficient would become a complicated function of the spatial coordinates and of time.

Apart from their work on D_{conv} in Ref. [65], Amatore and co-workers performed a number of experimental studies that suggest the involvement of convective effects under nominally diffusion-only conditions. In [65], the observed deviation of chronoamperometric currents at a macroelectrode from Cottrellian behaviour was satisfactorily accounted for using the expression for D_{conv} referenced above when δ was treated as an empirical adjustable parameter and D was chosen from a fit of the data at short times. In the follow-up papers to [65], CA was performed at macro- [77] and microsized disc electrodes [78]; CV was conducted for disc electrodes of various sizes [79]; concentration profiles were imaged in the vicinity of microdiscs [80]. Microband electrodes were considered as well – CV and CA were performed at a single electrode of this type [72], and CA was done in the case of a microband array [68]. The influence of electromigration was also studied in the same context for the case of macroelectrodes [81, 82]. Crucially, concentration profiles near electrodes were probed with a separate amperometric ultramicroelectrode [65, 77, 79, 81, 82] of radius between ≈ 0.5 [79] and 5 μm [82], or with SECM [68, 72, 78-80]; good agreement was found between the experimental currents and concentrations and the predictions of the 'spontaneous convection' model. In their later papers [68-70, 72, 73, 78-80, 82] Amatore and co-authors refer to the phenomenon which they assert to be the source of the deviation from purely diffusional behaviour as both 'natural convection' and 'spontaneous natural convection'.

The experiments referenced above were seemingly not thermostated; hence δ 'depends on the external environment and other phenomena such as local vibrations and temperature gradients' [72] and its value is reported to be between 135 [77] and 250 μm [72]. These experimental studies are important as they provide evidence for the role of convection in electrochemical experiments performed in a nominally quiescent solution – the latter has important implications for 'diffusion-only' voltammetry in general and SECM in particular.

2.11. Conclusions

As the research summarized in this chapter indicates, natural convection has been studied in relation with a broad spectrum of electrochemical phenomena, ranging from thermogalvanic and fuel cells to sensors. Natural convective effects are routinely taken into account in certain areas, e.g., the modelling of the electrorefining process, but are often ignored and have received little attention in electroanalytical contexts, not always with rigorous justification. The core chapters of this thesis (3-6) aim to address this issue and shed light on some important problems within that area.

2.12. References

[1] V.G. Levich, Physicochemical Hydrodynamics, Prentice-Hall, Inc., Englewood Cliffs, N.J., 1962.

[2] J.O.M. Bockris, A.K.N. Reddy, M.E. Gamboa-Aldeco, Modern Electrochemistry 2A: Fundamentals of Electrodics, Kluwer Academic Publishers, Boston, 2000.

[3] S. Mühlenhoff, K. Eckert, A. Heinze, M. Uhlemann, Controlled Retardation of Electrochemical Rayleigh–Bénard Convection During Copper Electrolysis, J. Electroanal. Chem., 611 (2007) 241-249.

[4] R.B. Bird, W.E. Stewart, E.N. Lightfoot, Transport Phenomena, Second ed., John Wiley & Sons, New York, 2002.

[5] T. Mizushina, The Electrochemical Method in Transport Phenomena, in: T.F. Irvine Jr., J.P. Hartnett (Eds.) Advances in Heat Transfer, vol. 7, 1971, pp. 87-161.

[6] J.R. Selman, J. Newman, Free-Convection Mass Transfer with a Supporting Electrolyte, J. Electrochem. Soc., 118 (1971) 1070-1078.

[7] Y. Awakura, Y. Kondo, Concentration Profile of $CuSO_4$ in the Cathodic Diffusion Layer, J. Electrochem. Soc., 123 (1976) 1184-1192.

[8] Y. Fukunaka, Y. Kondo, Momentum and Mass Transfer in the Transient Natural Convection Along Plane Vertical Electrode, Electrochim. Acta, 26 (1981) 1537-1546.

[9] V. Sahore, A. Kreidermacher, F.Z. Khan, I. Fritsch, Visualization and Measurement of Natural Convection from Electrochemically-Generated Density Gradients at Concentric Microdisk and Ring Electrodes in a Microfluidic System, J. Electrochem. Soc., 163 (2016) H3135-H3144.

[10] M.A. Patrick, A.A. Wragg, Optical and Electrochemical Studies of Transient Free Convection Mass Transfer at Horizontal Surfaces, Int. J. Heat Mass Transfer, 18 (1975) 1397-1407.

[11] A.A. Wragg, Use of Electrochemical Techniques to Study Natural Convection Heat and Mass Transfer, J. Appl. Electrochem., 21 (1991) 1047-1057.

[12] J. Urban, A. Zloczewska, W. Stryczniewicz, M. Jönsson-Niedziolka, Enzymatic Oxygen Reduction under Quiescent Conditions - the Importance of Convection, Electrochem. Commun., 34 (2013) 94-97.

[13] V.M. Volgin, A.D. Davydov, Natural-Convective Instability of Electrochemical Systems: A Review, Russ. J. Electrochem., 42 (2006) 567-608.

[14] D.A. Bograchev, A.D. Davydov, The Effect of Invalidity of Boussinesq Approximation on the Onset of Natural Convection in the Electrochemical System, Russ. J. Electrochem., 44 (2008) 453-458.

[15] A. Ehrl, G. Bauer, V. Gravemeier, W.A. Wall, A Computational Approach for the Simulation of Natural Convection in Electrochemical Cells, J. Comput. Phys., 235 (2013) 764-785.

[16] G. Bauer, V. Gravemeier, W.A. Wall, A Stabilized Finite Element Method for the Numerical Simulation of Multi-Ion Transport in Electrochemical Systems, Comput. Methods Appl. Mech. Eng., 223-224 (2012) 199-210.

[17] R.H. Nilson, S.K. Griffiths, Natural Convection in Trenches of High Aspect Ratio, J. Electrochem. Soc., 150 (2003) C401-C412.

[18] K. Ngamchuea, S. Eloul, K. Tschulik, R.G. Compton, Advancing from Rules of Thumb: Quantifying the Effects of Small Density Changes in Mass Transport to Electrodes. Understanding Natural Convection, Anal. Chem., 87 (2015) 7226-7234.

[19] X. Gao, J. Lee, H.S. White, Natural Convection at Microelectrodes, Anal. Chem., 67 (1995) 1541-1545.

[20] S.W. Feldberg, E.R. Lewis, Concentration and Density Changes at an Electrode Surface and the Principle of Unchanging Total Concentration, J. Electrochem. Soc., 163 (2016) H3167-H3172.

[21] A. Bejan, Convection Heat Transfer, Fourth ed., Wiley, Hoboken, N.J., 2013.

[22] G.A. Amaya-Ventura, S. Rodríguez-Romo, LBM for Cyclic Voltammetry of Electrochemically Mediated Enzyme Reactions and Rayleigh-Bénard Convection in Electrochemical Reactors, Heat Mass Transf., 48 (2012) 373-390.

[23] M.C. Ribeiro, L.G.C. Rego, P.C.T. D'Ajello, Effect of Intermittent Convection Movements on Voltammogram and Current Transients, J. Chem. Phys., 128 (2008) 054501.

[24] L.-T. Huang, L. Chao, Flow Patterning Capability of Localized Natural Convection, Phys. Chem. Chem. Phys., 18 (2016) 25380-25387.

[25] Y. Kamotani, L.W. Wang, S. Ostrach, H.D. Jiang, Experimental Study of Natural Convection in Shallow Enclosures with Horizontal Temperature and Concentration Gradients, Int. J. Heat Mass Transfer, 28 (1985) 165-173.

[26] B. Gebhart, L. Pera, The Nature of Vertical Natural Convection Flows Resulting from the Combined Buoyancy Effects of Thermal and Mass Diffusion, Int. J. Heat Mass Transfer, 14 (1971) 2025-2050.

[27] H. Saraç, A.A. Wragg, M.A. Patrick, Natural Convection Mass Transfer at a Horizontal Cylinder Electrode with an Opposed Thermal Buoyancy Effect, Electrochim. Acta, 38 (1993) 2589-2598.

[28] A.V. Pismensky, M.K. Urtenov, V.V. Nikonenko, P. Sistat, N.D. Pismenskaya, A.V. Kovalenko, Model and Experimental Studies of Gravitational Convection in an Electromembrane Cell, Russ. J. Electrochem., 48 (2012) 756-766.

[29] G.I. Taylor, C.F. Sharman, A Mechanical Method for Solving Problems of Flow in Compressible Fluids, Proc. R. Soc. A, 121 (1928) 194-217.

[30] S.A. Mareev, V.S. Nichka, D.Y. Butylskii, M.K. Urtenov, N.D. Pismenskaya, P.Y. Apel, V.V. Nikonenko, Chronopotentiometric Response of an Electrically Heterogeneous Permselective Surface: 3D Modeling of Transition Time and Experiment, J. Phys. Chem. C, 120 (2016) 13113-13119.

[31] B. Wang, K.J. Aoki, J. Chen, T. Nishiumi, Slow Scan Voltammetry for Diffusion-Controlled Currents in Sodium Alginate Solutions, J. Electroanal. Chem., 700 (2013) 60-64.

[32] K. Aoki, B. Wang, J. Chen, T. Nishiumi, Diffusion Coefficients in Viscous Sodium Alginate Solutions, Electrochim. Acta, 83 (2012) 348-353.

[33] H. Kang, S. Hwang, Electrochemical Characterization on the Hydrophobic Interaction and the Natural Convection within Agarose Gel, Int. J. Electrochem. Sci., 10 (2015) 9706-9713.

[34] K. Park, E. Kim, J.H. Park, S. Hwang, Influence of an Active Vibration Isolator and Electrochemical Cell Design on Electrochemical Measurements to Minimize Natural Convection, Electrochem. Commun., 82 (2017) 93-97.

[35] H. Ikeuchi, M. Kanakubo, Y. Watanabe, T. Naito, G.P. Satô, Chronoamperometric Determination of Diffusion Coefficients under Microgravity Conditions, J. Electroanal. Chem., 562 (2004) 105-110.

[36] Z. Sun, V.M. Agafonov, Numerical Modeling of a Four-Electrode Electrochemical Accelerometer Based on Natural Convection: The Boussinesq Flow Model Vs. The Compressible Flow Model, Russ. J. Electrochem., 48 (2012) 835-842.

[37] N.M. Contento, S. Semancik, Thermal Characteristics of Temperature-Controlled Electrochemical Microdevices, Sens. Actuators B, 225 (2016) 279-287.

[38] A. Boika, Z. Zhao, First Principles of Hot-Tip Scanning Electrochemical Microscopy: Differentiating Substrates According to Their Thermal Conductivities, Electrochem. Commun., 68 (2016) 36-39.

[39] R. Antunes, M. Skrzypkiewicz, Chronoamperometric Investigations of Electro-Oxidation of Lignite in Direct Carbon Bed Solid Oxide Fuel Cell, Int. J. Hydrogen Energy, 40 (2015) 4357-4369.

[40] D.P. Sikovsky, S.M. Kharlamov, V.I. Palymsky, K.G. Dobroselsky, M.G. Vlasenko, B.B. Ilyushin, Heat Transfer and Thermohydrodynamic Fluctuations in Aluminum–Air Fuel Cell, J. Eng. Thermophys., 24 (2015) 386-397.

[41] P.F. Salazar, S. Kumar, B.A. Cola, Design and Optimization of Thermo-Electrochemical Cells, J. Appl. Electrochem., 44 (2014) 325-336.

[42] A. Gunawan, H. Li, C.H. Lin, D.A. Buttry, V. Mujica, R.A. Taylor, R.S. Prasher, P.E. Phelan, The Amplifying Effect of Natural Convection on Power Generation of Thermogalvanic Cells, Int. J. Heat Mass Transfer, 78 (2014) 423-434.

[43] R. Hreiz, L. Abdelouahed, D. Fünfschilling, F. Lapicque, Electrogenerated Bubbles Induced Convection in Narrow Vertical Cells: A Review, Chem. Eng. Res. Des., 100 (2015) 268-281.

[44] A. Sokolichin, G. Eigenberger, A. Lapin, Simulation of Buoyancy Driven Bubbly Flow: Established Simplifications and Open Questions, AlChE J., 50 (2004) 24-45.

[45] J. Schillings, O. Doche, J. Deseure, Modeling of Electrochemically Generated Bubbly Flow under Buoyancy-Driven and Forced Convection, Int. J. Heat Mass Transfer, 85 (2015) 292-299.

[46] P. Mandin, Z. Derhoumi, H. Roustan, W. Rolf, Bubble Over-Potential During Two-Phase Alkaline Water Electrolysis, Electrochim. Acta, 128 (2014) 248-258.

[47] Z. Derhoumi, P. Mandin, H. Roustan, R. Wüthrich, Experimental Investigation of Two-Phase Electrolysis Processes: Comparison with or without Gravity, J. Appl. Electrochem., 43 (2013) 1145-1161.

[48] G. Sakuma, Y. Fukunaka, H. Matsushima, Nucleation and Growth of Electrolytic Gas Bubbles under Microgravity, Int. J. Hydrogen Energy, 39 (2014) 7638-7645.

[49] M. Wang, Z. Wang, Z. Guo, Deposit Structure and Kinetic Behavior of Metal Electrodeposition under Enhanced Gravity-Induced Convection, J. Electroanal. Chem., 744 (2015) 25-31.

[50] M. Wang, Z. Wang, X. Gong, Z. Guo, Progress toward Electrochemistry Intensified by Using Supergravity Fields, ChemElectroChem, 2 (2015) 1879-1887.

[51] W. Zeng, S. Wang, M.L. Free, Experimental and Simulation Studies of Electrolyte Flow and Slime Particle Transport in a Pilot Scale Copper Electrorefining Cell, J. Electrochem. Soc., 163 (2016) E111-E122.

[52] W. Zeng, S. Wang, M.L. Free, A Comparative Study of Electrolyte Flow and Slime Particle Transport in a Newly Designed Copper Electrolytic Cell and a Laboratory-Scale Conventional Electrolytic Cell, JOM, 69 (2017) 1876-1887.

[53] M. Najminoori, A. Mohebbi, B.G. Arabi, S. Daneshpajouh, CFD Simulation of an Industrial Copper Electrowinning Cell, Hydrometallurgy, 153 (2015) 88-97.

[54] L.M.A. Monzon, J.M.D. Coey, Magnetic Fields in Electrochemistry: The Lorentz Force. A Mini-Review, Electrochem. Commun., 42 (2014) 38-41.

[55] L.M.A. Monzon, J.M.D. Coey, Magnetic Fields in Electrochemistry: The Kelvin Force. A Mini-Review, Electrochem. Commun., 42 (2014) 42-45.

[56] V.R. Rao, A.C. Hegde, Effect of Induced Magnetic Field on Electrocrystallization of Zn-Ni Alloy and Their Corrosion Study, J. Mater. Eng. Perform., 23 (2014) 2067-2074.

[57] X. Yang, S. Mühlenhoff, P.A. Nikrityuk, K. Eckert, The Initial Transient of Natural Convection During Copper Electrolysis in the Presence of an Opposing Lorentz Force: Current Dependence, Eur. Phys. J. Special Topics, 220 (2013) 303-312.

[58] D. Koschichow, G. Mutschke, X. Yang, A. Bund, J. Fröhlich, Numerical Simulation of the Onset of Mass Transfer and Convection in Copper Electrolysis Subjected to a Magnetic Field, Russ. J. Electrochem., 48 (2012) 682-691.

[59] D. Baczyzmalski, T. Weier, C.J. Kähler, C. Cierpka, Near-Wall Measurements of the Bubble- and Lorentz-Force-Driven Convection at Gas-Evolving Electrodes, Exp. Fluids, 56:162 (2015).

[60] D. Baczyzmalski, F. Karnbach, X. Yang, G. Mutschke, M. Uhlemann, K. Eckert, C. Cierpka, On the Electrolyte Convection around a Hydrogen Bubble Evolving at a Microelectrode under the Influence of a Magnetic Field, J. Electrochem. Soc., 163 (2016) E248-E257.

[61] C.K. Lim, B.J. Chung, Influence of a Center Anode in Analogy Experiments of Long Flow Ducts, Int. Commun. Heat Mass Transfer, 56 (2014) 174-180.

[62] J.Y. Moon, B.J. Chung, Time-Dependent Rayleigh-Benard Convection: Cell Formation and Nusselt Number, Nucl. Eng. Des., 274 (2014) 146-153.

[63] J.H. Heo, M.S. Chae, B.J. Chung, Influences of Vertical and Horizontal Pitches on the Natural Convection of Two Staggered Cylinders, Int. J. Heat Mass Transfer, 57 (2013) 1-8.

[64] H. Vogt, Single-Phase Free Convective Mass Transfer in Electrochemical Reactors, Can. J. Chem. Eng., 94 (2016) 368-373.

[65] C. Amatore, S. Szunerits, L. Thouin, J.-S. Warkocz, The Real Meaning of Nernst's Steady Diffusion Layer Concept under Non-Forced Hydrodynamic Conditions. A Simple Model Based on Levich's Seminal View of Convection, J. Electroanal. Chem., 500 (2001) 62-70.

[66] A.S. Demeter, O. Dolgikh, A.C. Bastos, D. Deconinck, S. Lamaka, V. Topa, J. Deconinck, Multi-Ion Transport and Reaction Model Used to Improve the Understanding of Local Current Density Measurements in Presence of Concentration Gradients around a Point Current Source, Electrochim. Acta, 127 (2014) 45-52.

[67] L.C. Abodi, Y. Gonzalez-Garcia, O. Dolgikh, C. Dan, D. Deconinck, J.M.C. Mol, H. Terryn, J. Deconinck, Simulated and Measured Response of Oxygen SECM-Measurements in Presence of a Corrosion Process, Electrochim. Acta, 146 (2014) 556-563.

[68] C. Pebay, C. Sella, L. Thouin, C. Amatore, Mass Transport at Infinite Regular Arrays of Microband Electrodes Submitted to Natural Convection: Theory and Experiments, Anal. Chem., 85 (2013) 12062-12069.

[69] O.V. Klymenko, I. Svir, C. Amatore, New Theoretical Insights into the Competitive Roles of Electron Transfers Involving Adsorbed and Homogeneous Phases, J. Electroanal. Chem., 688 (2013) 320-327.

[70] O.V. Klymenko, I. Svir, C. Amatore, A New Approach for the Simulation of Electrochemiluminescence (ECL), ChemPhysChem, 14 (2013) 2237-2250.

[71] O. Dolgikh, A.S. Demeter, A.C. Bastos, V. Topa, J. Deconinck, A Practical Way to Model Convection in Non-Agitated Electrolytes, Electrochem. Commun., 37 (2013) 20-23.

[72] C. Amatore, C. Pebay, C. Sella, L. Thouin, Mass Transport at Microband Electrodes: Transient, Quasi-Steady-State, and Convective Regimes, ChemPhysChem, 13 (2012) 1562-1568.

[73] C. Amatore, O.V. Klymenko, I. Svir, Importance of Correct Prediction of Initial Concentrations in Voltammetric Scans: Contrasting Roles of Thermodynamics, Kinetics, and Natural Convection, Anal. Chem., 84 (2012) 2792-2798.

[74] V.G. Levich, Fiziko-Khimicheskaia Gidrodinamika, Second ed., Gos. izd-vo fiziko-matematicheskoi lit-ry, Moscow, 1959.

[75] E.L. Cussler, Diffusion: Mass Transfer in Fluid Systems, Third ed., Cambridge University Press, Cambridge, 2009.

[76] K.-Q. Xia, C. Sun, S.-Q. Zhou, Particle Image Velocimetry Measurement of the Velocity Field in Turbulent Thermal Convection, Phys. Rev. E, 68:066303 (2003).

[77] C. Amatore, S. Szunerits, L. Thouin, J.-S. Warkocz, Monitoring Concentration Profiles in Situ with an Ultramicroelectrode Probe, Electroanalysis, 13 (2001) 646-652.

[78] C. Amatore, C. Pebay, L. Thouin, A. Wang, J.S. Warkocz, Difference between Ultramicroelectrodes and Microelectrodes: Influence of Natural Convection, Anal. Chem., 82 (2010) 6933-6939.

[79] C. Amatore, C. Pebay, L. Thouin, A. Wang, Cyclic Voltammetry at Microelectrodes. Influence of Natural Convection on Diffusion Layers as Characterized by in Situ Mapping of Concentration Profiles, Electrochem. Commun., 11 (2009) 1269-1272.

[80] N. Baltes, L. Thouin, C. Amatore, J. Heinze, Imaging Concentration Profiles of Redox-Active Species with Nanometric Amperometric Probes: Effect of Natural Convection on Transport at Microdisk Electrodes, Angew. Chem. Int. Ed., 43 (2004) 1431-1435.

[81] C. Amatore, K. Knobloch, L. Thouin, First Direct Experimental Evidence of Migration Contributions through Monitoring of Concentration Profiles at Low Supporting Electrolyte Concentration, Electrochem. Commun., 6 (2004) 887-891.

[82] C. Amatore, K. Knobloch, L. Thouin, Alteration of Diffusional Transport by Migration and Natural Convection. Theoretical and Direct Experimental Evidences Upon Monitoring Steady-State Concentration Profiles at Planar Electrodes, J. Electroanal. Chem., 601 (2007) 17-28.

3. The Influence of Reaction-Induced Thermal Convection on the Electrical Currents Measured in Chronoamperometry and Cyclic Voltammetry

Overview

Electrochemical reactions invariably occur with a change in the molar volume between reactant and product, as well as a change in enthalpy. These factors give rise to natural convective flows driven respectively by concentration and temperature gradients and affect the mass transport in the system, but reaction-induced thermal convection in particular has received very little attention in the scientific literature. The present study attempts to fill this gap by quantifying the effect of the free convection generated by the intrinsic heat of an electrochemical reaction on the electrical currents in chronoamperometry and cyclic voltammetry. To this end, finite element numerical simulations of both electroanalytical techniques have been performed over a broad range of electrode radii (0.25 to 25 mm) for the electrochemical oxidation of hexacyanoferrate (II) to hexacyanoferrate (III). The results presented here indicate that for chronoamperometry, natural convection has a substantial *overall* effect on the current, but reaction-induced *thermal* convection in particular is practically negligible for the studied systems. In contrast, for cyclic voltammetry performed under similar conditions, neither type of convection plays a significant role.

3.1. Introduction

As we have stressed in the preceding chapters, natural convective flows arise in solutions that contain gradients of concentration and/or temperature. Given that electrochemical reactions bring about both types of gradients, mass transport by natural convection can never be completely eliminated in electroanalytical experiments such as chronoamperometry, cyclic voltammetry and scanning

electrochemical microscopy (SECM). However, natural convective flows are rarely considered in the literature as they significantly complicate the interpretation of data from these techniques. While the importance of natural convection can be minimized by employing low concentrations of the redox species, micro-sized electrodes and short experimental timescales [1], Ngamchuea et al. have recently demonstrated [2] that the assumption for purely diffusional mass transport may be severely restricted in certain experimental configurations.

In contrast to the case of *forced* convection, where the flow is imposed by an external factor (as with the rotating disc electrode), *natural* convective flows are driven by buoyancy forces arising within the fluid. Depending on the driving force, we can distinguish between two types of natural convection – one is driven by concentration gradients (solutal) and the other – by temperature gradients (thermal). Solutal convection unavoidably arises in the course of electrochemical processes – electrochemical reactions occur with a transfer of charge to or from the reacting species, which in turn leads to a change in its partial molar volume due to electrostriction [3, 4]. The importance of solute-driven natural convection in electrochemical systems has been discussed for various systems, e.g. reactions occurring at vertical macroelectrodes in the work of Selman and Newman [5] and cyclic voltammetry at macroelectrodes in an experimental study by Bond et al. [6] (see Section 2.3 for a more comprehensive overview of the literature on the subject). Nevertheless, the effect of natural convection due to density gradients is difficult to quantify and model and is usually assumed to be negligible. Gao et al. [7] demonstrated that this assumption is justified for microelectrodes and low analyte concentrations. However, according to a previous study by the Compton group [2], natural convection is important even at analyte concentrations as low as 10 mM for electrode radii of the order of 0.1 mm or larger. Furthermore, as both Gao et al. [7] and Ngamchuea et al. [2] show, the magnitude of the effect strongly depends on the orientation of the electrode.

Similarly, thermal convection in electrochemical systems is usually disregarded on the basis of the assumption that thermostating of the experimental cell

eliminates all variations in temperature. Temperature variations caused by external factors, e.g. heating of the electrode, have been studied in the literature, see e.g. Ref. [8] and Sections 2.2-2.3 of this thesis. The temperature variations induced by the change of enthalpy of the electrochemical process itself, however, have not received much attention.

Our aim[4] in the present study is to assess the importance of thermal convection driven by the intrinsic enthalpy change of an electrochemical process, thereby throwing light on a little-studied but ubiquitous phenomenon. As we are interested in determining whether the effect can become important under any circumstances, we will only consider configurations that maximize it, e.g. by choosing the electrode orientation that yields the largest possible effect and assuming that all of the heat generated by the electrochemical reaction is dissipated in the solution. Since the main purpose of this study is to establish whether convective effects are important under these optimal conditions rather than to quantify them precisely, we will restrict our treatment to the main effects in the system and neglect sources of additional complexity that do not lead to a qualitatively different behaviour. Effects that are present in our system, but not essential for its qualitative behaviour, will be neglected, e.g., the finite size of the insulating sheath in real systems and the influence of the nonelectroactive species on the variation in the solution density. Following Ngamchuea et al. [2], we will use the well-studied redox couple hexacyanoferrate (III)/ hexacyanoferrate (II) as a model system.

3.2. Theory

The first part of this section contains the mathematical equations that we use to describe the coupled thermal and solutal convection in electrochemical systems. In the second part, we give a brief outline of the simulation procedures we utilize in solving these equations.

[4] This chapter is based on a paper published in the *Journal of Physical Chemistry C* and co-authored by myself, S. Eloul and R.G. Compton [J.K. Novev, S. Eloul, R.G. Compton, J. Phys. Chem. C 120 (2016) 13549-13562].

3.2.1. **Model**

3.2.1.A *Mass transfer*

In this chapter, we study a single-electron electrochemical oxidation that occurs at the surface of a disc-shaped electrode,

$$\mathrm{Red} - \mathrm{e}^- \rightleftarrows \mathrm{Ox}. \tag{3.1}$$

The effect of a solute on density is dictated by its molar volume; as the latter depends on charge due to the electrostriction effect [3, 4], it is affected by the charge-transfer reaction (3.1). Furthermore, the reaction is accompanied by a change in enthalpy (ΔH), which means that, depending on the sign of ΔH, the electrode becomes either a heat source or a heat sink. The changes in both enthalpy and partial molar volume generate local variations in the density of the solution, and therefore, buoyancy forces.

Our goal in this study is to determine the effect of thermal convective flows induced by the heat intrinsic to the electrochemical reaction (3.1) on the electrical currents measured in chronoamperometric and voltammetric experiments. To do that, we need to solve the convection-diffusion equation for the reduced species,

$$\partial_t C_{\mathrm{Red}} + \boldsymbol{v} \cdot \nabla C_{\mathrm{Red}} = D_{\mathrm{Red}} \nabla^2 C_{\mathrm{Red}}, \tag{3.2}$$

where the notation is as in Chapter 1 – C_{Red} denotes the concentration of the reduced species, D_{Red} – its diffusion coefficient, t is time and $\boldsymbol{v}$ stands for the velocity field. In Eq. (3.2), we treat a system that contains an excess of supporting electrolyte and, hence, the influence of migration on the mass transport of the electroactive species is negligible [9, 10]. Eq. (3.2) also contains the approximation that the fluid is incompressible (see Eq. (3.28)). For the low velocities that arise in our system, this makes the calculations considerably simpler without introducing a significant error [11].

In our treatment of the problem, we neglect the difference between the diffusion coefficients of the oxidized and the reduced species, setting both to D_{Red}. As explained in Section 1.5, this approximation leads to

$$C_{\mathrm{Red}} + C_{\mathrm{Ox}} = C_{\mathrm{bulk}}, \tag{3.3}$$

where C_{Ox} refers to the concentration of the oxidized species and C_{bulk} is the initial concentration of the reduced species (see Eq. (3.4) below). The simple relationship between C_{Ox} and C_{Red} enables us to determine the concentrations of both species from the solution of Eq. (3.2) [9]. It is worth pointing out that in reality, the diffusion coefficient of the oxidized species is significantly higher than that of the reduced one [12]. Thus, here we underestimate the rate of diffusion of the oxidized species. Since the accumulation of the oxidized species is the factor that perturbs the local density distribution and thus drives the natural convective flow, we can expect that the real system would be less susceptible to convection because the density perturbation would dissipate more quickly via diffusion.

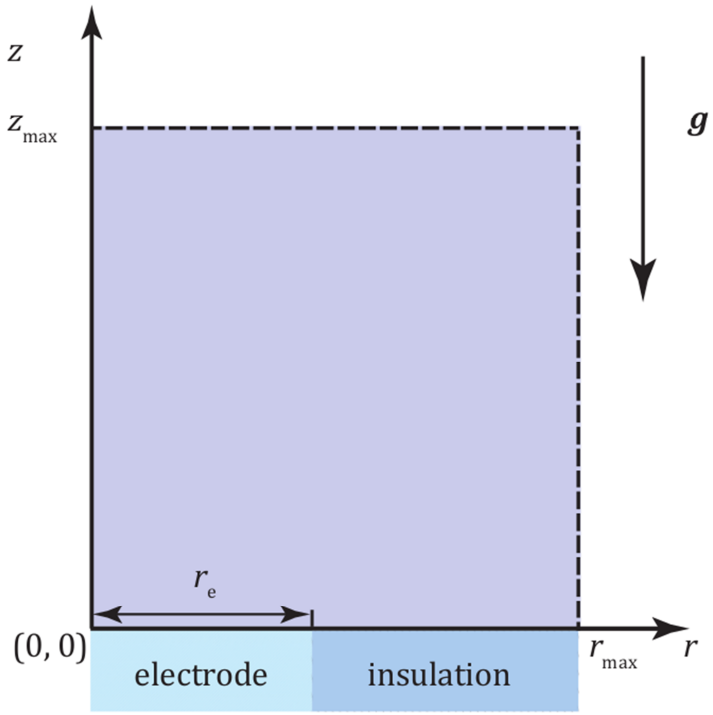


Figure 3.1. Schematic drawing of the simulated cell (not to scale). Because of the rotational symmetry of the problem, it is sufficient to solve the equations for a rectangular region of dimensions r_{max} by z_{max}. The coordinate origin is in the centre of the disc-shaped electrode of radius r_e. The annular region next to electrode, corresponding to $z = 0$ and $r_e < r < r_{max}$, is thermally and electrically insulated, i.e. no flux passes through it. The vector of gravitational acceleration is $\boldsymbol{g} = -|\boldsymbol{g}|\mathbf{e}_z$, where $\mathbf{e}_z$ is the unit vector in the normal direction.

We model a disc-shaped electrode in contact with a cylindrical volume of fluid of radius r_{max} and height z_{max}, see Figure 3.1. The dimensions r_{max} and z_{max} are chosen so that the perturbations in concentration, velocity and temperature caused by the chemical reaction are negligible at the boundaries of the simulated region. Thus, the simulations can be seen either as an approximation to the problem of an electrode situated in an infinite volume of fluid or as a model for a reaction occurring in a solid cylindrical container of radius r_{max} and height z_{max}.

Because of the symmetry of the simulated region, it is convenient to introduce cylindrical coordinates (r – radial, z – normal), with the coordinate origin at the centre of the disc electrode of radius r_e, as shown schematically in Figure 3.1. Due to the symmetry of the problem, all studied quantities are independent of the polar angle ϕ. The direction of the z-axis is opposite to that of the gravitational force, i.e., the electrode is situated at the bottom of the electrochemical cell – as shown by Ngamchuea et al. [2], this configuration corresponds to a maximum effect of natural convection on the chronoamperometric current. The annular region surrounding the electrode ($z = 0$, $r_e < r < r_{max}$) is made of a thermally and electrically insulating material and has a radius much larger than r_e.

At the start of the process, $t = 0$, only the reduced species is present, and we assume its concentration to be homogeneous and equal to C_{bulk},

$$C_{Red}(t = 0) = C_{bulk}. \tag{3.4}$$

At the boundaries of the simulated cell, the concentration is unperturbed from its initial bulk value,

$$C_{Red}(t, z = z_{max}) = C_{bulk}; \tag{3.5}$$

$$C_{Red}(t, r = r_{max}) = C_{bulk}. \tag{3.6}$$

Employing a boundary condition for the flux instead of the concentration at $r = r_{max}$ makes it easier to obtain an accurate numerical solution to the problem [9]. For that reason, the simulations were performed with

$$\left.\frac{\partial C_{Red}}{\partial r}\right|_{t, r=r_{max}} = 0 \tag{3.7}$$

instead of Eq. (3.6). The dimensions of the simulated domain, r_{max} and z_{max}, are chosen in such a way as to guarantee that none of the properties of the solution are

perturbed at the edges of the cell. At $r_e \sim 1$ cm or below, the perturbation in temperature spreads furthest (see Figures 3.8 in Section 3.3 below) to distances of the order of $L_{therm} \sim \sqrt{t_{max}\chi}$, where t_{max} is the duration of the simulated experiment and χ [$m^2 \cdot s^{-1}$] is the thermal diffusivity of the fluid. For that reason, simulations of electrodes of $r_e < 1$ cm were performed with $r_{max} = r_e + 6\sqrt{t_{max}\chi}$ and $z_{max} = 6\sqrt{t_{max}\chi}$. For $r_e > 1$ cm, the perturbations in the fluid velocity have the largest spatial extent, $L_{hydr} \sim r_e$ (see Figure 3.9 below), and the dimensions of the cell were chosen to be $r_{max} = z_{max} = 4 \cdot r_e$. The concentration profile needs to be symmetric around $r = 0$, i.e.

$$\left.\frac{\partial C_{Red}}{\partial r}\right|_{r=0} = 0. \tag{3.8}$$

Assuming that the electrode kinetics of the reaction (3.1) are fast in relation to the rate of mass transport, we can use a Nernstian boundary condition for the concentration of the reduced species at the electrode surface, see Section 1.5 and Ref. [9]:

$$C_{Red}|_{r \le r_e, z=0} = C_{bulk} \Big/ \left\{1 + \exp\left[\frac{F\left(E - E_{formal}\right)}{RT}\right]\right\}, \tag{3.9}$$

where notation is as in Chapter 1. The insulating surface acts as a reflecting boundary and therefore, there must be no normal flux through it:

$$\left.\frac{\partial C_{Red}}{\partial z}\right|_{z=0, r_e \le r \le r_{max}} = 0. \tag{3.10}$$

Applying the general definition (1.52) of the electrical current density i to the present case, we obtain

$$i = FD_{red}\left.\frac{\partial C_{Red}}{\partial z}\right|_{z=0}. \tag{3.11}$$

As per Eq. (1.53), the total electrical current (I) is the integral of Eq. (3.11) over the electrode surface,

$$I = 2\pi \int_0^{r_e} ir\mathrm{d}r. \tag{3.12}$$

3.2.1.B *Heat transfer*

The heat transfer in the system is coupled to the mass transport and, as we discussed in Section 1.1, to determine the concentration profile, we also need to solve the convective heat transfer equation,

$$\partial_t T + \boldsymbol{v} \cdot \nabla T = \chi \nabla^2 T, \tag{3.13}$$

where notation is again analogous to that in Chapter 1.

The boundary conditions for T at the edge of the cell, the initial condition and the symmetry condition are analogous to (3.4)-(3.8) for C_{Red},

$$T(t=0) = T_{\mathrm{bulk}}; \tag{3.14}$$
$$T(t, z=z_{\max}) = T_{\mathrm{bulk}}; \tag{3.15}$$
$$T(t, r=r_{\max}) = T_{\mathrm{bulk}}; \tag{3.16}$$
$$\left.\frac{\partial T}{\partial r}\right|_{r=0} = 0. \tag{3.17}$$

As with the mass transport problem, it is more computationally efficient to employ a Neumann boundary condition at $r = r_{\max}$ instead of Eq. (3.16):

$$\left.\frac{\partial T}{\partial r}\right|_{t, r=r_{\max}} = 0. \tag{3.18}$$

The cell dimensions are large enough to guarantee that the temperature at its edges remains unchanged, and thus Eq. (3.15) can also be replaced with a Neumann boundary condition,

$$\left.\frac{\partial T}{\partial z}\right|_{t, z=z_{\max}} = 0. \tag{3.19}$$

Due to the thermal insulation, the heat flux through $z = 0$ is zero at $r > r_{\mathrm{e}}$,

$$\left.\frac{\partial T}{\partial z}\right|_{z=0, r_{\mathrm{e}} \le r \le r_{\max}} = 0. \tag{3.20}$$

The electrochemical reaction occurs with a change in enthalpy, which gives rise to a heat flux at the electrode surface. In the Nernstian limit, neglecting ohmic losses, the normal heat flux is proportional to the normal mass flux [13]:

$$q|_{z=0} = -\Delta H \cdot D_{\mathrm{Red}} \left.\frac{\partial C_{\mathrm{Red}}}{\partial z}\right|_{z=0}. \tag{3.21}$$

On the other hand, from Fourier's law, the heat flux can also be expressed through the temperature gradient:

$$q|_{z=0} = -\kappa \left.\frac{\partial T}{\partial z}\right|_{z=0}, \tag{3.22}$$

where κ [W·m^{-1}·K^{-1}] is the thermal conductivity of the fluid, $\kappa = \rho\chi c_p$, with c_p being the specific heat capacity in J·kg^{-1}·K^{-1}.

In general, the enthalpy of the reaction is a function of concentration. From the definitions of the total enthalpy and Gibbs energy, which include electrostatic contributions, it follows that under isothermal conditions, for the overall process

$$\Delta H = \Delta G + T\Delta S. \tag{3.23}$$

At equilibrium, $\Delta G = 0$, which leaves

$$\begin{aligned}\Delta H = T\Delta S &= T\left(\Delta S_{\text{reaction}} + \Delta S_{\text{migration}}\right)\\ &= T\left(-\frac{\partial \Delta G_{\text{reaction}}}{\partial T} + \Delta S_{\text{migration}}\right)\\ &= T\left(F\frac{\partial E}{\partial T} + \Delta S_{\text{migration}}\right)\end{aligned}$$

$$= FT\frac{\partial}{\partial T}\left(E_{\text{formal}} + \frac{RT}{F}\ln\frac{a_{\text{Ox}}}{a_{\text{Red}}}\right) + T\Delta S_{\text{migration}}, \tag{3.24}$$

where $\Delta S_{\text{reaction}}$ and $\Delta G_{\text{reaction}}$ are respectively the change in entropy and Gibbs energy change intrinsic to reaction (3.1) and a_{i} is the activity of species 'i'. To obtain the final form of Eq. (3.24), we used the definition of the electrode potential and the Nernst equation. The activities a_{Ox} and a_{Red} and their derivatives with respect to temperature depend on the concentrations of the reduced and oxidized species, as well as that of the supporting electrolyte. The term $T{\cdot}\Delta S_{\text{migration}}$ accounts for the heat of transport of the non-electroactive ions in the solution [14] and is also dependent upon the concentration of the supporting electrolyte. However, as we are mostly interested in the qualitative effect of temperature-induced free convection, we will treat ΔH as a constant. For our simulations, we will use the value of 45.35 kJ·mol^{-1} measured by Boudeville and Tallec [13] for 0.1 M $[Fe(CN)_6]^{3-}$/ 0.1 M $[Fe(CN)_6]^{4-}$, which is in close agreement with the value of the standard enthalpy of 45.62 kJ·mol^{-1} that Fang et al. [15] obtained by extrapolating their data for ΔH to infinite dilution of the reacting species.

Eqs. (3.21) and (3.22) enable us to assess the order of magnitude of the temperature change caused by the reaction. From dimensional analysis, the order of magnitude of $\partial T/\partial z$ is $\Delta T/L_{\text{therm}}$, where L_{therm} is the characteristic length of the thermal boundary layer and $\Delta T = T(z = 0) - T(z = L_{\text{therm}})$ is the change in

temperature over that distance. Similarly, $\partial C_{\mathrm{Red}}/\partial z \sim \Delta C_{\mathrm{Red}}/L_{\mathrm{diff}}$. Inserting these results in Eqs. (3.21) and (3.22) and equating the right-hand sides, we obtain

$$\Delta T \sim -\Delta H \Delta C_{\mathrm{Red}} \frac{D_{\mathrm{Red}}}{\kappa} \frac{L_{\mathrm{therm}}}{L_{\mathrm{diff}}}. \tag{3.25}$$

For convection-free mass and heat transport, $L_{\mathrm{diff}} = \sqrt{D_{\mathrm{Red}} t}$ and $L_{\mathrm{therm}} = \sqrt{\chi t}$. In the cases studied here, the inclusion of convection has no effect on the order of magnitude of L_{diff} and L_{therm}, which enables us to rewrite Eq. (3.25) as

$$\begin{aligned} \Delta T \sim -\Delta H \Delta C_{\mathrm{Red}} \frac{D_{\mathrm{Red}}}{\kappa} \sqrt{\frac{\chi}{D_{\mathrm{Red}}}} = \\ -\Delta H \Delta C_{\mathrm{Red}} \frac{D_{\mathrm{Red}}}{\kappa} \sqrt{\frac{\kappa}{\rho c_p D_{\mathrm{Red}}}} = -\Delta H \Delta C_{\mathrm{Red}} \sqrt{\frac{D_{\mathrm{Red}}}{\rho c_p \kappa}}. \end{aligned} \tag{3.26}$$

3.2.1.C *Hydrodynamics*

To determine the velocity of the fluid, which appears in Eqs. (3.2) and (3.13), we need to solve the Navier-Stokes equation for an incompressible viscous fluid,

$$\rho \left(\frac{\partial \boldsymbol{v}}{\partial t} + \boldsymbol{v} \cdot \nabla \boldsymbol{v} \right) = -\nabla p + \eta \nabla^2 \boldsymbol{v} + \rho \boldsymbol{g}, \tag{3.27}$$

where, in analogy with the notation of Chapter 1, ρ is the solution density, η is its viscosity, p is the pressure and $\boldsymbol{g}$ is the gravitational acceleration.

The Navier-Stokes equation must be solved together with the continuity equation, which for an incompressible fluid has the form

$$\nabla \cdot \boldsymbol{v} = 0. \tag{3.28}$$

The fluid is at rest at the start of the simulated experiment, $t = 0$,

$$\boldsymbol{v}(t = 0) = \mathbf{0}. \tag{3.29}$$

As the simulated region is considerably larger than the spatial extent of the reaction-induced flow, we assume it to be unperturbed,

$$\boldsymbol{v}|_{r=r_{\max}} = \boldsymbol{v}|_{z=z_{\max}} = \mathbf{0}. \tag{3.30}$$

At the solid surface ($z = 0$), the velocity obeys a no-slip boundary condition,

$$\boldsymbol{v}|_{z=0} = \mathbf{0}. \tag{3.31}$$

At the cylinder axis, we employ symmetry boundary conditions,

$$v_r|_{r=0} = 0; \tag{3.32}$$

$$\left. \frac{\partial v_z}{\partial r} \right|_{r=0} = 0. \tag{3.33}$$

Equations (3.32)-(3.33) are equivalent to Eqs. 1.3-1.4 in Demkowicz's paper for a system with plane symmetry [16]. The paper on which this chapter is based gives an additional symmetry boundary condition, $\partial_z v_r|_{r=0} = 0$, but, as we noted in a later paper (see Chapter 5), this condition is trivially fulfilled as a consequence of Eq. (3.32).

The chemical reaction (3.1) affects the solution density in two ways – through the formation of a product which differs in partial molar volume from the reactant, as well as through variations in the temperature of the solution caused by the heat flux (3.22). Assuming both effects lead to small perturbations, we can approximate the density ρ with its first-order Taylor expansion,

$$\rho \approx \rho_0 + \left(\frac{\partial \rho}{\partial C_{\mathrm{Red}}}\right)_{T,p} (C_{\mathrm{Red}} - C_{\mathrm{bulk}}) + \left(\frac{\partial \rho}{\partial T}\right)_{p,C_{\mathrm{Red}}} (T - T_{\mathrm{bulk}}) \approx$$
$$\rho_0[1 + \beta(C_{\mathrm{bulk}} - C_{\mathrm{Red}}) - \alpha(T - T_{\mathrm{bulk}})], \tag{3.34}$$

where ρ_0 is the density of the unperturbed solution, β [m^3·mol^{-1}] is the densification coefficient for the specific reaction and $\alpha = -1/\rho_0 \cdot (\partial \rho_0/\partial T)_{p,C_{\mathrm{Red}}}$[K^{-1}] is the thermal expansion coefficient of the initial solution. In Eq. (3.34), we have used that at constant temperature the density of the solution can be expressed through the concentrations of the ionic species present and their individual densification coefficients [5], (β_{i}),

$$\rho - \rho_0 = \rho_0 \textstyle\sum_{\forall\, \mathrm{i}} \beta_{\mathrm{i}} (C_{\mathrm{i}} - C_{\mathrm{i}}(t = 0)). \tag{3.35}$$

Note that the sum in Eq. (3.35) is over all species and the coefficients β_{i} are defined for each individual ion, in contrast to the definition used by Selman and Newman [5]. Assuming that the concentrations of the nonelectroactive species are unperturbed and using the approximate mass balance (3.3), we obtain the concentration-dependent term from (3.34) with $\beta = \beta_{\mathrm{Ox}} - \beta_{\mathrm{Red}}$ as follows. The change in density in a two-component mixture with a solute of concentration C, molar mass M and partial molar volume v is [17] $\rho - \rho_{\mathrm{S}} = (M - \rho_{\mathrm{S}} v)C$, where for dilute solutions v can be regarded as a constant and ρ_{S} is the density of the pure solvent. For an arbitrary number of components, this generalizes to [18]

$$\rho - \rho_{\mathrm{S}} = \textstyle\sum_{\forall\, \mathrm{i}} (M_i - \rho_{\mathrm{S}} v_{\mathrm{i}})\, C_{\mathrm{i}}. \tag{3.36}$$

Neglecting the difference between the density of the unperturbed solution, ρ_0 and that of the pure solvent, ρ_S, we substitute the right-hand side of Eq. (3.36) in Eq. (3.35) to obtain the equation

$$\rho - \rho_S = \sum_{\forall i} (M_i - \rho_S v_i)\big(C_i - C_i(t=0)\big). \tag{3.37}$$

from which it is apparent that $\beta_i \approx M_i/\rho_S - v_i$. Our system contains KNO_3 as a supporting electrolyte and thus Eq. (3.37) includes contributions from four types of ions ($[Fe(CN)_6]^{4-}$, $[Fe(CN)_6]^{3-}$, K^+, NO_3^-). However, as we are mainly interested in the qualitative effect of convection on the mass transport, we will only consider the leading term, i.e., the contribution of the electroactive ions. As we work under the approximation that the diffusion coefficients of the reduced and oxidized species are equal, we can use the mass balance (3.3) to reach

$$\begin{aligned}\rho - \rho_0 = \rho_0(\beta_{Ox} - \beta_{Red})(C_{bulk} - C_{Red}) = \rho_0(v_{Red} - v_{Ox})(C_{bulk} - \\ C_{Red}) = \\ = \rho_0\beta(C_{bulk} - C_{Red})\end{aligned} \tag{3.38}$$

Note that, had we not approximated ρ_0 with ρ_S above, we would arrive at $\beta \approx \rho_S(v_{Ox} - v_{Red})$ instead of $\beta \approx \rho_0(v_{Ox} - v_{Red})$, i.e. an expression that differs by a factor of ρ_S/ρ_0. For the solution that we study (~ 0.5 M KNO_3), $\rho_S/\rho_0 = 0.97$; considering that using different literature values of the molar volumes can yield variations in $v_{Ox} - v_{Red}$ of as much as 30% (see Ref. [19]), the factor ρ_S/ρ_0 is immaterial.

We can follow the approach employed by Feldberg and Lewis [18] to estimate the effect of the supporting electrolyte on the solution density. Using the condition for local electroneutrality and the approximation that the diffusion coefficients of *all* present species are equal, we can estimate that including the contribution of the supporting electrolyte would lead to the expression

$$\rho - \rho_0 = \rho_0 \left(\beta_{Ox} - \beta_{Red} + \frac{\beta_{NO_3^-} - \beta_{K^+}}{2}\right)(C_{bulk} - C_{Red}). \tag{3.39}$$

Using literature data for the individual ionic partial molar volumes [19], we can assess the term due to the supporting electrolyte:

$$\frac{1}{2}\left(\beta_{NO_3^-} - \beta_{K^+}\right) = \frac{1}{2}\left(\frac{M_{NO_3^-} - M_{K^+}}{\rho_S} + v_{K^+} - v_{NO_3^-}\right) = -0.397 \times 10^{-5}\ \mathrm{m^3 \cdot mol^{-1}}, \tag{3.40}$$

while $\beta_{\mathrm{Ox}} - \beta_{\mathrm{Red}} = v_{\mathrm{Red}} - v_{\mathrm{Ox}} = -4.13 \times 10^{-5}\ \mathrm{m^3 \cdot mol^{-1}}$, i. e., the effect of the supporting electrolyte on the solution density is one order of magnitude weaker than that of the electroactive species. Thus, as we are more interested in the qualitative effect of natural convection than its precise quantification, we employ Eq. (3.38) for all our calculations.

As we noted in Section 1.1, it is convenient to rewrite the Navier-Stokes equation in terms of the difference in pressure with respect to the initial state instead of the absolute pressure,

$$\Delta p = p - p_0 + \rho_0 z|\boldsymbol{g}|, \tag{3.41}$$

where p_0 is the pressure at $z = 0$. The initial condition for Δp is that

$$\Delta p|_{t=0} = 0. \tag{3.42}$$

Substituting Eqs. (3.34)-(3.41) in Eq. (3.27) and neglecting terms of second or higher order leads to a modified form of the Navier-Stokes equation [20],

$$\rho_0 \left(\frac{\partial \boldsymbol{v}}{\partial t} + \boldsymbol{v} \cdot \nabla \boldsymbol{v}\right) = -\nabla \Delta p + \eta \nabla^2 \boldsymbol{v} + \boldsymbol{F}_{\mathrm{b}}, \tag{3.43}$$

in which $\boldsymbol{F}_{\mathrm{b}}$ is the buoyancy force generated by the chemical reaction,

$$\boldsymbol{F}_{\mathrm{b}} = (\rho - \rho_0)\boldsymbol{g} = \rho_0[\beta(C_{\mathrm{bulk}} - C_{\mathrm{Red}}) - \alpha(T - T_{\mathrm{bulk}})]\boldsymbol{g}. \tag{3.44}$$

The upper limit for $|\boldsymbol{F}_{\mathrm{b}}|$ is its value in the vicinity of the electrode, where the perturbations in concentration and temperature originate. Therefore, we can substitute $T - T_{\mathrm{bulk}}$ with ΔT from Eq. (3.26), to obtain an assessment of the order of magnitude of the buoyancy force:

$$\boldsymbol{F}_{\mathrm{b}} = (\rho - \rho_0)\boldsymbol{g} \sim \rho_0 \beta \Delta C_{\mathrm{Red}} \left(1 + \Delta H \frac{\alpha}{\beta} \frac{D_{\mathrm{Red}}}{\kappa} \frac{L_{\mathrm{therm}}}{L_{\mathrm{diff}}}\right) \boldsymbol{g} \approx$$
$$\rho_0 \left(\beta \Delta C_{\mathrm{Red}} + \alpha \Delta H \Delta C_{\mathrm{Red}} \sqrt{\frac{D_{\mathrm{Red}}}{\rho c_p \kappa}}\right) \boldsymbol{g} = \rho_0 \beta \Delta C_{\mathrm{Red}} \left(1 + \Delta H \frac{\alpha}{\beta} \sqrt{\frac{D_{\mathrm{Red}}}{\rho c_p \kappa}}\right) \boldsymbol{g}. \tag{3.45}$$

Our model reaction, the oxidation of hexacyanoferrate (II) to hexacyanoferrate (III), has a negative densification coefficient β, which means that the buoyancy force $\boldsymbol{F}_{\mathrm{b}}$ opposes the gravitational force. Ngamchuea et al. [2] have shown that in this case, solutal convection is most intense if the electrode is placed in the bottom of the cell, which is the reason we model this particular configuration.

Thermal convection can either oppose or reinforce solutal convection and as we see from Eq. (3.45), this depends on the sign of the ratio between the densification coefficient (β) and the enthalpy of the reaction (ΔH). For our model reaction, $\Delta H/\beta < 0$, i.e., thermal convection counteracts solutal convection. Nevertheless, to

test qualitatively the relative importance of thermal convection, we performed simulations in which the sign of ΔH was reversed so that $\Delta H/\beta > 0$, both with the measured absolute value of the enthalpy and with a limiting one whose magnitude was several times greater. In practice, the magnitude of ΔH can be substantially increased for an irreversible endothermic process by applying a high overpotential, see Eq. 2.9 in Vetter's book [21].

The dimensionless quantity $N = \alpha \left|\frac{\Delta H}{\beta}\right| \sqrt{\frac{D_{\mathrm{Red}}}{\rho c_p \kappa}}$ in Eq. (3.45) reflects the ratio between the buoyancy forces caused by the variation in temperature and density. N is equivalent to the *buoyancy ratio* defined by Pringle and Glass in their treatment of a similar coupled heat- and mass-transfer problem that involves [22]. N can also be interpreted as the ratio of the Rayleigh numbers for natural convection driven by gradients in temperature and concentration, as in the work of Singh and Srinivasan [23]. Substituting the characteristic numerical values for our problem, we can estimate its order of magnitude:

$$N = \alpha \left|\frac{\Delta H}{\beta}\right| \sqrt{\frac{D_{\mathrm{Red}}}{\rho c_p \kappa}} = \frac{2.06\mathrm{x}10^{-4}\mathrm{x}4.53\mathrm{x}10^{4}}{4.13\mathrm{x}10^{-5}} \sqrt{\frac{7.53\mathrm{x}10^{-10}}{998\mathrm{x}4182\mathrm{x}0.5984}} = 3.93\mathrm{x}10^{-3}. \qquad (3.46)$$

Above, the parameters of the solution were approximated by their values for pure water, $\alpha = 2.06\times10^{-4}\ \mathrm{K^{-1}}$, $\kappa = 0.5984\ \mathrm{W\cdot m^{-1}\cdot K^{-1}}$, $\rho = 998\ \mathrm{kg\cdot m^{-3}}$ and $c_p = 4181.8\ \mathrm{J\cdot kg^{-1}\cdot K^{-1}}$ at 293.15 K, taken from the CRC Handbook of Chemistry and Physics [24]. The densification coefficient of the oxidation of hexacyanoferrate (II) to hexacyanoferrate (III), $\beta = \beta_{\mathrm{Ox}} - \beta_{\mathrm{Red}} = \nu_{\mathrm{Red}} - \nu_{\mathrm{Ox}} = -4.13\mathrm{x}10^{-5}\ \mathrm{m^3\cdot mol^{-1}}$, was calculated from the data tabulated by Marcus [19] and its enthalpy change, ΔH = 45.35 $\mathrm{kJ\cdot mol^{-1}}$, was taken from Boudeville and Tallec [13]; the diffusion coefficient of both species was taken to be equal to its value at T = 298.15 K, D_{Red} = $7.53\mathrm{x}10^{-10}\ \mathrm{m\cdot s^{-2}}$, as determined by Ngamchuea et al. [25]. The fact that $N \sim 10^{-3}$ means that the buoyancy force caused by reaction-induced temperature fluctuations is negligible for the oxidation of hexacyanoferrate (II) to hexacyanoferrate (III). Moreover, it appears unlikely that it will be important for any type of reaction in the problem we consider, as this would require a variation of orders of magnitude in ΔH or β. This conclusion is supported by the results from our simulations, as described below.

3.2.2. **Simulations**

Simulations of chronoamperometry and cyclic voltammetry were performed with the finite-element package COMSOL Multiphysics 5.2, see Ref. [26] for a discussion of the latter's suitability for modelling of electrochemical processes and Ref. [27] for its application to convective transport problems.

The values of α, β, κ, c_p and D_{Red} given in Section 3.2.1.C were used for all simulations. The duration of all simulated experiments was $t_{\max}$ = 60 s; the formal potential was approximated with the standard potential of the couple $[Fe(CN)_6]^{3-}/[Fe(CN)_6]^{4-}$ with respect to the standard hydrogen electrode, $E_{\mathrm{formal}} = 0.358$ V. The simulations were performed with values of the viscosity and the density corresponding to 0.509 M KNO_3 as a supporting electrolyte at T_{bulk} = 293.15 K, i.e. η = 0.980 mPa·s, ρ_0 = 1029.8 kg·m^{-3} [24]. The initial concentration of $[Fe(CN)_6]^{4-}$ was set to the value used by Ngamchuea et al. [2], C_{bulk} = 9.5 mM. We should note that, as elsewhere in this thesis, we have used the Boussinesq approximation in the governing equations of the system, Eqs. (3.2), (3.13) and (3.43). Namely, we have approximated the temperature and concentration dependences of density on temperature with linear functions insofar as the buoyancy term is concerned, and treated all properties of the solution as constant elsewhere. This approach is justified for the small variations in C_{Red} and T that we consider – see the work of Gray and Giorgini [28] for a detailed analysis of the validity of the Boussinesq approximation for thermal convection problems. As $(T - T_{\mathrm{bulk}})/T_{\mathrm{bulk}} \ll 1$, we neglect the variation in temperature everywhere except in the heat transfer equation (3.13) and the buoyancy force (3.44) in the Navier-Stokes equation.

Three spatial configurations were used for the simulations: 1) electrode radius r_{e} = 0.25 mm and cell dimensions $r_{\max} = r_{\mathrm{e}} + 6\sqrt{t_{\max}\kappa/(\rho_0 c_p)} = 17.58$ mm by $z_{\max}$ = 17.33 mm; 2) r_{e} = 2.5 mm, $r_{\max} = r_{\mathrm{e}} + 6\sqrt{t_{\max}\kappa/(\rho_0 c_p)} = 19.82$ mm and $z_{\max} = 6\sqrt{t_{\max}\kappa/(\rho_0 c_p)} = 17.33$ mm; 3) r_{e} = 25 mm, $r_{\max} = 4r_{\mathrm{e}} = 100$ mm and $z_{\max} = 4 \cdot r_{\mathrm{e}} = 100$ mm.

Three types of simulations were performed for each electrode radius.

1) Diffusion-only – with a velocity field set to $\boldsymbol{v} = \mathbf{0}$ and no account for convection.

2) Diffusion coupled with solutal convection but no variations in temperature, corresponding to the simulations performed by Ngamchuea et al. [2].

3) Diffusion coupled with both solutal and reaction-induced thermal convection. Three values were used for the reaction enthalpy – a) the experimental value measured by Boudeville and Tallec [13], ΔH = 45.35 kJ·mol^{-1}, b) the same multiplied by a factor of minus unity and c) an extreme value of −100 kJ·mol^{-1}. The purpose of simulating case c) was to increase the effect of thermal convection to its reasonable limits and judge its relative importance.

For chronoamperometry, the applied electrode potential was E_{chrono} = 0.863 V vs. SHE, corresponding to a dimensionless potential $\theta = F\left(E - E_{\text{f}}^{0}\right)/(RT) = 20$ and a surface concentration of the reduced species $C_{\text{Red}}(r \leq r_{\text{e}}, z = 0) \sim 10^{-8}\ \text{mol} \cdot \text{m}^{-3}$.

For the simulations of cyclic voltammetry, the electrode potential was varied according to the equation

$$E = \begin{cases} E_{\text{i}} + vt, t < t_{\text{max}}/2 \\ 2E_{\text{v}} - E_{\text{i}} - vt, t \geq t_{\text{max}}/2 \end{cases}, \tag{3.47}$$

where E_{i} = −0.147 V vs. SHE is the potential at the start of the scan, E_{v} = 0.863 V vs. SHE is its value at the vertex (corresponding to −20 and 20 in θ) and the scan rate is $v = 2(E_{\text{v}} - E_{\text{i}})\ /t_{\text{max}} = 33.7\ \text{mV} \cdot \text{s}^{-1}$.

The coupled transport problems were discretized with respect to time and space in such a way that the simulations gave results that were sufficiently close to the exact expressions for the convection-free case, see below. Linear shape functions were used for C_{Red}, T, Δp and $\boldsymbol{v}$ for every simulation except those of chronoamperometric experiments at r_{e} = 0.25 mm. In the latter case, cubic elements were employed for the concentration and linear for the other unknown functions.

For chronoamperometric simulations, the calculated current was compared to that predicted by the Shoup-Szabo equation given in Section 1.7 [29][5],

[5] Due to a typographical mistake, the expression for the Shoup-Szabo current in the paper on which this chapter is based differs by a factor of π from the correct one. However, all calculations were performed with the correct expression (3.48).

$$I = 4FD_{\mathrm{Red}} r_{\mathrm{e}} C_{\mathrm{bulk}} \left\{ 0.7854 + 0.4431 \frac{r_{\mathrm{e}}}{\sqrt{D_{\mathrm{Red}} t}} + 0.2146 \cdot \exp\left(-0.7823 \frac{r_{\mathrm{e}}}{2\sqrt{D_{\mathrm{Red}} t}} \right) \right\}, \tag{3.48}$$

and all simulations were performed with settings for the discretization that guaranteed agreement of within 1% between the predicted current for the diffusion-only problem and Eq. (3.48) at $t > 15$ s (see Figures 3.3, 3.5 and 3.7). At $t < 0.01$ s, the simulated currents for all cases exhibited considerable oscillations caused by the singularity of the current at $t \to 0$. At 0.01 s < t < 15 s, the relative deviation of the convection-free simulation from Eq. (3.48) goes through a peak value of approximately 3%. As convection only starts to have an appreciable effect at $t > 15$ s (see Figures 3.2-3.7, compare with Figure 5 in the work of Ngamchuea et al. [2]), we disregard this initial period.

The height of the forward peak for the diffusion-only case was used as a criterion for the accuracy for simulations of cyclic voltammetry. The simulated peak height was compared to the one calculated from the empirical equation given in Section 1.8 [30][6],

$$I_{\mathrm{max}} = 4FD_{\mathrm{Red}} r_{\mathrm{e}} C_{\mathrm{bulk}} \left(0.34\mathrm{e}^{-0.66\sqrt{\sigma}} + 0.66 - 0.13\mathrm{e}^{-\frac{11}{\sqrt{\sigma}}} + 0.351\sqrt{\sigma} \right), \tag{3.49}$$

in which σ is the dimensionless scan rate, $\sigma = Fr_{\mathrm{e}}^2 v / (RTD_{\mathrm{Red}})$. The mesh and the time-stepping were chosen so that the difference between Eq. (3.49) and the simulated peak current was within 1% for the convection-free case.

The dimensionless scan rate σ is much larger than unity for the r_{e} we consider here (σ ranges from $\sim 1.1\times10^2$ at $r_{\mathrm{e}} = 0.25$ mm to 1.1×10^6 at $r_{\mathrm{e}} = 25$ mm at the studied scan rate of 33.7 mV · s^{-1}), hence the electrodes in this study behave as macroelectrodes as far as cyclic voltammetry is concerned [31]. Thus, equations (1.57)-(1.58) for the peak-to-peak separation ΔE_{pp} and the midpoint potential E_{mid} are applicable. However, the discretization scheme we used yielded only an approximately correct result for the peak-to-peak separation, (1.57) for simulations

[6] Due to a typographical mistake, the expression for the peak height in the paper on which this chapter is based differs by a factor of π from the correct one. However, all calculations were performed with the correct expression (3.49).

of reversible cyclic voltammetry with diffusion as the sole mode of mass transport [9].

As the electrode potential E in cyclic voltammetry is controlled function of time (see Eq. (3.47)), the time-stepping scheme for the problem determines the set of values of E for which the equations are solved and thus affects the accuracy of E_{mid}. Our choice of time-stepping gives a result for E_{mid} that is within 1% of Eq. (1.58) for the diffusion-only problem, but is comparatively insensitive to changes in E_{mid} due to the relatively large interval between two consecutive values of E in the simulation. Thus, neither ΔE_{pp} nor E_{mid} is useful for quantifying the effect of natural convection on the cyclovoltammetric currents determined from our simulations.

3.3. Results and discussion

This section presents the results obtained from the simulations of chronoamperometry and cyclic voltammetry described in Section 3.2.2.

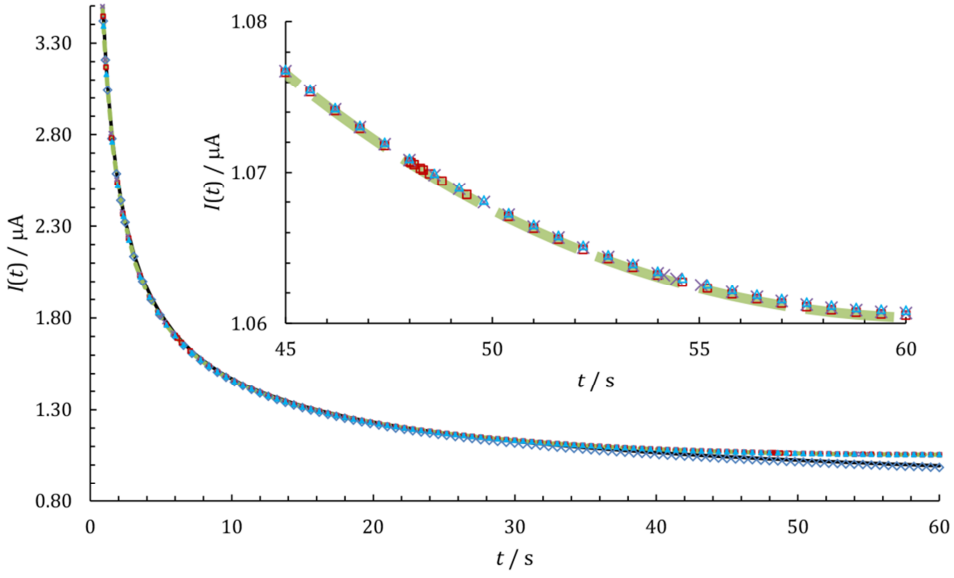


Figure 3.2. Dependence of current on time at r_e = 0.25 mm for various simulations plotted together with the Shoup-Szabo current (solid line). Simulations that account for the following modes of mass transport are represented: diamonds – diffusion-only; squares – solute-driven free convection; dashed line – thermosolutal natural convection with ΔH = 45.35 kJ·mol^{-1}; crosses – thermosolutal free convection, ΔH =

−45.35 kJ·mol^{-1}; triangles – thermosolutal free convection, ΔH = −100.0 kJ·mol^{-1}. The inset shows the current for the various convective simulations at long times. For all simulations, $r_{max} = r_e + 6\sqrt{t_{max}\kappa/(\rho_0 c_p)} = 17.58$ mm and $z_{max} = 6\sqrt{t_{max}\kappa/(\rho_0 c_p)} = 17.33$ mm.

3.3.1. **Chronoamperometry**

The $I(t)$ curves obtained from the chronoamperometric simulations described in Section 3.2.2 are plotted in Figures 3.2, 3.4 and 3.6 for r_e = 0.25, 2.5 and 25 mm, respectively. The relative difference between the simulated and the Shoup-Szabo currents is plotted against time in Figures 3.3, 3.5 and 3.7. Figures 3.8 and 3.9 show 'snapshots' of C, T and $\boldsymbol{v}$ from simulations that include both types of natural convection performed with the experimentally measured enthalpy of the modelled reaction at r_e = 0.25 mm and 25 mm respectively. Section A.1 in Appendix A contains additional plots of the concentration, temperature and velocity distributions for various simulations of chronoamperometry.

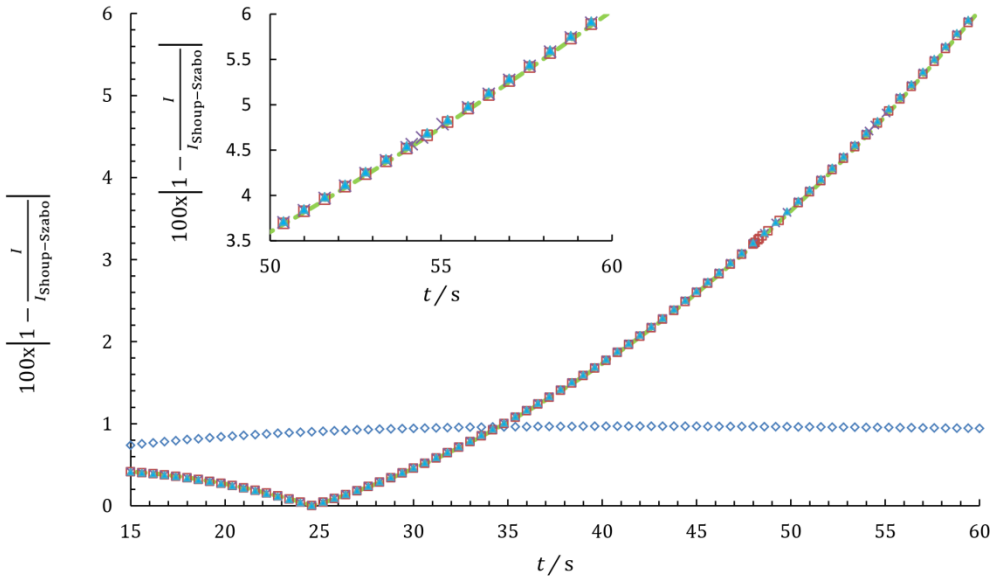


Figure 3.3. Relative difference between the currents obtained from various types of simulations and the Shoup-Szabo current at r_e = 0.25 mm (legend as in Figure 3.2). The inset shows the relative deviation from the diffusional current for the various

convective simulations at long times. For all simulations, $r_{max} = r_e + 6\sqrt{t_{max}\kappa/(\rho_0 c_p)} = 17.58$ mm and $z_{max} = 6\sqrt{t_{max}\kappa/(\rho_0 c_p)} = 17.33$ mm.

Figures 3.2-3.7 indicate that, as shown by Ngamchuea et al. [2], the effect of solutal convection on the chronoamperometric current is appreciable even at an analyte concentration as low as 9.5 mM and timescales as short as 60 s. Just as in Ref. [2] (consult Table 1 therein), the relative difference at $t = t_{max}$ is largest for millimetre-sized electrodes, ranging from ~ 6% at $r_e = 0.25$ mm through ~ 12% for $r_e = 2.5$ mm and diminishing to ~ 1% at $r_e = 25$ mm. Where differences are observable between simulations of thermosolutal convection at different values of ΔH, these differences are comparable to the deviation between the respective diffusion-only simulation and Eq. (3.48).

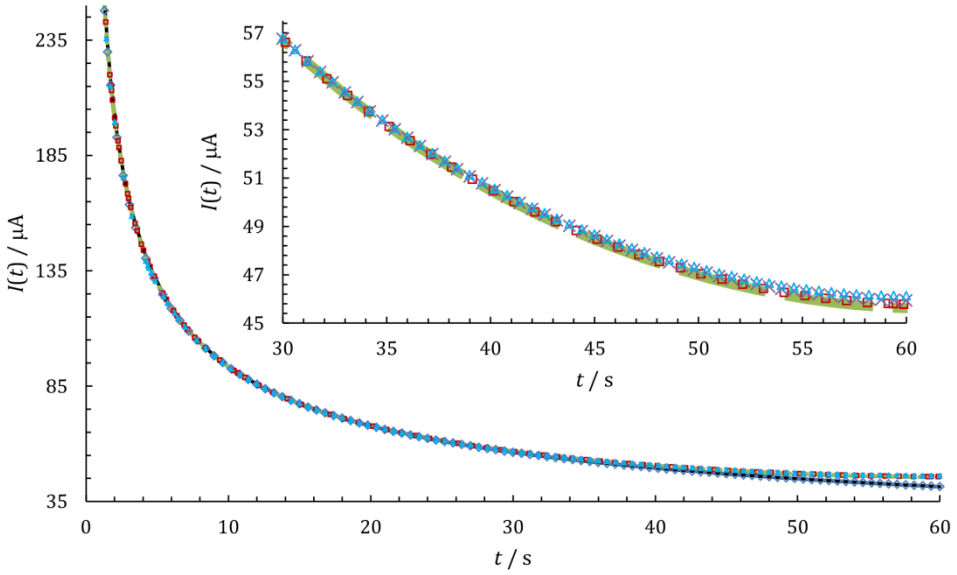


Figure 3.4. Dependence of current on time for various simulations at $r_e = 2.5$ mm plotted together with the Shoup-Szabo current (solid line, legend as in Figure 3.2). The inset shows the current for the various convective simulations at long times. For all simulations, $r_{max} = r_e + 6\sqrt{t_{max}\kappa/(\rho_0 c_p)} = 19.82$ mm and $z_{max} = 6\sqrt{t_{max}\kappa/(\rho_0 c_p)} = 17.33$ mm.

The results for the concentration and velocity profiles shown in Figs. 3.8-3.9 are in qualitative agreement with the ones obtained by Ngamchuea et al. [2][7] for solutal convection – at short times ($0 < t \sim 20$ s), the absolute value of the velocity is too low ($|\boldsymbol{v}| \sim 10^{-6}$ m·s^{-1}) to have an appreciable effect on the concentration profile. As time progresses, the product of the reaction accumulates and the convective flux intensifies, leading to a distorted concentration boundary layer, whose exact shape depends on the electrode size (see Figs. 3.8A, 3.9A). The simulated concentration profiles are practically identical for simulations involving only solute-driven convection and those that take thermal convection into account (compare Figs. 3.8A, 3.9A with Figs. A.2A and A.7A in Appendix A) and so are the predicted electrical currents, as seen in Figs. 3.2-3.7. The same is observed even in simulations for which the magnitude of the reaction enthalpy is increased and its sign is reversed ($\Delta H = -100$ kJ·mol^{-1} instead of 45.35 kJ·mol^{-1}). In the latter case, the temperature and velocity profiles are altered (compare Figs. 3.8B-C, 3.9B-C with Figure A.3B-C and Figure A.8B-C), but the electrical currents are not appreciably affected (Figs. 3.2-3.7), even though thermal and solutal free convection act synergistically.

The explanation for the negligibility of reaction-induced thermal convection lies in the low value ($\sim 10^{-3}$) of the buoyancy ratio N (3.46) for our problem. The numerical estimate for N given in Section 3.2.1.C relies on the approximation that the characteristic normal dimensions of the thermal and diffusive boundary layers are of the same order of magnitude as for the convection-free problems, $\sqrt{t\chi}$ and $\sqrt{tD_{\mathrm{red}}}$, respectively. This assumption is supported by the results from our numerical simulations. Using the parameters given below, we can calculate that

[7] Note that quantitative agreement cannot be obtained as Ngamchuea et al. [2] used inaccurate values for the densification coefficients β_i; the latter are taken from Ref. [5] and include the contribution of the supporting electrolyte to the solution density, but they pertain to the case with NaOH as the supporting electrolyte, rather than KNO_3 as in the system studied here and in Ref. [2]. For that reason, the value of the total densification coefficient used in Ref. [2], $\beta = \beta_{\mathrm{Ox}} - \beta_{\mathrm{Red}} = -5.9 \times 10^{-5}$ m$^3 \cdot$ mol^{-1}, differs significantly from the one calculated here as $\beta \approx v_{\mathrm{Red}} - v_{\mathrm{Ox}} = -4.1 \times 10^{-5}$ m$^3 \cdot$ mol^{-1}. However, as our studies are chiefly concerned with the order of magnitude of natural convective effects, the precise value of β is only of secondary importance.

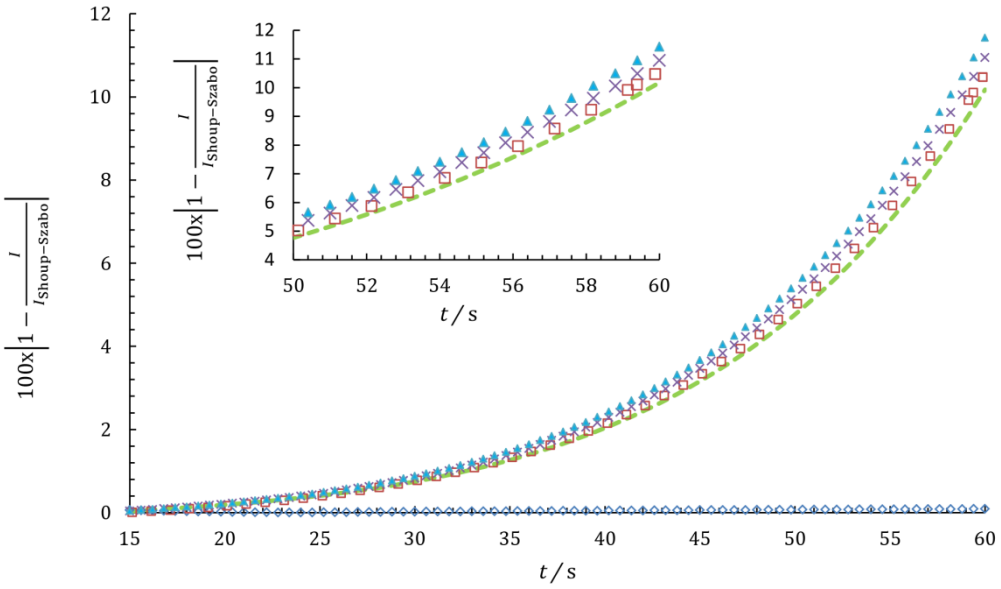


Figure 3.5. Relative deviation of the currents obtained from various simulations at r_e = 2.5 mm from the Shoup-Szabo current (legend as in Figure 3.2). The inset shows the relative deviation from the diffusional current for the various convective simulations at long times. For all simulations, $r_{max} = r_e + 6\sqrt{t_{max}\kappa/(\rho_0 c_p)} =$ 19.82 mm and $z_{max} = 6\sqrt{t_{max}\kappa/(\rho_0 c_p)} = 17.33$ mm.

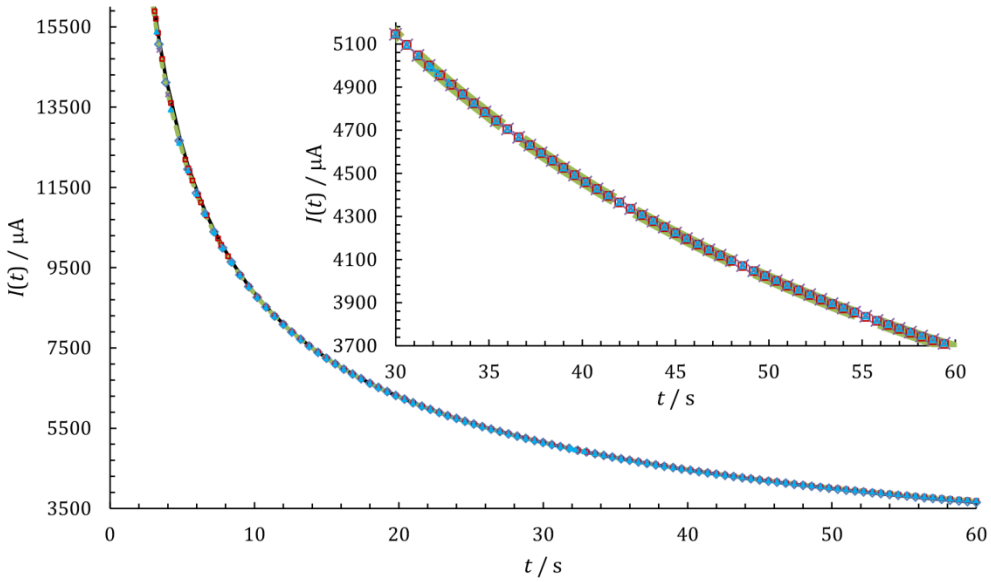


Figure 3.6. Dependence of current on time for various simulations plotted together with the Shoup-Szabo current (solid line, legend as in Figure 3.2) for an electrode of

radius r_e = 25 mm. The inset shows the current for the various convective simulations at long times. For all simulations, $r_{max} = z_{max} = 4 \cdot r_e = 100$ mm.

$$L_{diff} = \sqrt{D_{red} t} = \begin{cases} 1.2\text{x}10^{-4}\ \text{m}, & t = 20\ \text{s} \\ 1.7\text{x}10^{-4}\ \text{m}, & t = 40\ \text{s} \\ 2.1\text{x}10^{-4}\ \text{m}, & t = 60\ \text{s} \end{cases} \tag{3.50}$$

and

$$L_{therm} = \sqrt{\chi t} = \begin{cases} 16.7\text{x}10^{-4}\ \text{m}, & t = 20\ \text{s} \\ 23.6\text{x}10^{-4}\ \text{m}, & t = 40\ \text{s} \\ 28.9\text{x}10^{-4}\ \text{m}, & t = 60\ \text{s} \end{cases}. \tag{3.51}$$

In Figures 3.8-3.9, we see that the numbers in Eqs. (3.50)-(3.51) give the correct order of magnitude for the extent of the respective boundary layers in the z-direction, even though the concentration profiles at t > 40 s exhibit shapes significantly different from those in the diffusion-only case (compare Figure 3.8A and Figure 3.9A with Figure A.1 in Appendix A). It is evident from Eq. (3.46) for the buoyancy ratio that a change in the orders of magnitude of L_{diff} and L_{therm} would be required to make the effect of thermal convection appreciable.

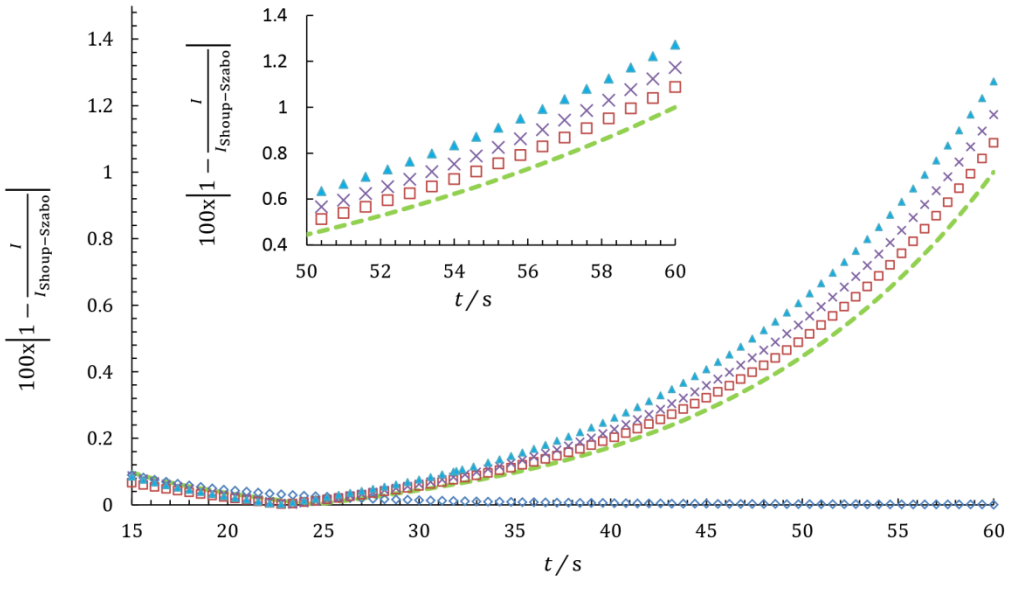


Figure 3.7. Relative difference between the currents obtained from various simulations and the Shoup-Szabo current (legend as in Figure 3.2) for an electrode of radius r_e = 25 mm. The inset shows the relative deviation from the diffusional

current for the various convective simulations at long times. For all simulations, r_{max} = z_{max} = 4·r_e = 100 mm.

The compliance of the observed boundary layer thicknesses with Eqs. (3.50)-(3.51) can be explained via dimensional analysis. The relative importance of convective and diffusive mass transport is quantified by the relevant Péclet number [11],

$$Pe_{\mathrm{mass}} = \frac{|\boldsymbol{v}| r_e}{D_{\mathrm{Red}}}; \tag{3.52}$$

similarly, the Péclet number for heat transfer compares heat transport by convection and conduction [11],

$$Pe_{\mathrm{heat}} = \frac{|\boldsymbol{v}| r_e}{\chi}. \tag{3.53}$$

The order of magnitude of the flow velocity generated by the electrochemical reaction reaches $|\boldsymbol{v}| \sim 1.6\times10^{-5}$ m·s^{-1} at the end of the simulated experiment for all configurations, see Figs. 3.8-3.9. Substituting this value for $|\boldsymbol{v}|$, r_e = 0.25 mm and the diffusivities given below, we obtain the assessments $Pe_{mass} \sim 10$ and $Pe_{heat} \sim 10^{-2}$ for the Péclet numbers. This means that, by $t = t_{max}$, convection becomes the main mode of mass transfer, but heat is still predominantly dissipated via conduction, i.e., the term $\boldsymbol{v} \cdot \nabla T$ in Eq. (3.13) is negligible and the thermal boundary layer does indeed have a characteristic length of $L_{therm} = \sqrt{\chi t}$. Even though convection is the main mode of mass transport by the end of the simulations, the low flow velocities generated by the chemical reaction do not change the order of magnitude of L_{diff}. Therefore, Eq. (3.46) gives an accurate assessment of the buoyancy ratio and thermal convection is much less important than solutal convection. Both Pe_{mass} and Pe_{heat} increase with r_e, and at the largest electrode size, r_e = 25 mm, we have $Pe_{mass} \sim 10^3$ and $Pe_{heat} \sim 1$, i.e., convection plays a significant role in both mass and heat transfer. However, even under those circumstances Eqs. (3.50)-(3.51) are correct to an order of magnitude (see Figure 3.9), which means that Eq. (3.46) is approximately valid and thermal convection is still much less important than solutal convection.

Nevertheless, it is visible from Figures 3.3, 3.5 and 3.7 that the relative significance of thermal convection increases with r_e – while the curves for all simulations involving convection are indistinguishable from one another at r_e = 0.25 mm, small differences (within 1 percentage point) are observed between the various simulations involving convection at the larger electrodes. While in all cases for sufficiently long t solutal convection causes a current (squares) that is significantly higher than the purely diffusional one (solid line), for the reaction we study this effect is mitigated to a small extent by thermal convection – see Eq. (3.45) and the dashed line in Figs. 3.5, 3.7. By the same token, performing the simulations with a value of the enthalpy change that is reverse in sign leads to a current higher than that obtained from the case with solutal convection only (triangles and crosses), and the magnitude of the change depends on the absolute value of ΔH. As Figures 3.5 and 3.7 demonstrate, the differences between the various simulations involving natural convection are subtle and it would be difficult to separate their role from that of external factors typically present in electrochemical experiments, e.g. vibrations [32]. Moreover, as these differences are smaller than the error of the diffusion-only simulations (diamonds in Figs. 3.2-3.7), they need to be interpreted with care.

While the observations given above are valid for all the configurations studied here, they need not necessarily apply to all circumstances – at sufficiently long times and sufficiently large electrodes, thermal and solutal convection may become comparable and the interplay between them more complex. This case, however, goes beyond the scope of our study, which is concerned with typical experimental conditions encountered in electroanalysis.

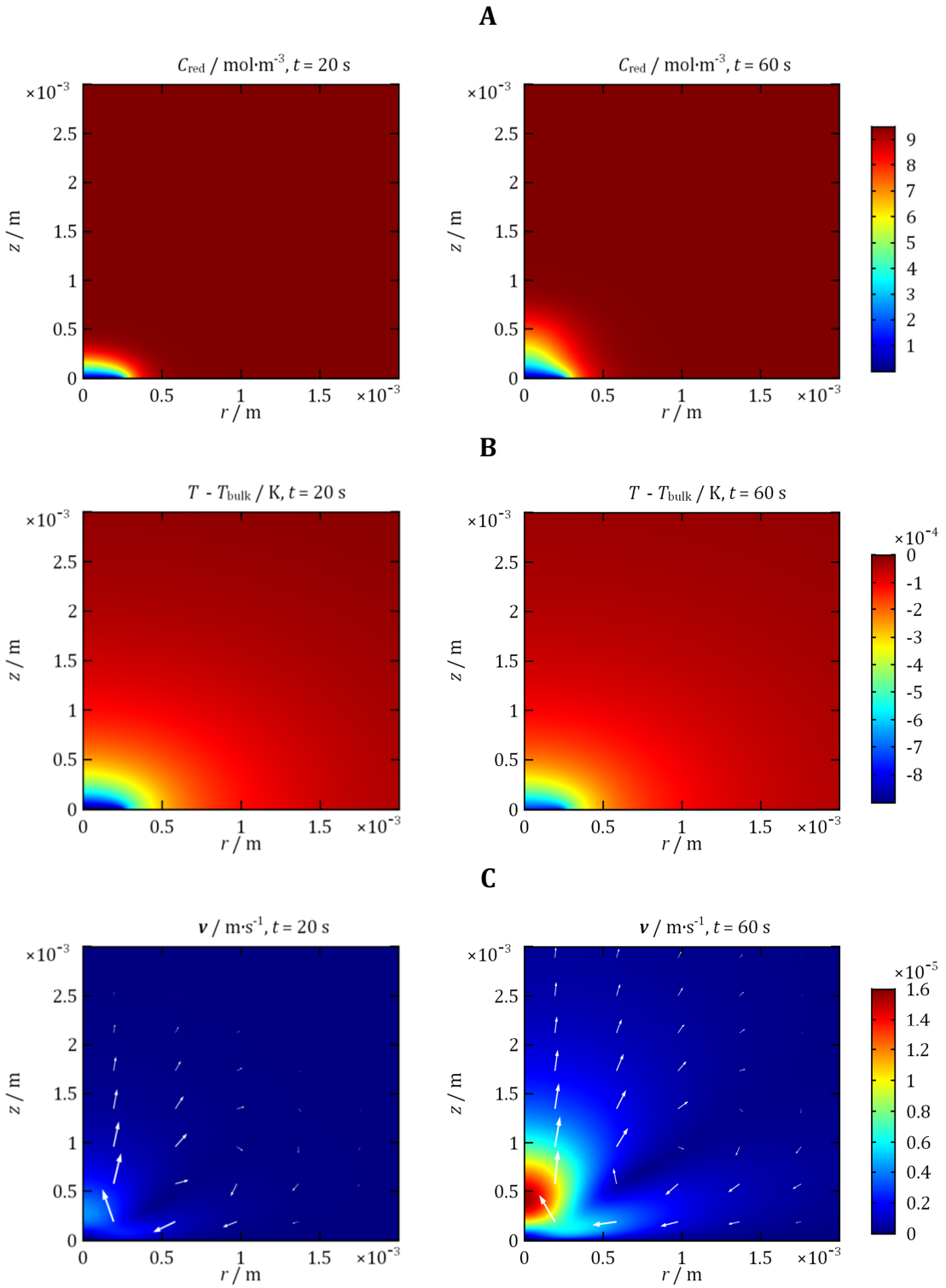


Figure 3.8. Concentration (**A**), temperature (**B**) and velocity profiles (**C**) at t = 20 and 60 s for a chronoamperometric oxidation of $[Fe(CN_6)]^{4-}$ at an electrode of radius r_e = 0.25 mm. The simulation includes both types of natural convection and is performed with the experimentally measured enthalpy of the reaction [13], ΔH = 45.35 kJ·mol^{-1} and a cell of dimensions $r_{max} = r_e + 6\sqrt{t_{max}\kappa/(\rho_0 c_p)}$ = 17.58 mm by $z_{max} = 6\sqrt{t_{max}\kappa/(\rho_0 c_p)}$ = 17.33 mm. The length of the arrows representing the velocity vector is proportional to the natural logarithm of $|\boldsymbol{v}|$.

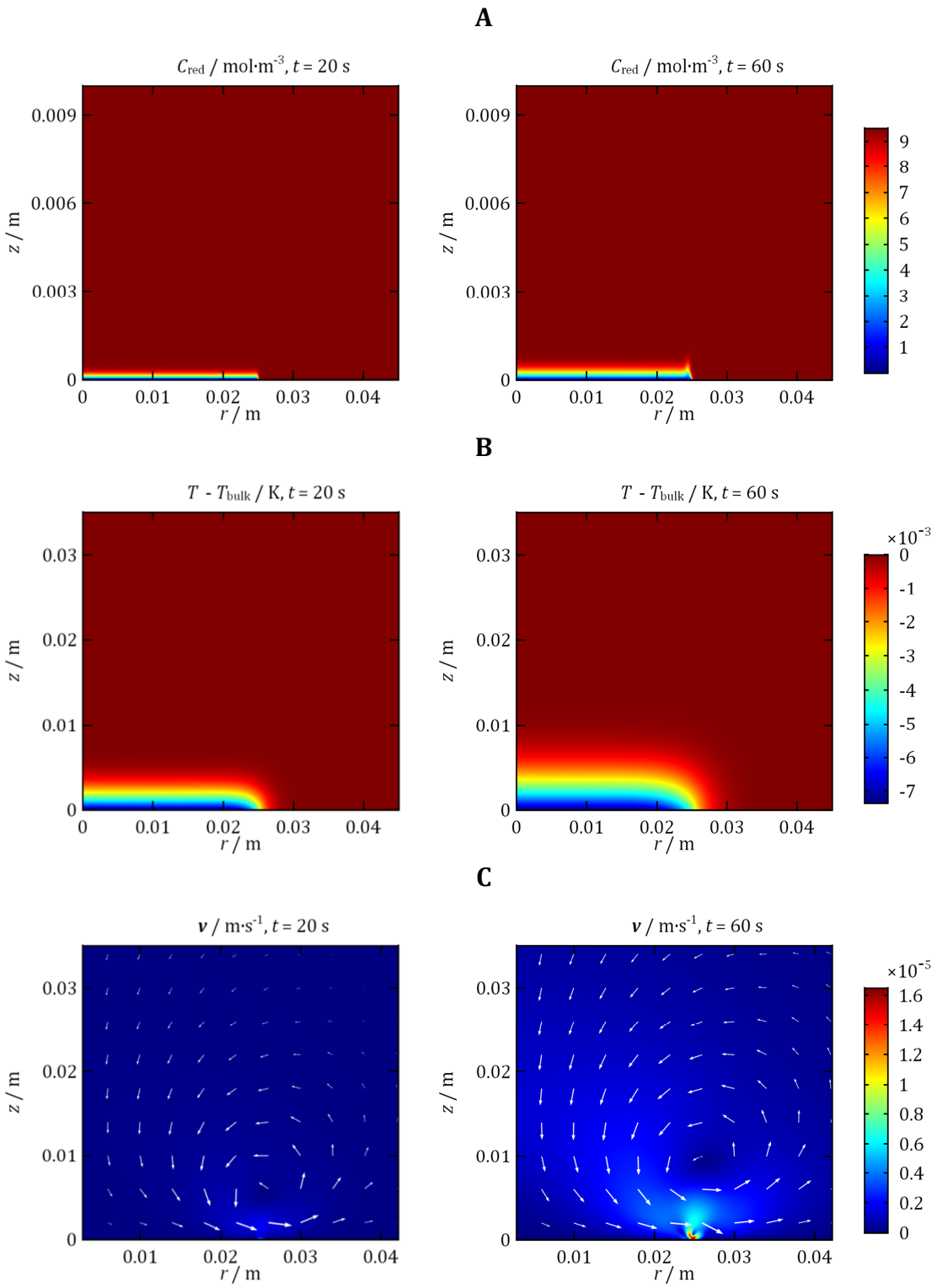


Figure 3.9. Concentration (**A**), temperature (**B**) and velocity profiles (**C**) at t = 20 and 60 s for a chronoamperometric oxidation of $[Fe(CN_6)]^{4-}$ at an electrode of radius r_e = 25 mm. The simulation includes both types of natural convection and is performed with the experimentally measured enthalpy of the reaction [13], ΔH = 45.35 kJ·mol^{-1} and cell dimensions of $r_{max} = z_{max} = 4 \cdot r_e$ = 100 mm. The length of the arrows representing the velocity vector is proportional to the natural logarithm of $|\boldsymbol{v}|$. Note the different length scale of the perturbation in C (**A**).

3.3.2. **Cyclic voltammetry**

The $I(E)$ curves for all simulations of cyclic voltammetry described in Section 3.2.2 are plotted in Figures 3.10-3.12. The profiles of C_{red}, $\boldsymbol{v}$ and T for some illustrative studied cases are given in Section A.2, Appendix A.

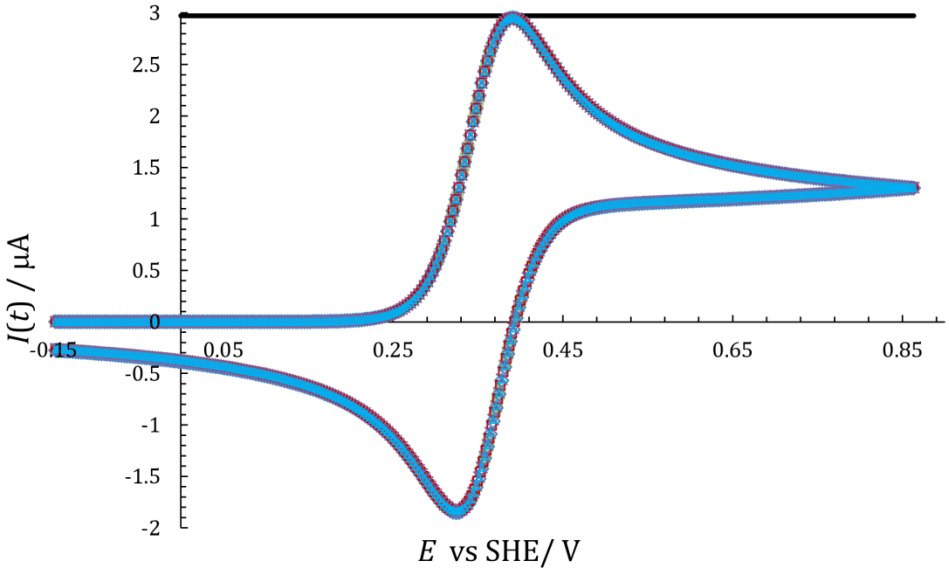


Figure 3.10. Cyclic voltammogram for r_e = 0.25 mm at a scan rate of 33.7 mV·s^{-1}. Legend as follows: solid line – exact expression for the height of the forward peak in the diffusion-only case (Eq. (3.49)); diamonds – diffusion-only simulation; squares – simulation with convection driven by concentration gradients; dashed line – simulation with convection driven by concentration and temperature gradients with ΔH = 45.35 kJ·mol^{-1}; crosses – simulation with convection driven by gradients in concentration and temperature with ΔH = −45.35 kJ·mol^{-1}; triangles – simulation with convection driven by concentration and temperature gradients with ΔH = −100.0 kJ·mol^{-1}. For all simulations, $r_{\text{max}} = r_e + 6\sqrt{t_{\text{max}}\kappa/(\rho_0 c_p)} = 17.58$ mm, $z_{\text{max}} = 6\sqrt{t_{\text{max}}\kappa/(\rho_0 c_p)} = 17.33$ mm.

The heights of the forward and backward peak were used as criteria for the relative differences between them. Within the precision of our simulations, these two characteristics are indistinguishable from their values for the convection-free case. Thus, we conclude that, in contrast with chronoamperometry, under the studied conditions cyclic voltammetry is unaffected by either solutal or thermal

convection. The reason for this qualitative difference is that the electrode potential is varied continuously (Eq. (3.47)) between a value at which no reaction occurs and the limiting-current one applied in chronoamperometry (E_v = E_{chrono}). As the scan rate in our simulations is chosen so that the duration of the entire scan (t_{max}) is equal to that of the chronoamperometric oxidation, this means that reaction (3.1) occurs over a much shorter time period in cyclic voltammetry than in chronoamperometry. Consequently, the build-up of product that drives the solutal convection is much less pronounced. Furthermore, in cyclic voltammetry, the cumulative effect resulting from the build-up of product over the course of the whole process is reversed in the second half of the potential scan.

Although the simulated electrical currents are unaffected by the presence of convection, the same is not true for the concentration profiles (see Section A.2 in Appendix A) and it is possible for convective flows to become important under different conditions, e.g., a lower scan rate and/or a longer duration of the scan.

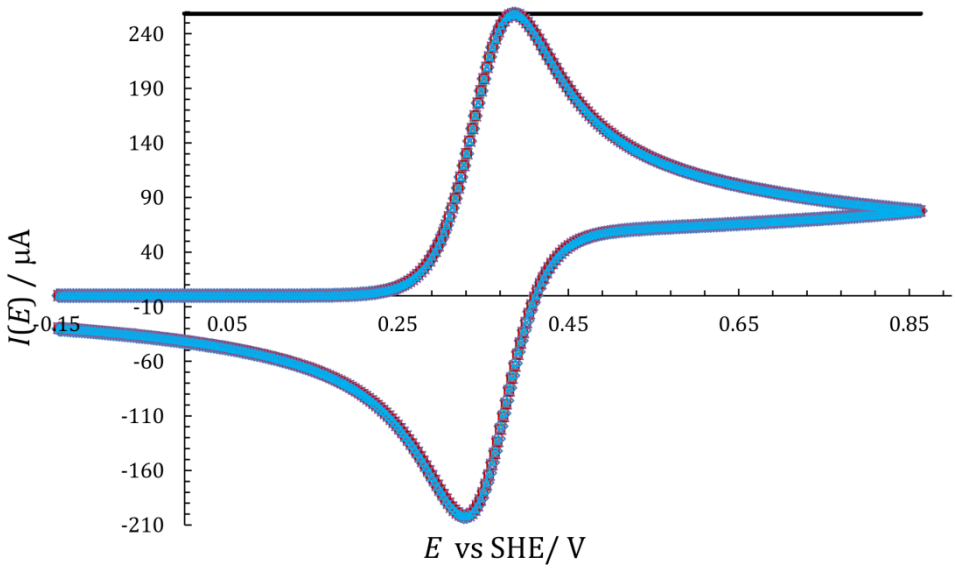


Figure 3.11. Cyclic voltammogram for r_e = 2.5 mm at a scan rate of 33.7 mV·s^{-1}. Legend as in Figure 3.10. For all simulations, r_{max} = r_e+$6\sqrt{t_{max}\kappa/(\rho_0 c_p)}$ = 19.82 mm, z_{max} = $6\sqrt{t_{max}\kappa/(\rho_0 c_p)}$ = 17.33 mm.

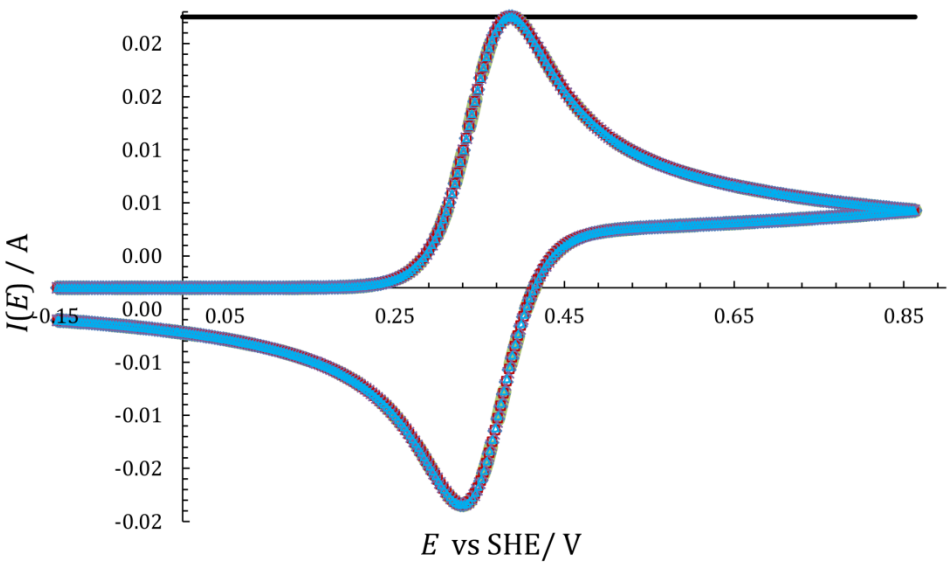


Figure 3.12. Cyclic voltammogram for r_e = 25 mm at a scan rate of 33.7 mV·s^{-1}. Legend as in Figure 3.10. For all simulations, r_{max} = z_{max} = 0.100 m.

3.4. Conclusions

In this chapter, we have investigated the effect of natural convection driven by reaction-induced gradients in temperature and solute concentration on the currents measured in the important electroanalytical techniques chronoamperometry and cyclic voltammetry. We have performed numerical simulations of the electrochemical oxidation of hexacyanoferrate (II) to hexacyanoferrate (III) at a range of electrode sizes.

In agreement with the results reported in a recent study by Ngamchuea et al. [2], we see that if the model reaction occurs under chronoamperometric conditions, solutal convection enhances mass transport and leads to a significantly higher electrical current than in the diffusion-only case (Figures 3.2-3.7). Even though thermal convective flows are always generated by the change of enthalpy associated with the electrochemical reaction, our results indicate that their role is negligible for all cases considered here. The explanation behind this lies in the different length scales over which the perturbations in temperature and concentration spread. As heat propagates through the solution much faster than mass, the characteristic

length of the thermal boundary layer is much larger than that of the diffusion boundary layer, which results in a low buoyancy ratio N and a negligible contribution of the variations in temperature to the buoyancy force, see Eqs. (3.45)-(3.46) above. This assertion is confirmed by the results from our simulations at all considered electrode sizes (ranging from 0.25 to 25 mm). Even at an enthalpy change several times greater in absolute value and reverse in sign with respect to the measured one (ΔH = −100.0 kJ·mol^{-1} instead of 45.35 kJ·mol^{-1}), the effect of thermal convection on the electrical current is within the numerical accuracy of the simulations.

Remarkably, our simulations show that neither solute-driven nor thermal convection exerts an appreciable influence on the electrical current measured in cyclic voltammetry under the studied conditions. As discussed in Section 3.3.2, the contrast with respect to chronoamperometry is due to the shorter timescale over which the model reaction takes place in cyclic voltammetry and the occurrence of the reverse reaction during the second half of the voltammetric scan.

To summarize, the main finding of this chapter is that the thermal convection induced by the intrinsic heat of an electrochemical reaction has a negligible effect on the currents measured in both chronoamperometry and cyclic voltammetry. Our work provides important physical insight into a phenomenon that has received little attention in the literature despite its ubiquity, thereby furthering the understanding of the studied electroanalytical techniques. A logical development of the topic would be a study of the effect of natural convection on measurements made with SECM. Having in mind the results presented here, we do not expect reaction-induced thermal convection to be important in this case. Thus, in Chapters 4 and 5 we focus on thermal convection driven by imperfect thermostating.

Additional data. Appendix A contains plots of the concentration, temperature and velocity profiles for the simulations described in Sections 3.2-3.3.

3.5. References

[1] V. Sahore, A. Kreidermacher, F.Z. Khan, I. Fritsch, Visualization and Measurement of Natural Convection from Electrochemically-Generated Density Gradients at Concentric Microdisk and Ring Electrodes in a Microfluidic System, J. Electrochem. Soc., 163 (2016) H3135-H3144.

[2] K. Ngamchuea, S. Eloul, K. Tschulik, R.G. Compton, Advancing from Rules of Thumb: Quantifying the Effects of Small Density Changes in Mass Transport to Electrodes. Understanding Natural Convection, Anal. Chem., 87 (2015) 7226-7234.

[3] J. Padova, Ion—Solvent Interaction. II. Partial Molar Volume and Electrostriction: A Thermodynamic Approach, J. Chem. Phys., 39 (1963) 1552-1557.

[4] F.J. Millero, Molal Volumes of Electrolytes, Chem. Rev., 71 (1971) 147-176.

[5] J.R. Selman, J. Newman, Free-Convection Mass Transfer with a Supporting Electrolyte, J. Electrochem. Soc., 118 (1971) 1070-1078.

[6] A.M. Bond, D.C. Coomber, S.W. Feldberg, K.B. Oldham, T. Vu, An Experimental Evaluation of Cyclic Voltammetry of Multicharged Species at Macrodisk Electrodes in the Absence of Added Supporting Electrolyte, Anal. Chem., 73 (2001) 352-359.

[7] X. Gao, J. Lee, H.S. White, Natural Convection at Microelectrodes, Anal. Chem., 67 (1995) 1541-1545.

[8] A. Beckmann, B.A. Coles, R.G. Compton, P. Gründler, F. Marken, A. Neudeck, Modeling Hot Wire Electrochemistry. Coupled Heat and Mass Transport at a Directly and Continuously Heated Wire, J. Phys. Chem. B, 104 (2000) 764-769.

[9] R.G. Compton, E. Laborda, K.R. Ward, Understanding Voltammetry: Simulation of Electrode Processes, Imperial College Press, 2014.

[10] E.J.F. Dickinson, J.G. Limon-Petersen, N.V. Rees, R.G. Compton, How Much Supporting Electrolyte Is Required to Make a Cyclic Voltammetry Experiment Quantitatively “Diffusional”? A Theoretical and Experimental Investigation, J. Phys. Chem. C, 113 (2009) 11157-11171.

[11] R.B. Bird, W.E. Stewart, E.N. Lightfoot, Transport Phenomena, Second ed., John Wiley & Sons, New York, 2002.

[12] S.J. Konopka, B. McDuffie, Diffusion Coefficients of Ferri- and Ferrocyanide Ions in Aqueous Media, Using Twin-Electrode Thin-Layer Electrochemistry, Anal. Chem., 42 (1970) 1741-1746.

[13] P. Boudeville, A. Tallec, Electrochemistry and Calorimetry Coupling: IV. Determination of Electrochemical Peltier Heat, Thermochim. Acta, 126 (1988) 221-234.

[14] T. Ozeki, N. Ogawa, K. Aikawa, I. Watanabe, S. Ikeda, Thermal Analysis of Electrochemical Reactions. Influence of Electrolytes on Peltier Heat for Cu(0)/Cu(II) and Ag(0)/Ag(I) Redox Systems, J. Electroanal. Chem., 145 (1983) 53-65.

[15] Z. Fang, S. Wang, Z. Zhang, The Peltier Heat and the Standard Electrode Potential of Ferro-Ferricyanide Couple at 298.15 K Determined by Electrochemical-Calorimetry, J. Therm. Anal. Calorim., 106 (2011) 937-943.

[16] L. Demkowicz, A Note on Symmetry Boundary Conditions in Finite Element Methods, Appl. Math. Lett., 4 (1991) 27-30.

[17] H.S. Harned, B.B. Owen, The Physical Chemistry of Electrolytic Solutions, Reinhold, New York, 1958.

[18] S.W. Feldberg, E.R. Lewis, Concentration and Density Changes at an Electrode Surface and the Principle of Unchanging Total Concentration, J. Electrochem. Soc., 163 (2016) H3167-H3172.

[19] Y. Marcus, Ion Properties, Marcel Dekker, New York, 1997.

[20] L.D. Landau, E.M. Lifshitz, Fluid Mechanics, Second ed., Pergamon Press, Oxford, 1987.

[21] K.J. Vetter, Electrochemical Kinetics: Theoretical and Experimental Aspects, Academic Press, New York, 1967.

[22] S.E. Pringle, R.J. Glass, Double-Diffusive Finger Convection: Influence of Concentration at Fixed Buoyancy Ratio, J. Fluid Mech., 462 (2002) 161-183.

[23] O.P. Singh, J. Srinivasan, Effect of Rayleigh Numbers on the Evolution of Double-Diffusive Salt Fingers, Phys. Fluids, 26 (2014) 062104.

[24] D.R. Lide (Ed.), CRC Handbook of Chemistry and Physics, Internet Version 2005, CRC Press, Boca Raton, FL, 2005.

[25] K. Ngamchuea, S. Eloul, K. Tschulik, R.G. Compton, Planar Diffusion to Macro Disc Electrodes—What Electrode Size Is Required for the Cottrell and Randles-Sevcik Equations to Apply Quantitatively?, J. Solid State Electrochem., 18 (2014) 3251-3257.

[26] E.J.F. Dickinson, H. Ekström, E. Fontes, COMSOL Multiphysics®: Finite Element Software for Electrochemical Analysis. A Mini-Review, Electrochem. Commun., 40 (2014) 71-74.

[27] D.W. Pepper, J.C. Heinrich, The Finite Element Method: Basic Concepts and Applications with Matlab®, Maple, and COMSOL, Third ed., CRC Press, Boca Raton, FL, 2017.

[28] D.D. Gray, A. Giorgini, The Validity of the Boussinesq Approximation for Liquids and Gases, Int. J. Heat Mass Transfer, 19 (1976) 545-551.

[29] D. Shoup, A. Szabo, Chronoamperometric Current at Finite Disk Electrodes, J. Electroanal. Chem., 140 (1982) 237-245.

[30] R.G. Compton, C.E. Banks, Understanding Voltammetry, Second ed., Imperial College Press, London, 2011.

[31] A.J. Bard, L.R. Faulkner, Electrochemical Methods: Fundamentals and Applications, Second ed., John Wiley & Sons, Inc., New York, 2001.

[32] C. Amatore, S. Szunerits, L. Thouin, J.-S. Warkocz, The Real Meaning of Nernst's Steady Diffusion Layer Concept under Non-Forced Hydrodynamic Conditions. A Simple Model Based on Levich's Seminal View of Convection, J. Electroanal. Chem., 500 (2001) 62-70.

4. Convective Heat Transfer in a Measurement Cell for Scanning Electrochemical Microscopy

Overview

Electrochemical experiments, especially those performed with scanning electrochemical microscopy (SECM), are often carried out without taking seeking to thermostat the solution; it is usually assumed that its temperature is homogeneous and equal to the ambient. The present study aims to test this assumption via numerical simulations of the heat transfer in a particular system – the typical measurement cell for SECM. It is assumed that the temperature of the solution is initially homogeneous but different from that of its surroundings; convective heat transfer in the solution and the surrounding air is taken into account within the framework of the Boussinesq approximation. The hereby presented theoretical treatment indicates that an initial temperature difference of the order of 1 K dissipates with a characteristic time scale of ~ 1000 s; the thermal equilibration is accompanied by convective flows with a maximum velocity of $\sim 10^{-4}$ m·s^{-1}; furthermore, the temporal evolution of the temperature profile is influenced by the sign of the initial difference. These results suggest that, unless the temperature of the solution is rigorously controlled, natural convection may significantly compromise the interpretation of data from SECM and other electrochemical techniques, which is usually done on the basis of diffusion-only models.

4.1. Introduction

Scanning electrochemical microscopy (SECM) is a widely-used experimental technique that consists in measuring the faradaic current passing through a microelectrode when the latter is moved through an electroactive solution in relation to a substrate [1]. SECM has a wide range of applications, including topographic imaging of substrates, shape characterisation of microelectrodes, studies of living cells, measurements of the rates of surface reactions [1], etc. Measurements done with the scanning electrochemical microscope are generally interpreted under the assumption that throughout the experiment, the temperature of the solution is homogeneous and equal to the ambient [2] so that thermal convection does not contribute to the mass transport. Apart from the Schuhmann group in Bochum, few authors devote special attention to thermostating the solution in SECM measurements [2].

Despite that, some studies in which the temperature is controlled can be found in the literature; in most of them, the solution temperature is varied across a range of values. Notably, Zhang et al. [3] investigated an electron-transfer reaction at the interface between an organic liquid and a mixture of ice and a supporting electrolyte; this study involved a low-temperature electrochemical cell capable of maintaining temperatures down to −35 °C. Delville et al. [4] measured the temperature dependence of the rate of an electron-transfer reaction occurring across a monolayer at the interface of two immiscible electrolyte solutions. Wang et al. [5] did variable-temperature imaging of DNA hybridization via SECM; Hirano et al. [6] performed a low-temperature SECM study of living cells that used a custom-made heat bath. Kim et al. [7] constructed an isothermal chamber for SECM experiments in which the temperature varied by less than 0.3 K over the course of a whole day.

Other modifications of the SECM technique that involve thermal effects have been devised, e.g. Boika and Zhao [8] reported that using heated SECM tips, electrically insulating substrates can be distinguished based on differences in their

thermal conductivities. Sode et al. [9] have determined the temperature distribution in the direction normal to the SECM tip through measurements of the open circuit potential in an SECM cell. Zhang et al. [10] have designed a microelectrode that also contains a thermocouple; if applied to SECM, such an electrode would give information on the local distribution of temperature in addition to the concentration profile that the standard measurements probe. Schäfer et al. [2] used a Peltier element to control the temperature of the sample and the solution in the SECM cell in an interval of over 100 K, taking special care to ensure that the temperature distribution was spatially homogeneous. In spite of that, the images they obtained at higher temperature were of lower resolution, which they ascribed to convection. In a follow-up study [11], the same research group took advantage of the fact the heating pulses that the Peltier element applies to the substrate cause it to expand. They improved the spatial resolution of the technique by synchronising the current acquisition with the oscillations of the substrate temperature.

In this study, we focus on the process of heat transfer in an SECM cell in contact with the ambient air, rather than the electrochemical reaction itself. Our aim is to determine the timescale for reaching thermal equilibrium in a typical SECM measurement cell. We suppose that initially there is a small temperature difference between the solution and its surroundings. In experimental studies with no temperature control it is implicitly assumed that even if such differences exist at the start of an experiment, they dissipate quickly and the temperature rapidly becomes homogeneous throughout the solution. If this assumption is violated, the resulting buoyancy flows will contribute to the measured electrical current, which is typically regarded as purely diffusive; they may also result in a loss of imaging quality, as suggested by Schäfer et al. [2]. To our knowledge, no theoretical treatment of this particular problem has so far been published in the literature, despite its broad implications for the interpretation of SECM data in particular and for electrochemistry in general.

4.2. Model

4.2.1. Theory

4.2.1.A *Heat transfer*

In this section, we present an approximate model of the heat transfer in a standard SECM measurement cell (CH Instruments, Inc., Austin, TX, USA, https://www.chinstruments.com), pictured in Figure 4.1A.

As we are most interested in simulating the behaviour of the studied system semi-qualitatively, rather than modelling all its details, we use a simplified model of the cell geometry that is expected to yield a realistic result. Ignoring the aperture at the bottom that exposes the studied substrate (see Figure 4.1A) and irregularities such as the semi-circular indentation in the wall that typically holds the reference electrode (not shown), we regard the cell as a cylinder of height h_{cell}, inner radius r_{cell} and outer radius $r_{\mathrm{cell}} + d_{\mathrm{wall}}$, filled with solution to a height of h_{cell}. While the actual cell is not filled to its full capacity, the volume of solution in our model corresponds to that in a typical measurement, see Section 4.2.2 for more details. The cell is situated on top of a thermally insulating surface and is surrounded by a large body of air that acts as a heat bath. The measurement cell we model is made out of polytetrafluoroethylene; we approximate the material properties of the solution within it with those of pure water.

The temperature of the solution (T^{L}) is initially homogeneous, but different by ΔT from that of the cell (T^{C}) and the surrounding air (T^{G}), which at that moment are equal to T_{∞}. Over time, heat exchange causes T^{L} and T^{G} and therefore the densities of both fluids to become spatially inhomogeneous, thereby inducing convective flows.

The heat transfer in each of the three phases is governed by the convective heat equation,

$$\frac{\partial T^{\mathrm{i}}}{\partial t} + \boldsymbol{v}^{\mathrm{i}} \cdot \nabla T^{\mathrm{i}} = \chi^{\mathrm{i}} \nabla^2 T^{\mathrm{i}}, \tag{4.1}$$

where 'i' = L (liquid), G (gas) or C (cell), depending on the region in question, t denotes time, $\boldsymbol{v}^{i}$ is the fluid velocity and χ^{i} is the respective thermal diffusivity [$m^2 \cdot s^{-1}$]. In the solid part of the cell, $\boldsymbol{v}^{C} = \boldsymbol{0}$, and the heat transfer is purely conductive. We assume that the problem is axisymmetric; in that case, it is convenient to employ cylindrical coordinates (r, ϕ, z); it follows from the symmetry of the problem that all quantities are independent of the polar angle ϕ and there is no fluid motion in its direction, $v_\phi = 0$.

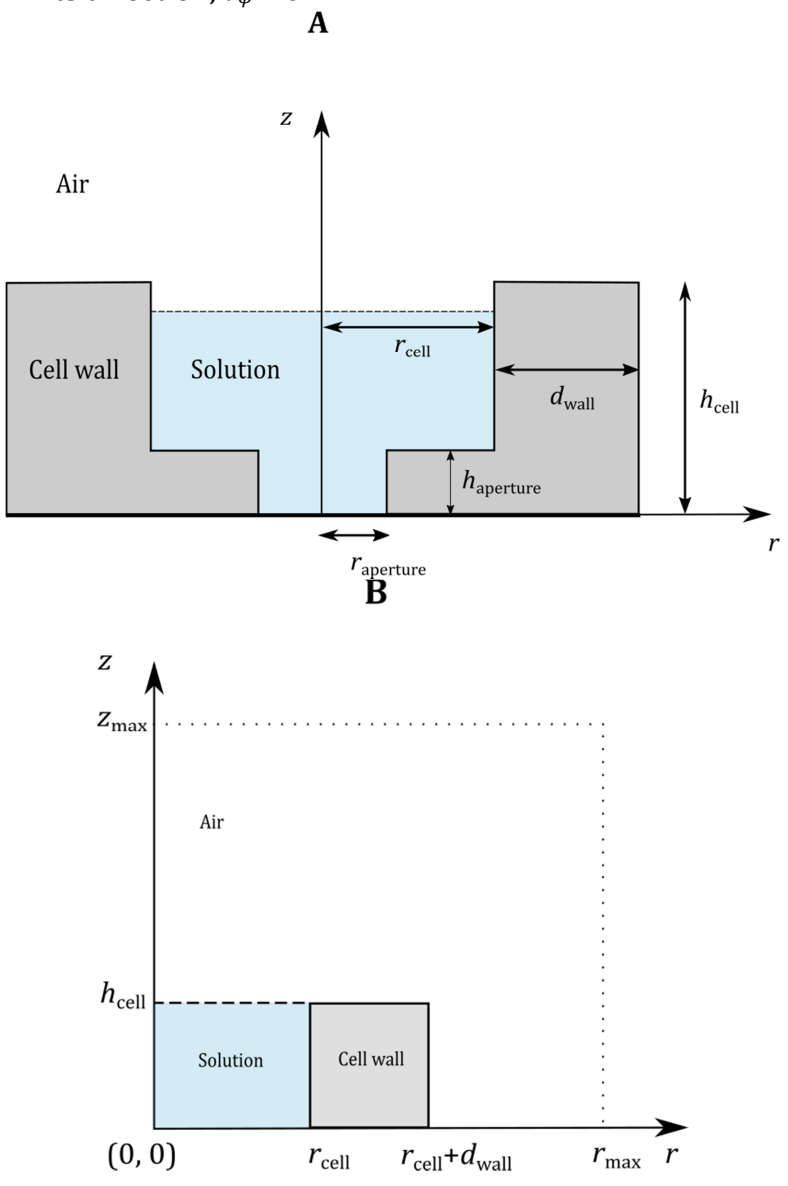


Figure 4.1. Schematic drawings of the geometry of an experimental cell [12] (**A**) and the approximate geometry we adopt for the model (**B**).

The coordinate system is chosen so that its origin is at the centre of the cell bottom, and the vector of gravitational acceleration ($\boldsymbol{g}$) is aligned opposite to the positive z-direction.

For the temperature of the gaseous phase, the initial condition is

$$T^{\mathrm{G}}(t = 0) = T_{\infty}. \tag{4.2}$$

In our model, the gas phase is treated as an infinite heat bath. For the purpose of solving the problem numerically, however, we restrict our treatment of the air to a cylinder of radius $r_{\max}$ and height $z_{\max}$ that extends far beyond the measuring cell, with $r_{\max} \gg r_{\mathrm{cell}} + d_{\mathrm{wall}}$ and $z_{\max} \gg h_{\mathrm{cell}}$. At the boundaries of the simulated region, the temperature is presumed to be unaffected, which corresponds to the boundary conditions

$$T^{\mathrm{G}}\Big|_{z = z_{\max}} = T^{\mathrm{G}}\Big|_{r = r_{\max}} = T_{\infty}. \tag{4.3}$$

In addition, both the temperature and the heat flux must be continuous at the boundaries between the different phases [13], thus requiring that

$$(T^{\mathrm{G}} - T^{\mathrm{C}})\Big|_{r_{\mathrm{cell}} < r < r_{\mathrm{cell}} + d_{\mathrm{wall}},\, z = h_{\mathrm{cell}}} = 0; \tag{4.4}$$

$$\left(\kappa^{\mathrm{G}}\frac{\partial T^{\mathrm{G}}}{\partial z} - \kappa^{\mathrm{C}}\frac{\partial T^{\mathrm{C}}}{\partial z}\right)\Bigg|_{r_{\mathrm{cell}} < r < r_{\mathrm{cell}} + d_{\mathrm{wall}},\, z = h_{\mathrm{cell}}} = 0; \tag{4.5}$$

$$(T^{\mathrm{G}} - T^{\mathrm{C}})\Big|_{r = r_{\mathrm{cell}} + d_{\mathrm{wall}},\, 0 < z < h_{\mathrm{cell}}} = 0; \tag{4.6}$$

$$\left(\kappa^{\mathrm{G}}\frac{\partial T^{\mathrm{G}}}{\partial r} - \kappa^{\mathrm{C}}\frac{\partial T^{\mathrm{C}}}{\partial r}\right)\Bigg|_{r = r_{\mathrm{cell}} + d_{\mathrm{wall}},\, 0 < z < h_{\mathrm{cell}}} = 0, \tag{4.7}$$

$$(T^{\mathrm{G}} - T^{\mathrm{L}})\Big|_{0 < r < r_{\mathrm{cell}},\, z = h_{\mathrm{cell}}} = 0; \tag{4.8}$$

where κ^{i} is the heat conductivity of the respective material.[8]

At the air-liquid interface, the *total* heat flux, i.e., the sum of the convective and conductive contributions must be continuous,

$$\left(\kappa^{\mathrm{G}}\frac{\partial T^{\mathrm{G}}}{\partial z} + v_z^{\mathrm{G}}\rho_0^{\mathrm{G}}\Delta E^{\mathrm{G}} - \kappa^{\mathrm{L}}\frac{\partial T^{\mathrm{L}}}{\partial z} - v_z^{\mathrm{L}}\rho_0^{\mathrm{L}}\Delta E^{\mathrm{L}}\right)\Bigg|_{0 < r < r_{\mathrm{cell}},\, z = h_{\mathrm{cell}}} = 0, \tag{4.9}$$

where ΔE^{i} is the change of internal energy per unit mass for each fluid, with ρ_0^{i} being the density of the respective fluid at t = 0. However, we also require that no mass

[8] Due to a typographical mistake, in the paper on which this chapter is based, gives derivatives with respect to r instead of z in Eq. (4.5) and derivatives with respect to z instead of r in Eq. (4.7); however, all calculations have been performed with the correct expressions.

transfer occurs though the air-water interface, which means that the normal velocities vanish at $z = h_{\text{cell}}$ (consult Section 4.2.1.B) and Eq. (4.9) simplifies to

$$\left(\kappa^{\text{G}} \frac{\partial T^{\text{G}}}{\partial z} - \kappa^{\text{L}} \frac{\partial T^{\text{L}}}{\partial z}\right)\Bigg|_{0 < r < r_{\text{cell}}, z = h_{\text{cell}}} = 0. \tag{4.10}$$

The air is assumed to be in contact with a perfectly thermally insulating solid surface at $z = 0$,

$$\partial_z T^{\text{G}}\Big|_{r_{\text{cell}} + d_{\text{wall}} < r < r_{\text{max}}, z = 0} = 0. \tag{4.11}$$

Due to the symmetry of the system, the temperature of the gas at the cell axis also obeys the condition

$$\partial_r T^{\text{G}}\Big|_{r = 0, h_{\text{cell}} < z < z_{\text{max}}} = 0. \tag{4.12}$$

We now turn our attention to the heat transfer in the liquid phase. At the start of the studied time period, the temperature of the liquid differs by ΔT from the ambient,

$$T^{\text{L}}(t = 0) = T_\infty - \Delta T, \tag{4.13}$$

where ΔT can be either positive or negative. Continuity of the temperature and the heat flux at the gas-liquid interface is ensured by Eqs. (4.8)-(4.9); at the solid-liquid interface, we have to impose analogous boundary conditions,

$$(T^{\text{C}} - T^{\text{L}})\Big|_{r = r_{\text{cell}}, 0 < z < h_{\text{cell}}} = 0; \tag{4.14}$$

$$\left(\kappa^{\text{C}} \frac{\partial T^{\text{C}}}{\partial r} - \kappa^{\text{L}} \frac{\partial T^{\text{L}}}{\partial r}\right)\Bigg|_{r = r_{\text{cell}}, 0 < z < h_{\text{cell}}} = 0. \tag{4.15}$$

The cell bottom situated at $z = 0$ is presumed to be a perfect thermal insulator, which means that

$$\partial_z T^{\text{L}}\Big|_{0 < r < r_{\text{cell}}, z = 0} = 0. \tag{4.16}$$

A symmetry condition analogous to Eq. (4.12) applies to the temperature of the liquid,

$$\partial_r T^{\text{L}}\Big|_{r = 0, 0 < z < h_{\text{cell}}} = 0. \tag{4.17}$$

For the solid cell, the initial condition is identical to that for the gas,

$$T^{\text{C}}(t = 0) = T_\infty. \tag{4.18}$$

Continuity of the temperature and the heat flux at the solid walls is guaranteed by Eqs. (4.4)-(4.7) and (4.14)-(4.15). The cell bottom is assumed to be a perfect thermal insulator,

$$\partial_z T^{\mathrm{C}} \Big|_{r_{\mathrm{cell}} < r < r_{\mathrm{cell}} + d_{\mathrm{wall}}, z = 0} = 0. \tag{4.19}$$

Note that in the treatment above, we have neglected the enthalpy change intrinsic to the electrochemical reaction itself; we have shown in a previous study that this is justified to a high level of approximation [14]. Furthermore, as the typical SECM electrode has a diameter of ~ 20 μm including its insulating sheath, whereas the diameter of the measurement cell is ~ 16 mm, the total heat flux through the tip is guaranteed to be negligible in comparison with the flux through the walls of the cell and through the liquid-gas interface.

4.2.1.B *Momentum transfer*

In this section, we will describe our approach to solving the hydrodynamic part of the problem under consideration.

As we stated in the Introduction to this chapter (Section 4.1), the heat transfer brings about temperature gradients in the liquid phases, which in turn cause density gradients and buoyancy forces to arise, a phenomenon known as free convection [13]. For that reason, the temperature profiles T^{L}, T^{G} and T^{C} must be determined by solving Eqs. (4.1) in conjunction with the Navier-Stokes equations for the two fluid phases,

$$\rho_0^{\mathrm{i}} \left(\frac{\partial \boldsymbol{v}^{\mathrm{i}}}{\partial t} + \boldsymbol{v}^{\mathrm{i}} \cdot \nabla \boldsymbol{v}^{\mathrm{i}} \right) = -\nabla p^{\mathrm{i}} + \eta^{\mathrm{i}} \nabla^2 \boldsymbol{v}^{\mathrm{i}} + \boldsymbol{F}^{\mathrm{i}}, \tag{4.20}$$

where, as above, 'i' = L and G for the liquid and the gas, p^{i} is the hydrodynamic pressure in each phase, η^{i} is its viscosity, and $\boldsymbol{F}^{\mathrm{i}}$ is the gravitational force that acts upon it. The force term is approximately given by the relation

$$\boldsymbol{F}^{\mathrm{i}} = \rho_0^{\mathrm{i}} \boldsymbol{g} \left[1 - \alpha^{\mathrm{i}} \left(T^{\mathrm{i}} - T^{\mathrm{i}}(t = 0) \right) \right], \tag{4.21}$$

where α denotes the isobaric thermal expansion coefficient of the fluid, $\alpha = -1/\rho \cdot (\partial \rho / \partial T)_p$. For the solution we use the value for water at the initial

temperature, $\alpha^{\mathrm{L}}|_{T^{\mathrm{L}}=(T_\infty-\Delta T)}$, while for the air, we use the ideal gas approximation, $\alpha^{\mathrm{G}} \approx 1/T_\infty$.

The Navier-Stokes equations are paired with a continuity equation for each of the fluids,

$$\nabla \cdot \boldsymbol{v}^{\mathrm{i}} = 0. \tag{4.22}$$

Eqs. (4.20)-(4.22) implicitly state that in our model, we only consider the variations in density with temperature insofar as buoyancy forces are concerned. We neglect the dependence of all other fluid properties on temperature, which is justified as long as $\left(T^{\mathrm{i}} - T^{\mathrm{i}}(t=0)\right)/T^{\mathrm{i}}(t=0)$ is sufficiently small, consult Gray and Giorgini [15]. Furthermore, Eq. (4.22) also states that the gas phase is incompressible, which is evidently not true, but is sufficiently accurate for flows with a low Mach number like the ones we consider [16]. The system of equations comprising Eqs. (4.1) and (4.20)-(4.22) is known as the Boussinesq approximation for free convection [13, 16].

Initially, neither of the fluid phases is in motion,

$$\boldsymbol{v}^{\mathrm{i}}(t=0) = \mathbf{0}. \tag{4.23}$$

The velocity of the air vanishes infinitely far away from the source of the disturbance (the measurement cell); in our numerical treatment of the problem, this condition is substituted with

$$\boldsymbol{v}^{\mathrm{G}}\Big|_{r=r_{\max}} = \boldsymbol{v}^{\mathrm{G}}\Big|_{z=z_{\max}} = \mathbf{0}. \tag{4.24}$$

To ensure that the model is equivalent to a measurement cell in contact with an infinite air bath, we choose the dimensions of the simulated region $r_{\max}$ and $z_{\max}$ as large as is computationally realistic such that $r_{\max} = 10 \cdot r_{\mathrm{cell}}$ and $z_{\max} = 40 \cdot z_{\mathrm{cell}}$, noting that these distances are of the order of the characteristic length of heat transfer, which for our simulations is $L \sim \sqrt{t\chi^{\mathrm{G}}} = \sqrt{3600 \cdot 2 \times 10^{-5}} \sim 0.2$ m.

No-slip boundary conditions equivalent to (4.24) are also required at the solid-air boundaries [13], namely at the walls of the cell and the insulating surface on top of which the cell is situated,

$$\begin{aligned}\boldsymbol{v}^{\mathrm{G}}\Big|_{r_{\mathrm{cell}} < r < r_{\mathrm{cell}} + d_{\mathrm{wall}},\, z = h_{\mathrm{cell}}} &= \boldsymbol{v}^{\mathrm{G}}\Big|_{r = r_{\mathrm{cell}} + d_{\mathrm{wall}},\, 0 < z < h_{\mathrm{cell}}} \\ &= \boldsymbol{v}^{\mathrm{G}}\Big|_{r_{\mathrm{cell}} + d_{\mathrm{wall}} < r < r_{\max},\, z = 0} = \mathbf{0}.\end{aligned} \tag{4.25}$$

Analogously, the velocity must vanish at the solid-liquid boundaries,

$$\boldsymbol{v}^{\mathrm{L}}\Big|_{0 < r < r_{\mathrm{cell}},\, z = 0} = \boldsymbol{v}^{\mathrm{L}}\Big|_{r = r_{\mathrm{cell}},\, 0 < z < h_{\mathrm{cell}}} = \mathbf{0}. \tag{4.26}$$

The fluid velocities are also subject to symmetry boundary conditions at the cylinder axis,

$$v_r^{\mathrm{i}}\Big|_{r\,=\,0} = 0; \tag{4.27}$$

$$\frac{\partial v_z^{\mathrm{i}}}{\partial r}\Big|_{r\,=\,0} = 0. \tag{4.28}$$

Equations (4.27)-(4.28) are analogous to Eqs. 1.3-1.4 in Demkowicz's paper on symmetry conditions in Cartesian coordinates [17][9].

In addition to the conditions given so far, (4.24)-(4.28), we must specify boundary conditions at the liquid-gas interface. At the boundary between the two viscous fluids, the tangential velocity is continuous [18],

$$v_r^{\mathrm{L}}\Big|_{z\,=\,h_{\mathrm{cell}}} = v_r^{\mathrm{G}}\Big|_{z\,=\,h_{\mathrm{cell}}}. \tag{4.29}$$

Neglecting the mass transport between the two phases, we equate the normal velocities on both sides of the interface to zero,

$$v_z^{\mathrm{L}}\Big|_{z\,=\,h_{\mathrm{cell}}} = v_z^{\mathrm{G}}\Big|_{z\,=\,h_{\mathrm{cell}}} = 0. \tag{4.30}$$

Eq. (4.30) can be viewed as a special case of Eq. 2.79 in the paper by Oron et al. [19] for a stationary interface through which there is no normal mass flux.

The kinematic boundary conditions (4.29)-(4.30) are complemented by the force balance at the surface. In the tangential direction, this reads

$$\eta^{\mathrm{L}}\left(\frac{\partial v_z^{\mathrm{L}}}{\partial r} + \frac{\partial v_r^{\mathrm{L}}}{\partial z}\right)\Big|_{z\,=\,h_{\mathrm{cell}}} = \eta^{\mathrm{G}}\left(\frac{\partial v_z^{\mathrm{G}}}{\partial r} + \frac{\partial v_r^{\mathrm{G}}}{\partial z}\right)\Big|_{z\,=\,h_{\mathrm{cell}}} = 0. \tag{4.31}$$

i.e., the tangential viscous stress must be continuous at the interface. Eq. (4.31) neglects the effect of the interfacial tension on the flow. In a system like the presently discussed one, where the surface temperature is a function of the radial coordinate *r*, there is a non-zero gradient of the surface tension γ, which results in a

[9] Note that in the paper on which this chapter is based [J.K. Novev, R.G. Compton, Phys. Chem. Chem. Phys. 18 (2016) 29836-29846], we state that we also use the boundary condition $\partial v_r^{\mathrm{i}}/\partial z\big|_{r=0}$. As we have noted in a later paper [J.K. Novev, R.G. Compton, Phys. Chem. Chem. Phys. 19 (2017) 12759-12775] and in Chapters 3 and 7 of this thesis, this condition is in fact trivially fulfilled as a consequence of the Eq. (4.27).

force tangential to the interface and thermocapillary motion [18], otherwise known as the thermal Marangoni effect. Even though it may become important for surfactant-free surfaces like the one under consideration, we will neglect it here in the interest of simplicity.

In general, the normal stress balance for our system has the form [20]

$$\left(-p^{\mathrm{L}} + 2\eta^{\mathrm{L}}\frac{\partial v_z^{\mathrm{L}}}{\partial z} + p^{\mathrm{G}} - 2\eta^{\mathrm{G}}\frac{\partial v_z^{\mathrm{G}}}{\partial z}\right)\Bigg|_{z\,=\,h_{\mathrm{cell}}} = 2\gamma H. \tag{4.32}$$

where H is the mean curvature of the interface [21]. Disregarding the variations in the hydrodynamic pressure due to buoyancy effects and noting that viscous stresses in the gas are negligible in comparison with those in the liquid leaves

$$\eta^{\mathrm{L}}\frac{\partial v_z^{\mathrm{L}}}{\partial z}\Bigg|_{z=h_{\mathrm{cell}}} \approx \gamma H. \tag{4.33}$$

A dimensionless criterion, known as the capillary number [13], quantifies the ratio between the capillary and the viscous stress,

$$Ca = \frac{\eta^{\mathrm{L}} v_0}{\gamma}. \tag{4.34}$$

where v_0 is the characteristic normal velocity at the surface. The viscous stress is comparable to the capillary stress only if $Ca \sim 1$, which for water corresponds to $v_0 \sim \gamma / \eta^{\mathrm{L}} \sim 72$ m/s. The velocities in our case are orders of magnitude lower than this value (see Section 4.3), and therefore $\gamma H \approx 0$ at all times, i.e. the surface behaves as non-deformable and remains flat. In this approximation, the hydrodynamic problem is completely defined by the kinematic boundary conditions and the boundary condition for the lateral stress. As in the Rybczynski-Hadamard problem for a liquid drop moving through an ambient fluid, stating the shape of the surface in advance means that we cannot impose a boundary condition on the normal stress [20].

Since we are treating both fluids as incompressible, only the gradients of the pressures p^{L} and p^{G} have physical meaning [22]. Thus, it is most convenient to set the pressures p^{i} at the start of the simulated experiments to zero, and to impose the condition $p^{\mathrm{G}}(r_{\max}, z_{\max}) = 0$ at the edge of the simulated region.

It should be noted that flows of the type studied here exhibit considerable complexity and axisymmetric modes may be inherently unstable. Their stability is

determined by the values of the parameters of the system, and is particularly sensitive to the driving force ΔT and the aspect ratio of the cylindrical enclosure, h_{cell}/r_{cell}. It has been demonstrated by Neumann [23] that in a similar system, no axisymmetric flows can be stable at certain values of the aspect ratio. Furthermore, as shown by Yamaguchi et al. [24] for another system resembling the presently discussed one, even if the flows are assumed to be axisymmetric, they may exhibit complex patterns with multiple cells in both the radial and the axial direction. As we are most interested in establishing the order of magnitude of the flow velocity due to convection, we will assume that the flows are axisymmetric and we will not deal with the question of their stability, which goes beyond the aims of our study.

4.2.2. **Simulations**

This section gives a detailed description of the simulations we have performed and lists the values of the parameters we have used to that end.

Simulations of the heat transfer in an SECM measurement cell were performed with the commercial software package COMSOL Multiphysics ® 5.2 – see Refs. [25] and [26] for discussion of the suitability of COMSOL for electrochemical and convective heat transport problems, respectively. The equations governing the transfer of heat and momentum in the system were solved numerically via the finite element method. Quadratic shape functions were used for the fluid velocity components and linear – for the hydrodynamic pressure; quintic shape functions were employed for the temperature distribution.

Rather than modelling the exact geometry of the cell (Figure 4.1A), we treated it as a cylinder filled with solution to its full capacity; for its height we used the value h_{cell} = 7 mm, for the inner radius – r_{cell} = 8 mm and for the wall thickness – d_{wall} = 7 mm. The parameters were chosen so as to guarantee that the total amount of solution in the model corresponded to that in a typical SECM experiment. For a standard measurement cell (CH Instruments, Inc.) as the one pictured in Figure 4.1A, r_{cell} = 8 mm, h_{cell} = 11 mm, $r_{aperture}$ = 3 mm, $h_{aperture}$ = 3 mm, d_{wall} = 7 mm [12].

Treating the aperture and the wider part of the cell as perfectly cylindrical, we can calculate that the total cell volume is V_{tot} = 1.69 mL; a cell is typically filled to approximately $V_{\mathrm{experimental}} = 0.8 \cdot V_{\mathrm{tot}}$ [12]. Approximating the cell with a cylinder of radius r_{cell} = 8 mm, we calculate that we need to set the model cell height to $h_{\mathrm{cell}} \approx 7$ mm in order to keep the volume in the model equal to $V_{\mathrm{experimental}}$.

For all simulations, the simulated region was of dimensions $r_{\mathrm{max}} = 10 \cdot r_{\mathrm{cell}} = 8 \times 10^{-2}$ m by $z_{\mathrm{max}} = 40 \cdot h_{\mathrm{cell}} = 0.28$ m; though this finite configuration cannot give the exact pattern of convection in the air, we expect it to yield a correct result for the timescale of the heat transfer in the system, which is what we seek to determine.

For the ambient temperature, we used the value T_∞ = 298.15 K. Simulations were performed with $\Delta T = -5$ and 5 K, corresponding to an initial temperature of the solution higher and lower than the ambient, respectively. The properties of the liquid phase were approximated with those of water at the respective initial temperature, $T^{\mathrm{L}}(t = 0) = T_\infty - \Delta T$. At $T^{\mathrm{L}}(t = 0) = 293.15$ K, we used the values $\rho_0^{\mathrm{L}} = 998.21\ \mathrm{kg \cdot m^{-3}}$, $\eta^{\mathrm{L}} = 1.002$ mPa·s, $\kappa^{\mathrm{L}} = 0.5984\ \mathrm{W \cdot m^{-1} \cdot K^{-1}}$ and $\alpha^{\mathrm{L}} = 2.06 \times 10^{-4}\ \mathrm{K^{-1}}$, while at $T^{\mathrm{L}}(t = 0) = 303.15$ K, we calculated with $\rho_0^{\mathrm{L}} = 995.6\ \mathrm{kg \cdot m^{-3}}$, $\eta^{\mathrm{L}} = 0.7977$ mPa·s, $\kappa^{\mathrm{L}} = 0.6154\ \mathrm{W \cdot m^{-1} \cdot K^{-1}}$ and $\alpha^{\mathrm{L}} = 3.02 \times 10^{-4}\ \mathrm{K^{-1}}$; the thermal diffusivity was calculated as $\chi^{\mathrm{L}} = \kappa^{\mathrm{L}} / (\rho_0^{\mathrm{L}} C_p^{\mathrm{L}})$ with C_p^{L} (293.15 K) = $4.1818 \times 10^3\ \mathrm{J \cdot kg^{-1} \cdot K^{-1}}$ and C_p^{L} (303.15 K) = $4.1784 \times 10^3\ \mathrm{J \cdot kg^{-1} \cdot K^{-1}}$ [27].

The density of the air was taken to be $\rho_0^{\mathrm{G}} = 1.161\ \mathrm{kg \cdot m^{-3}}$; the values $\eta^{\mathrm{G}} = 18.6$ μPa·s, $\kappa^{\mathrm{G}} = 2.62 \times 10^{-2}\ \mathrm{W \cdot m^{-1} \cdot K^{-1}}$ and $C_p^{\mathrm{G}} = 1.007 \times 10^3\ \mathrm{J \cdot kg^{-1} \cdot K^{-1}}$ were used for its heat conductivity and heat capacity, respectively [27].

As a typical SECM measurement cell (CH Instruments, Inc.), the cell in our model is made of polytetrafluoroethylene, for which $\rho^{\mathrm{C}} = 2200\ \mathrm{kg \cdot m^{-3}}$ [28], $\kappa^{\mathrm{C}} = 0.259\ \mathrm{W \cdot m^{-1} \cdot K^{-1}}$ [29] and $C_p^{\mathrm{C}} = 898.1\ \mathrm{J \cdot kg^{-1} \cdot K^{-1}}$ [30]. Note that in reality, the properties of polytetrafluoroethylene vary with the average molecular mass of the polymer and therefore these parameters may be only approximately correct for the material of the measurement cell. However, in view of our approximate treatment of the cell geometry and the semi-quantitative nature of this study, this level of accuracy of the material properties is sufficient.

The duration of the simulated experiment was 3600 s in each case. Simulations that involved conductive heat transfer only in all phases were run for comparison; for that case, Eq. (4.1) was solved with the initial and boundary conditions (4.2)-(4.19) and $\boldsymbol{v}^{\mathrm{i}}$ set to $\mathbf{0}$.

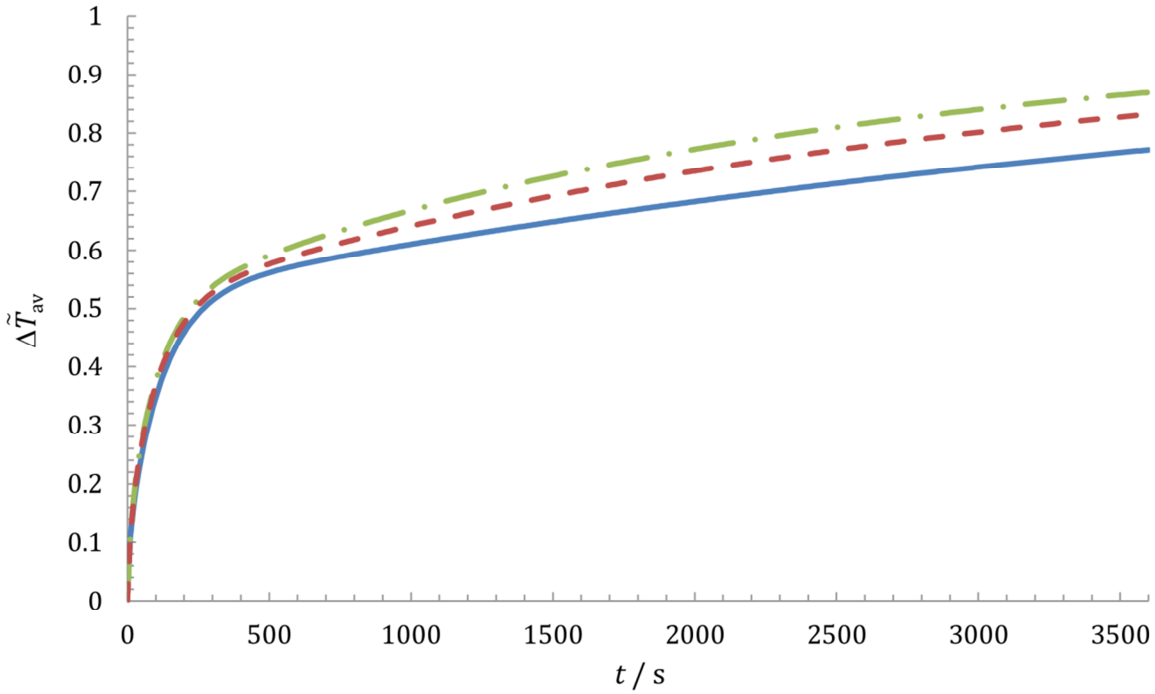


Figure 4.2. $\Delta\tilde{T}_{\mathrm{av}}$ plotted against t for three investigated cases: purely conductive heat transfer (solid line) and heat transfer with convection in a solution that is colder (dashed line, ΔT = 5 K) or warmer (dashdot line, ΔT = −5 K) than its surroundings at t = 0. Note that convection enhances the heat transfer in both cases, but does so to a greater extent if ΔT < 0. The reason for that is the more intense flow that corresponds to this configuration, see the text.

4.3. Results and discussion

The heat transfer across the whole solution is best illustrated by the volume-averaged *dimensionless* temperature change,

$$\Delta\tilde{T}_{\mathrm{av}} = \left|\frac{\int_V \left(T^{\mathrm{L}} - T^{\mathrm{L}}(t=0)\right)\mathrm{d}V}{\int_V \left(T^{\mathrm{L}}(t=0) - T_\infty\right)\mathrm{d}V}\right| = \frac{1}{\pi r_{\mathrm{cell}}^2 h_{\mathrm{cell}}}\frac{1}{\Delta T}\int_V \left(T^{\mathrm{L}} - T^{\mathrm{L}}(t=0)\right)\mathrm{d}V, \qquad (4.35)$$

where the integration is over the cylindrical cell volume. It is evident from this definition that $\Delta\tilde{T}_{av}$ goes from 0 at the start of the process (t = 0) to 1 at as the system approaches thermal equilibrium ($t \to \infty$).

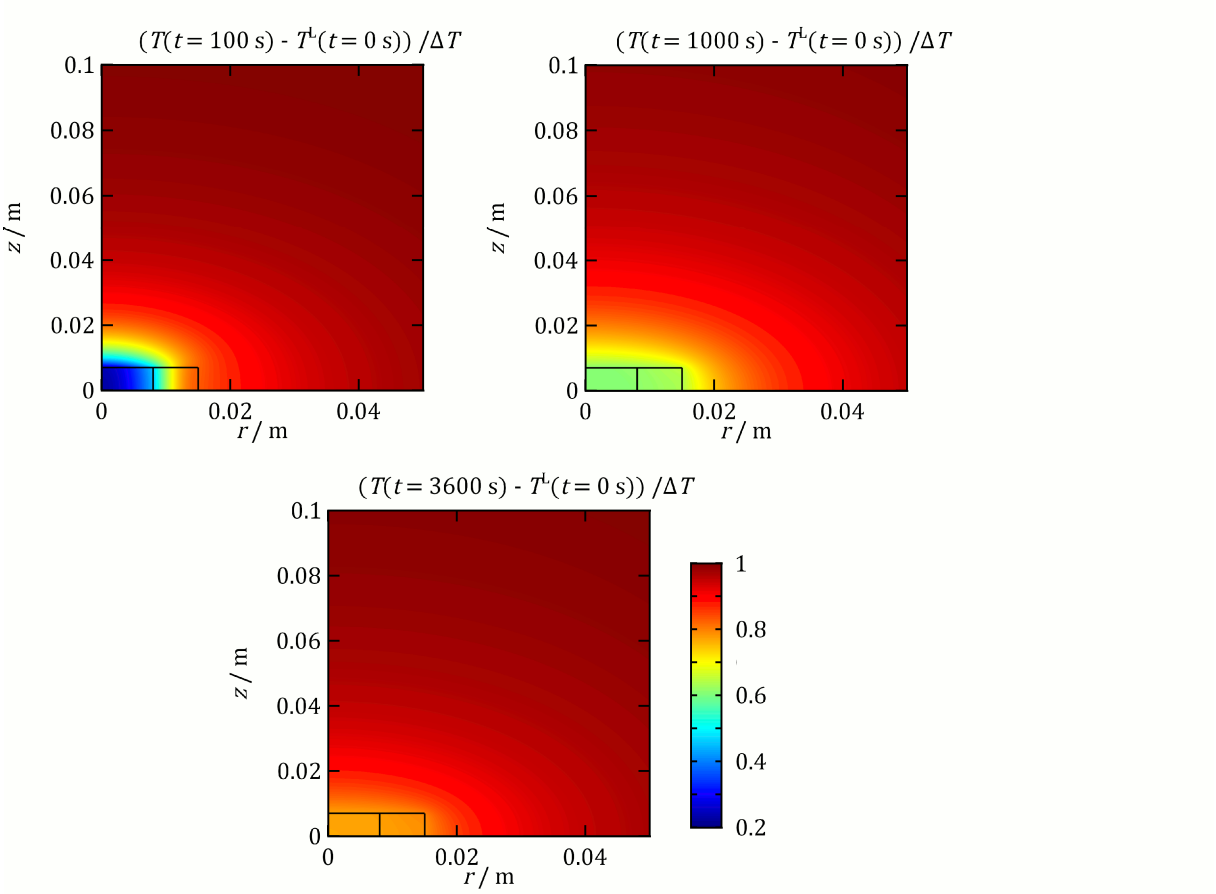


Figure 4.3. 'Snapshots' of the dimensionless temperature distribution, $\tilde{T} = (T - T^L(t = 0))/\Delta T$ at t = 100 s, t = 1000 s and t = 3600 s as predicted by a simulation including only heat transfer by conduction.

Eq. (4.35) is plotted as a function of time in Figure 4.2 for the various investigated cases. As $\Delta\tilde{T}_{av}$ varies by less than a percent between the conduction-only simulations depending on the sign of the initial temperature difference ΔT, only the curve corresponding to ΔT = −5 K is shown in the figure. Figure 4.2 demonstrates that in the simulation with the full model, the timescale for reaching thermal equilibrium is of the order of 10^3 s. The heat transfer becomes significantly affected by convection after a time period of ~ 100 s that is necessary for the flow patterns to be established. After that initial period, the average temperature

difference $\Delta\tilde{T}_{av}$ differs by as much as 10% between the convective simulations and the one with conduction only. Furthermore, it is evident from the plot that the magnitude of the convective contribution to $\Delta\tilde{T}_{av}$ depends on the sign of the initial temperature difference between solution and surroundings.

This dependence is easily explainable in qualitative terms – if at t = 0, the solution is colder than the surrounding air ($\Delta T > 0$), the liquid layers adjacent to the interface start to become warmer and become less dense, meaning that they experience a buoyancy force directed upwards (Eq. (4.21)), but as they are already situated at the top of the cell, this does not cause intense mixing in the liquid; the opposite is true for the case with $\Delta T < 0$. As the convective flows play an important role for the overall heat transfer, starting with a warmer solution ($\Delta T < 0$) leads to faster equilibration, see Figure 4.2.

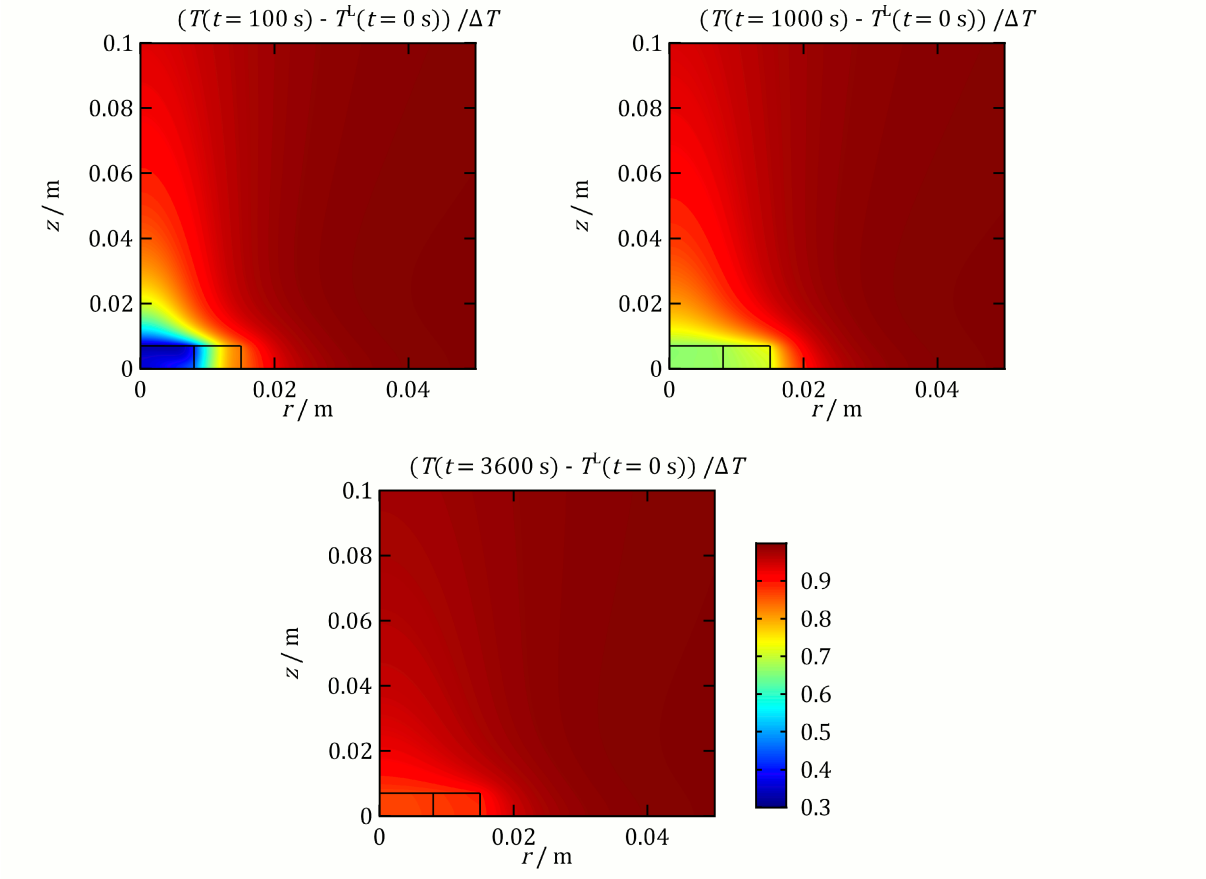


Figure 4.4. Dimensionless temperature distribution, $\tilde{T} = (T - T^{L}(t = 0))/\Delta T$, plotted at t = 100 s, t = 1000 s and t = 3600 s for ΔT = −5 K, i.e. for a solution that is initially warmer than its surroundings.

Figures 4.3-4.9 illustrate this point by showing the evolution of the temperature and the flow in the studied system. A dimensionless quantity,

$$\tilde{T} = \frac{1}{\Delta T}\left(T - T^{\mathrm{L}}(t=0)\right), \tag{4.36}$$

is plotted in the figures rather than the temperature profiles themselves. $\tilde{T}$ is the local equivalent of $\Delta\tilde{T}_{\mathrm{av}}$ (Eq. (4.35)); at t = 0, it varies between 0 for the liquid and 1 for the solid cell and air; at thermal equilibrium, $\tilde{T}$ would be equal to 1 throughout the system. Figure 4.3 shows 'snapshots' of the spatial distribution of $\tilde{T}$ corresponding to purely conductive heat transfer at ΔT = −5 K; just like $\Delta\tilde{T}_{\mathrm{av}}$, $\tilde{T}$ depends very weakly on the initial difference for the convection-free simulations; for that reason, the case with ΔT = 5 K is not illustrated. Figures 4.4 and 4.5 contain plots of $\tilde{T}$ for simulations that involve convection with initial conditions corresponding to a solution that is respectively warmer and colder than the surroundings. It is clear from Figures 4.3-4.5 that the temperature profile in the gaseous phase is considerably distorted by the inclusion of convection in the model, but those in the liquid and the cell are not as strongly affected. In qualitative terms, this can be explained by calculating the Péclet numbers that compare the importance of convective and conductive heat transport in the two phases. For the heat transport in the gas phase at $t \sim 100$ s,

$$Pe^{\mathrm{G}} = \frac{z_{\max}|\boldsymbol{v}^{\mathrm{G}}|}{\chi^{\mathrm{G}}} \sim 100, \tag{4.37}$$

whereas for the liquid phase,

$$Pe^{\mathrm{L}} = \frac{h_{\mathrm{cell}}|\boldsymbol{v}^{\mathrm{L}}|}{\chi^{\mathrm{L}}} \sim 10, \tag{4.38}$$

where we have used the orders of magnitude of the velocities from Figures 4.6-4.9. As Pe^{G} is an order of magnitude larger than Pe^{L}, convective heat transport is much more important for the gaseous phase than for the liquid phase.

Comparison between Figures 4.3-4.5 for the dimensionless temperature profile $\tilde{T}$ and Figures 4.6-4.7 for $\boldsymbol{v}^{\mathrm{G}}$ shows that the form of the temperature profile in the air is largely determined by the convective flow. These figures also demonstrate the differences in the intensity of the flow and the length scale to which the initial disturbance propagates depend on the sign of ΔT. For ΔT = −5 K, i.e., for a solution warmer than its surroundings at t = 0, the maximum velocity $|\boldsymbol{v}^{\mathrm{G}}_{\max}|$ is of the order

of 4×10^{-2} m·s^{-1} and the flow encompasses the whole height of the cell ($\sim10^{-1}$ m), while for ΔT = 5 K $|\boldsymbol{v}^{\mathrm{G}}_{\mathrm{max}}|$ only reaches about 6×10^{-3} m·s^{-1}, and the flow is restricted to the lower region of the cell ($\sim 10^{-2}$ m); the direction of the circulation inside the simulated region of the cell also changes with the sign of ΔT.

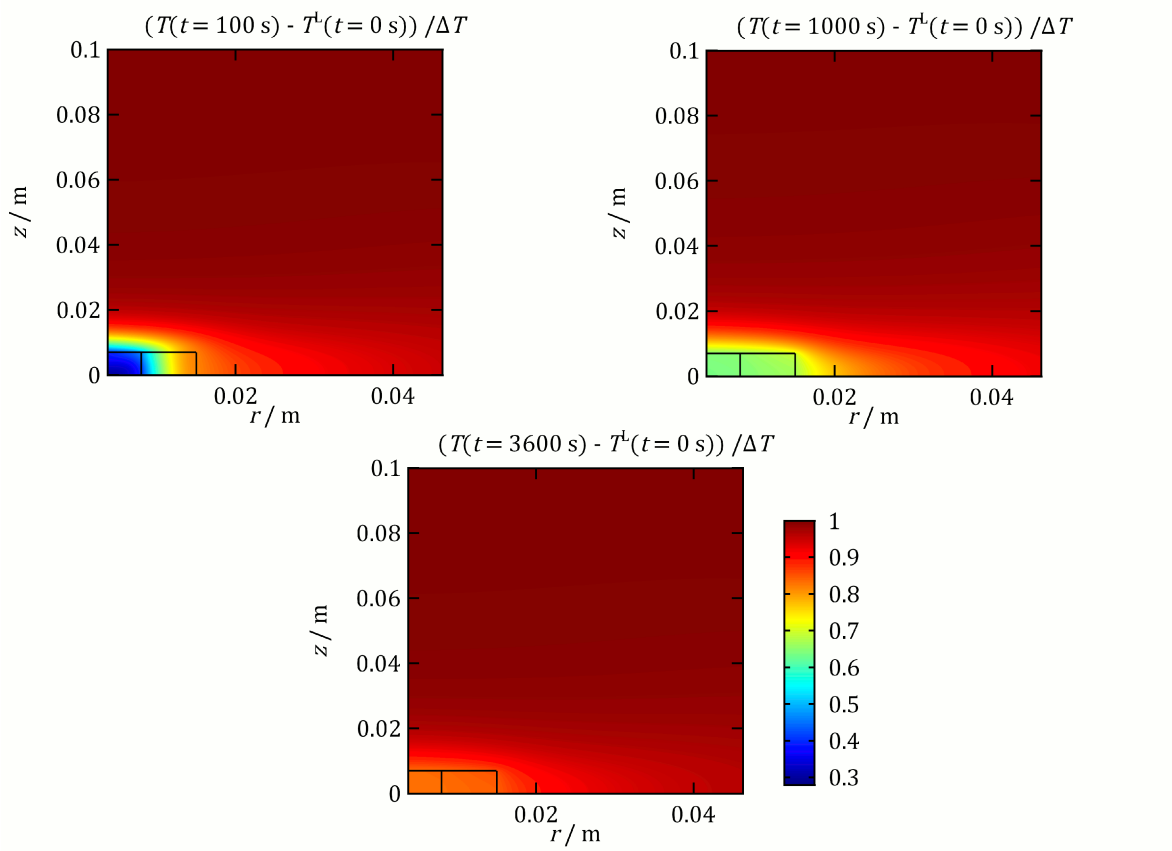


Figure 4.5. Dimensionless temperature distribution, $\tilde{T}$ = (T – $T^{\mathrm{L}}(t$ = 0))/ΔT, plotted at t = 100 s, t = 1000 s and t = 3600 s for ΔT = 5 K, i.e. for a solution that is initially colder than its surroundings.

Figures 4.8 and 4.9, which contain 'snapshots' of $\boldsymbol{v}^{\mathrm{L}}$, demonstrate the effect the sign of the initial temperature change exerts on the flow patterns in the liquid phase. As in the gas phase, the direction of the flow in the simulated part of the cylinder and the magnitude of the maximum velocity are predicted to depend on the sign of ΔT, but the overall patterns are similar ($|\boldsymbol{v}^{\mathrm{L}}_{\mathrm{max}}| \sim 3\times10^{-4}$ vs. 2×10^{-4} m·s^{-1}).

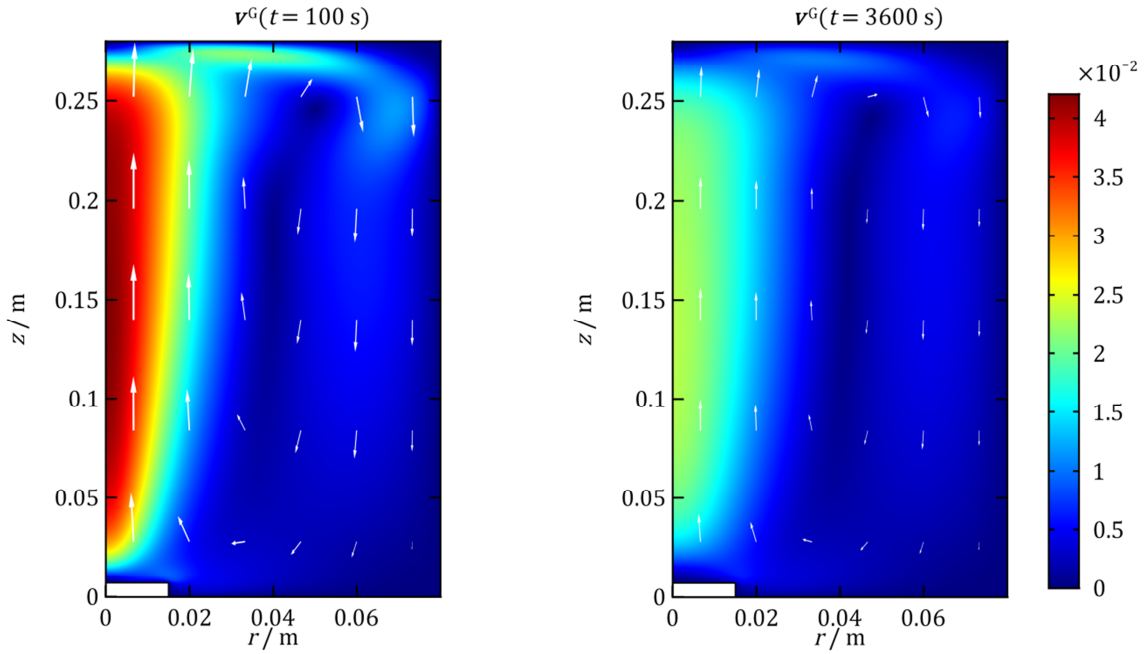


Figure 4.6. Velocity field in the gas phase ($\boldsymbol{v}^G$) plotted at t = 100 s and t = 3600 s for ΔT = −5 K, i.e. for a solution that is initially warmer than its surroundings. The length of the arrows is proportional to the natural logarithm of $|\boldsymbol{v}^G|$.

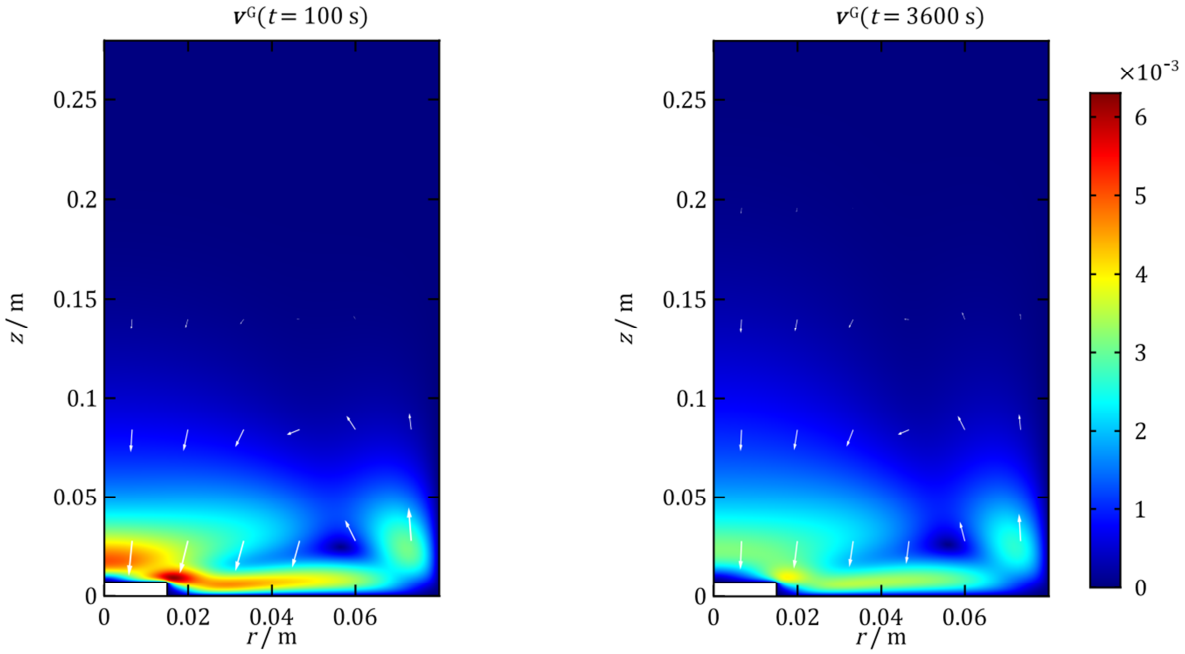


Figure 4.7. Velocity field in the gas phase ($\boldsymbol{v}^G$) plotted at t = 100 s, and t = 3600 s for ΔT = 5 K, i.e. for a solution that is initially colder than its surroundings. The length of the arrows is proportional to the natural logarithm of $|\boldsymbol{v}^G|$.

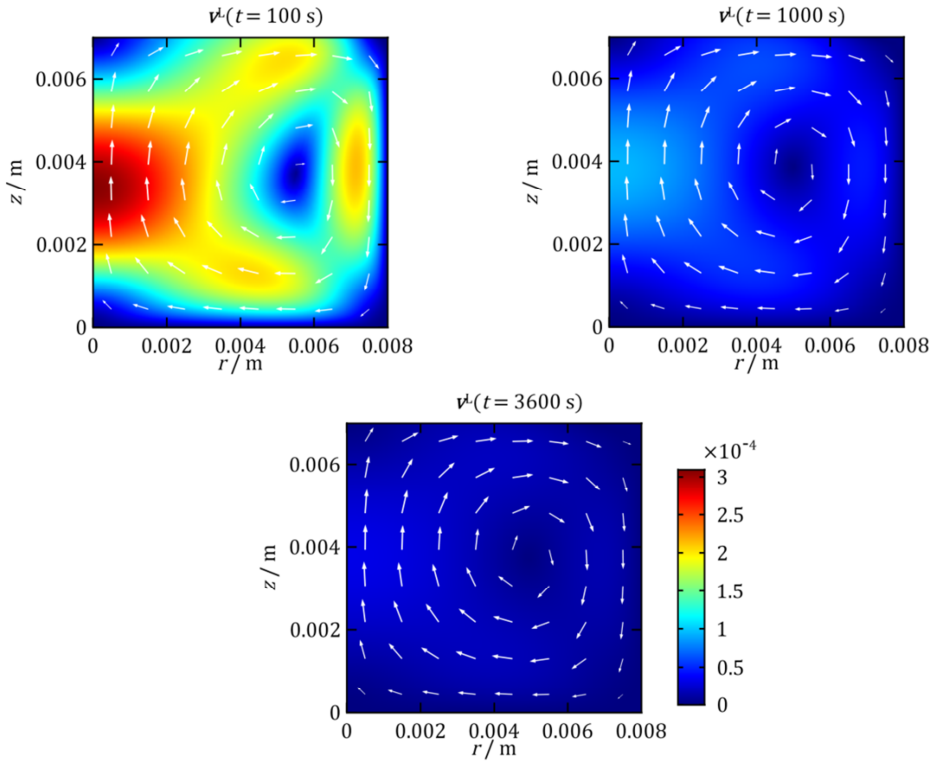


Figure 4.8. Velocity in the liquid phase ($\boldsymbol{v}^{\mathrm{L}}$) plotted at t = 100 s, t = 1000 s and t = 3600 s for ΔT = −5 K, i.e. for a solution that is initially warmer than its surroundings. The length of the arrows is proportional to the natural logarithm of $|\boldsymbol{v}^{\mathrm{L}}|$.

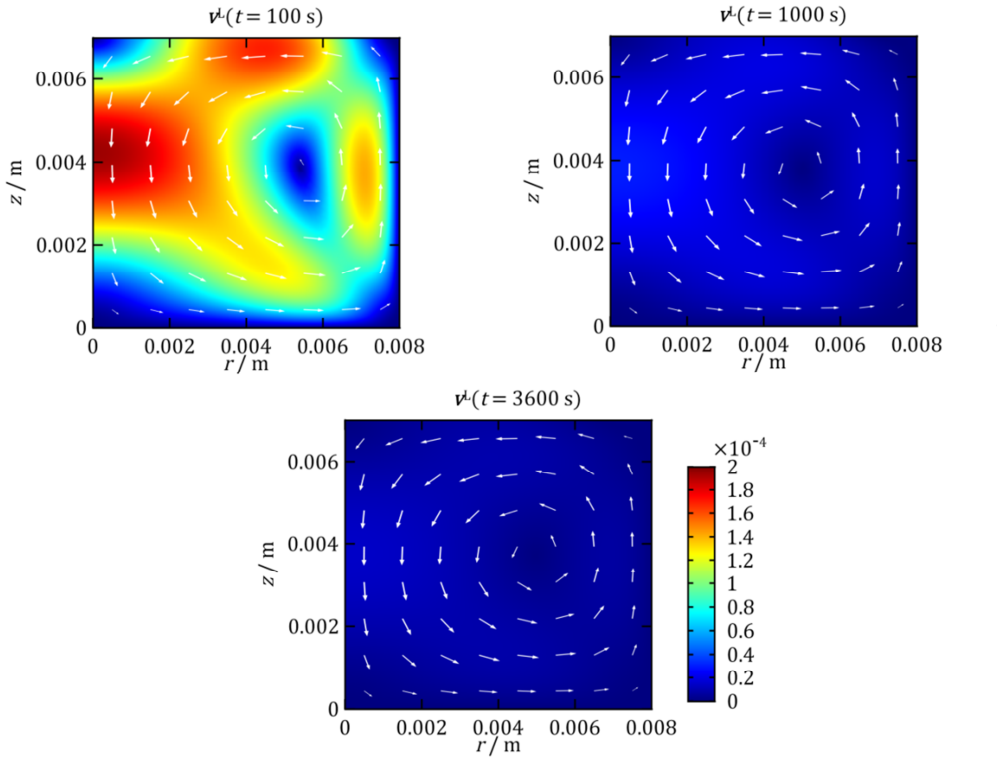


Figure 4.9. Velocity field in the liquid phase ($\boldsymbol{v}^{\mathrm{L}}$) plotted at t = 100 s, t = 1000 s and t = 3600 s for ΔT = 5 K, i.e. for a solution that is initially colder than its surroundings. The length of the arrows is proportional to the natural logarithm of $|\boldsymbol{v}^{\mathrm{L}}|$.

4.4. Conclusions

We have investigated the heat transfer in a typical SECM measuring cell by performing numerical simulations based on an approximate model. We have demonstrated that, if there is an initial difference between the temperature of the solution and its surroundings, (ΔT, with $|\Delta T| \sim 1$ K), the characteristic time for reaching thermal equilibrium is of the order of one hour – longer than what one might expect for such a small volume of liquid ($V_{\mathrm{tot}} \approx 2$ mL). Our treatment of the conjugate heat and momentum transfer in the system within the framework of the Boussinesq approximation indicates that a significant amount of heat is transported via convection, and that the intensity of the convective heat transfer depends on the sign of ΔT because the intensity of the convective flows in the cell and the surrounding air is determined by the initial temperature distribution.

Most SECM experiments do not include thermostating of the solution either by use of a special design for that purpose or by waiting for thermal equilibrium to set in [2], assuming instead that the temperature throughout the liquid phase quickly becomes homogeneous and equal to the ambient. As we have shown, this assumption is incorrect and may lead to substantial errors in the determination of temperature-sensitive qualities such as reaction rate constants, not least since the solution viscosity is strongly temperature-sensitive (see for example Kampmeyer's paper [31] on the viscosity of pure water) and therefore the same is true of the diffusion coefficients of electroactive species. Our results also raise questions about the interpretation of data from other electrochemical experiments for which no special care for thermostating is taken.

Moreover, as temperature-generated buoyancy forces induce velocities as high as $10^{-4}\,\mathrm{m{\cdot}s^{-1}}$ in the solution (during the initial ~ 100 s), there will also be a convective contribution to the electrical currents measured at the SECM tip. It must be borne in mind, though, that the flow patterns observed in an SECM cell would be different from those seen here due to the presence of the electrode. Specifically, the velocity of convective flow in the immediate vicinity of the tip, which is most

relevant to the mass transport, would be considerably lower than the bulk velocity discussed here due to the retarding effect of both the solid tip and the substrate. The order of magnitude of the diffusional mass flux at the tip is $D\Delta C/L$, where D is the diffusion coefficient of the electroactive species, ΔC is the characteristic local variation of its concentration, and L is the normal distance between the tip and the substrate. Thus, the convective contribution to the flux, $|v|\Delta C$, would be comparable to the diffusional one if $|v| \sim D/L$. For the typical parameters of the system in question ($D \sim 10^{-9}$ m^2·s^{-1}, $L \sim 10^{-6}$ m), this yields a required order of magnitude for the velocity in the thin film between tip and substrate of $|v| \sim 10^{-3}$ m^2·s^{-1}, i.e., a higher velocity than the maximum *bulk* one observed here. Thus, mass transport can be expected to be dominated by diffusion in the vicinity of the tip. However, thermal convection in the bulk solution can potentially exert an influence on electrical current by affecting the boundary condition applied to the bulk of the solution in the mass transport problem. A quantitative assessment of this influence would require simulating the coupled transport of mass, heat and momentum.

4.5. References

[1] A.J. Bard, M.V. Mirkin (Eds.), Scanning Electrochemical Microscopy, Second ed., CRC Press, Boca Raton, FL, 2012.

[2] D. Schäfer, A. Puschhof, W. Schuhmann, Scanning Electrochemical Microscopy at Variable Temperatures, Phys. Chem. Chem. Phys., 15 (2013) 5215-5223.

[3] Z. Zhang, J. Ye, P. Sun, Y. Yuan, Y. Tong, J. Hu, Y. Shao, Study of Electron Transfer across the Liquid/Ice-Like Matrix Interface by Scanning Electrochemical Microscopy, Anal. Chem., 74 (2002) 1530-1536.

[4] M.-H. Delville, M. Tsionsky, A.J. Bard, Scanning Electrochemical Microscopy Studies of Electron Transfer through Monolayers Containing Conjugated Species at the Liquid−Liquid Interface, Langmuir, 14 (1998) 2774-2779.

[5] J. Wang, F. Song, F. Zhou, Silver-Enhanced Imaging of DNA Hybridization at DNA Microarrays with Scanning Electrochemical Microscopy, Langmuir, 18 (2002) 6653-6658.

[6] Y. Hirano, Y. Nishimiya, K. Kowata, F. Mizutani, S. Tsuda, Y. Komatsu, Construction of Time-Lapse Scanning Electrochemical Microscopy with Temperature Control and Its Application to Evaluate the Preservation Effects of Antifreeze Proteins on Living Cells, Anal. Chem., 80 (2008) 9349-9354.

[7] J. Kim, M. Shen, N. Nioradze, S. Amemiya, Stabilizing Nanometer Scale Tip-to-Substrate Gaps in Scanning Electrochemical Microscopy Using an Isothermal Chamber for Thermal Drift Suppression, Anal. Chem., 84 (2012) 3489-3492.

[8] A. Boika, Z. Zhao, First Principles of Hot-Tip Scanning Electrochemical Microscopy: Differentiating Substrates According to Their Thermal Conductivities, Electrochem. Commun., 68 (2016) 36-39.

[9] A. Sode, M. Nebel, P. Pinyou, S. Schmaderer, J. Szeponik, N. Plumeré, W. Schuhmann, Determination of Temperature Gradients with Micrometric Resolution by Local Open Circuit Potential Measurements at a Scanning Microelectrode, Electroanalysis, 25 (2013) 2084-2091.

[10] H. Zhang, X. Xiao, T. Su, X. Gu, T. Jin, L. Du, J. Tang, A Novel Thermocouple Microelectrode for Applications in SECM and Variable Temperature Electrochemistry, Electrochem. Commun., 47 (2014) 71-74.

[11] J. Clausmeyer, D. Schäfer, M. Nebel, W. Schuhmann, Temperature-Induced Modulation of the Sample Position in Scanning Electrochemical Microscopy, ChemElectroChem, 2 (2015) 946-948.

[12] A.J. Wain, Personal Communication, National Physical Laboratory, Teddington, Middlesex, TW11 0LW, United Kingdom, 2016.

[13] R.B. Bird, W.E. Stewart, E.N. Lightfoot, Transport Phenomena, Second ed., John Wiley & Sons, New York, 2002.

[14] J.K. Novev, S. Eloul, R.G. Compton, Influence of Reaction-Induced Thermal Convection on the Electrical Currents Measured in Chronoamperometry and Cyclic Voltammetry, J. Phys. Chem. C, 120 (2016) 13549-13562.

[15] D.D. Gray, A. Giorgini, The Validity of the Boussinesq Approximation for Liquids and Gases, Int. J. Heat Mass Transfer, 19 (1976) 545-551.

[16] P.K. Kundu, I.M. Cohen, Fluid Mechanics, Second ed., Academic Press, San Diego, California, 2002.

[17] L. Demkowicz, A Note on Symmetry Boundary Conditions in Finite Element Methods, Appl. Math. Lett., 4 (1991) 27-30.

[18] V.G. Levich, Physicochemical Hydrodynamics, Prentice-Hall, Inc., Englewood Cliffs, N.J., 1962.

[19] A. Oron, S.H. Davis, S.G. Bankoff, Long-Scale Evolution of Thin Liquid Films, Rev. Mod. Phys., 69 (1997) 931-980.

[20] G.K. Batchelor, An Introduction to Fluid Dynamics, Cambridge University Press, Cambridge, UK, 2000.

[21] P.A. Kralchevsky, K. Nagayama, Particles at Fluid Interfaces and Membranes, Elsevier, Amsterdam, 2001.

[22] W.M. Lai, D.H. Rubin, E. Krempl, Introduction to Continuum Mechanics, Fourth ed., Elsevier Science, Burlington, MA, 2009.

[23] G. Neumann, Three-Dimensional Numerical Simulation of Buoyancy-Driven Convection in Vertical Cylinders Heated from Below, J. Fluid Mech., 214 (1990) 559-578.

[24] Y. Yamaguchi, C.J. Chang, R.A. Brown, Multiple Buoyancy-Driven Flows in a Vertical Cylinder Heated from Below, Phil. Trans. R. Soc. Lond. A, 312 (1984) 519-552.

[25] E.J.F. Dickinson, H. Ekström, E. Fontes, COMSOL Multiphysics®: Finite Element Software for Electrochemical Analysis. A Mini-Review, Electrochem. Commun., 40 (2014) 71-74.

[26] D.W. Pepper, J.C. Heinrich, The Finite Element Method: Basic Concepts and Applications with MATLAB®, MAPLE, and COMSOL, (2017).

[27] D.R. Lide (Ed.), CRC Handbook of Chemistry and Physics, Internet Version 2005, CRC Press, Boca Raton, FL, 2005.

[28] C.A. Harper (Ed.), Modern Plastics Handbook, McGraw-Hill, New York, NY, 1999.

[29] D.M. Price, M. Jarratt, Thermal Conductivity of PTFE and PTFE Composites, Thermochim. Acta, 392-393 (2002) 231-236.

[30] S. Fai Lau, H. Suzuki, B. Wunderlich, The Thermodynamic Properties of Polytetrafluoroethylene, J. Polym. Sci. Polym. Phys. Ed., 22 (1984) 379-405.

[31] P.M. Kampmeyer, The Temperature Dependence of Viscosity for Water and Mercury, J. Appl. Phys., 23 (1952) 99-102.

5. Thermal Convection in Electrochemical Cells. Boundaries with Heterogeneous Thermal Conductivity and Implications for Scanning Electrochemical Microscopy

Overview

In this chapter, we investigate the heat transfer in a cylinder-shaped electrochemical cell with solid, thermally insulating walls. The cell is filled with a liquid and a solid substrate that is thermostated from below is situated at its base. The initial temperature of the liquid is different from that of the substrate so as to mimic imperfect thermostating in an electrochemical experiment; as heat transfer acts to diminish the temperature difference between the two, natural convection ensues. The influence of inhomogeneities in the thermal conductivity of the solid is studied – numerical simulations of the heat transfer in the system are conducted for substrates that are comprised of a thermally conductive material, an insulating one or a combination thereof. It is shown that the thermal conductivity profile of the substrate strongly influences the structure and intensity of the natural convective flows emerging in the system. The present work demonstrates that under the idealized conditions under consideration, depending on the substrate structure, natural convection due to imperfect solution thermostating may give rise to flows whose local velocity can reach values as high as 10^{-3} m·s^{-1}. Moreover, as comparison between cells of two different radii shows, both the intensity and the temporal evolution of the flows arising in this system are highly sensitive to the precise geometry of the experimental cell. These results can have far-reaching consequences for the interpretation of results from experimental techniques such as scanning electrochemical microscopy.

5.1. Introduction

The understanding of electrochemical systems requires an appreciation of the interplay of a broad spectrum of physical phenomena including electron transfer, mass transport, chemical reactions, adsorption/desorption processes, etc., all of which are temperature-sensitive. Accordingly, for decades it has been a *sine qua non* that investigations of electrical interfaces are conducted under conditions of effective thermostating to ensure a known and uniform temperature throughout the system under study. That this is achieved is important because of the strong temperature dependence of quantities determined via electrochemical techniques, e.g. rate constants (both homogeneous and interfacial), diffusion coefficients and equilibrium constants. Moreover, it is very frequently the case that electrochemical experiments are interpreted and modelled on the basis of the assumption that the transport of reactants, intermediates and products in the vicinity of the electrode|solution interface occurs exclusively via diffusion and sometimes electromigration. The latter assumption can only be true if the cell temperature is uniform – should there be a temperature gradient, this would inevitably drive a natural convective flux, which could contribute significantly to the measured electrical current.

In Chapter 3 and the corresponding paper [1], we have shown that the enthalpy change associated with electrode processes is, for typical reactions under conventional measurement conditions, insufficient to induce a convective flow of magnitude sufficient to perturb the electrochemical process or preclude its interpretation in terms of diffusion-only transport, the reason being that heat dissipation, for example in aqueous media, occurs orders of magnitude faster than diffusional mass transport. Nonetheless, as we have also shown in Ref. [1], confirming the earlier result of Ngamchuea et al. [2], the occurrence of an electrochemical reaction can lead to non-negligible convective mass currents driven by concentration gradients. Furthermore, as we discussed in Chapter 4 and the associated paper [3], detailed simulation indicates that in the absence of

thermostating, an initial temperature difference of several kelvin can give rise to significant thermal convective flows that persist for thousands of seconds. Thus, if the cell contents are at a different temperature to their surroundings at the onset of the experiment, the analysis of data from the latter on the assumption of diffusion-only transport may be compromised. Hence, meticulous thermostating of electrochemical cells is necessary if convection is to be rigorously excluded [3]. That said, the vital importance of temperature control in electrochemical systems has been recognised for many years and measures have been taken to implement it [4].

One widely-used electrochemical technique, dating back now more than two decades [5-7], in which effective thermostating is difficult and rarely performed, is the so-called scanning electrochemical microscopy (SECM). In this experiment, a microelectrode is rastered across a solid|liquid interface of interest, electrochemical or otherwise, and a faradaic current is measured at the microelectrode surface as a function of the microelectrode position. Thus currents measured at a constant electrode-substrate separation are used to 'image' the surface of the latter whilst 'approach curves' are used to obtain quantitative information of different types. All of this presumes an absence of convection as the latter may invalidate quantitative analyses made on the basis of diffusion-only models and either 'smear' or fully obscure an image. Our previous work demonstrates the role of imperfect thermostating in promoting natural convection in a model SECM cell [3]. There, we assumed that the lower boundary of the cell was perfectly thermally insulating. Experimentally, it is often the case that the lower boundary of the cell is the substrate whose structure is of interest in SECM, see e.g. Schäfer et al. [8] Examples include the study of electron-transfer reactions at non-uniform surfaces, for instance at boron-doped diamond (BDD) electrodes [9] and also for graphitic surfaces where the contributions of basal plane and edge plane components of the surface have been known to show contrasting electron transfer kinetics since the pioneering work of McCreery and co-workers [10-12].

In this chapter, we explore the role of substrate composition in heat transfer within a model electrochemical cell and its influence on *local* convection under

conditions of imperfect thermostating. Specifically, we consider a surface composed of zones of different but isotropic thermal conductivity. Such substrates occur in experimental practice – examples include particle/polymer composites where metal surfaces are surrounded by poor conductors and electrodes embedded in an insulator. A similar situation can also arise for instance in the case of non-monocrystalline graphitic substrates as the thermal conductivity of graphite is strongly anisotropic – at 300 K, the thermal conductivity in the direction of the basal plane is reported to be between 100 and 1000 times greater than in the orthogonal direction [13, 14].

5.2. Theoretical model

Here, we describe the theoretical basis of our simulations of convective heat and momentum transfer in electrochemical cells with inhomogeneous substrates.

As in Chapter 4 and the associated paper on thermal convection in SECM [3], we consider a solution whose temperature is initially uniform but different from that of its surroundings. Heat transfer with the environment leads to local variations in temperature and density, which in turn lead to buoyancy forces within the fluid. The substrate temperature is initially also homogeneous, and its value at the lower substrate surface is held constant by a thermostat throughout the simulated experiment. This configuration conceptually resembles the experimental setup of Schäfer et al. [8], although in their case heat is supplied in pulses.

In contrast to our work on SECM from the preceding chapter, here we do not account for the heat transfer in the solid cell and the surrounding air. Instead, we model a highly idealized cylindrical cell that has solid, thermally insulated top and side walls and deal only with the heat transfer within the solution and the substrate. Furthermore, we assume that the problem is axisymmetric and therefore that all quantities are independent of the polar angle ϕ. We make these considerable simplifications in order to isolate and maximize the effect under study, namely, the influence of non-uniformities in the substrate's thermal conductivity on the

predicted convective patterns. We should, however, point out that this limits our current work to a 'proof-of-concept' study as, for example, the substitution of the free solution|air boundary with a solid one alters the velocity distribution in the liquid phase. In the present formulation, the problem deals with a form of Rayleigh-Bénard convection, a phenomenon that has been studied in the literature, with most extensive coverage existing for the flow between infinite horizontal planes [15]. Studies for the case of cylindrical enclosures have also been performed, e.g. [16]; as we observe below, heat transfer induces circulatory convective motion in the fluid.

We consider two different idealized models for the electrochemical cell, both of them approximating it as a thermally insulated cylinder with solid walls, radius r_{cell} and height h_{cell} situated on top of a cylindrical substrate of height h_s and radius r_{cell}; the coordinate origin is at the centre of the substrate's lower surface, as illustrated in Figure 5.1. The first model accurately reflects the typical radius of the aperture containing the substrate in a typical SECM measurement cell, r_{cell} = 3 mm (CH Instruments, Inc., Austin, TX, USA, http://www.chinstruments.com, see Figure 4.1 for an illustration). Thus, the substrate radius corresponds to the maximum substrate size that could be studied experimentally in this cell. In the second model, we set the radius of the solid container and the substrate to be equal to that of the wider part of the cell, that is, 8 mm. The height of the cell is the same for both models and for the second one ensures that the volume of liquid within the cylinder corresponds to that in the typical SECM experiment. As we show below, the cell dimensions strongly affect both the intensity and the evolution of the convective flows generated by the initial temperature difference, which reinforces our point on the importance of rigorous thermostating in electrochemical experiments.

We explore several different cases for the solid substrate at the bottom of the cell. Our study deals with homogeneous substrates comprised of either BDD or polytetrafluoroethylene (teflon) – two materials that differ markedly in their thermal conductivity κ_i. Furthermore, we study substrates comprised mainly of one of these materials with an embedded annular band of the other that has a width of d_{band} and is situated between $r_1 = (r_{cell} - d_{band})/2$ and $r_1 + d_{band}$, see Section 5.3 for

details. Among these configurations, the one with a ring of BDD embedded in teflon is particularly relevant experimentally, as it can serve as a model for an annular band electrode.

Let us note that natural convection coupled with heat transfer in a solid body has been studied before in the literature, for example Kaminski and Prakash [17] have analysed numerically the effect of conduction in one of the vertical walls of a square enclosure, Saeid [18] has dealt with a similar problem for a two-dimensional porous enclosure via simulations, and Kim and Viskanta [19] have studied natural convection in a square cavity with conducting walls through both simulations and experiments.

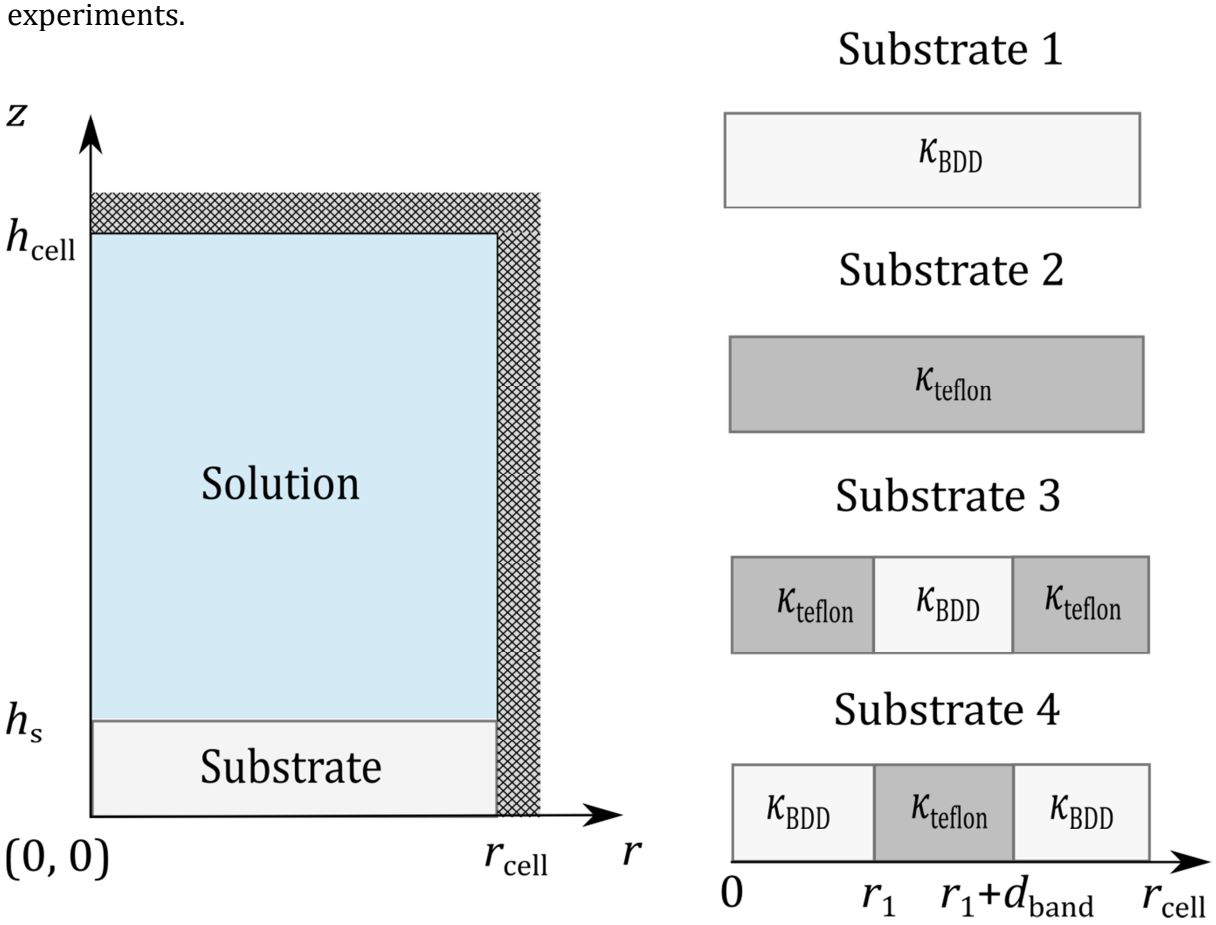


Figure 5.1. Geometry of the model we use for the measurement cell and structure of the studied substrates – 1) homogeneous BDD cylinder; 2) homogeneous teflon cylinder; 3) teflon cylinder with a BDD annular band; 4) BDD cylinder with a teflon annular band; r_1 is defined as $r_1 = (r_{cell} - d_{band})/2$. We presume that the temperature and velocity distributions are axially symmetric and we therefore only need to simulate the region pictured in the figure.

The temperature profile in the solution follows a convective heat equation of the form

$$\frac{\partial T^{\mathrm{L}}}{\partial t} + \boldsymbol{v} \cdot \nabla T^{\mathrm{L}} = \chi^{\mathrm{L}} \nabla^2 T^{\mathrm{L}}, \tag{5.1}$$

where t is time, χ^{L} – is the thermal diffusivity [$\mathrm{m^2 \cdot s^{-1}}$] of the liquid, $\boldsymbol{v}$ is its velocity determined from the Navier-Stokes equation and T^{L} is its temperature.

In the solid phase, the temperature is influenced only by heat conduction, and obeys a simpler form of the heat equation,

$$\frac{\partial T^{\mathrm{S}}}{\partial t} = \chi^{\mathrm{S}} \nabla^2 T^{\mathrm{S}}, \tag{5.2}$$

where χ^{S} and T^{S} are the thermal diffusivity and the temperature of the substrate. Throughout the text, we use the symbol T to refer to the temperature profile in the whole system, i.e., to T^{L} and T^{S} collectively.

Initially, the temperature of the substrate is homogeneous,

$$T^{\mathrm{S}}\Big|_{t\,=\,0} = T_{\mathrm{thermostat}}. \tag{5.3}$$

The temperature of the substrate's bottom surface is maintained constant throughout the simulated experiment

$$T^{\mathrm{S}}\Big|_{z\,=\,0} = T_{\mathrm{thermostat}}; \tag{5.4}$$

in practice this may be achieved by having a thermostat at the plane $z = 0$.

At the start of the studied process, the temperature of the solution is uniform but different from that of the substrate,

$$T^{\mathrm{L}}\Big|_{t\,=\,0} = T_{\mathrm{thermostat}} - \Delta T, \tag{5.5}$$

where the initial temperature difference ΔT can be either positive or negative.

Rather than considering the heat transfer through the walls of the cell as in Chapter 4 and the associated paper [3], we model the boundaries of the cell as thermally insulating,

$$\frac{\partial T^{\mathrm{L}}}{\partial r}\Big|_{r\,=\,r_{\mathrm{cell}}} = 0; \tag{5.6}$$

$$\frac{\partial T^{\mathrm{L}}}{\partial z}\Big|_{z\,=\,h_{\mathrm{s}} + h_{\mathrm{cell}}} = 0; \tag{5.7}$$

In reality, as our previous simulations indicate [3], there can be a substantial heat flux through the side walls of the cell; however, we choose to neglect it here in

the interest of simplicity and in order to highlight the qualitative local effects of the inhomogeneities in the substrate thermal conductivity.

Likewise, we assume there is no radial heat flux through the boundary of the substrate,

$$\left.\frac{\partial T^{\mathrm{S}}}{\partial r}\right|_{r = r_{\mathrm{cell}}} = 0. \tag{5.8}$$

At the interface between the substrate and the solution, both the temperature and the heat flux need to be continuous [20],

$$\left.(T^{\mathrm{L}} - T^{\mathrm{S}})\right|_{z = h_{\mathrm{s}}} = 0; \tag{5.9}$$

$$\left.(\kappa^{\mathrm{L}}\partial_z T^{\mathrm{L}} - \kappa^{\mathrm{S}}\partial_z T^{\mathrm{S}})\right|_{z=h_{\mathrm{s}}} = 0, \tag{5.10}$$

where $\kappa^{\mathrm{i}} = \rho_{\mathrm{i}} \cdot C_{p\,\mathrm{i}} \cdot \chi^{\mathrm{i}}$ is the thermal conductivity [W·m^{-1}·K^{-1}] of the respective medium, ρ_{i} – its density, and $C_{p\,\mathrm{i}}$ – its specific heat capacity at constant pressure.

The solid substrate plays a key role in our present study, and we study several different configurations for its structure. In the simplest case, we take the substrate to be homogeneous and consisting either of boron-doped diamond or of teflon. However, the main focus of our study is on inhomogeneous substrates; the inhomogeneity considered is an annular band of conductivity κ_{band} and thickness d_{band} situated between a disc of radius $r_1 = (r_{\mathrm{cell}} - d_{\mathrm{band}})/2$ and an outer band of radius r_{cell}, both of them with conductivity κ_0:

$$\kappa^{\mathrm{S}} = \begin{cases} \kappa_0, r < r_1 \\ \kappa_{\mathrm{band}}, r_1 < r < r_1 + d_{\mathrm{band}} \\ \kappa_0, r_1 + d_{\mathrm{band}} < r < r_{\mathrm{cell}} \end{cases} \tag{5.11}$$

The substrate's other properties, such as its density and heat capacity, follow analogous distributions. For substrates with annular bands, the solid temperature and the heat flux obey conditions analogous to Eqs. (5.9)-(5.10) at the boundaries between the two materials, situated at $r = r_1$ and $r = r_1 + d_{\mathrm{band}}$.

We now turn to the hydrodynamic problem. We assume that the fluid is incompressible and Newtonian; therefore, the velocity field is controlled by the Navier-Stokes equation [21], for which we use the approximate form

$$\rho_0 \left(\frac{\partial \boldsymbol{v}}{\partial t} + \boldsymbol{v} \cdot \nabla \boldsymbol{v}\right) = -\nabla \Delta p + \eta \nabla^2 \boldsymbol{v} - \rho_0\, \alpha (T^{\mathrm{L}} - T^{\mathrm{L}}|_{t=0}) \boldsymbol{g}, \tag{5.12}$$

where η is the solution viscosity and α – its thermal expansion coefficient at constant pressure, $\alpha = -\rho\cdot(\partial\rho/\partial T)_p$, $\boldsymbol{g} = -|\boldsymbol{g}|\mathbf{e}_z = -9.81\text{m}\cdot\text{s}^{-2}\,\mathbf{e}_z$ is the gravitational acceleration vector, and Δp is defined as the difference between the pressure at a given time and the initial value,

$$\Delta p = p - p_0 + \rho_0 z|\boldsymbol{g}|, \tag{5.13}$$

with p_0 being the pressure $z = 0$ at the start of the simulated experiment.

We solve the Navier-Stokes equation in conjunction with the continuity equation

$$\nabla \cdot \boldsymbol{v} = 0. \tag{5.14}$$

As in our previous papers [1, 3] and the rest of this thesis, we adopt the Boussinesq approximation of the governing equations (5.1), (5.12) and (5.14) – namely, we linearize the fluid density with respect to temperature and treat all of its other properties as constant. Furthermore, within this standard approach, we only consider the temperature-dependence of density in the buoyancy force term and not in the continuity equation (5.14) – see e.g. Kundu and Cohen for a justification [21].

In line with our aim to simplify the model as much as possible, we apply no-slip conditions to the boundaries of the cell, which is equivalent to treating all of them as solid,

$$\begin{aligned}\boldsymbol{v}\Big|_{r = r_{\text{cell}},\, h_\text{s} < z < h_{\text{cell}} + h_\text{s}} &= \boldsymbol{v}\Big|_{0 < r < r_{\text{cell}},\, z = h_{\text{cell}} + h_\text{s}} \\ &= \boldsymbol{v}\Big|_{0 < r < r_{\text{cell}},\, z = h_\text{s}} = \mathbf{0}.\end{aligned} \tag{5.15}$$

The boundary conditions (5.6)-(5.7) for the heat flux and (5.15) for the velocity mean that in our model, the solution is enclosed in a solid, thermally insulating cell. Let us note once more that, in reality, SECM measurement cells are open to the surrounding air (see e.g. Chapter 2 in the book on SECM edited by Bard and Mirkin [22]) and heat transfer through the solution|air interface and the side walls of the cell plays a role [3].

At the beginning of the simulated experiment, the solution under study is stagnant,

$$\boldsymbol{v}\Big|_{t = 0} = \mathbf{0}. \tag{5.16}$$

Utilizing the assumed symmetry of the problem, we seek a numerical solution of the equations (5.1)-(5.2), (5.12) and (5.14) only in a rectangular region of dimensions r_{cell} by h_{cell} + h_{s} (pictured in Figure 5.1). For that reason, we impose additional boundary conditions at the symmetry axis, r = 0. For the temperature profiles, the symmetry condition requires that there is no radial flux at r = 0,

$$\left.\frac{\partial T^{\mathrm{L}}}{\partial r}\right|_{r\,=\,0} = 0. \tag{5.17}$$

$$\left.\frac{\partial T^{\mathrm{S}}}{\partial r}\right|_{r\,=\,0} = 0. \tag{5.18}$$

From symmetry considerations, the radial velocity at the cylinder axis is subject to the constraints [23]

$$\left. v_r \right|_{r\,=\,0} = 0. \tag{5.19}$$

$$\left.\frac{\partial v_z}{\partial r}\right|_{r\,=\,0} = 0. \tag{5.20}$$

Note that the continuity conditions (5.9)-(5.10) at the interfaces and the symmetry conditions (5.17)-(5.20) are implicitly handled by the COMSOL Multiphysics [24] modules for Heat Transfer in Fluids and Laminar Flow applied to systems with axial symmetry.

In our previous papers on natural convection in electrochemistry [1, 3], we stated that we also use the boundary condition $\partial v_r / \partial z\big|_{r=0} = 0$. While this equation holds both in the simulations in Chapters 3-4 [1, 3] and those we discuss here, it cannot be regarded as a separate boundary condition because it follows directly from Eq. (5.19).

Further, we note that our assumption for axial symmetry of the flows is not necessarily fulfilled – previous studies, notably that by Neumann [25], who performed three-dimensional simulations, indicate that axisymmetric flows in related systems are inherently unstable and more complex flow patterns are realized instead. On the other hand, Torrance and Rockett [26] have experimentally observed axisymmetric flows for another similar system. Thus, it is difficult to make a prediction regarding the symmetry of the flows for our specific case. In this study we assume that the flows are axially symmetric; a more rigorous approach would

involve performing three-dimensional simulations or gathering experimental data to test this assumption.

We can gain some insight into the parameters that control the flow of the solution by introducing the dimensionless variables

$$\tilde{r} = \frac{r}{h_{\text{cell}}}; \tilde{z} = \frac{z}{h_{\text{cell}}}; \tilde{\boldsymbol{v}} = \frac{h_{\text{cell}}}{\chi^{\text{L}}}\boldsymbol{v}; \tilde{p} = \frac{h_{\text{cell}}^2}{\rho_0(\chi^{\text{L}})^2}\Delta p\,; \tilde{t} = \frac{\chi^{\text{L}}}{h_{\text{cell}}^2}t$$

$$\tilde{T} = \frac{T^{\text{L}} - T^{\text{L}}|_{t=0}}{T_{\text{thermostat}} - T^{\text{L}}|_{t=0}} = \frac{T^{\text{L}} - T^{\text{L}}|_{t=0}}{\Delta T}, \tag{5.21}$$

as well as the Rayleigh and Prandtl numbers,

$$Ra = \frac{\rho_0 \alpha h_{\text{cell}}^3 |\Delta T||\boldsymbol{g}|}{\chi^{\text{L}}\eta} \tag{5.22}$$

and

$$Pr = \frac{\eta}{\rho_0 \chi^{\text{L}}}. \tag{5.23}$$

The governing equations for the fluid phase therefore assume the form [25]:

$$\tilde{\nabla} \cdot \tilde{\boldsymbol{v}} = 0; \tag{5.24}$$

$$\partial_{\tilde{t}}\tilde{\boldsymbol{v}} + \tilde{\boldsymbol{v}} \cdot \tilde{\nabla}\tilde{\boldsymbol{v}} = -\tilde{\nabla}\Delta\tilde{p} + Pr\tilde{\nabla}^2\tilde{\boldsymbol{v}} + RaPr\,\text{sgn}(\Delta T)\tilde{T}\mathbf{e}_z; \tag{5.25}$$

$$\partial_{\tilde{t}}\tilde{T} + \tilde{\boldsymbol{v}} \cdot \tilde{\nabla}\tilde{T} = \tilde{\nabla}^2\tilde{T}, \tag{5.26}$$

where sgn(x) refers to the sign function. Note that Eqs. (5.24)-(5.26) are not identical to the governing equations (1.38)-(1.40) in Chapter 1 because of the different choice of nondimensionalization for the variables. Nevertheless, the dimensionless parameters controlling the heat and mass transport in the system are again controlled by *Ra* and *Pr*. We study cells of specified height h_{cell} and conduct all our calculations for water, taking its properties to be constant and equal to their values at the initial temperature. Hence, the only parameter that we can vary to modify the behaviour of the system is the initial temperature difference ΔT; its value is particularly important because in problems of the type studied, natural convection becomes significant and starts to influence the heat transfer once the Rayleigh number exceeds a certain critical value, Ra_{cr}.

Note that the dimensionless temperature $\tilde{T}$ is defined so that it tends to unity as t approaches infinity – at equilibrium, $T^{\text{L}} = T_{\text{thermostat}}$ – and the force term becomes constant and can no longer drive convective motion. More precisely, the order of magnitude for the characteristic time required for $\tilde{T}$ to reach unity is the same as for

one-dimensional heat conduction, $\tau = h_{cell}^2/\chi^L \sim 10^2$ s, in contrast with our previous results for a cell of the same dimensions, where $\tau \sim 10^3$ s (see Chapter 4/ Ref. [3]). This difference comes from the fact that in our current study, the thermostat at the bottom of the cell serves as a heat source or sink, depending on the sign of ΔT, whereas in our previous model this role is performed by the air at a finite but large distance from the cell and heat is lost or gained through the side walls of the electrochemical cell.

Studies of problems similar to ours but possessing a constant driving force for the convection, e.g. those by Yamaguchi et al. [23], have examined the dependence of the critical Rayleigh number on the cylinder aspect ratio (r_{cell}/h_{cell}). Moreover, as discussed by Yamaguchi et al. [23], in principle there are infinitely many possible modes of flow consisting of multiple convective rolls, each of them having a different critical *Ra*. The complexity of the flow patterns that can arise in systems like the one under consideration here is a compelling argument for the importance of eliminating natural convection as a factor in electrochemical experiments. The sensitivity of the flows to the parameters of the system, particularly the aspect ratio (r_{cell}/h_{cell}), makes accounting for the convective contribution to the electrical currents measured in those experiments a daunting task.

5.3. Simulations

This section deals with the implementation of our simulations and discusses our choice of parameters.

We have simulated a substrate of height h_s = 1 mm and cells of height h_{cell} = 7 mm and radius r_{cell} = 3 mm and 8 mm, as discussed above.

The properties of the solution were approximated with those of water at either 293.15 K or 303.15 K, i.e., at the initial temperature $T^L(t = 0) = T_\infty - \Delta T$ corresponding to ΔT = 5 K and ΔT = −5 K, respectively. The values $\alpha = 2.06\times10^{-4}$ K^{-1} for the thermal expansion coefficient, η = 1.002 mPa·s for the viscosity, κ^L = 0.5984 W·m^{-1}·K^{-1} for the thermal conductivity, ρ_0 = 998.21 kg·m^{-3} for the

density and C_p^{L} = 4.1818×10^3 J·kg^{-1}·K^{-1} for the heat capacity were used at $T^{\mathrm{L}}(t = 0)$ = 293.15 K, whereas at $T^{\mathrm{L}}(t = 0)$ = 303.15 K, the calculations were done with α = 3.02×10^{-4} K^{-1}, η = 0.7977 mPa·s, κ^{L} = 0.6154 W·m^{-1}·K^{-1}, ρ_0 = 995.65 kg·m^{-3} and C_p^{L} = 4.1784×10^3 J·kg^{-1}·K^{-1}; all values were taken from the CRC Handbook of Chemistry and Physics [14].

The parameters of water at 293.15 K were also used for all simulations with varying negative ΔT conducted for r_{cell} = 3 mm to establish approximate bounds for Ra_{cr}; similarly, for the simulations with $\Delta T > 0$, the properties of water were taken at. As our approximate model is most appropriate for small $|\Delta T|$, we have only performed simulations with $|\Delta T|$ = 3, 4 and 5 K; initial temperature differences larger than 5 K in absolute value are also less likely to arise in the experiment. The parameters we use correspond to Prandtl numbers Pr = 5.4 at negative and 7.0 at positive ΔT, and to Rayleigh numbers in the range between Ra = 2.6×10^4 and 4.3×10^4 and 1.4×10^4 and 2.4×10^4, respectively.

As we have stated above, we consider substrates comprised of BDD, teflon or an annular band of one material embedded within a cylinder of the other one (see Figure 5.1). For annular bands, the material properties of the solid follow an equation of the form (5.11). For cells of radius 3 mm, we have simulated substrates with three different thicknesses of the annular band – $d_{\mathrm{band}}/r_{\mathrm{cell}}$ = 1/3, 1/9 and 1/27, whereas for r_{cell} = 8 mm, we have only considered $d_{\mathrm{band}}/r_{\mathrm{cell}}$ = 1/3.

For the density and heat capacity of substrates of high thermal conductivity, we use the values for non-doped diamond at 298.15 K from the CRC Handbook [14], ρ_{diamond} = 3513 kg·m^{-3}, $C_{p,\,\mathrm{diamond}}$ = 508.33 J·mol^{-1}·K^{-1}; we take its thermal conductivity to be κ_{BDD} = 1600 W·m^{-1}·K^{-1}, as reported for BDD by Prikhodko et al. [27] This value of κ_{BDD} is for a level of boron content typical of BDD substrates for power devices and is substantially different from that of undoped diamond [27].

The thermally insulating substrate in our model is polytetrafluoroethylene (teflon). The properties of the polymer vary depending on the exact form that is in use, e.g., on its average molecular mass, and handbooks typically give a range for them, see Ref. [28]. For the purpose of this semi-quantitative study, it is sufficient to

employ realistic values of the substrate properties, rather than to replicate those for a specific sample of the material. For that reason, we take the upper limit for the density given in Ref. [28], $\rho_{\text{teflon}} = 2200\ \text{kg}\cdot\text{m}^{-3}$, and set the thermal conductivity [29] to $\kappa_{\text{teflon}} = 0.26\ \text{W}\cdot\text{m}^{-1}\cdot\text{K}^{-1}$. We should point out that in Chapter 4 and the paper on which it is based [3], we used the same value of κ_{teflon}, citing a study by Price and Jarratt [30] that refers to 323.15 K; however, given the weak temperature dependence of κ_{teflon} [29], this has very little effect the accuracy of our calculations. For the heat capacity of teflon, we take the value for the crystalline form measured at 298.15 by Lau et al. [31] – $C_{p\ \text{teflon}} = 898.1\ \text{J}\cdot\text{mol}^{-1}\cdot\text{K}^{-1}$; note that for the amorphous form the value would be $1025.5\ \text{J}\cdot\text{mol}^{-1}\cdot\text{K}^{-1}$.

The governing equations (5.1)-(5.2), (5.12) and (5.14) were solved numerically via the finite element method in the commercial software package COMSOL Multiphysics 5.2 – see Refs. [24] and [32] for discussions of the latter's suitability to electrochemical simulations and convective heat transfer problems, respectively. Linear shape functions were used for the velocity components, the pressure and the temperature profiles in most simulations. In several cases, noted below, quadratic shape functions were used for the temperature.

Unless otherwise noted, the simulated experiments were with a duration of 600 s, which is the typical time scale for reaching thermal equilibrium in the studied systems.

For comparison, we also performed simulations with no account for convection. In them, we only solved Eqs. (5.1)-(5.2) with the fluid velocity set to zero; the settings for the mesh and the time stepping were identical to those for the simulations involving convection, with the exception that only linear elements were used for T.

5.4. Results and discussion

In this section, we discuss the properties of the natural convective flows for the various substrate structures under study.

For the purpose of analysing the different cases, we define the volume-averaged velocity and temperature, which give a measure of the overall motion and heat transfer within the liquid,

$$|\boldsymbol{v}_{\mathrm{av}}| = \frac{1}{V}\int_V \sqrt{v_r^2 + v_z^2}\,\mathrm{d}V \tag{5.27}$$

and

$$\Delta\tilde{T}_{\mathrm{av}} = \left|\frac{\int_V \left(T^{\mathrm{L}} - T^{\mathrm{L}}|_{t=0}\right)\mathrm{d}V}{\int_V \left(T^{\mathrm{L}}|_{t=0} - T_{\mathrm{thermostat}}\right)\mathrm{d}V}\right| = \frac{1}{\pi r_{\mathrm{cell}}^2 h_{\mathrm{cell}}}\frac{1}{\Delta T}\int_V \left(T^{\mathrm{L}} - T^{\mathrm{L}}|_{t=0}\right)\mathrm{d}V, \tag{5.28}$$

where V denotes the volume of the liquid in the cell. At long t, as the system tends towards equilibrium, the temperature throughout becomes homogeneous and equal to that of the thermostat, therefore at this limit, the value of $\Delta\tilde{T}_{\mathrm{av}}$ is unity.

Below, we illustrate the development of the convective flows on the scale of the whole cell through plots of the dependence of $|\boldsymbol{v}_{\mathrm{av}}|$ on time. In all studied cases, the solution is stagnant at t = 0, see Eq. (5.16), and, after passing through one or several extrema, its average velocity approaches zero at long t. The reason for this characteristic dependence of $|\boldsymbol{v}_{\mathrm{av}}|$ on t is that the driving force for convective motion, i.e., the temperature difference between the thermostat and the solution, diminishes with time, and eventually reaches zero at equilibrium. Alongside the plots of $|\boldsymbol{v}_{\mathrm{av}}(t)|$, we also present 'snapshots' of the temperature and velocity profiles that illustrate the local properties of the distributions at some of the extrema in $|\boldsymbol{v}_{\mathrm{av}}(t)|$.

In all studied systems, we are chiefly concerned with the semi-quantitative description of the system and, most importantly, the order of magnitude of the velocity fields that natural convection generates. For that reason, instead of characterizing the convective flows in detail, we only focus on their main features.

5.4.1. **Simulations for** r_{cell} = 3 mm

First, we give a detailed account of the flows that arise within a cylindrical cell whose radius corresponds to the maximum substrate radius that can fit in a standard cell for SECM (CH Instruments). This configuration yields relatively

simpler flows than the larger cell, for which r_{cell} = 8 mm. For that reason, we analyse the flows arising at r_{cell} = 3 mm more thoroughly; later in this chapter (Section 5.4.2), we apply the same methodology to the more experimentally relevant cell.

5.4.1.A *Solution colder than substrate at t = 0 ($\Delta T > 0$)*

In this case, the fluid is heated from below, which causes the fluid layers in contact with the substrate to expand and rise upwards, thereby enhancing the heat transfer.

Homogeneous BDD substrate

For a homogeneous BDD substrate, we observe two qualitatively different types of flow, depending on the order of the shape function employed for T. Both patterns consist in a single toroidal roll, but are set apart by the direction of the fluid motion within it – linear elements lead to clockwise motion in the simulated region, whereas quadratic give rise to a flow of the opposite direction. This is discussed below.

The two flows differ in their intensity – whereas the clockwise flow pattern exhibits local velocities as high as $|\boldsymbol{v}_{local}| \sim 10^{-4}$ m·s^{-1} and $|\boldsymbol{v}_{av}| \sim 10^{-5}$ m·s^{-1} (see Figure 5.2A-B), for the anticlockwise one, $|\boldsymbol{v}_{local}| \sim 10^{-6}$ m·s^{-1} and $|\boldsymbol{v}_{av}| \sim 10^{-7}$ m·s^{-1} (Figure B.2A, C in Appendix B). This difference is easily understandable in intuitive terms – from the symmetry condition (5.20) and the no-slip condition at the cylinder side wall, it follows that $|v_z|$ has an extremum at r = 0. As in this case there is heating from below and the buoyancy force has a positive z-component, the fluid can be expected to have a positive vertical velocity at r = 0, thus giving a clockwise flow pattern in the simulated region. For an anticlockwise pattern to be established, the liquid at r = 0 needs to move downwards against the buoyancy force, which explains the reduced magnitude of its velocity.

The temperature distributions corresponding to the two flows are also markedly different – whereas the clockwise flow perturbs T significantly and gives rise to a distribution that has a maximum at r = 0 (Figure 5.2C), in the other case, T depends

only weakly on the radial coordinate (Figure B.2D). Note that on the scale of the whole cell, neither type of flow affects the temperature distribution strongly – the difference in $\Delta\tilde{T}_{\mathrm{av}}$ with respect to the conduction-only case is at most $\sim 1\%$ for the clockwise flow and significantly less for the anticlockwise one, see Figure B.1 and Figure B.2B in Appendix B. As even at $|\Delta T|$ = 5 K the effect on temperature is so small, we do not attempt to establish bounds for Ra_{cr} for a homogeneous BDD substrate.

It is not surprising that we obtain more than one solution to the same problem in view of the fact that the Navier-Stokes equation (5.12) is nonlinear. The system thus permits the existence of multiple solutions, and flows with upwelling either at the centre or at the side walls of a cylindrical container have been reported by Yamaguchi et al. [23], Müller et al. [33] and Touihri et al. [16] for similar configurations. Note, however, that if multiple solutions do exist, they need not be of the same stability. It is also worth pointing out that if the Rayleigh number is increased significantly beyond the values we consider in this work, flows of greater complexity are likely to arise, for example ones that consist of multiple rolls lined up in the radial or the normal direction, as previous studies report [16, 23].

As a qualitative way of assessing the stability of the two types of solutions we observed, we modified the boundary condition at the top cylinder wall to

$$T^{\mathrm{L}}\Big|_{z\,=\,h_{\mathrm{cell}}\,+\,h_{\mathrm{s}}} = T_{\mathrm{thermostat}} - \Delta T, \tag{5.29}$$

so that the driving force of the convective flow does not go to zero as t tends to infinity and there is a stationary state with a non-zero velocity. At the steady state, we observed the same two types of flow we discussed above, but in contrast to the time-dependent case, the velocity magnitudes were nearly identical.

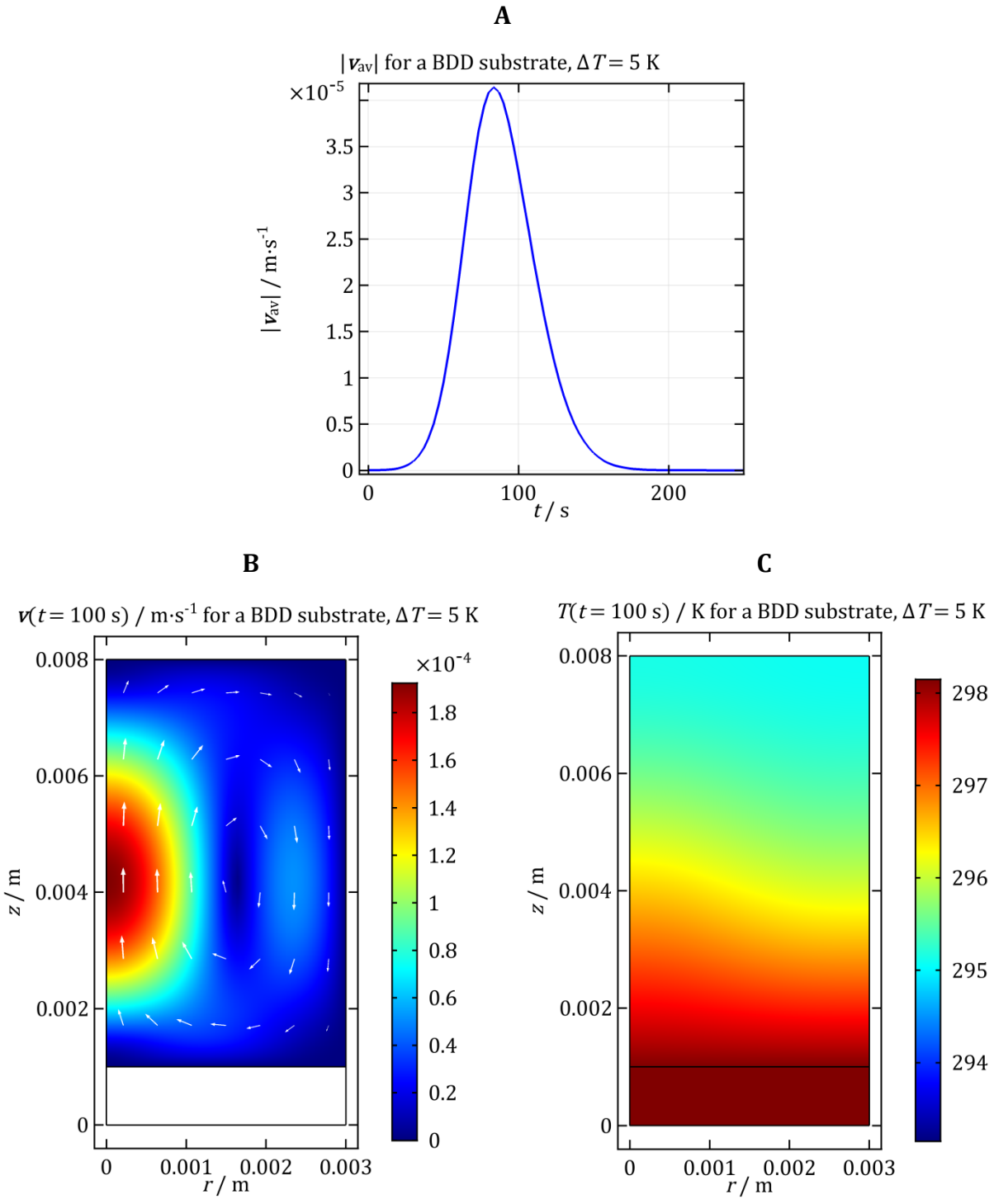


Figure 5.2. Results for a homogeneous BDD substrate obtained from a simulation that uses linear elements for T: **A** – volume-averaged velocity magnitude vs. time; **B** and **C** – 'snapshots' respectively of $\boldsymbol{v}$ and T at t = 100 s. The length of the arrows in **B** is proportional to the natural logarithm of $|\boldsymbol{v}|$. For this simulation, the solution is colder by ΔT = 5 K than the substrate at the initial moment.

To assess the relative stability of the clockwise and anticlockwise flow, we used the stationary distributions of T, $\boldsymbol{v}$ and p from the simulation that yielded one type of pattern as an initial condition for the other one; for all simulations of BDD substrates, the flow direction remained unchanged. Furthermore, the stationary flow patterns obtained from simulations with an initially stagnant solution were preserved upon reverting from Eq. (5.29) back to a no-flux boundary condition.

These results imply that the velocity distributions in Figure 5.2 and Figure B.2 are manifestations of two equally stable flow patterns that can be obtained from one another via reflection with respect to the plane $z = h_s$. The reason simulations with a no-flux top boundary predict a higher intensity of the clockwise flow is that in the latter, the fluid movement at the cylinder axis – where the velocity magnitude is maximal – is directed upwards, i.e., in the direction of the buoyancy force. For the anticlockwise flow, the normal velocity at $r = 0$ is negative and the fluid has to move against the buoyancy force, which results in a reduced velocity magnitude. A lower velocity magnitude in turn means that convective heat transfer is less efficient in this case, which is why we observe that the temperature profile (Figure B 2D) is approximately independent of r, indicating that heat is transported effectively solely by conduction. The difference with T corresponding to the clockwise flow from Figure 5.2 is due to the different temporal evolution of $\boldsymbol{v}$ in this problem; were the driving force to remain independent of time, the temperature distributions corresponding to both flow types would become distorted to the same degree, as we have shown in Appendix B (Figure B.3C and Figure B.4C).

While we obtain dissimilar types of flow depending on the specific discretization scheme that we use, we only observe such a discrepancy for systems that involve homogeneous substrates. Our qualitative stability tests indicate that in this case alone, there exist two similarly stable flow patterns of equivalent stability. Given that the initial state is unstable due to heating from below, in principle, an infinitesimal variation in the initial conditions may cause the system to enter either pattern and which is realized is likely determined by small differences in the numerical discretization. Below, we show that, for substrates with annular bands,

the direction of flow plays a role in the stability of the convective patterns and that for the presently discussed value of r_{cell}, a single one is consistently obtained regardless of the discretization. The likely reason is that for inhomogeneous substrates, the variations in temperature induced by the substrate inhomogeneity are sufficient to make one direction of flow or the other preferable.

Homogeneous teflon substrate

In contrast to BDD, teflon is a thermal insulator ($\kappa_{teflon}/\kappa_{BDD} \sim 10^{-4}$), leading to a much lower heat flux through the solid. For that reason, in a system with a teflon substrate, heat conduction through the liquid is fast enough to prevent the build-up of strong perturbations in the density near the substrate-solution interface, which in turn leads to negligible velocities – $|\boldsymbol{v}_{av}| \lesssim 10^{-8}$ m·s^{-1}. Accordingly, the temperature in the fluid remains essentially unperturbed by the flow and independent of *r*, see Figures B.6- B.7 in Appendix B for details. The magnitude of the predicted velocity suggests that the solution is approximately stagnant under such conditions; in an experimental system, sources of motion other than thermal convection, e.g. external vibrations [34] can be expected to induce fluid motion of comparable or higher intensity.

BDD substrates with teflon annular bands

Convective flows consisting of a single toroidal roll with anticlockwise motion in the simulated region (i.e., upwelling next to the wall) arise in the simulations of conducting substrates with an insulating annular band. Accordingly, the solution temperature reaches its maximum value along *r* at the side wall and has a minimum at the centre of the cylinder. As Figure 5.3A illustrates, the maximum volume-averaged velocity $|\boldsymbol{v}_{av}|_{max}$ for this case (6 to 9×10^{-5} m·s^{-1}) is higher than in the clockwise flow observed for a homogeneous BDD substrate (4×10^{-5} m·s^{-1}, Figure 5.2A), but has the same order of magnitude.

The properties of the flow for this case are markedly dependent upon the substrate structure – increasing the width of the insulating band leads to an

increase in $|\boldsymbol{v}_{\mathrm{av}}|_{\max}$ and a shorter induction time for establishing the convective flow. The explanation behind this is that a substrate with a wider band causes a stronger perturbation in the liquid temperature at $z \sim h_{\mathrm{s}}$ (compare Figure 5.3C with Figure B.8B and D). The temperature within the conducting region remains homogeneous and approximately equal to that of the thermostat. In contrast, as seen in Figure 5.3C, the insulating region cools down noticeably because heat is lost to the liquid at a higher rate than it is gained from the thermostat at $z = 0$. The width of the annular band affects the extent of the perturbation and whereas for small d_{band} the latter is effectively smoothed out by the heat transfer in the liquid, for the larger values it affects the density distribution considerably and leads to the quicker establishment of a convective flow pattern. In Appendix B, we provide 'snapshots' of the temperature and velocity distribution for $d_{\mathrm{band}}/r_{\mathrm{cell}} = 1/9$ and $1/27$, which complement those presented in Figure 5.3 for $d_{\mathrm{band}}/r_{\mathrm{cell}} = 1/3$.

Furthermore, by varying the initial temperature difference, we see that thermal convection affects the overall heat transfer as characterized by $\Delta\tilde{T}_{\mathrm{av}}(t)$ significantly at $\Delta T = 5$ K, but not at $\Delta T = 4$ K (see Fig. B.9), placing Ra_{cr} between 1.9×10^4 and 2.4×10^4. The comparison between the results for $\Delta T_{\mathrm{av}}(t)$ at different ΔT and simulations with no convection is shown in Figure B.9 in Appendix B.

Our simulations that utilize the alternate boundary condition (5.29) indicate that the flow with upwelling at $r = 0$ is of equivalent stability to the one shown in Figure 5.3 under conditions that admit a stationary state with non-zero velocity. However, starting from the stationary distributions of $\boldsymbol{v}$, T and p obtained in this configuration and changing the boundary condition at the top wall back to no-flux, we see that for this substrate structure, only the pattern with downward motion at $r = 0$ is stable under transient conditions; for more details on the stability tests, see Appendix B. At a qualitative level, the preferred direction of flow is due to the presence of a conductive outer band, which leads to a higher T^{L} in the vicinity of the side wall than next to the insulating band. Even though the same is true for the inner band, as the latter is in contact with a much smaller amount of liquid, the perturbation at $r \sim r_{\mathrm{cell}}$ is the determining factor and causes the fluid to move upwards next to the wall.

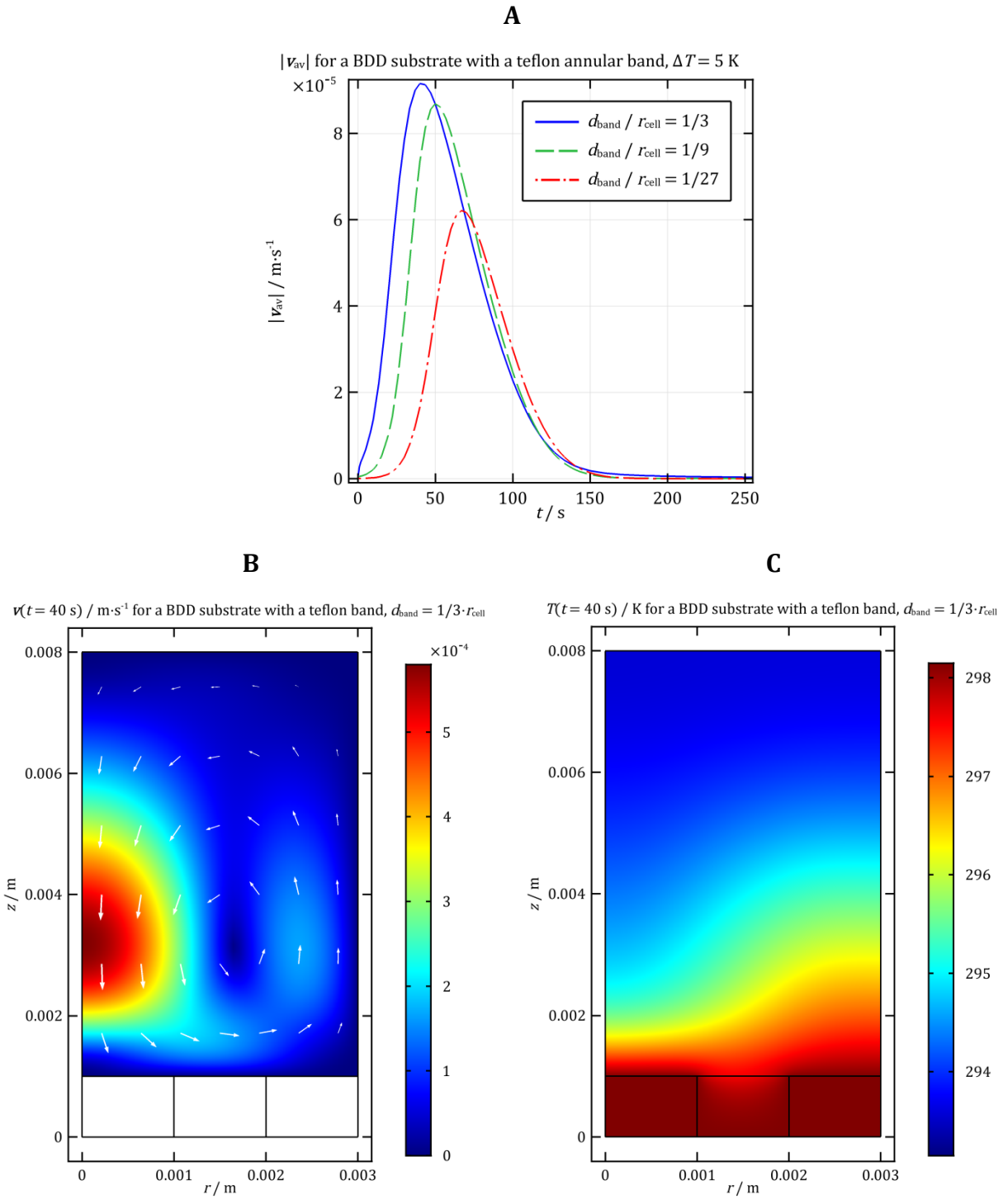


Figure 5.3. Results for BDD substrates with teflon annular bands. **A** – volume-averaged velocity magnitude vs. time; **B** and **C** – 'snapshots' respectively of $\boldsymbol{v}$ and T at t = 40 s for a band with d_{band}/r_{cell} = 1/3. The length of the arrows in **B** is proportional to the natural logarithm of $|\boldsymbol{v}|$. For this simulation, the solution is colder by ΔT = 5 K than the substrate at the initial moment.

Teflon substrates with BDD annular bands

Single toroidal rolls with upwelling in the centre of the cylinder and temperature profiles that have a maximum at the axis except in the vicinity of the thermally insulating substrate are observed for this case (Figures 5.4 and B.13), contrasting with the results for BDD substrates with teflon annular bands. As seen in Figures 5.4 and B.15, the average velocity is $|\boldsymbol{v}_{\mathrm{av}}| \sim 10^{-4}\ \mathrm{m{\cdot}s^{-1}}$ – compare with the case for a homogeneous teflon substrate, in which $|\boldsymbol{v}_{\mathrm{av}}| \lesssim 10^{-8}\ \mathrm{m{\cdot}s^{-1}}$ (Figs. B.6A, B.7A in Appendix B).

By analogy with the 'inverse' configuration, we performed studies at varying ΔT with the aim of establishing bounds for Ra_{cr}. Again as with the case of a BDD substrate with a teflon annular band, we observe that convection only starts to have an appreciable influence over $\Delta\tilde{T}_{\mathrm{av}}$ when the initial temperature difference is increased from 3 K to 4 K, and that this is caused by a substantial increase in the peak average velocity, as illustrated in Figure 5.5 for $d_{\mathrm{band}}/r_{\mathrm{cell}} = 1/3$ (see Figure B.14-Figure B.15 for details on the other studied substrates). Thus, we obtain that for this case, Ra_{cr} is between 1.4×10^4 and 1.9×10^4; as seen in Appendix B, for the other values of d_{band}, the critical ΔT is between 4 and 5 K and Ra_{cr} is between 1.9×10^4 and 2.4×10^4. [10]

As with the 'inverse' configuration, increasing the band width intensifies the convective flow due to the stronger perturbation of the temperature profile at $z \sim h_{\mathrm{s}}$. The induction time for the onset of convection decreases as d_{band} is increased (Figure 5.4A), but the dependence is much weaker than for a conducting substrate with an insulating annular band, compare with Figure 5.3A. Another similarity with the case of a conducting substrate with an insulating band is that the flow shown in Figure 5.4 and its approximate mirror image with respect to $z = h_{\mathrm{s}}$ are approximately equivalent in stability in systems that permit a stationary flow, but not if the driving force for convection decays to zero at long t.

[10] In the paper on which this chapter is based [J.K. Novev, R.G. Compton, Phys. Chem. Chem. Phys. 19 (2017) 12759-12775], we did not explicitly note that the critical ΔT is in the interval [4 K, 5 K] for $d_{\mathrm{band}} = 1/9$ and $1/27$ rather than [3 K, 4 K] as for $d_{\mathrm{band}} = 1/3$. However, the difference in the critical values is visible from the Figs. 5 and S14-S15 in the paper (corresponding to Figs. 5.5 and B.14- B.15 in this thesis).

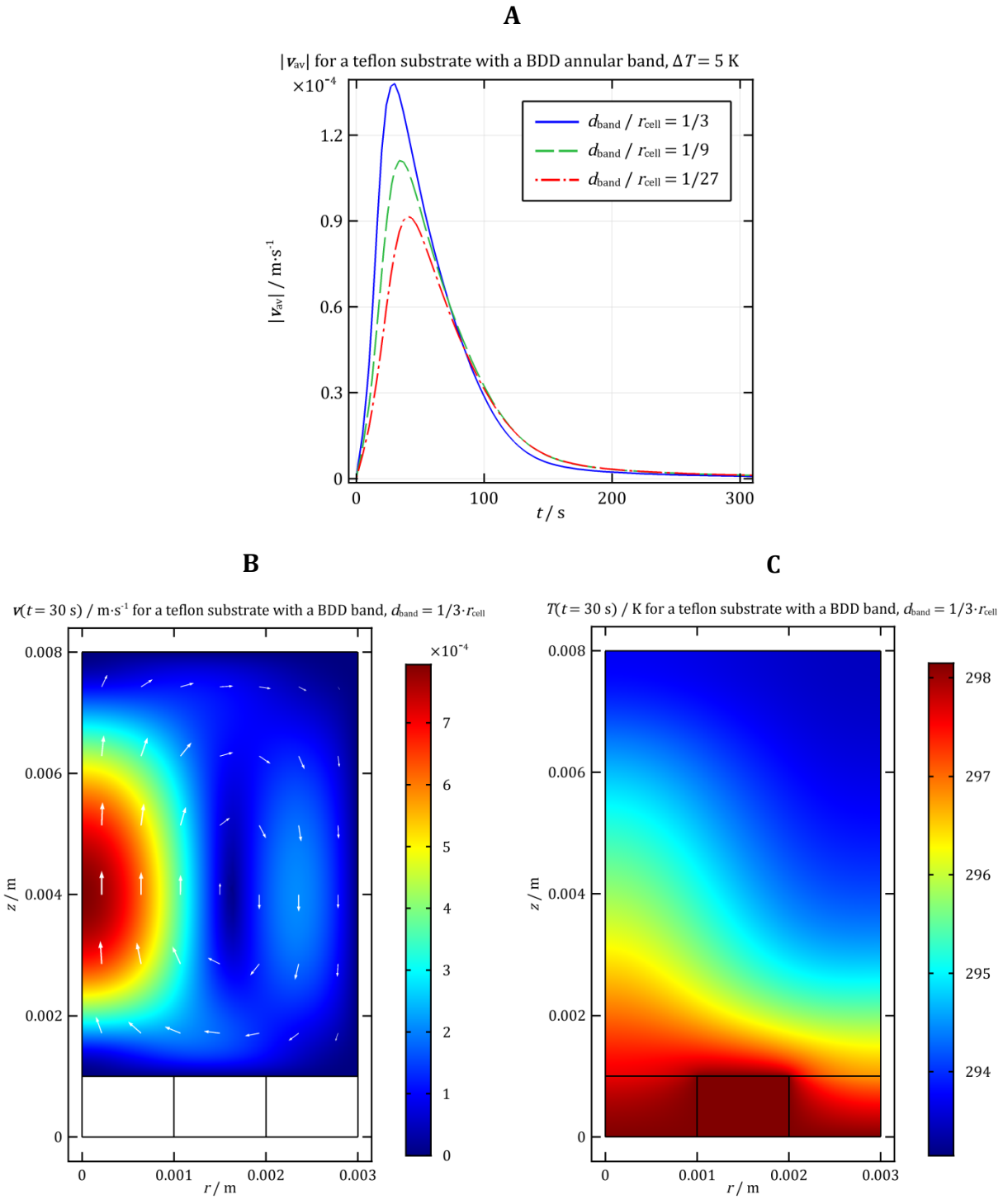


Figure 5.4. Results for teflon substrates with BDD annular bands. **A** – volume-averaged velocity magnitude vs. time; **B** and **C** – 'snapshots' respectively of $\boldsymbol{v}$ and T at t = 30 s for a band with d_{band}/r_{cell} = 1/3. The length of the arrows in **B** is proportional to the natural logarithm of $|\boldsymbol{v}|$. For this simulation, the solution is colder by ΔT = 5 K than the substrate at the initial moment.

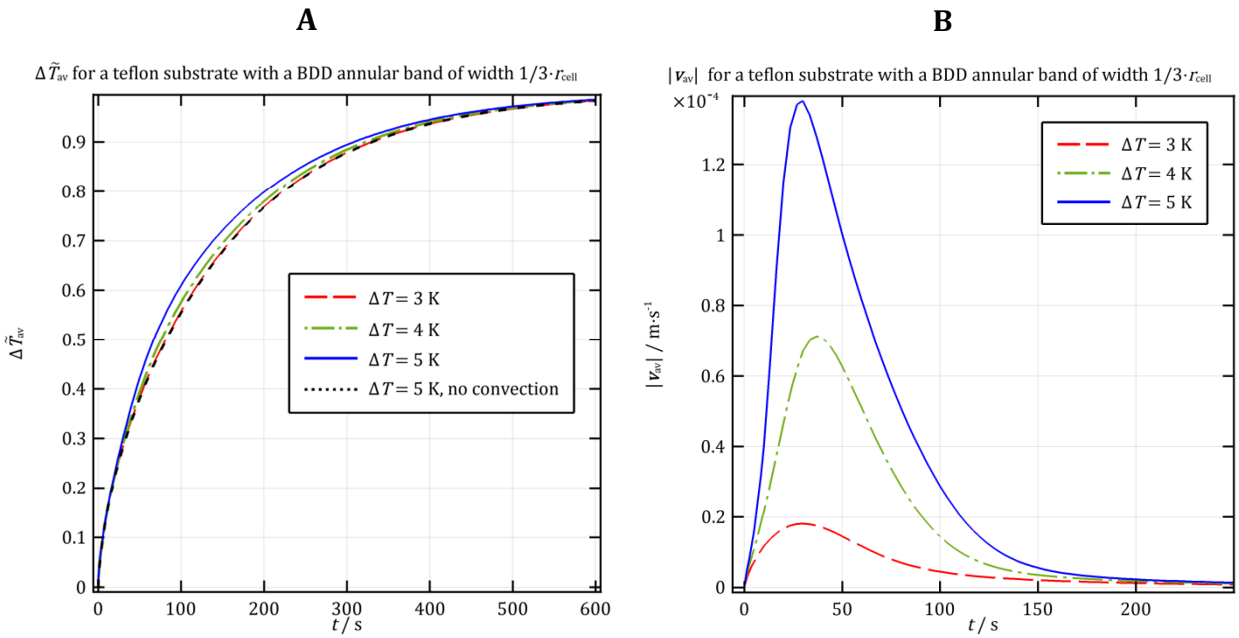


Figure 5.5. Threshold value of the initial temperature difference ΔT for inducing convective heat transport, illustrated for a teflon substrate with a BDD annular band of width $d_{band} = 1/3{\cdot}r_{cell}$. **A** – volume-averaged temperature difference $\Delta\tilde{T}_{av}(t)$ – comparison of simulations involving convection with various ΔT and the purely conductive case; **B** – volume-averaged velocity $|\boldsymbol{v}_{av}(t)|$ plotted for different ΔT.

Qualitatively, the difference in flow direction with the 'inverse' case comes from the absence of a strong positive perturbation in T^{L} at $r \sim r_{cell}$. Without this factor, the fluid follows the direction of the buoyancy force at $r = 0$, leading to a normal velocity profile that exhibits a maximum rather than a minimum at the cylinder axis.

Lastly, we comment that upon magnification of the velocity distributions discussed in this chapter for both $r_{cell} = 3$ mm and $r_{cell} = 8$ mm, it is possible to discern small additional vortices, which are situated at (r_{cell}, h_s) and (r_{cell}, $h_s + h_{cell}$) and move in the opposite direction to the main one. These vortices may be numerical artefacts or true features of the solution (solutions of this type are seen in Ref. [23]), but since they have an intensity that is multiple orders of magnitude lower than the main flow, we do not discuss them in more detail.

5.4.1.B *Solution warmer than substrate at $t = 0$ ($\Delta T < 0$)*

As it can be expected for a solution that is being cooled from below, for this case heat conduction leads to a stably stratified temperature profile that is not perturbed by the convective flows. Thus, heat transfer is not noticeably affected by convection in any of the studied configurations. Nevertheless, as the temperature in the vicinity of inhomogeneous substrates exhibits local variations, non-negligible convective flows arise in cells with substrates of this type, and we describe their most important features below.

Homogeneous substrates

Both for BDD and teflon substrates, the predicted flow in the solution is negligible ($|\boldsymbol{v}_{\mathrm{av}}|_{\max} \sim 10^{-10}$–$10^{-9}$ m·s^{-1}) and does not lead to a significant perturbation of the temperature profile with respect to the conduction-only case, see Figures B.18- B.21 in Appendix B for details. Furthermore, the velocity profiles obtained from these simulations contain high levels of numerical noise, as seen in Figure B.18C. It is not surprising that only weak convective currents arise for $\Delta T < 0$, since, in this case, the fluid is cooled from below, leading to a local density that is a diminishing function of z, i.e., a stably stratified liquid.

BDD substrates with teflon annular bands

For substrates of this type, the inhomogeneity of the solid leads to the development of convective currents with an average velocity that strongly depends on d_{band} and is non-negligible for the widest annular band, $d_{\mathrm{band}}/r_{\mathrm{cell}} = 1/3$ ($|\boldsymbol{v}_{\mathrm{av}}| \sim 10^{-6}$ m·s^{-1}), but the temperature profile in the solution remains unperturbed by the fluid motion (see Figures B.22- B.23). Interestingly, the flow patterns observed in this configuration are more complicated than for $\Delta T = 5$ K. Instead of a single toroidal roll, they consist of a main roll with a clockwise motion in the simulated region (see Figure 5.1) that occupies approximately the space between r_1 and r_{cell} along r and between h_{s} and $h_{\mathrm{s}} + h_{\mathrm{cell}}/2$ along z, as well as secondary rolls of lower intensity and

direction opposite to that of the main one, see Figure B.22; Figure 5.6 below illustrates a similar flow structure for the 'inverse' configuration.

Furthermore, in analogy the case with ΔT = 5 K, the direction of fluid motion in the rolls is relevant to their stability – patterns in which the former is reversed with respect to that shown in Figure B.22B are unstable – see Appendix B for more details. The direction of flow in the main roll in the stable pattern can be rationalized qualitatively by a similar argument to the one we invoked for inhomogeneous substrates at $\Delta T > 0$. Since the heat conductivity of the teflon annular band is much lower than that of the rest of the substrate, the solution next to it cools down more slowly and rises upwards, leading to the formation of a primary roll with clockwise motion situated between r_1 and r_{cell}.

Teflon substrates with BDD annular bands

For insulating substrates with conductive bands, the average velocity reaches a peak value that is of the order of 10^{-5} m·s^{-1} for all d_{band} in a characteristic time period of ≈ 5 s (see Figure 5.6A) and exhibits slower decay than for ΔT = 5 K (compare with Figure 5.4A). The pattern of flow here is similar to the one we observed for the 'inverse' configuration – conductive substrates with insulating bands – but with the liquid moving in the opposite direction within the rolls. As Figure 5.6B shows, there is a main roll with an anticlockwise motion in the simulated region (see Figure 5.1) occupying approximately the space between r_1 and r_{cell} along r and between h_s and $h_s + h_{\text{cell}}/2$ along z, as well as two secondary ones that possess a much lower intensity and an opposite direction of flow. As we observed for BDD substrates with teflon annular bands, reversing the direction of flow within the rolls leads to an unstable flow pattern – see Appendix B for details. Qualitatively, the temperature of the solution next to the side walls drops more slowly than at the BDD annular band, which induces an anticlockwise main roll at r between r_1 and r_{cell}.

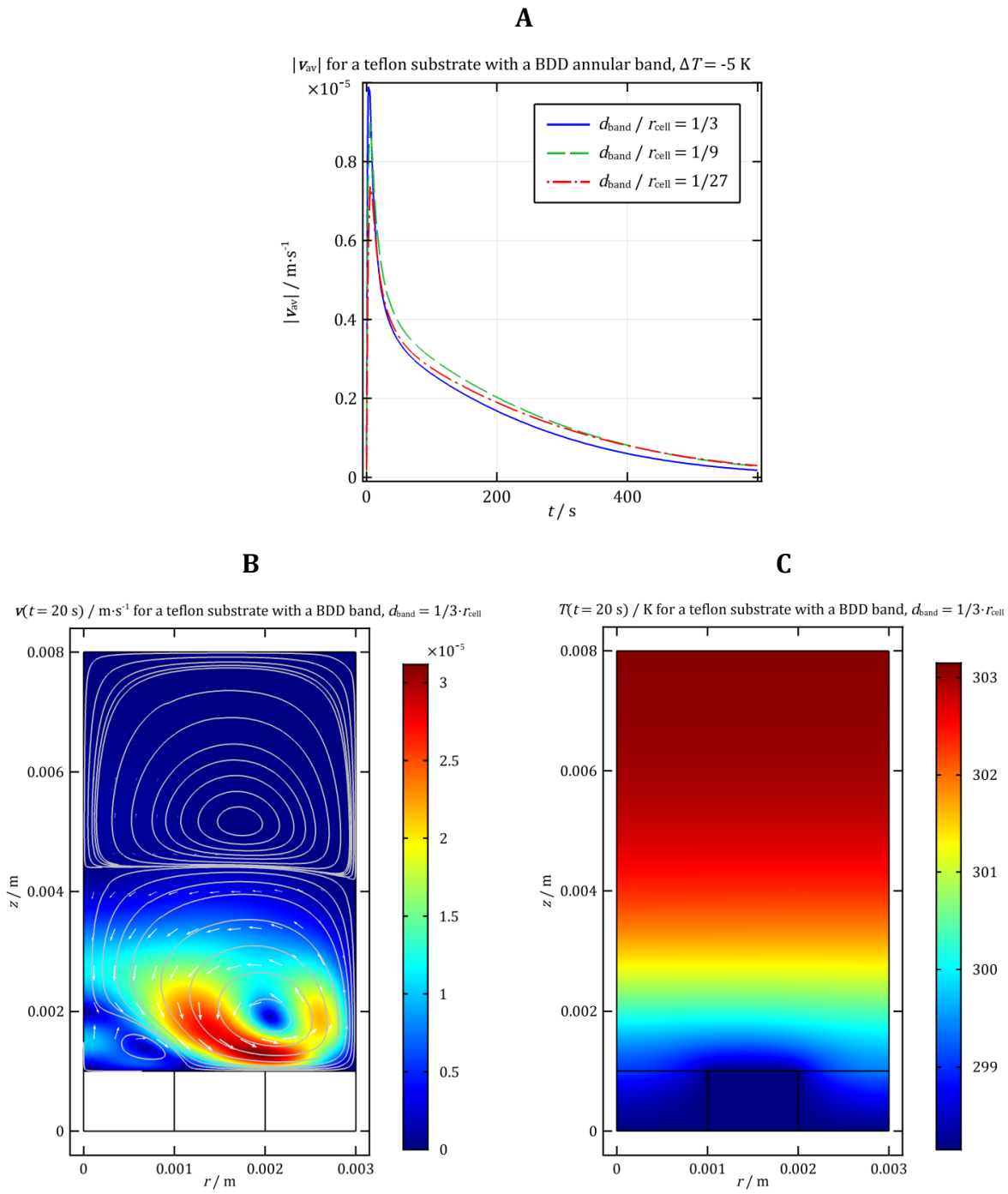


Figure 5.6. Results for a teflon substrate with a BDD annular band (d_{band}/r_{cell} = 1/3) and ΔT = −5 K, corresponding to a solution colder than substrate at t = 0. **A** – volume-averaged $|\boldsymbol{v}|$ vs. time; **B** and **C** – 'snapshots' respectively of $\boldsymbol{v}$ and T at t = 20 s for a band with d_{band}/r_{cell} = 1/3. The streamlines in **B** illustrate the structure of the flow pattern – the main roll with an anticlockwise movement, at the simulated region for r between r_1 and r_{cell} along r and h and $h_s + h_{cell}/2$ along z, as well as two secondary rolls – one situated between 0 and r_1 along r and between h_s and ~ h_s + $h_{cell}/4$ along r and another, possessing the lowest intensity, at the upper half of the cylindrical cell. The length of the arrows in **B** is proportional to ln($|\boldsymbol{v}|$).

Despite the comparatively high average velocity within the solution, the temperature within it retains a profile that is indistinguishable from that for heat transfer by conduction only, as demonstrated in 5.6C and Figure B.27.

5.4.2. **Simulations for** r_{cell} = 8 mm

Here, we apply the approach of Section 5.4.1 to the flows within the cell whose radius is chosen so as to guarantee that the volume of liquid in the simulation is approximately equal to that in the experiment. Due to the similarity with the case of a smaller cell, we give fewer details and for substrates with annular bands, we only consider the case $d_{band}/r_{cell} = 1/3$. Furthermore, as for this geometry all studied cells are either significantly below or above the critical Rayleigh number, we do not attempt to set bounds for its value.

5.4.2.A *Solution colder than substrate at* $t = 0$ ($\Delta T > 0$)

BDD substrate

In this case, the natural convective flows reach a peak average velocity of approximately 4×10^{-4} m·s^{-1}, an order of magnitude higher than for the smaller cell. The change in the aspect ratio of the cylinder exerts a strong effect on not just the intensity, but also the pattern of flow patterns. Between $t = 0$ and $t \approx 50$ s, the flow consists of two rolls lined up in the radial direction and having a width of approximately $r_{cell}/2$. The two rolls are comparable in intensity and give rise to a temperature distribution with maxima at $r = 0$ and $r = r_{cell}$ (see Figure B.30C-F in Appendix B). Due to the much stronger convective flow within the solution in comparison with that for the smaller cell, the effect on $\Delta\tilde{T}_{av}$ is more pronounced and reaches ≈ 30% at most (Figure B.30B). As illustrated in Figure B.30, the intensity and shape of these rolls have a complicated evolution, which gives rise to two maxima and two minima in $|\boldsymbol{v}_{av}|$ in the interval [0, 50 s]. At $t \sim 85$ s, the average solution velocity passes through a third maximum as the two rolls merge into one

toroidal roll with anticlockwise motion in the simulated region. The roll in question spans the entire cell and corresponds to the same mode observed in simulations for the smaller cell; the average velocity in the solution tends to zero at $t \approx 400$ s. The transition to a single-roll flow pattern leads to the formation of a temperature distribution with a single maximum at $r = r_{cell}$.

We should point out that, unlike the case of a BDD substrate situated in a smaller cell, at $r_{cell} = 8$ mm the direction of flow at long times is the same for simulations using quadratic and linear shape functions for T; however, the corresponding $|\boldsymbol{v}_{av}(t)|$ are not completely identical. Such differences in the predicted evolution of the flows are to be expected in a system for which the onset of convection is controlled by infinitesimal inhomogeneities in temperature.

Furthermore, we performed simulations with the boundary condition (5.29), which permits a non-zero velocity at $t \to \infty$. The evolution of the velocity and temperature profiles for this case is similar to that illustrated in Figure B.30 for a cell with insulated walls and the stationary flow pattern is once again a single toroidal roll. In contrast with what we observed for the smaller cell, the stationary pattern has downward motion in the cylinder centre and a maximum of T at $r = r_{cell}$, regardless of the choice of shape function order for the temperature. However, if we use a reflection of this flow pattern with respect to $z = h_s$, and a reflection of its corresponding temperature distribution with respect to $r = 0$ as initial conditions (with $\Delta p(t = 0) = 0$), we observe that they also correspond to a stationary state. As in the case with the smaller cell, both flows maintain their direction if the boundary condition at the top wall is changed from (5.29) back to no-flux. Thus, as was seen for $r_{cell} = 3$ mm, the cell with a homogeneous BDD substrate allows for two modes of flow that are equivalent in stability under stationary conditions.

Teflon substrate

In contrast with our results for the same substrate in the smaller cell, here, we observe significant convective flows that strongly perturb the temperature distribution. As previous studies, e.g. that by Yamaguchi et al. [23] show, the critical

Ra required to induce the various possible modes of flow in a systems like the presently discussed one is a function of the aspect ratio of the cylinder; thus, it is not surprising that non-negligible flows arise for r_{cell} = 8 mm, but not for r_{cell} = 3 mm.

As with the other cells with a homogeneous substrate at their bottom that exhibit significant convective flows, we observe two modes of flow. The two flow patterns both exhibit a main toroidal roll that occupies most of the cell with either upward or downward motion at r = 0, corresponding to a maximum of T at r = 0 or r = r_{cell}, respectively. In both cases, the flow contains an additional roll with a direction opposite to the main flow; the size and intensity of the latter diminish over time. For the pattern with positive normal velocity at r = 0, this roll is situated at the vicinity of the point (r_{cell}, h_s) and leads to an additional perturbation in the temperature profile, which is eventually smoothed out (see Figure B.31C-F in Appendix B). For the other pattern, the smaller roll is situated approximately at (r_{cell}, h_s + h_{cell}) and does not perturb the temperature distribution (Figure B.32C-D).

Similarly to the case of a BDD substrate at r_{cell} = 3 mm, the two flow patterns that differ by the sign of v_z at r = 0 can be obtained by varying the order of the shape functions for T. Applying the same methodology used for the stability analysis of flows generated in cells with homogeneous BDD substrates at r_{cell} = 3 mm leads to the conclusion that, once again, the two observed modes of flow are equivalent in stability. Notably, in contrast to the flows observed in the smaller cell for the same substrate composition, $|\boldsymbol{v}_{av}|$ is similar for the two contrasting patterns.

The average solution velocity passes through several extrema, reaching a global maximum value of 3.2 and 4.1×10^{-4} m·s^{-1} for the pattern with upflow and downflow at r = 0, respectively. The effect of convection on $\Delta\tilde{T}_{av}$, while substantial, is not as strong as in the analogous system with a conductive substrate and reaches at most 10 and 14% for the flows with upwelling and downward motion at r = 0. Plots of $|\boldsymbol{v}_{av}|$, $\Delta\tilde{T}_{av}$, as well as 'snapshots' of the velocity and temperature distributions can be found in Appendix B (Figure B.31-Figure B.32).

BDD substrate with a teflon annular band

The convective flows generated in this case evolve through multiple stages; the volume-averaged solution velocity reaches a peak value of 4.5×10^{-4} m·s^{-1}, an approximately fivefold increase with respect to the result for the smaller cell – compare Figure 5.3A and Figure 5.7A. The heat transfer in the liquid is strongly affected, and the difference in $\Delta\tilde{T}_{av}$ induced by convection peaks at 44%, see Figure 5.7B.

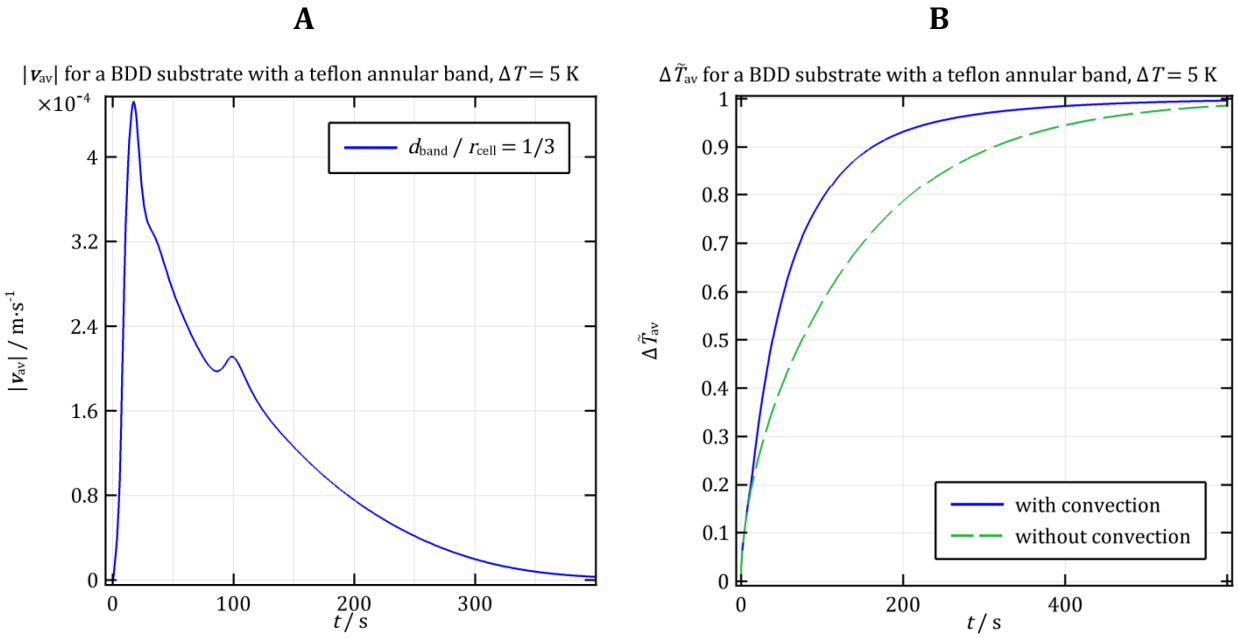


Figure 5.7. Results for a BDD substrate with a teflon annular band situated at the bottom of a cell of radius 8 mm. The solution is initially colder than the substrate (ΔT = 5 K). **A** – $|\boldsymbol{v}_{av}|$ vs. t; **B** – volume-averaged dimensionless $\Delta\tilde{T}_{av}$ vs. t.

As observed for a homogeneous BDD substrate, the flow initially consists of two counterrotating rolls stacked in the radial direction that give rise to a temperature distribution with maxima at r = 0 and r = r_{cell}, as illustrated in Figure 5.8A-B. Notably, the intense heat flux coming through the BDD surface causes the fluid in contact with it to rise upwards, leading to the formation of a two rolls, the more intense of which is situated at $r \lesssim r_{cell}/2$ along r and has clockwise motion in the simulated region. Another similarity with the case of a BDD substrate is that as time progresses, the two rolls merge into one that occupies the whole cylinder and has

upwelling next to the walls (Figure 5.8C). As a consequence of that, the temperature distribution adopts a shape with a maximum at $r = r_{\text{cell}}$ (Figure 5.8D).

Qualitative stability analysis of the flow patterns in this system, explained in more detail in Appendix B, shows that for a thermally insulated cell, the single roll with upward motion next to the walls is stable and that its mirror image with respect to $z = h_{\text{s}}$ is unstable. This is analogous to our result for a substrate of the same type situated at the bottom of a smaller cell.

Teflon substrate with a BDD annular band

This configuration gives rise to convective flows that have a peak average velocity of 5×10^{-4} m·s^{-1}, a nearly fivefold increase with respect to the case of the smaller cell (compare Figure 5.4A and Figure B.33A). Furthermore, the effect of convection on the temperature distribution is much more substantial, amounting to a 39% difference in $\Delta\tilde{T}_{\text{av}}$ at most, as illustrated in Figure B.33B in Appendix B.

As in the 'inverse' configuration, the flow initially consists in two counter-rotating rolls. The latter perturb the temperature profile strongly and induce a maximum in T at $r \sim r_1$, as seen in Figure B.33C-D. Once again, the fluid motion is most intense and directed upwards in the vicinity of the BDD due to the local increase in temperature there, causing a roll to appear at $r \gtrsim r_{\text{cell}}/2$; in the region of space considered in our simulation, the fluid within this roll moves clockwise. At longer times, the two convective cells merge to form a single toroidal roll that occupies the whole cylinder and has upwelling at $r = 0$; the temperature profile corresponding to it has a warmer region at $r = 0$. The evolution of the distributions of T and $\boldsymbol{v}$ is illustrated in Figure B.33C-F in Appendix B.

By applying the same qualitative stability analysis we used in our treatment of substrates of the same type at $r_{\text{cell}} = 3$ mm, we see that in this case, as we observed for the smaller cell, the roll in which the fluid moves downward instead of upward at $r = 0$ is unstable.

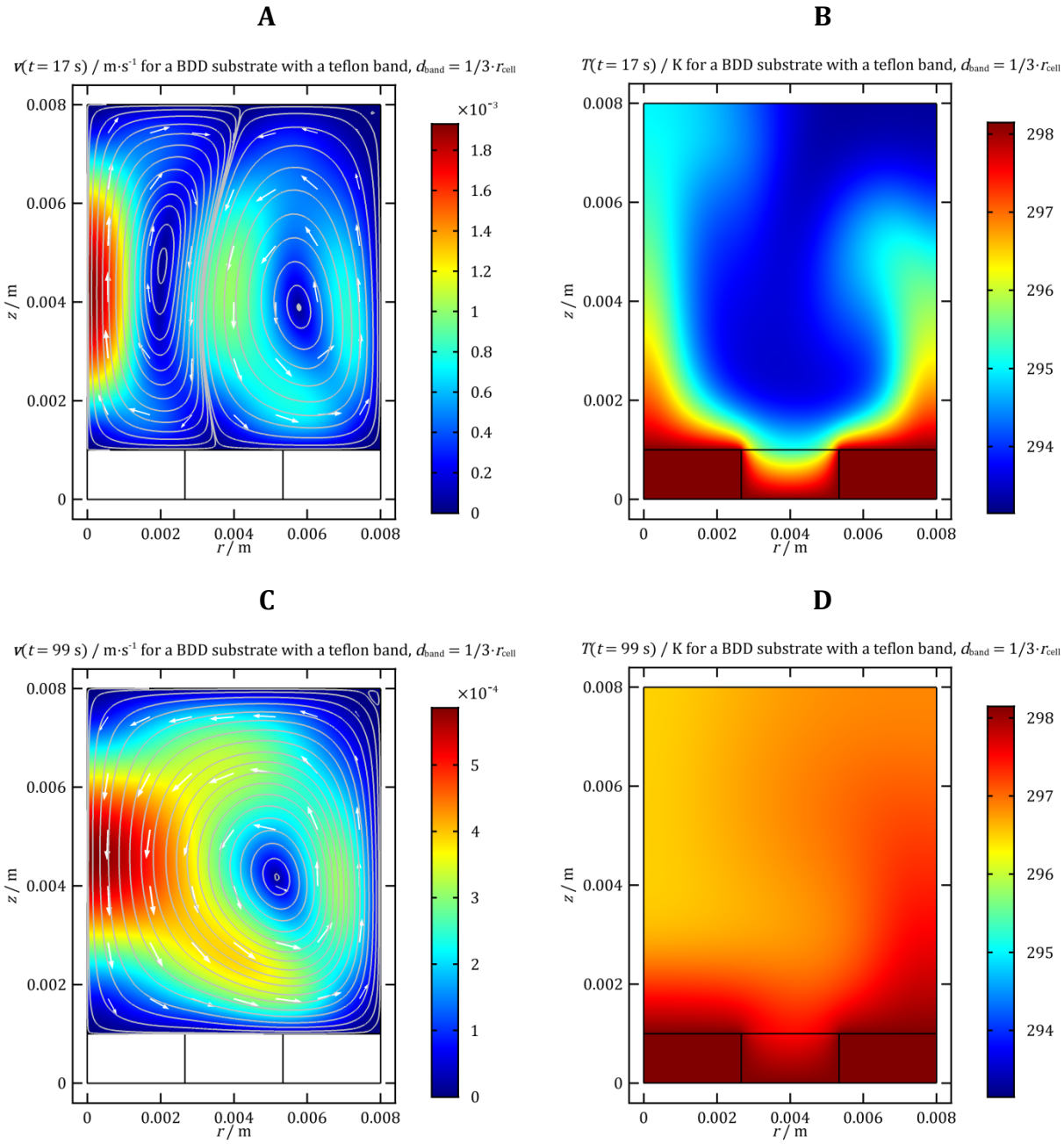


Figure 5.8. Profiles of $\boldsymbol{v}$ and T for a BDD substrate with a teflon band (d_{band}/r_{cell} = 1/3). The 'snapshots' of the velocity and temperature distributions in **A**-**D** are taken at the two maxima of $|\boldsymbol{v}_{av}|$, t = 17 s and t = 99 s. **A** illustrates the velocity distribution with streamlines marking the two transient convective rolls; **B** – the temperature distribution that this flow pattern brings about. **C** shows the single-roll velocity pattern that results from the merging of the two rolls in **A**; **D** demonstrates the profile of T corresponding to it. The length of the arrows in **A** and **C** is proportional to the natural logarithm of $|\boldsymbol{v}|$. For this simulation, the solution is colder than the substrate at t = 0 (ΔT = 5 K).

5.4.2.B *Solution warmer than substrate at t = 0 (ΔT < 0)*

Homogeneous substrates

As in the smaller cell, due to the stable stratification of the fluid, no significant convective flows arise within the system if it contains a homogeneous substrate that is colder than the solution at t = 0. For both BDD and teflon substrates, the simulations yield negligible fluid motion ($|\boldsymbol{v}_{\mathrm{av}}| \sim 10^{-9}$ m·s^{-1}) that does not influence the temperature profile.

BDD substrate with a teflon annular band

In this system, the inhomogeneity of the substrate generates local density variations in the liquid and convective flows, but the intensity of the latter is greater by an order of magnitude than it is for the smaller cell ($|\boldsymbol{v}_{\mathrm{av}}| \sim 10^{-5}$ vs. 10^{-6} m·s^{-1}). Despite the considerable velocity of the fluid, the temperature profiles remain unaffected by convection, as they do for the smaller cell. The flow undergoes complex evolution but passes through a three-roll configuration similar to that observed for the small cell – a main roll with clockwise movement in the simulated region (see Figure 5.1) situated approximately between $r_1 + d_{\mathrm{band}}/2$ and r_{cell} along r and h_{s} and $h_{\mathrm{s}} + h_{\mathrm{cell}}/2$ along z, as well as two secondary rolls of opposing direction and lower intensity. Plots of $|\boldsymbol{v}_{\mathrm{av}}|$, $\Delta\tilde{T}_{\mathrm{av}}$ and 'snapshots' of the velocity and temperature distributions can be found in Appendix B (Figure B.34).

The flow pattern in this system was subjected to the same stability tests described for the smaller cell. Once again, the tests indicate that the direction of flow within the rolls is determined by the substrate structure and that reversing the former leads to an unstable flow pattern. Though there are differences between the velocity profiles observed for r_{cell} = 3 and 8 mm, the qualitative explanation for the flow direction in the main roll is the same – the fluid next to the annular band is cooled down at a slower rate than that in contact with the rest of the substrate, which leads to a circulatory pattern for r between r_1 and r_{cell} that moves clockwise in the simulated region of space (see Figure 5.1).

Teflon substrate with a BDD annular band

As with the 'inverse' configuration, significant convective flows arise in this system and their intensity is increased with respect to the simulations for the smaller cell ($|\boldsymbol{v}_{\mathrm{av}}|_{\max} \sim 4\times10^{-5}$ vs. 0.9×10^{-5} m·s^{-1}, compare Figs. B.35A and 5.6A). As in the other systems with a substrate that is initially colder than the solution, the temperature profile in the liquid remains unaffected by convection in spite of the non-negligible flows. The velocity profile has a complicated evolution, but passes through a configuration with three rolls, as for a BDD substrate with a teflon annular band. Importantly, as we observed in the case with r_{cell} = 3 mm, the direction of flow within the rolls is opposite to that for substrates with the 'inverse' structure.

The direction of movement in the rolls has the same qualitative explanation we invoked in the discussion of the results for the smaller cell. Due to the lower heat conductivity of the teflon, the fluid in contact with the outer ring between $r_1 + d_{\mathrm{band}}$ and r_{cell} remains warmer than that in touch with the boron-doped diamond and rises upward, thus giving rise to a main roll with anticlockwise movement for the simulated region (Figure 5.1).

The analysis of the stability of this flow pattern, performed in a completely analogous way to the one we did for the smaller container, indicates that the direction of flow in the convective cells is once again determined by the profile of the heat conductivity within the solid substrate; reversing the sense of the flow in the rolls leads to an unstable configuration.

Appendix B contains additional data on this system in the form of plots of $|\boldsymbol{v}_{\mathrm{av}}|$, $\Delta\tilde{T}_{\mathrm{av}}$ and 'snapshots' of the velocity and temperature distributions (see Figure B.35).

Non-aqueous solvents

Our study deals specifically with aqueous solutions as this is the medium used for the vast majority of electrochemical and SECM experiments, but it would be straightforward to apply the approach described in this chapter to other solvents. Naturally, using a more viscous solvent – for example, dimethyl sulfoxide, whose viscosity is higher than that of water by a factor of two [35] – would lead to less

pronounced natural convective currents. Conversely, using a less viscous solvent, such as N,N-dimethylformamide ($\eta(T$ = 298.15 K) = 0.794 mPa.s [14]) would make natural convection even more pronounced. However, the precise behaviour of the liquid would be determined by the corresponding values of *Pr* and *Ra*. Taking the example of DMF and the following values for its material properties at 298.15 K: α_{DMF} = 1.013×10^{-3} K^{-1} from Ref. [36], $\kappa_{\mathrm{DMF}} = 0.183\ \mathrm{W \cdot m^{-1} \cdot K^{-1}}$, ρ_{DMF} = 944.5 kg·m^{-3} and $C_{p\mathrm{DMF}}$ = 2.06×10^{3} J·kg·K^{-1} from Ref. [14], we can compare the values of *Ra* and *Pr* with those for water at 293.15, obtaining $Pr_{\mathrm{DMF}}/Pr_{\mathrm{H_2O}} =$ 1.3 and $Ra_{\mathrm{DMF}}/Ra_{\mathrm{H_2O}} = 8.9$, the latter indicating that flows in DMF would be considerably more susceptible to natural convection driven by thermal gradients. However, it is worth mentioning that changing the solvent would also affect the mass transport in the system through the temperature dependence of the viscosity, and therefore the diffusion coefficients of the species present in solution.

5.5. Conclusions

This chapter presents a numerical study of the convective heat transfer in an idealized model of an electrochemical measurement cell consisting of a solid substrate whose thermostated lower surface is situated at the bottom of a cylindrical container with solid, thermally insulated walls. We have shown that under the conditions prescribed in the model, the substrate structure, or, more precisely, the spatial distribution of thermal conductivity, plays an important role in the evolution of the temperature and velocity profiles. The simulations described here demonstrate that an initial temperature difference between the solution and the substrate of absolute value ~ 5 K may generate flows which evolve over a time scale of ~ 100 s and have average velocities as high in order in magnitude as 10^{-4} m·s^{-1}. Such flows can strongly perturb the temperature profile within the solution and presumably also influence mass transport. Moreover, we have shown that the intensity and direction of these flows may vary depending on the initial

temperature difference and on the spatial distribution of thermal conductivity within the substrate.

As discussed in Section 5.4.1, for homogeneous substrates in the cell of radius 3 mm, appreciable natural convective flows (of $|\boldsymbol{v}_{\mathrm{av}}| \sim 10^{-5}$ m·s^{-1}) only arise if the liquid is initially colder than the substrate and the latter is thermally conductive. We have also demonstrated that convective flows of non-negligible intensity (of $|\boldsymbol{v}_{\mathrm{av}}| \sim 10^{-6}$-$10^{-5}$ m·s^{-1}) arise in the case of inhomogeneous substrates with an annular band, and that the width of the band in question influences the velocity magnitude in the fluid (see Figs. 5.3A, 5.4A and 5.6A). This is true regardless of the sign of the initial temperature difference between solution and substrate, even though convection only leads to a strong perturbation of the temperature if the solution is colder than the substrate at the initial moment (compare Figs. 5.5, B.9 and B.14 with Figs. B.23 and B.27). In addition to that, analysis of the stability of the natural convective flows in all studied systems with inhomogeneous substrates – regardless of the sign of ΔT – indicates that the direction of fluid movement within the stable flow pattern is determined by the spatial distribution of the substrate heat conductivity.

For the larger cell, provided that the solution is initially colder than the solid substrate ($\Delta T > 0$), significant convective flows arise regardless of the conductivity of the latter. In the case of a conductive substrate, the volume-averaged velocity reaches a maximum value of the order of 10^{-4} m·s^{-1}, an increase of one order of magnitude in comparison with the result for the smaller cell. A similar increase is observed in the effect of convection on $\Delta\tilde{T}_{\mathrm{av}}$ – for the large container, it reaches as much as 40% instead of several percent. Furthermore, we have observed that at $r_{\mathrm{cell}} = 8$ mm, the velocity and temperature profiles undergo a much more complex evolution (compare Figure 5.2 and Figure B.30). For $\Delta T > 0$, the velocity and the effect on $\Delta\tilde{T}_{\mathrm{av}}$ see an approximately fivefold increase for systems containing substrates with annular bands (compare Figs. 5.7-5.8 with Fig. 5.3 and Fig. B.33 with Fig. 5.4). Both for conducting and insulating bands, the velocity profiles at long times consist of a single toroidal roll occupying the whole cylinder. For the case of

$\Delta T < 0$, for which the solution is warmer than the substrate at $t = 0$, we observe no qualitative difference between the two studied cells – for both, significant convective flows ($|\boldsymbol{v}_{\mathrm{av}}| \sim 10^{-5}$ m·s^{-1}) arise only for substrates with inhomogeneous thermal conductivity. While the velocity magnitude increases by up to an order of magnitude when r_{cell} is increased from 3 to 8 mm, the temperature distribution remains unperturbed by convection (compare Fig. B.34 with Fig. B.23 and Fig. B.35 with Figs. 5.6, B.27). As we observed for the smaller cell, the direction of the flow in the stable flow patterns in systems with inhomogeneous substrates is determined by the substrate structure.

Our results for the velocity distribution, although pertaining to a highly idealized system, highlight the importance substrate structure can have on electrochemical experiments performed with thermostating through the said substrate unless it is ensured that the system has reached thermal equilibrium before any measurements are performed. As we noted in Section 5.1 and our previous work dealing with imperfect thermostating (see Chapter 4 and the associated paper [3]), the observed natural convective flows have the potential to seriously compromise data from such electrochemical experiments. In particular, our results indicate that conclusions drawn from non-thermostated SECM measurements of heterogeneous surfaces such as basal/edge plane graphite need to be treated with caution, especially where they deviate from inferences made under more rigorous conditions. This caveat applies in equal measure to stationary and transient SECM measurements.

On a more general note, as the simulations of two different cells discussed here show, even in a highly simplified system there are multiple factors that can influence the intensity and structure of the flows generated by imperfect thermostating, and the precise geometry of the container is of particular importance. Thus, attempting to take natural convection into account in experimental setups where thermal convection is likely to arise would be impractical. Moreover, results obtained in the presence of natural convective flows would not be reproducible between containers that differ in shape. These difficulties could be avoided by ensuring that the solution temperature is

homogeneous during the measurements, which would render the contribution of thermal convection to mass transport negligible.

Additional data. Appendix B contains more information on the systems studied in this section; plots of the temperature and velocity in the solution, in terms of both their volume-averages and 'snapshots' of their distributions. The appendix also gives more details on the discretization employed for the various simulations, as well as the stability tests applied to the various encountered flow patterns.

5.6. References

[1] J.K. Novev, S. Eloul, R.G. Compton, Influence of Reaction-Induced Thermal Convection on the Electrical Currents Measured in Chronoamperometry and Cyclic Voltammetry, J. Phys. Chem. C, 120 (2016) 13549-13562.

[2] K. Ngamchuea, S. Eloul, K. Tschulik, R.G. Compton, Advancing from Rules of Thumb: Quantifying the Effects of Small Density Changes in Mass Transport to Electrodes. Understanding Natural Convection, Anal. Chem., 87 (2015) 7226-7234.

[3] J.K. Novev, R.G. Compton, Convective Heat Transfer in a Measurement Cell for Scanning Electrochemical Microscopy, Phys. Chem. Chem. Phys., 18 (2016) 29836-29846.

[4] D.T. Sawyer, A. Sobkowiak, J.L. Roberts, Electrochemistry for Chemists, Second ed., Wiley, New York, 1995.

[5] A.J. Bard, F.-R.F. Fan, J. Kwak, O. Lev, Scanning Electrochemical Microscopy. Introduction and Principles, Anal. Chem., 61 (1989) 132-138.

[6] J. Kwak, A.J. Bard, Scanning Electrochemical Microscopy. Apparatus and Two-Dimensional Scans of Conductive and Insulating Substrates, Anal. Chem., 61 (1989) 1794-1799.

[7] M.V. Mirkin, W. Nogala, J. Velmurugan, Y. Wang, Scanning Electrochemical Microscopy in the 21st Century. Update 1: Five Years After, Phys. Chem. Chem. Phys., 13 (2011) 21196-21212.

[8] D. Schäfer, A. Puschhof, W. Schuhmann, Scanning Electrochemical Microscopy at Variable Temperatures, Phys. Chem. Chem. Phys., 15 (2013) 5215-5223.

[9] K.B. Holt, A.J. Bard, Y. Show, G.M. Swain, Scanning Electrochemical Microscopy and Conductive Probe Atomic Force Microscopy Studies of Hydrogen-Terminated Boron-Doped Diamond Electrodes with Different Doping Levels, J. Phys. Chem. B, 108 (2004) 15117-15127.

[10] R.J. Bowling, R.T. Packard, R.L. McCreery, Activation of Highly Ordered Pyrolytic Graphite for Heterogeneous Electron Transfer: Relationship between Electrochemical Performance and Carbon Microstructure, J. Am. Chem. Soc., 111 (1989) 1217-1223.

[11] R.L. McCreery, Advanced Carbon Electrode Materials for Molecular Electrochemistry, Chem. Rev., 108 (2008) 2646-2687.

[12] R. McCreery, A. Bergren, A. Morteza-Najarian, S.Y. Sayed, H. Yan, Electron Transport in All-Carbon Molecular Electronic Devices, Faraday Discuss., 172 (2014) 9-25.

[13] G.A. Slack, Anisotropic Thermal Conductivity of Pyrolytic Graphite, Phys. Rev., 127 (1962) 694-701.

[14] D.R. Lide (Ed.), CRC Handbook of Chemistry and Physics, Internet Version 2005, CRC Press, Boca Raton, FL, 2005.

[15] P. Bergé, M. Dubois, Rayleigh-Bénard Convection, Contemp. Phys., 25 (1984) 535-582.

[16] R. Touihri, H. Ben Hadid, D. Henry, On the Onset of Convective Instabilities in Cylindrical Cavities Heated from Below. I. Pure Thermal Case, Phys. Fluids, 11 (1999) 2078-2088.

[17] D.A. Kaminski, C. Prakash, Conjugate Natural Convection in a Square Enclosure: Effect of Conduction in One of the Vertical Walls, Int. J. Heat Mass Transfer, 29 (1986) 1979-1988.

[18] N.H. Saeid, Conjugate Natural Convection in a Porous Enclosure: Effect of Conduction in One of the Vertical Walls, International Journal of Thermal Sciences, 46 (2007) 531-539.

[19] D.M. Kim, R. Viskanta, Effect of Wall Heat Conduction on Natural Convection Heat Transfer in a Square Enclosure, J. Heat Transfer, 107 (1985) 139-146.

[20] R.B. Bird, W.E. Stewart, E.N. Lightfoot, Transport Phenomena, Second ed., John Wiley & Sons, New York, 2002.

[21] P.K. Kundu, I.M. Cohen, Fluid Mechanics, Second ed., Academic Press, San Diego, California, 2002.

[22] A.J. Bard, M.V. Mirkin (Eds.), Scanning Electrochemical Microscopy, Second ed., CRC Press, Boca Raton, FL, 2012.

[23] Y. Yamaguchi, C.J. Chang, R.A. Brown, Multiple Buoyancy-Driven Flows in a Vertical Cylinder Heated from Below, Phil. Trans. R. Soc. Lond. A, 312 (1984) 519-552.

[24] E.J.F. Dickinson, H. Ekström, E. Fontes, COMSOL Multiphysics®: Finite Element Software for Electrochemical Analysis. A Mini-Review, Electrochem. Commun., 40 (2014) 71-74.

[25] G. Neumann, Three-Dimensional Numerical Simulation of Buoyancy-Driven Convection in Vertical Cylinders Heated from Below, J. Fluid Mech., 214 (1990) 559-578.

[26] K.E. Torrance, L. Orloff, J.A. Rockett, Experiments on Natural Convection in Enclosures with Localized Heating from Below, J. Fluid Mech., 36 (1969) 21-31.

[27] D. Prikhodko, S. Tarelkin, V. Bormashov, A. Golovanov, M. Kuznetsov, D. Teteruk, A. Volkov, S. Buga, Thermal Conductivity of Synthetic Boron-Doped Single-Crystal HPHT Diamond from 20 to 400 K, MRS Commun., 6 (2016) 71-76.

[28] C.A. Harper (Ed.), Modern Plastics Handbook, McGraw-Hill, New York, NY, 1999.

[29] J. Blumm, A. Lindemann, M. Meyer, C. Strasser, Characterization of PTFE Using Advanced Thermal Analysis Techniques, Int. J. Thermophys., 31 (2010) 1919-1927.

[30] D.M. Price, M. Jarratt, Thermal Conductivity of PTFE and PTFE Composites, Thermochim. Acta, 392-393 (2002) 231-236.

[31] S. Fai Lau, H. Suzuki, B. Wunderlich, The Thermodynamic Properties of Polytetrafluoroethylene, J. Polym. Sci. Polym. Phys. Ed., 22 (1984) 379-405.

[32] D.W. Pepper, J.C. Heinrich, The Finite Element Method: Basic Concepts and Applications with MATLAB®, MAPLE, and COMSOL, Third ed., CRC Press, Boca Raton, FL, 2017.

[33] G. Müller, G. Neumann, W. Weber, Natural Convection in Vertical Bridgman Configurations, J. Cryst. Growth, 70 (1984) 78-93.

[34] C. Amatore, S. Szunerits, L. Thouin, J.-S. Warkocz, The Real Meaning of Nernst's Steady Diffusion Layer Concept under Non-Forced Hydrodynamic Conditions. A Simple Model Based on Levich's Seminal View of Convection, J. Electroanal. Chem., 500 (2001) 62-70.

[35] J.N. Butler, Electrochemistry in Dimethyl Sulfoxide, J. Electroanal. Chem., 14 (1967) 89-116.

[36] G.I. Egorov, A.M. Kolker, The Thermal Properties of Water-N,N-Dimethylformamide Solutions at 278–323.15 K and 0.1–100 Mpa, Russian Journal of Physical Chemistry A, 82 (2008) 2058-2064.

6. A Thermostated Cell for Electrochemistry: Minimising Natural Convection and Investigating the Role of Evaporation and Radiation

Overview

An optimised thermostated electrochemical cell is designed and implemented. This is informed by experimental and computational studies characterizing the extent to which the thermostating of an electrochemical cell via a heated bath can be realised, covering the cases with the cell closed and open to the environment. The heat transfer in the system is simulated and probed experimentally; special emphasis is put on heat loss due to radiation and evaporation. Experiments and simulations demonstrate that these two mechanisms of heat transfer lead to a steady temperature in the cell that differs from that of the thermostat by ~ 0.1 K. Simulations indicate that spatial inhomogeneities in the stationary temperature drive natural convective flows with a significant velocity. These new physical insights inform the design of a new electrochemical cell and its application.

6.1. Introduction

As we have stressed in the preceding chapters, precise electrochemical measurements require rigorous thermostating [1] because the probed processes and quantities such as diffusion coefficients and rate constants are typically highly sensitive to temperature, see for instance Refs. [2-7]. Moreover, as we have shown in Chapters 4 and 5, temperature gradients arising from imperfect thermostating have the potential to generate non-negligible natural convective flows in solutions that would otherwise be presumed quiescent. Thus, temperature variations can potentially invalidate the 'standard' assumption that mass transport is purely diffusive in the absence of external stirring, thereby leading to incorrect interpretation of electrochemical data.

In this chapter, we[11] first perform experiments and simulations in order to establish the key factors in the evolution of temperature in a model electrochemical system - a cylindrical cell containing the solution under study immersed in a thermostated water bath; to make the approach described in Chapter 1 applicable here, we only consider small initial differences in temperature ($\sim$ 1 K) between the cell and the thermostat. Our observations of this system demonstrate the time scale for reaching a steady temperature distribution and indicate that the main factors controlling the heat transfer are natural convection, thermal conduction and radiation, as well as evaporation. Experimental data demonstrates the important physical insight that even for a 'model' system, the temperature of the cell can differ measurably from that of the heated bath used for thermostating the cell and that the said difference ranges from 0.05 to 0.2 K depending on the exact experimental details. As heat is transferred through the walls of the cell and is radiated – or transferred via evaporation in an open system – away from the top boundary, the temperature distribution remains inhomogeneous even at the steady state.

Moreover, we show through simulation that the influence of gravity gives rise to buoyancy flows broadly similar to those in the extensively studied Rayleigh–Bénard problem that concerns flows between horizontal solid surfaces [8]. Consequently, the thermostated cell tends not towards a quiescent state but a convective stationary one with a non-zero flow velocity. An important physical insight provided by the experiments is that, unless heat transfer through evaporation and radiation is eliminated, the solution temperature approaches a steady non-homogeneous distribution which locally differs from the desired temperature by ~ 0.1 K. Simulations predict that those temperature inhomogeneities sustain convective flows with velocities of $\sim 10^{-4}$ m·s^{-1}, implying that the assumption of

[11] The work in this chapter was done in collaboration with X. Li, C. Batchelor-McAuley and R.G. Compton. The home-made thermostated cell was designed by X. Li, C. Batchelor-McAuley and R.G. Compton; the experimental data presented here was obtained by X. Li and C. Batchelor-McAuley.

purely diffusional mass transport needs to be critically assessed even for thermostated systems having the vertical dimensions of the ones considered here.

Having gained that insight into the important factors that control the thermostating of an electrochemical cell, we provide a set of criteria for effective cell thermostating and design a cell that fulfils them. Proof-of-concept experiments for the characterization of nanoparticulate suspensions were then performed at different temperatures with this novel cell. The experiments applied the so-called 'nano-impact' technique [9], which in this case consists in measuring the current generated by the destructive oxidation of individual nanoparticles at a microelectrode. More information on the nano-impact experiments are given in the paper associated with this chapter; as natural convection was not accounted for in the interpretation of data from them, they fall outside the scope of this thesis and we will not discuss them further.

Thermostating measurements

The model experimental system was a cylindrical container with 10 mL of deionized water, illustrated schematically in Figure 6.1. The inner and outer radii of the cell were r_{in} = 1.15 cm and $r_{out} = r_{in} + d_{wall}$, where d_{wall} = 0.9 mm, respectively. The cell was thermostated via a bath containing 1 L of water that was magnetically stirred and heated from below via a thermostat (Stuart Stirrer Hotplate UC 152 Ceramic plate with an SCT1 Digital Contact Thermometer). The temperature in the cell was recorded at a point situated on the cylinder axis at the vertical midpoint of the column of liquid; this was done continuously via a temperature probe (PT100 Sensor, R.S. Components Ltd, Corby, UK) over a period t_{exp} of between 560 and 600 s; the temperature of the water in the bath was measured thereafter and this value was used for $T_{thermostat}$. The temperature of the water in the bath was monitored and controlled continuously via a digital temperature controller (SCT1 Digital contact thermometer). The thermostating experiment in the closed cell was carried out by sealing the cell with a cap which had an opening in the middle where

the probe was tightly held, while for the open-cell measurements no cap was used and the probe itself was clamped.

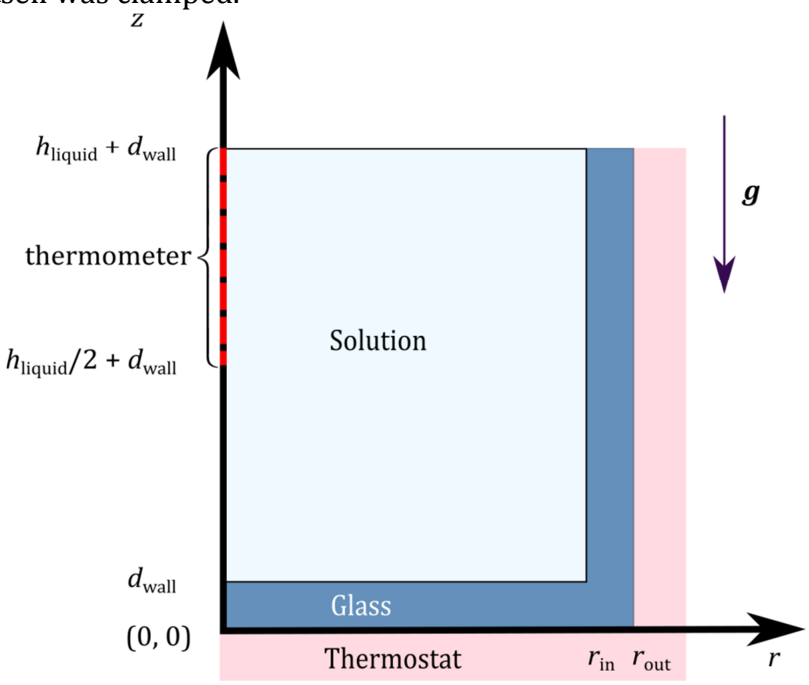


Figure 6.1. Sketch of the model. The solution is in a cylindrical container of wall thickness d_{wall}, inner radius r_{in} and outer radius $r_{out} = r_{in} + d_{wall}$; the bottom surface of the container is centred at $(r, z) = (0, 0)$ and the solution|air interface is at $z = h_{liquid} + d_{wall}$. The temperature at $(r, z) = (0, h_{liquid}/2 + d_{wall})$ is measured via a thermometer probe.

A control experiment was performed in a 10 mL aqueous solution containing 10 mg sodium dodecyl sulphate (SDS, Fluka). Since even a small quantity of surfactant can cause the liquid surface to behave as a no-slip boundary [10], this serves as a test for the appropriate interfacial hydrodynamic boundary condition. Furthermore, the mass of the liquid in the cell was measured before the start of a thermostating experiment performed with it open to the environment and after its conclusion; this data was used in quantifying the mass flux due to evaporation. Additionallly, the mass of both a sealed and an open unthermostated cell was measured continuously with an analytical balance over a 10-minute period.

Design of the homemade thermostat system

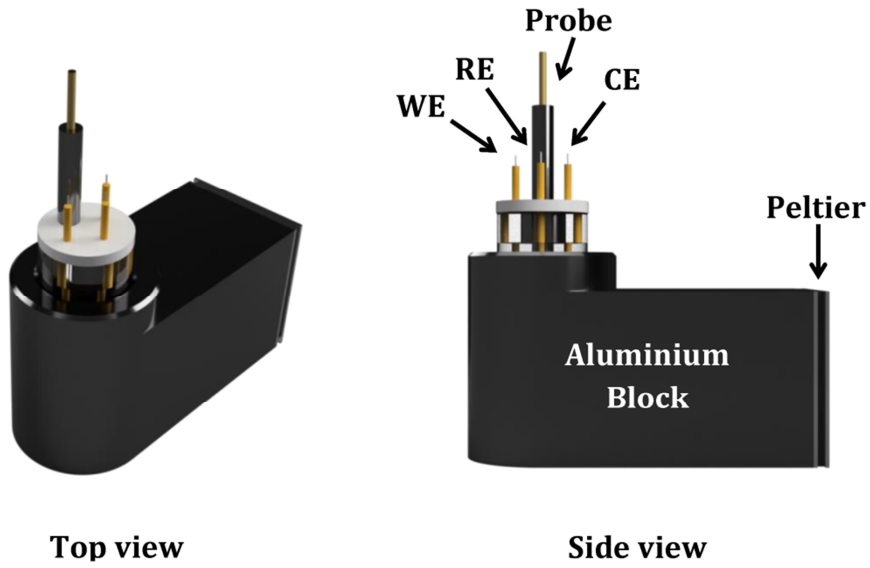


Figure 6.2. Schematic of the homemade thermostat system. WE, RE and CE represent the working electrode, reference electrode and counter electrode respectively. The probe together with the three electrodes was immersed in the electrochemical cell and the latter was warmed up or cooled down through direct contact with the aluminium block whose temperature is controlled by a Peltier element.

The homemade thermostat system (Figure 6.2) was fabricated using a Peltier-effect heat pump (type ETH-127-14-15-RS, supplied by R. S. Components Ltd, Corby, UK), 40 mm × 40 mm in area and 3.9 mm thick, with a maximum cooling capacity of 58.6 W and a maximum temperature difference of 65 K. The sample holder was an aluminium block with a cylindrical hole of diameter 22 mm and height 40 mm. A glass cell with a slightly smaller diameter than the hole was placed in the holder. The temperature of the solution in the glass cell was then monitored by the temperature probe (same as above) immersed in the solution. A proportional-integral-derivative (PID) loop script written in Python 3.5 controlled the Peltier element and the solution temperature. The homemade thermostat system was tested by changing and controlling the temperature of 10 mL H_2O from room temperature to 25°C and 35°C. For comparison, similar experiments were also

conducted with a conventional water bath-thermostat in which the cell was thermostated in a bath containing 1 L of water that was magnetically stirred and heated from below via a hotplate (Stuart Stirrer Hotplate UC152 Ceramic Plate). For numerical data on the comparison between the two thermostating systems, see Section C.7 and specifically Figure C.9 in Appendix C. As described above, the temperature in the cell was continuously recorded with a temperature probe (PT100 Sensor, R.S. Components Ltd, Corby, UK), and that of the bath was monitored and controlled via a digital thermometer (SCT1 Digital contact thermometer).

6.2. Theoretical model

The solution is thermostated via heat transfer through the glass wall of the cell, and as the heat conductivity of the latter is comparable to that of the liquid ($\kappa^{\mathrm{L}} \sim 0.6\ \mathrm{W{\cdot}m^{-1}{\cdot}K^{-1}}$ and $\kappa^{\mathrm{S}} \sim 1\ \mathrm{W{\cdot}m^{-1}{\cdot}K^{-1}}$), it would not be justified to assume thermal equilibrium between the solid phase and the water bath. Thus, we need to solve the heat equation for the temperature of the solid (T^{S}),

$$\partial_t T^{\mathrm{S}} = \chi^{\mathrm{S}} \nabla^2 T^{\mathrm{S}}, \tag{6.1}$$

where χ^{S} is the thermal diffusivity of the glass.

The temperature of the liquid phase (T^{L}) is governed by the convective heat equation,

$$\partial_t T^{\mathrm{L}} + \boldsymbol{v} \cdot \nabla T^{\mathrm{L}} = \chi^{\mathrm{L}} \nabla^2 T^{\mathrm{L}}, \tag{6.2}$$

where t is time, $\boldsymbol{v}$ – the velocity of the fluid and $\chi^{\mathrm{L}} = \kappa^{\mathrm{L}}/\left(\rho_0^{\mathrm{L}} C_p^{\mathrm{L}}\right)$ denotes its thermal diffusivity, with C_p^{L} – being its specific heat capacity at constant pressure [$\mathrm{J{\cdot}kg^{-1}{\cdot}K^{-1}}$], ρ^{L} – its density, and ρ_0^{L} – the value of the latter at its initial temperature, $T_{\text{solution }0}$; below, we refer to the overall temperature distribution in the system as T. As the velocity appears in the heat equation (6.2), to determine the temperature, we also need to solve the continuity and Navier-Stokes equations that govern the flow in the system. We employ the following approximate form of the latter:

$$\rho_0^{\mathrm{L}}(\partial_t \boldsymbol{v} + \boldsymbol{v} \cdot \nabla \boldsymbol{v}) = -\nabla \Delta p + \eta \nabla^2 \boldsymbol{v} - \rho_0^{\mathrm{L}} \alpha (T^{\mathrm{L}} - T_{\text{solution }0}) \boldsymbol{g}, \tag{6.3}$$

$$\nabla \cdot \boldsymbol{v} = 0; \tag{6.4}$$

where $\boldsymbol{g}$ is the acceleration due to gravity, η – the viscosity of the liquid, $\alpha = -(\partial \rho^{\mathrm{L}} / \partial T)_p / \rho^{\mathrm{L}}$ is its coefficient of thermal expansion at $T_{\text{solution }0}$; Δp is the pressure difference with respect to the hydrostatic pressure in the unperturbed liquid, $\Delta p = p - p_{\text{ref}} + \rho_0^{\mathrm{L}} |\boldsymbol{g}| (z - h_{\text{liquid}} - d_{\text{wall}})$ with p_{ref} being a reference value, and z – the normal coordinate. Eqs. (6.3)-(6.4), adopt the Boussinesq approximation [11], treating the solution density as a linear function of temperature in the buoyancy term in the Navier-Stokes equation and as constant elsewhere. Following the standard Boussinesq approach, which is valid at $|\alpha(T^{\mathrm{L}} - T_{\text{solution }0})| \ll 1$ [12], we neglect the temperature-dependence of all other properties of the liquid. We seek numerical solutions to equations (6.1)-(6.4) via the finite-element modelling software COMSOL Multiphysics® 5.3.

We treat the cell as a perfect cylinder and assume that the velocity and temperature distributions are rotationally symmetric. Accordingly, when using cylindrical coordinates, r and z, we only need to solve the problem for the 2-dimensional region pictured in Figure 6.1. We define the coordinates so that the positive z direction coincides with the symmetry axis of the cell and is aligned contrary to the vector of gravitational acceleration $\boldsymbol{g}$, as illustrated in the figure. The geometry of the glass container in the model approximately matches that of the experimental cell, having inner and outer radii of r_{in} and $r_{\text{out}} = r_{\text{in}} + d_{\text{wall}}$. The cell contains 10 mL of water, corresponding to a fluid column of height $h_{\text{liquid}} = 2.41$ cm. We only consider the heat transfer in the part of the solid cell that is in contact with the fluid, i.e., $z \in [0, h_{\text{liquid}} + d_{\text{wall}}]$. The temperature of the liquid is recorded at the tip of the thermometer, $T_{\text{probe}} = T^{\mathrm{L}}(r = 0, z = h_{\text{liquid}}/2 + d_{\text{wall}})$; in the present model, the latter is an infinitesimally thin line at $r = 0$ and $z \in [h_{\text{liquid}}/2 + d_{\text{wall}}, h_{\text{liquid}} + d_{\text{wall}}]$.

Initially, the temperature within the solution and the glass container is homogeneous and differs by $\Delta T = T_{\text{thermostat}} - T_{\text{solution }0} \sim 2$ K from that of the thermostat. We assume that the temperature of the stirred water bath is homogeneous and fixed at $T_{\text{thermostat}} = 298.15$ K throughout the experiment. Thus, at all times, the temperature of the outside walls of the container is

$$T^{\mathrm{S}}\big|_{r\in[0,\,r_{\mathrm{out}}],z=0} = T^{\mathrm{S}}\big|_{r=r_{\mathrm{out}},z\in[0,h_{\mathrm{liquid}}+d_{\mathrm{wall}}]} = T_{\mathrm{thermostat}}. \tag{6.5}$$

We make use of three types of boundary conditions for the top boundary of the cell. The first one corresponds to the limiting case in which the cell is thermally insulated and there is no normal heat flux through the surface $z = h_{\mathrm{liquid}} + d_{\mathrm{wall}}$,

$$\kappa^{\mathrm{L}}\,\partial_z T^{\mathrm{L}}\big|_{r\in[0,r_{\mathrm{in}}],z=h_{\mathrm{liquid}}+d_{\mathrm{wall}}} = 0 \text{ and} \tag{6.6}$$

$$\kappa^{\mathrm{S}}\,\partial_z T^{\mathrm{S}}\big|_{r\in[r_{\mathrm{in}},r_{\mathrm{out}}],z=h_{\mathrm{liquid}}+d_{\mathrm{wall}}} = 0. \tag{6.7}$$

As the top of the experimental cell is not in fact thermally insulated, a more realistic boundary condition for $z = h_{\mathrm{liquid}} + d_{\mathrm{wall}}$ has to consider the heat transfer with the environment. Here, we assume that Eq. (6.7) remains valid, but the liquid loses heat via grey-body radiation, corresponding to a heat flux of

$$\kappa^{\mathrm{L}}\,\partial_z T^{\mathrm{L}}\big|_{r\in[0,r_{\mathrm{in}}],z=h_{\mathrm{liquid}}+d_{\mathrm{wall}}} = -\varepsilon\sigma(T^4 - T^4_{\mathrm{ambient}})\big|_{r\in[0,r_{\mathrm{in}}],z=h_{\mathrm{liquid}}+d_{\mathrm{wall}}}, \tag{6.8}$$

where ε = 0.96 is the emissivity of pure water [13], σ = 5.67×10^{-8} W·m^{-2}·K^{-4} is the Stefan-Boltzmann constant, and T_{ambient} = 296.15 K is the temperature of the air in the laboratory. If the liquid is close to thermal equilibrium with the thermostat, Eq. (6.8) gives an outward flux of approximately 11.4 W·m^{-2}. Strictly viewed, Eq. (6.8) is a gross approximation as it is only valid for heat transfer to an infinite medium whose temperature is homogeneous and equal to T_{ambient}. In the real system, if the cell is sealed, the liquid is in direct contact with only a small volume of air that is separated from the outer environment by the cap. Furthermore, there are contributions to heat transfer not just from radiation but also from convection in the gas; however, as shown below, our treatment leads to satisfactory agreement with the experimental data.

Lastly, when simulating experiments in which the cell is open to the environment and evaporation takes place, it is necessary to account for the heat loss due to evaporation. Weighing the system before and after the experiment indicates that conducting the experiments with a cell open to the environment results in a mass loss Δm of approximately 4 mg, in contrast with the case of a sealed cell, whose mass remains constant within 0.1 mg. The mass loss due to evaporation in an

open cell corresponds to a considerable heat flux from the cell to the environment – the heat loss is $\Delta H = \Delta H_{\mathrm{e}}^{\mathrm{L}} \Delta m$, where $\Delta H_{\mathrm{e}}^{\mathrm{L}}(T = 298.15\ K) = 2.44\ \mathrm{kJ \cdot g^{-1}}$ is the vaporization enthalpy of water [14]. The temperature of the liquid would change by approximately $\Delta T_{\mathrm{evaporation}} = \Delta H / \left(V \rho_0^{\mathrm{L}} C_p^{\mathrm{L}}\right) \approx 0.2$ K (where V is its volume), if it lost the same amount of heat via a quasi-static process in the absence of thermostating. This considerable outward heat flux can be expected to have a strong effect on the temperature distribution in the cell, and we include it in the model by imposing a constant heat flux at the surface,

$$\kappa^{\mathrm{L}}\, \partial_z T^{\mathrm{L}}|_{r \in [0, r_{\mathrm{in}}], z = h_{\mathrm{liquid}} + d_{\mathrm{wall}}} = -\frac{\Delta H_{\mathrm{e}}^{\mathrm{L}} \Delta m}{\pi r_{\mathrm{in}}^2 t_{\mathrm{exp}}} \approx -39.2\ \mathrm{W \cdot m^{-2}}. \tag{6.9}$$

Eq. (6.9) is an approximate value of the heat flux averaged over the area of the interface and the duration of the experiment; thus, it ensures that the total amount of heat transferred due to evaporation in the model and the experiments is identical. A more detailed account of the evaporative heat flux would require modelling additional effects, such as the mass transport of vapour in the air surrounding the cell and would thus go outside the scope of the current study. Furthermore, the use of a condition for constant flux is indirectly supported by measurements of the mass of an open *unthermostated* cell as a function of time - in these experiments, the total mass of the liquid m decreases approximately linearly with t. However, we should note that these $m(t)$ measurements are conducted under conditions different from those for the thermostating experiments, which may affect the evaporative flux.

At the solid-liquid boundaries, the temperature and the conductive heat flux are continuous; the assumed symmetry of the system dictates that the radial flux is equal to zero at $r = 0$. These conditions are handled by the COMSOL Multiphysics® *Heat Transfer in Fluids* interface, which for the simulations discussed here utilizes quadratic elements for the temperature distributions T^{L} and T^{S}.

For the hydrodynamic problem, we assume that initially, the fluid is at rest and $\Delta p = 0$ throughout it. At the liquid|solid interfaces, including the thermometer probe, we impose no-slip boundary conditions at all times,

$$\boldsymbol{v}|_{r\,=\,0, z\,\in\,[h_{\mathrm{liquid}}/2\,+\,d_{\mathrm{wall}}, h_{\mathrm{liquid}}\,+\,d_{\mathrm{wall}}]} = \boldsymbol{v}|_{r\,=\,r_{\mathrm{in}}, z\,\in\,[d_{\mathrm{wall}}, h_{\mathrm{liquid}}\,+\,d_{\mathrm{wall}}]} = \boldsymbol{v}|_{r\,=\,\in[0, r_{\mathrm{in}}], z=\,d_{\mathrm{wall}}} = \mathbf{0}\,. \tag{6.10}$$

Furthermore, we assume that the velocity in the fluid is not affected by mass transport through the surface $z = h_{\mathrm{liquid}} + d_{\mathrm{wall}}$; therefore, we restrict v_z to 0 there. As in the heat transport problem, symmetry imposes a condition, at r = 0, in this case, v_r = 0; analogously, this condition is built-in in the COMSOL Multiphysics® *Laminar Flow* interface. We utilize quadratic elements for the velocity components and linear ones for the pressure in the hydrodynamic problem; this combination is known as P_2 + P_1, see [15]. Since we treat the fluid as incompressible, only the gradient of the pressure is physically meaningful [16]. Thus, it is possible to ease the numerical solution of the problem via offsetting Δp by a function of time and we do so through imposing the constraint $\Delta p(r = r_{\mathrm{out}}, z = h_{\mathrm{liquid}} + d_{\mathrm{wall}}) = 0$.

Next, we turn to the stress balance at the liquid|gas interface. We neglect curvature effects at the interface, and treat it as planar; as we prescribe the shape of the surface, we cannot impose a local balance of stress in the normal direction [17]. As for the surface tangential stress, here we model it via two types of boundary conditions for the velocity profile at the liquid|gas interface. The first of these is a constraint known as a free-surface boundary condition [18], which is a form of tangential mass balance at the interface that neglects the viscous stresses in the gas phase on account of it having a much lower velocity than the liquid, leading to the form

$$\eta(\partial_r v_z + \partial_z v_r)|_{r\in[0,r_{\mathrm{in}}],z=h_{\mathrm{liquid}}+d_{\mathrm{wall}}} = 0, \tag{6.11}$$

where it follows from the condition we impose on v_z at the interface that the first term in parenthesis is identically zero.

In general, the right-hand side of the tangential stress balance (6.11) contains the gradient of the surface tension γ, $\mathrm{d}\gamma/\mathrm{d}r = \partial_T\gamma \cdot \partial_r T^{\mathrm{L}}|_{z=\,h_{\mathrm{liquid}}+\,d_{\mathrm{wall}}}$, which could potentially drive a Marangoni flow [18]. We do not consider Marangoni flows here in the interest of simplicity; moreover, as previous studies on similar topics have shown, the thermal Marangoni effect that the radial temperature gradient at $z = h_{\mathrm{liquid}} + d_{\mathrm{wall}}$ induces can be completely suppressed in the presence of a surface-active contaminant. Hu and Larson [19] have demonstrated that for an evaporating sessile droplet, this happens at adsorptions as low as $5\mathrm{x}10^{-10}$ mol·m^{-2}.

Furthermore, Marangoni flows typically dominate in thin layers [18] rather than enclosures such as ours whose vertical and lateral dimensions are similar. We can assess the relative contributions of the surface-tension and buoyancy-driven flows by calculating the dimensionless criteria controlling the two, respectively the Marangoni and Rayleigh numbers, $Ma = |\partial_T \gamma| h_{\text{liquid}} |\Delta T| / (\eta_0 \chi^{\text{L}})$ and $Ra = \left(\rho_0^{\text{L}} \alpha h_{\text{liquid}}^3 |\Delta T| |\boldsymbol{g}|\right) / (\chi^{\text{L}} \eta_0)$. The ratio between them quantifies the relative importance of the two effects, see e.g. Keller and Bergman[20] and its low value, $Ma/Ra = |\partial_T \gamma| / \left(\rho_0^{\text{L}} \alpha h_{\text{liquid}}^2 |\boldsymbol{g}|\right) \approx 0.11$ (consult Section C.1 in Appendix C for values of the parameters), justifies neglecting the Marangoni flow.

Due to the ubiquity of surface-active contaminants, in many cases liquid surfaces behave as no-slip boundaries instead of free ones, see Refs. [10] and [20]. For this reason, we also consider the contrasting limiting case of a no-slip boundary,

$$\boldsymbol{v}|_{r \in [0, r_{\text{in}}], z = h_{\text{liquid}} + d_{\text{wall}}} = 0\,. \tag{6.12}$$

Note that even at the small ΔT considered here, the experimental system is strongly driven, with Rayleigh numbers *Ra* ranging from 3.3×10^5 to 5.4×10^5 in the experimentally studied interval for ΔT, [1.3, 2.3] K. Thus, the flows may no longer fulfil the assumption for axial symmetry upon which the model is based – see e.g. Ref. [21], where the transition to 3-D flows in a cylinder with a partially heated lateral walls and cooled horizontal walls is studied. However, our approximate treatment as outlined above fulfils the present study's aims for semi-quantitative agreement between simulation and experiment.

A useful characteristic of a convective flow is the magnitude of its velocity averaged over the whole volume of the liquid *V* as per the equation

$$|\boldsymbol{v}_{\text{av}}| = \frac{1}{V} \int_V \sqrt{v_r^2 + v_z^2}\, \mathrm{d}V. \tag{6.13}$$

6.3. Results

The following section considers the thermostating of an electrochemical cell with a water bath, first with the cell sealed and then with it open to the environment. First, we probe the heat transfer in the system through numerical simulation and model

experiments. Then, we formulate a set of design criteria on the basis of observations from both, and develop a thermostating system that fulfils them.

6.3.1. Thermostating a closed cell

A model thermostating experiment was performed by immersing a glass vial containing 10 mL of de-ionised water into a water bath set at 298.15 K; the temperature of the liquid in the vial was initially lower than that of the heated bath by 1.3 K. The vial was sealed with a cap and the temperature of the liquid inside it monitored as a function of time.

The results for the difference between the temperature of the thermostated water bath and that of the probe ($\Delta T_{\text{probe}} = T_{\text{thermostat}} - T_{\text{probe}}$) are plotted in Figure 6.3; two key observations can be made from this graph. First, it takes approximately 300 s for the probe to reach a temperature within 0.1 K of that of the bath. Second, even for this closed cell, the temperature of the water inside the vial does not become equal to that of the water bath even after thermostating for $t_{\text{exp}} = 600$ s – the temperature of the water in the vial stabilises to approximately 0.1 K below that of the water bath. The latter was measured with the probe used for recording the temperature in the cell at the end of the experiment; this confirms that the discrepancy is not associated with the accuracy of the thermometer monitoring the water bath temperature.

Importantly, the magnitude of this discrepancy between the temperatures of the two environments at steady state is sensitive to the vertical position of the vial within the water bath. As shown in Appendix C (Section C.5), immersion of the cell further into the water bath enables the temperature difference to be decreased to a magnitude of ca. 50 mK, but not fully eliminated. This sensitivity to the cell depth demonstrates that the temperature of the glass vial above the internal water line can have a non-negligible and measurable influence on the temperature control of a sample; it also suggests that, contrary to the assumption our model, the

temperature distribution in the water bath is not homogeneous. However, we do not consider either effect in the present semi-quantitative treatment of the problem.

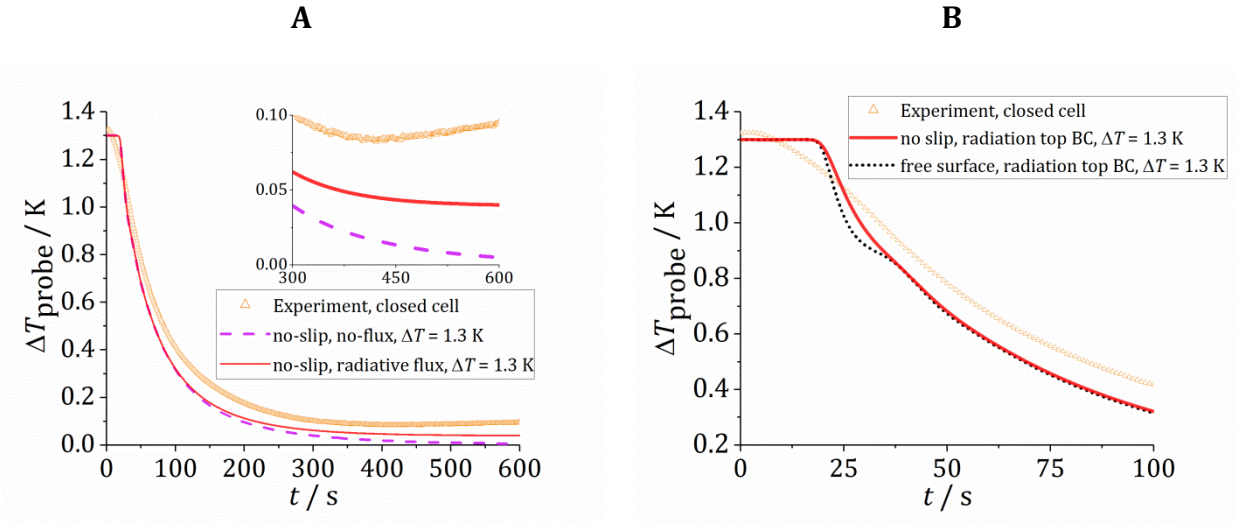


Figure 6.3. Difference between the temperature of the thermostat and that at the measurement point ($\Delta T_{probe} = T_{thermostat} - T^L(r = 0, z = h_{liquid}/2 + d_{wall})$) as a function of time at an initial ΔT of 1.3 K. **A**. Comparison of experimental data (points) and simulations with a no-slip boundary having 1) a no-flux boundary condition (dashed line) and 2) a radiative heat flux condition at the liquid|air interface (solid line). Note that the simulation with boundary condition for thermal insulation predicts that the solution temperature asymptotically tends towards $T_{thermostat}$, whereas the one with radiative heat flux predicts a temperature difference close to the experimentally observed one. **B**. Plot of the experimental data from **A** at short times and calculated values for simulations with radiative heat flux, 1) a no-slip hydrodynamic boundary condition (solid line) and 2) a free-surface one (dashed line). The free-surface simulation predicts fluctuations in ΔT_{probe} that are not observed experimentally; both curves go through several inflections (see text), although this is not clearly visible at this scale for the one with a no-slip boundary condition. Note that the choice of boundary condition for the hydrodynamic problem has only a minor effect on the measured temperature and that its influence is insignificant beyond $t \approx 50$ s; the comparison with experimental data suggests that a no-slip condition is more appropriate.

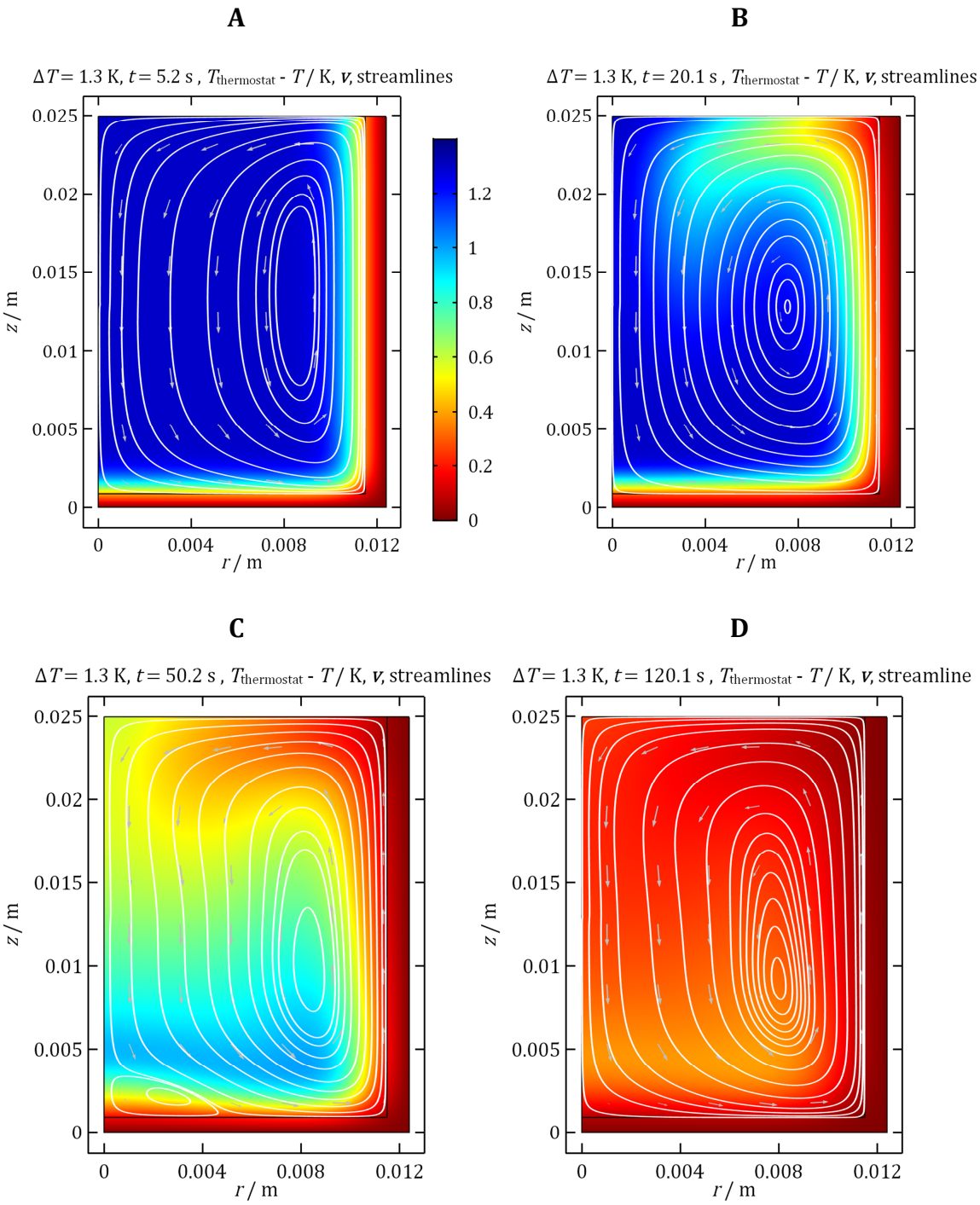


Figure 6.4. Temperature distribution, streamlines and arrow plot of the velocity field for a simulation with a no-slip surface, a boundary condition for radiative heat transfer through the liquid|gas interface and ΔT = 1.3 K. In each plot, the length of the arrows is proportional to the local value of $|\boldsymbol{v}|$, but the proportionality constant varies between frames. Note the evolution of the flow pattern and the direction of the main flow, the latter being dictated by the heating at the cell wall $r = r_{\text{out}}$. Heat

exchange causes the fluid density to become lower in the vicinity of the inner cell wall, leading to a positive local v_z and an anticlockwise flow in the shown region.

The experimental data in Figure 6.3A is overlaid with results from simulations performed with a no-slip hydrodynamic boundary condition. The model correctly predicts the time scale for approaching a thermal steady state and satisfactory agreement is observed between the experimental and simulated curves.

The model accounts for the conduction of heat across the glass walls of the cell and convective heat transfer in the internal aqueous environment, whereas the temperature of the water bath is taken to be homogeneous and independent of time. If we impose a condition for zero heat flux at the liquid|gas interface, the model predicts that the temperature of the cell asymptotically approaches the temperature of the heated bath. If instead we assume the radiative heat flux condition (6.8) at the interface, the balance between heat lost to radiation and gained from the water bath leads to a predicted temperature difference of ≈ 0.04 K at $t = t_{\text{exp}}$. This value is in agreement with the one measured experimentally for a cell deeply immersed (Appendix C.5) into the water bath and demonstrates that even for a closed cell system imperfections in the thermostat and radiative heat flux can lead to a measurable difference in the temperature between the cell and the water bath. As we noted in Section 6.2, applying the radiative flux (6.8) here is a gross approximation since the real system involves heat transfer through convection and conduction in the gas phase in contact with the liquid, which may be comparable or more intense to that due to radiation. Furthermore, heat transfer in the gas phase would diminish the difference $T^4 - T_{\text{ambient}}^4$ and thus the radiative flux itself. However, the absence of quantitative data on the heat flux through the liquid|gas interface makes it difficult to establish how accurate (6.8) is for the present system. As we do not intend to simulate the heat transfer in the surroundings of the cell for the purpose of the present semi-quantitative study, we assume that Eq. (6.8) is applicable.

The correspondence between the simulated and experimental results suggests that the present model correctly accounts for the main factors at play. With that in mind, we next turn to examine some of the features of the flow and heat transfer for the simulations with radiative heat flux and a no-slip boundary condition at the liquid|gas interface as illustrated in Figure 6.3. The primary observation is that the rate at which the cell approaches a steady temperature distribution is chiefly determined by the thermal convective flows thermostating induces in the cell. For example, if we completely neglect convection and simulate only the conductive heat transfer with a radiative flux boundary condition at the liquid|gas interface at ΔT = 1.3 K, ΔT_{probe} diminishes to within 0.1 K over a time scale of approximately 475 s, in sharp contrast with the ≈ 213 s predicted by the simulation of the same case that includes natural convection and a no-slip boundary condition.

The simulated curve in Figure 6.3, corresponding to ΔT = 1.3 K and radiative heat transfer, has a shallow maximum at short times ($t \approx 15.5$ s) – this is due to the heat loss through radiation – for this particular initial condition, the solution is warmer than the air at t = 0 and loses heat to it in accordance with Eq. (6.8). However, the magnitude of the maximum in question ($T - T_{\text{solution }0} \sim 5\times10^{-5}$ K) is well below the accuracy of the experimental data and we therefore disregard it. More importantly, the curve goes through four inflections in the interval $t \in$ [15 s, 5 s] that are not observed experimentally. These inflections are much more pronounced for the simulation with a free-surface boundary condition, as illustrated in Figure 6.3B, and are not seen in the experimental data, suggesting that the no-slip boundary condition is the more adequate one for the problem under study. Since the curvature of the line in that region is close to zero, the inflections in question are not easily visible even in Figure 6.3B, which zooms into the region of short times. As discussed above, a no-slip boundary condition is appropriate for experiments conducted in the presence of a surfactant; the fact that no qualitative difference in ΔT_{probe} is seen when the measurements we performed in that way is additional evidence that even the surface of distilled water behaves as a no-slip boundary.

The reason for the predicted disturbances in ΔT_{probe} is that the flow field undergoes complex evolution during that period. Figure 6.4 shows the distributions of T and $\boldsymbol{v}$ together with the streamlines of the flow. After an induction period in which convection does not affect the heat flow significantly (Figure 6.4A), the heating from the sides and the bottom generates a convective cell with anticlockwise motion in the studied region. This circulatory flow carries a warm front at the upper part of the cell radially inward towards the cylinder axis and downwards (Figure 6.4B). At $t \sim 30$ s, the system transitions from a regime with a single convective cell occupying the simulated region to one with a secondary counterrotating cell in the vicinity of the cylinder axis (compare Figure 6.4 B and C). The presence of the latter cell distorts the streamlines of the flow and hence also the heat flux at $r \sim 0$, thus perturbing the temperature at the probe. At long times ($t \gtrsim 120$ s), the warm fronts carried by the two convective cells meet and after their merging, the cell is again occupied by a single convective roll with anticlockwise motion in the studied region.

A qualitatively similar transient flow field has been observed by Lemembre and Petit [22], who studied the case of a cylinder with heated side walls, a cooled top wall and an insulated bottom wall. In contrast with the system they studied, in ours, the extent of the secondary flow is limited by the presence of the thermometer probe and the no-slip boundary condition imposed on it.

The disturbances in ΔT_{probe} generated by the changes in the flow described above are more significant for the free-surface system as the average flow velocity in the solution is higher in this case (see Figure C.7 in Section C.6), causing the temperature to be more strongly perturbed by the development of the velocity distribution than for a no-slip surface, as Figure 6.3B illustrates. A simple analysis given in Appendix C.2 indicates that perturbations such as those for the free-surface case could be recorded by our experimental equipment if they arose in the real system. As this is not the case, hereafter we exclusively discuss results obtained with a no-slip surface condition. It should be borne in mind, though, that ΔT_{probe} in the present model may be more prone to disturbances than in reality, as the

experimentally measured temperature is averaged over an area rather than recorded at a single point.

Notably, even for this closed-cell system, the radiative flux of heat from the top surface provides a driving force for convection at all times, causing the liquid to tend towards a stationary state with a non-zero velocity field and a spatially inhomogeneous temperature. Furthermore, the cooling of the upper layer of fluid due to the radiative flux leads to a configuration unstable with respect to convection and sustains circulation throughout the whole cell. Thus, regardless of the initial temperature difference, the system tends to a convective stationary state and at t = 600 s, the simulations predict local differences $T_{\text{thermostat}} - T^{\text{L}}$ of up to ~ 0.1 K and a single roll that occupies the whole cell and has a maximum local velocity of ~ 3×10^{-4} m·s^{-1}. The local temperature difference is largest in the vicinity of the point (r, z) = (0, d_{wall} + h_{liquid}), and the velocity is maximal in the vicinity of the temperature probe (r, z) = (0, d_{wall} + $h_{\text{liquid}}/2$).

Increasing the initial temperature difference ΔT qualitatively changes the observed flow patterns and thus also affects the simulated ΔT_{probe}. At ΔT = 1.8 K, the secondary convective cell at r = 0 and $z \sim d_{\text{wall}}$ becomes more distorted along the z-axis, forming an elongated roll. This secondary roll carries warm fluid from the heated wall surface to a considerably greater height than at ΔT = 1.3 K and thus perturbs the temperature distribution more strongly (see Figure C.4 in Appendix C.3), leading to greater changes in the curvature of $\Delta T_{\text{probe}}(t)$ and three inflections. As at ΔT = 1.3 K, at long times ($t \sim$ 150 s), the flow reverts to a single convective cell through the merging of the main and secondary rolls, the difference being that the velocity in the secondary cell exceeds that in the main one at intermediate timescales, explaining the stronger effect on ΔT_{probe}. Appendix C.3 contains a comparison of the simulated and measured $\Delta T_{\text{probe}}(t)$ at ΔT = 1.8 K, as well as additional data on the distributions of T and $\boldsymbol{v}$ at ΔT = 1.8 K.

6.3.2. Thermostating an open cell

After highlighting the complexities in thermostating a closed-cell system, we turn to consider the case of a cell that is open to the environment. Data for ΔT_{probe} from two such experiments at ΔT = 2.3 K where the cell has not been sealed are shown in Figure 6.5. As before, the cell approaches a stationary temperature over a time frame of approximately 600 s. However, the major difference is that at long times the measured temperature is markedly less stable and the temperature difference between the cell and the water bath is now ~ 0.2 K. This increased value of ΔT_{probe} reflects the influence of evaporation upon the system.

Figure 6.5 compares the predicted ΔT_{probe} for two simulations - one that only takes radiative heat transfer through Eq. (6.8) and one that combines it with the approximate account for the effect of evaporation on temperature through the boundary condition for constant heat flux, (6.9). As evident in the figure, the combination of Eqs. (6.8) and (6.9) predicts $\Delta T_{\text{probe}}(t_{\text{exp}}) \approx 0.15$ K, comparing better with the experiment than the value $\Delta T_{\text{probe}}(t_{\text{exp}}) \approx 0.04$ K resulting from Eq. (6.8) alone. We should note that simulations utilizing the evaporative heat flux boundary condition (6.9) predict that ΔT_{probe} initially exhibits an increase and goes through a maximum of height $T_{\text{solution }0} - T\,(t \approx 15\text{ s}) \sim 0.01$ K. This is due to the cooling effect of evaporation which is felt at the probe before the heating from the thermostat. However, the existence of this maximum cannot be ascertained from the experimental data in this study - in the initial period, the temperature recorded by the probe exhibits large fluctuations because it is briefly exposed to the air as the cell is immersed in the bath.

The cooling of the upper layers of the liquid via radiation at long times is in this case reinforced by the evaporative heat loss and the combination of them leads to sustained convective flows of greater intensity than in the case of a cell sealed to the environment. Specifically, the simulations described here predict local differences in the temperature of the cell up to $T_{\text{thermostat}} - T^{\text{L}} = 0.3$ K and maximum local velocity magnitudes of the convective flows of $\approx 8\times10^{-4}$ m·s^{-1}. As in the case with no

evaporation (see above), the flow at $t = t_{exp}$ is a single roll and its maximum velocity is in the region of the temperature probe $(r, z) = (0, d_{wall} + h_{liquid}/2)$, with the largest temperature difference in the region of the point $(r, z) = (0, d_{wall} + h_{liquid})$.

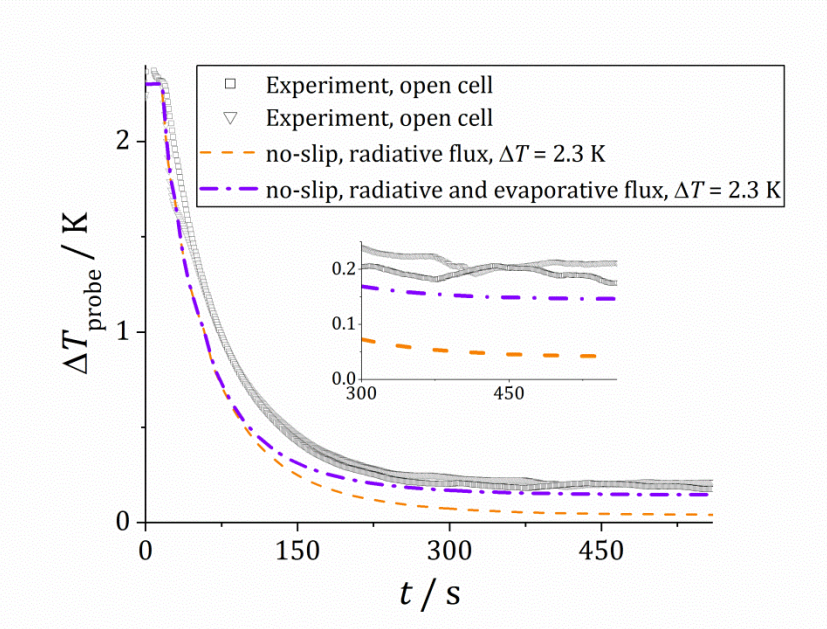


Figure 6.5. Difference between the temperature of the thermostat and that at the measurement point ($\Delta T_{probe} = T_{thermostat} - T^{L}(r = 0, z = h_{liquid}/2 + d_{wall})$) as a function of time at an initial ΔT of 2.3 K. The two sets of points correspond to experimental measurements for a cell open to the environment. Points at short t are not shown as they deviate strongly from the trend because the thermometer probe is exposed to the air when the cell is placed in the water bath. The two curves represent simulations with a no-slip surface and different thermal boundary conditions at the liquid|gas interface: 1) radiative heat flux (dashed line) and 2) radiative and evaporative heat flux (dash-dot line). The simulation that includes both evaporative and radiative heat transfer is in closer agreement with the experimental data, suggesting that the model including these two mechanisms for heat exchange is the most adequate for an open cell.

These observations and the comparison between Figure 6.5 and Figure 6.3 point to the conclusion that the heat transfer in the cells open to the environment is even more susceptible to convective effects than in sealed cells. We should also note that

evaporation can be expected to be of still greater importance for systems in which, in contrast to the present case, surface effects dominate over bulk ones, for example thin liquid layers.

6.3.3. Thermostating insights and design criteria

Several important insights can be extracted from our simulations and model experiments concerning the thermostating of open and closed-cell system. First, the simulations described here indicate that even a cell in contact with an ideal thermostat would not reach its exact desired temperature at the stationary state unless heat losses due to radiation and evaporation are eliminated. Hence, accurate reporting of a cell's temperature requires measurements to be made in the cell and not at the thermostat.

Second, since in all cases studied here these temperature differences arise from cooling of the upper layers of solution by radiative and/or evaporative mechanisms, they cause the system to tend towards a convective stationary state. These convective flows can be non-negligible, having a volume-average velocity $|\boldsymbol{v}_{av}|$ of $\sim 1\text{x}10^{-4}$ m·s^{-1} for the present system. At the end of simulated experiment, $t = t_{exp}$, simulations of a closed cell with initial temperature differences ΔT = 1.3 and 1.8 K respectively yield $\approx 6.5\times10^{-5}$ and $\approx 6.6\text{x}10^{-5}$ m·s^{-1};[12] the reason the initial condition has an influence on the final value of $|\boldsymbol{v}_{av}|$ is probably that a true steady state is not yet reached at $t = t_{exp}$. For an open cell, simulations accounting for evaporation at ΔT = 2.3 K predict that $|\boldsymbol{v}_{av}|$ reaches $\approx 1.7\times10^{-4}$ m·s^{-1} and $\approx 1.5\times10^{-4}$ m·s^{-1} with and

[12] Note that in the paper associated with this chapter, the values of $|\boldsymbol{v}_{av}|$ for ΔT = 1.3 and 1.8 K are switched because of a typographical mistake. However, the Supplementary Information to the paper (SI7, equivalent to Section C.7 here) gives the correct values. Moreover, the exact value of $|\boldsymbol{v}_{av}|$ at $t = t_{exp}$ is of little importance – what is notable is that it is influenced by the initial condition of the simulation.

without radiative heat transport, respectively – see Appendix C.6 for more details. Thus, the minimisation of evaporation by using a closed cell system is essential.

Third, the rate at which the system tends towards a steady state is mainly dictated by the convective heat transfer within it. Maintenance of a thermostated system will preferentially use forced convection between experiments to increase the rate of heat transfer and lead to an approximately homogeneous cell temperature.

A thermostating system was built on the basis of the above three design criteria. An additional desirable feature of the system was to be able to both raise and lower the temperature of the cell relative to the ambient conditions. The design of the thermostat system is described in the experimental section and a schematic of it shown in Figure 6.2. In this system, the probe together with the three electrodes is immersed in the cell directly, and the latter is sealed with a cap. During the course of the temperature control, a flow of nitrogen is used to simultaneously degas the solution and provide forced convection, ensuring an approximately homogeneous temperature distribution in the cell. Appendix C.7 presents data showing the variation of the cell's temperature as a function of time, evidencing that the thermostating of the cell is achieved within 600 s; data for a cell thermostated with a conventional water bath is also given for comparison. Studies of nanoparticulate suspensions via the nano-impact method were performed at different temperatures in the novel cell and described in the paper associated with this chapter; as these measurements are tangential to the subject of this thesis, we do not discuss them here.

6.4. Conclusions

As we have demonstrated above, even for *model* thermostating systems, the temperature of the sample being thermostated can differ markedly from that of the bath (0.1-0.2 K as measured here). Both evaporation and radiation can lead to significant cooling of the top layers of a solution. The resulting temperature

gradients cause such systems to tend to convective rather than quiescent stationary states. The volume-averaged flow velocities under such steady-state conditions can be significant – our simulations predict up to ca. 10^{-4} m·s^{-1} for the present case, specifically ~ 1×10^{-4} for a closed cell and ~ 2×10^{-4} m·s^{-1} for an open one. Note that the model described here does not include the mass transport in the cell – doing that would require solving a considerably more involved problem and thus exceed the aims of the current study. Nevertheless, we need to point out that the convective flows induced by temperature variations alone yield fluxes potentially comparable in magnitude to the diffusive ones commonly encountered in the electrochemical systems. Such flows can be expected to be of particularly high importance for macroelectrodes and processes occurring on comparatively long time scales, e.g. cyclic voltammetry performed at low scan rates. Conversely, convective effects can be reduced by employing microelectrodes [23] and/or high scan rates for cyclic voltammetry [24].

Based on our simulations and model experiments, we have formulated a set of design guidelines for thermostating, as follows.

1. The temperature of the sample needs to be measured directly as it can differ significantly from that of the heated bath.
2. Evaporation must be avoided in all cases by using a closed system. This is true even when using large (ca. mL) quantities of solution.
3. The time necessary for a cell to approach a steady state is to a large extent controlled by the convective flows in the cell. The use of forced convection to ensure a homogeneous temperature in the solution phase is advisable.

These insights are specifically useful for the design of electrochemical systems. However, the importance of heat transfer by evaporation and radiation in controlling the temperature of thermostated systems is of wider significance and can be applied to other systems that require the thermostating of a liquid phase, e.g. temperature-sensitive instrumental methods. Moreover, we need to emphasize that as the amount of solution being thermostated decreases and the area of the liquid|air interface increases relative to the volume, the importance of evaporation

in creating local temperature gradients can be expected to become ever more significant.

Additional data. Appendix C contains the following additional information: 1) details of the simulation procedure; 2) an analysis of the significance of the perturbations in ΔT_{probe} at short times; 3) data for a closed cell at ΔT = 1.8 K; 4) additional data for an open cell at ΔT = 2.3 K; 5) data on ΔT_{probe} for a cell immersed deeper in the water bath; 6) volume-averaged velocities of the observed flows; 7) comparison of thermostating systems.

6.3. References

[1] D.T. Sawyer, A. Sobkowiak, J.L. Roberts, Electrochemistry for Chemists, Second ed., Wiley, New York, 1995.

[2] A. Einstein, Über Die Von Der Molekularkinetischen Theorie Der Wärme Geforderte Bewegung Von in Ruhenden Flüssigkeiten Suspendierten Teilchen, Ann. Phys. (Leipzig), 322 (1905) 549-560.

[3] W. Sutherland, LXXV. A Dynamical Theory of Diffusion for Non-Electrolytes and the Molecular Mass of Albumin, Phil. Mag., 9 (1905) 781-785.

[4] J.A.V. Butler, Studies in Heterogeneous Equilibria. Part III. A Kinetic Theory of Reversible Oxidation Potentials at Inert Electrodes, Trans. Faraday Soc., 19 (1924) 734-739.

[5] J.A.V. Butler, Studies in Heterogeneous Equilibria. Part II.-the Kinetic Interpretation of the Nernst Theory of Electromotive Force, Trans. Faraday Soc., 19 (1924) 729-733.

[6] J.A.V. Butler, Studies in Heterogeneous Equilibria. Part I. Conditions at the Boundary Surface of Crystalline Solids and Liquids and the Application of Statistical Mechanics, Trans. Faraday Soc., 19 (1924) 659-665.

[7] A.J. Bard, L.R. Faulkner, Electrochemical Methods: Fundamentals and Applications, Wiley, 2000.

[8] P. Bergé, M. Dubois, Rayleigh-Bénard Convection, Contemp. Phys., 25 (1984) 535-582.

[9] W. Cheng, R.G. Compton, Electrochemical Detection of Nanoparticles by 'Nano-Impact' Methods, TrAC, Trends Anal. Chem., 58 (2014) 79-89.

[10] A. Sheludko, Thin Liquid Films, Adv. Colloid Interface Sci., 1 (1967) 391-464.

[11] L.D. Landau, E.M. Lifshitz, Fluid Mechanics, Second ed., Pergamon Press, Oxford, 1987.

[12] Y. Jaluria, Natural Convection, in: A. Bejan, A.D. Kraus (Eds.) Heat Transfer Handbook, John Wiley & Sons, Hoboken, New Jersey, 2003, Ch. 7, pp. 525-571.

[13] T.L. Bergman, A.S. Lavine, F.P. Incropera, D.P. Dewitt, Fundamentals of Heat and Mass Transfer, Seventh ed., Wiley, Hoboken, N.J., 2011.

[14] D.R. Lide (Ed.), CRC Handbook of Chemistry and Physics, Internet Version 2005, CRC Press, Boca Raton, FL, 2005.

[15] O. Pironneau, Finite Element Methods for Fluids, John Wiley & Sons, Chichester, West Sussex, England, 1989.

[16] W.M. Lai, D.H. Rubin, E. Krempl, Introduction to Continuum Mechanics, Fourth ed., Elsevier Science, Burlington, MA, 2009.

[17] I.B. Ivanov, D.S. Dimitrov, Hydrodynamics of Thin Liquid Films, Colloid. Polym. Sci., 252 (1974) 982-990.

[18] V.G. Levich, Physicochemical Hydrodynamics, Prentice-Hall, Inc., Englewood Cliffs, N.J., 1962.

[19] H. Hu, R.G. Larson, Analysis of the Effects of Marangoni Stresses on the Microflow in an Evaporating Sessile Droplet, Langmuir, 21 (2005) 3972-3980.

[20] J.R. Keller, T.L. Bergman, Thermosolutal Inducement of No-Slip Free Surfaces in Combined Marangoni-Buoyancy Driven Cavity Flows, J. Heat Transfer, 112 (1990) 363-369.

[21] B.F. Wang, Z.H. Wan, Z.W. Guo, D.J. Ma, D.J. Sun, Linear Instability Analysis of Convection in a Laterally Heated Cylinder, J. Fluid Mech., 747 (2014) 447-459.

[22] A. Lemembre, J.P. Petit, Laminar Natural Convection in a Laterally Heated and Upper Cooled Vertical Cylindrical Enclosure, Int. J. Heat Mass Transfer, 41 (1998) 2437-2454.

[23] X. Gao, J. Lee, H.S. White, Natural Convection at Microelectrodes, Anal. Chem., 67 (1995) 1541-1545.

[24] B. Wang, K.J. Aoki, J. Chen, T. Nishiumi, Slow Scan Voltammetry for Diffusion-Controlled Currents in Sodium Alginate Solutions, J. Electroanal. Chem., 700 (2013) 60-64.

7. Conclusions

This thesis is an in-depth study of a subject that has received relatively little attention in the literature on electrochemistry and highlights that, although natural convective flows in electrochemical systems are typically assumed to be negligible, they have a key role in many cases. The difficulty in their elimination implies that the standard assumption for purely diffusive mass transport is frequently not justified and may compromise the interpretation of experimental data.

The main physical insights gained from the simulation studies described in the preceding chapters can be summarized as follows.

1. Chapter 3 clarifies the effect of reaction-induced thermal convection in typical chronoamperometric and cyclic voltammetric measurements. For all considered problems, the flows driven by perturbations in temperature due to the intrinsic heat of the chemical reaction are negligible in comparison with those caused by the concentration gradient in the vicinity of the electrode. Furthermore, under the studied conditions, chronoamperometric currents exhibit a substantial convective contribution at long times, whereas cyclic voltammetric currents are practically unaffected.
2. In contrast with temperature variations due to the heat of the electrochemical reaction, externally imposed temperature differences can be a driving force for intense natural convection. Chapter 4 demonstrates that temperature differences between solution and environments that can realistically arise in electrochemical experiments in the absence of thermostating (~ 5 K) are sufficient to generate natural convective flows of considerable intensity. Crucially, this chapter shows that in the absence of thermostating, thermal equilibration of cells similar to those used in SECM occurs over a period of ~ 1000 s.
3. Chapter 5 elaborates on the subject of natural convective flows driven by imperfect thermostating. It demonstrates the complexity of the velocity and temperature distributions in electrochemical cells thermostated from below

through a substrate of spatially inhomogeneous thermal conductivity. The simulations described in this section of the text show that $\boldsymbol{v}$ and T are strongly dependent on both the exact geometry of the container and the spatial distribution of the substrate's thermal conductivity. These factors strongly suggest that accounting for the effect of natural convection on mass transport in similar systems is a very involved task and avoiding it altogether by taking great care for the thermostating of the experiment is advisable.

4. Chapter 6 demonstrates that natural convection can still be significant even in electrochemical experiments in which special effort is made for thermostating the solution; experimental data and simulations indicate that heat losses due to evaporation and radiation play a key role in generating free convective flows. Crucially, the simulations discussed in this chapter show that in the presence of such heat fluxes, a measurement cell that is being thermostated to a temperature higher than the ambient tends to a convective rather than a stagnant steady state.

These observations suggest that many systems that are typically assumed to exhibit exclusively diffusive mass transport are in fact susceptible to natural convective flows. The opinion of the author of this thesis is that the quantitative description of free convective mass transport in electroanalytical systems is a promising area for future research. Such studies would ideally involve systems whose geometry is simple, well-defined and allows for the precise modelling of the arising flows. Furthermore, direct experimental observation of the velocity distributions in such systems through, e.g., particle image velocimetry, would be of great value as a means of testing and improving the models employed here.

Appendix A: Additional Data for Chapter 3

This appendix contains plots of the concentration, velocity and temperature profiles obtained from the various simulations discussed in Section 3.3 of the main text. Section A.1 shows graphs of C_{red}, $\boldsymbol{v}$ and T for chronoamperometric simulations, while A.2 does the same for simulations of cyclic voltammetry.

For the diffusion-only simulations of chronoamperometry and cyclic voltammetry, the shape of the concentration profile is independent on the size of the electrode and, therefore it is only shown for r_{e} = 0.25 mm.

Plots are not given for simulations that use a reaction enthalpy of equal magnitude but opposite sign to the experimentally measured one (ΔH = −45.35 kJ·mol^{-1}), as both the cases of the measured ΔH (45.35 kJ·mol^{-1}) and a limiting value bearing the opposite sign (−100 kJ·mol^{-1}) are illustrated.

As described in the main text, different dimensions of the simulated cell were used for each electrode size (r_{e}), the three configurations being 1) $r_{\mathrm{max}} = r_{\mathrm{e}} + 6\sqrt{t_{\mathrm{max}}\kappa/(\rho_0 c_p)} = 17.58$ mm by $z_{\mathrm{max}} = 6\sqrt{t_{\mathrm{max}}\kappa/(\rho_0 c_p)} = 17.33$ mm for r_{e} = 0.25 mm; 2) $r_{\mathrm{max}} = r_{\mathrm{e}} + 6\sqrt{t_{\mathrm{max}}\kappa/(\rho_0 c_p)} = 19.82$ mm and $z_{\mathrm{max}} = 6\sqrt{t_{\mathrm{max}}\kappa/(\rho_0 c_p)} = 17.33$ mm for r_{e} = 2.5 mm; 3) $r_{\mathrm{max}} = 4 \cdot r_{\mathrm{e}} = 100$ mm and $z_{\mathrm{max}} = 4 \cdot r_{\mathrm{e}} = 100$ mm for r_{e} = 25 mm.

A.1. Concentration, temperature and velocity profiles for simulations of chronoamperometry

The governing equations were discretized with respect to time and space in such a way that the current predicted from the diffusion-only simulation was within 1% of the Shoup-Szabo equation, Eq. (3.48).

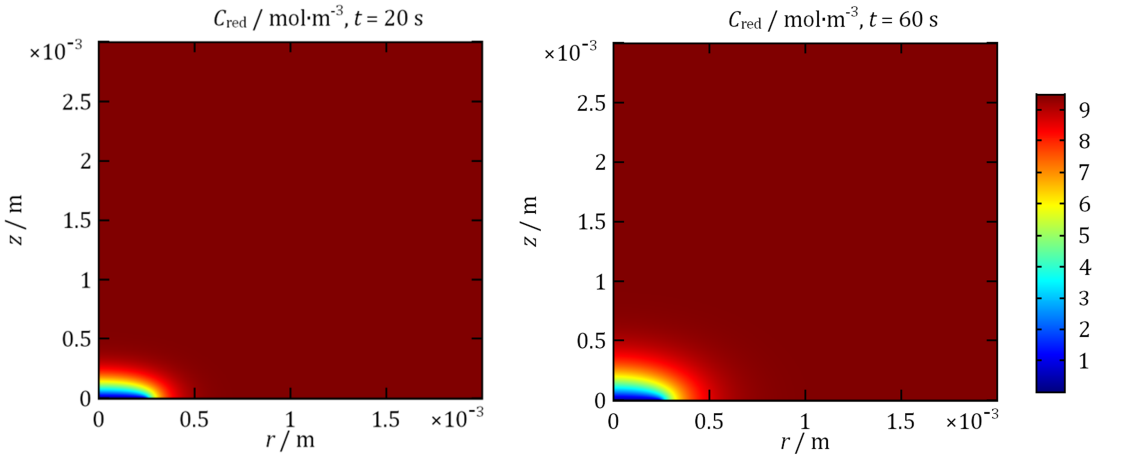


Figure A.1. Concentration profile at t = 20 and 60 s for a chronoamperometric oxidation of $[Fe(CN_6)]^{4-}$ at an electrode of radius r_e = 0.25 mm in the absence of convection.

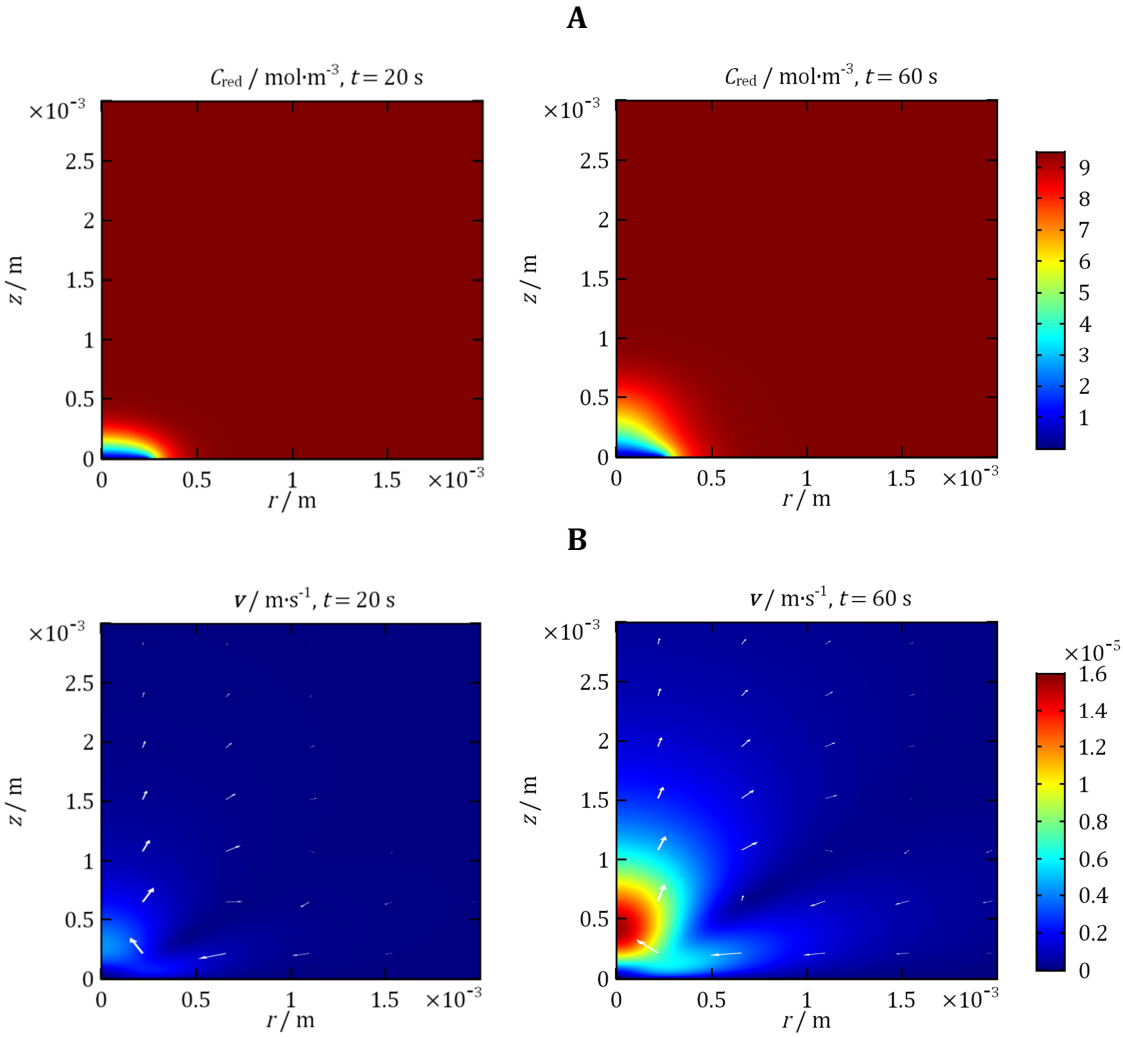


Figure A.2. C (**A**) and $\boldsymbol{v}$ profiles (**B**) at t = 20 and 60 s for a chronoamperometric oxidation of $[Fe(CN_6)]^{4-}$ at an electrode of radius r_e = 0.25 mm. The profiles are obtained from a simulation with diffusion and solute-driven free convection.

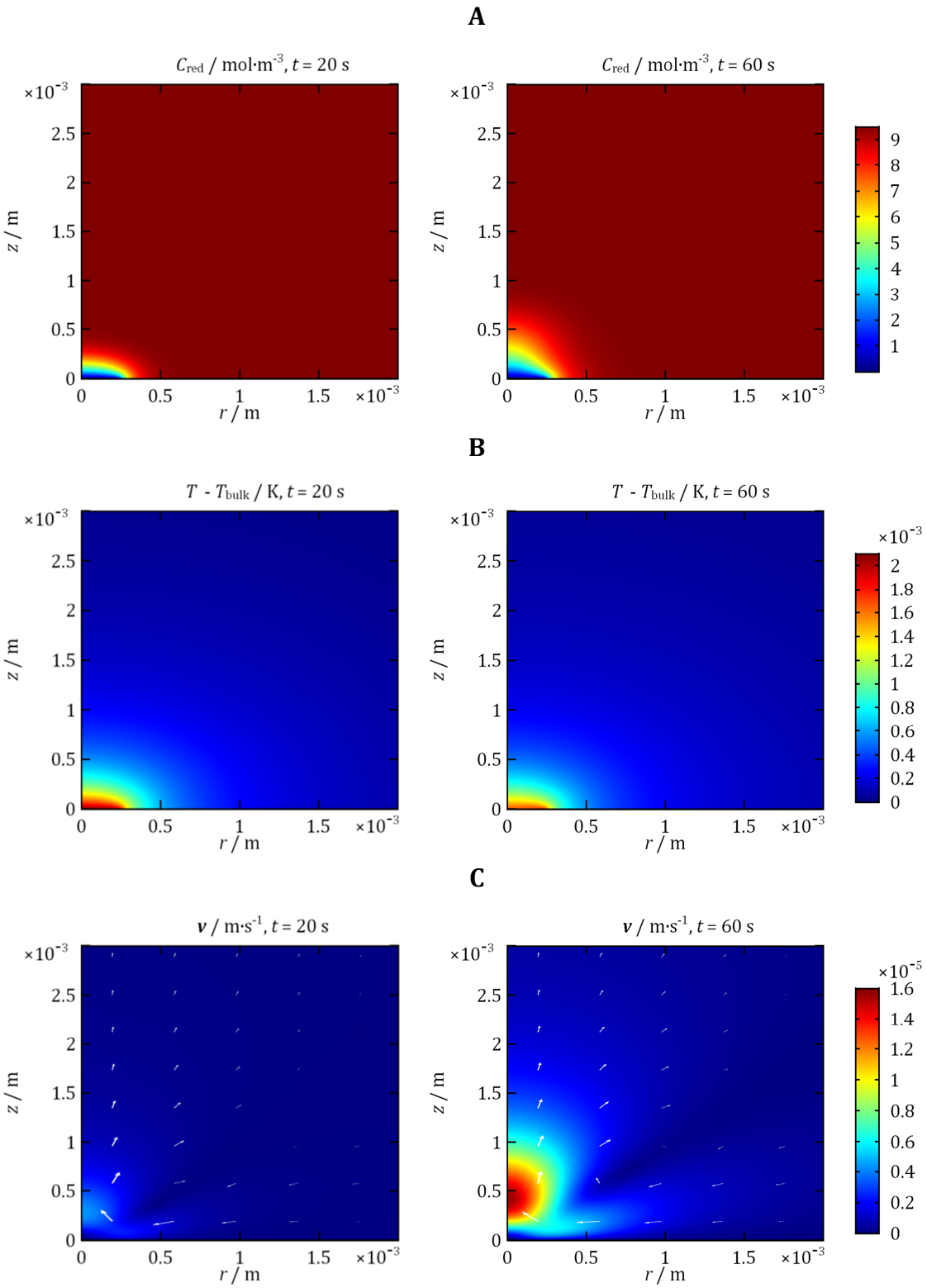


Figure A.3. C (**A**), T (**B**) and $\boldsymbol{v}$ profiles (**C**) at t = 20 and 60 s for a simulated chronoamperometric oxidation of $[Fe(CN_6)]^{4-}$ at r_e = 0.25 mm. The simulation includes both solutal and thermal convection and is performed with ΔH =

−100 kJ·mol^{-1} with the purpose of maximising the importance of thermal convection. The length of the arrows in **C** is proportional to ln(|***v***|).

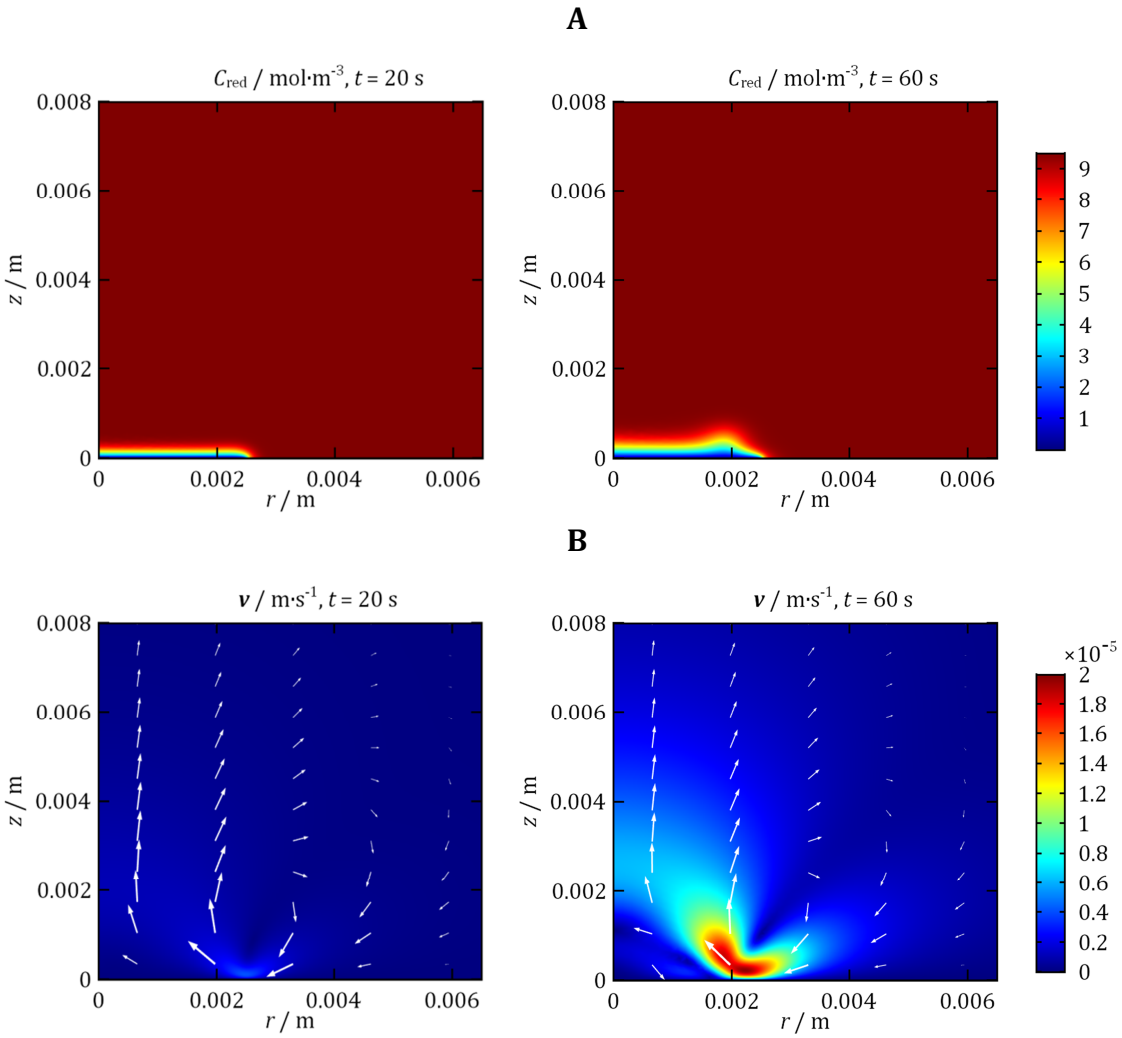


Figure A.4. Concentration (**A**) and velocity profiles (**B**) at t = 20 and 60 s for a chronoamperometric oxidation of $[Fe(CN_6)]^{4-}$ at an electrode of radius r_e = 2.5 mm for a simulation with diffusion and solute-driven natural convection.

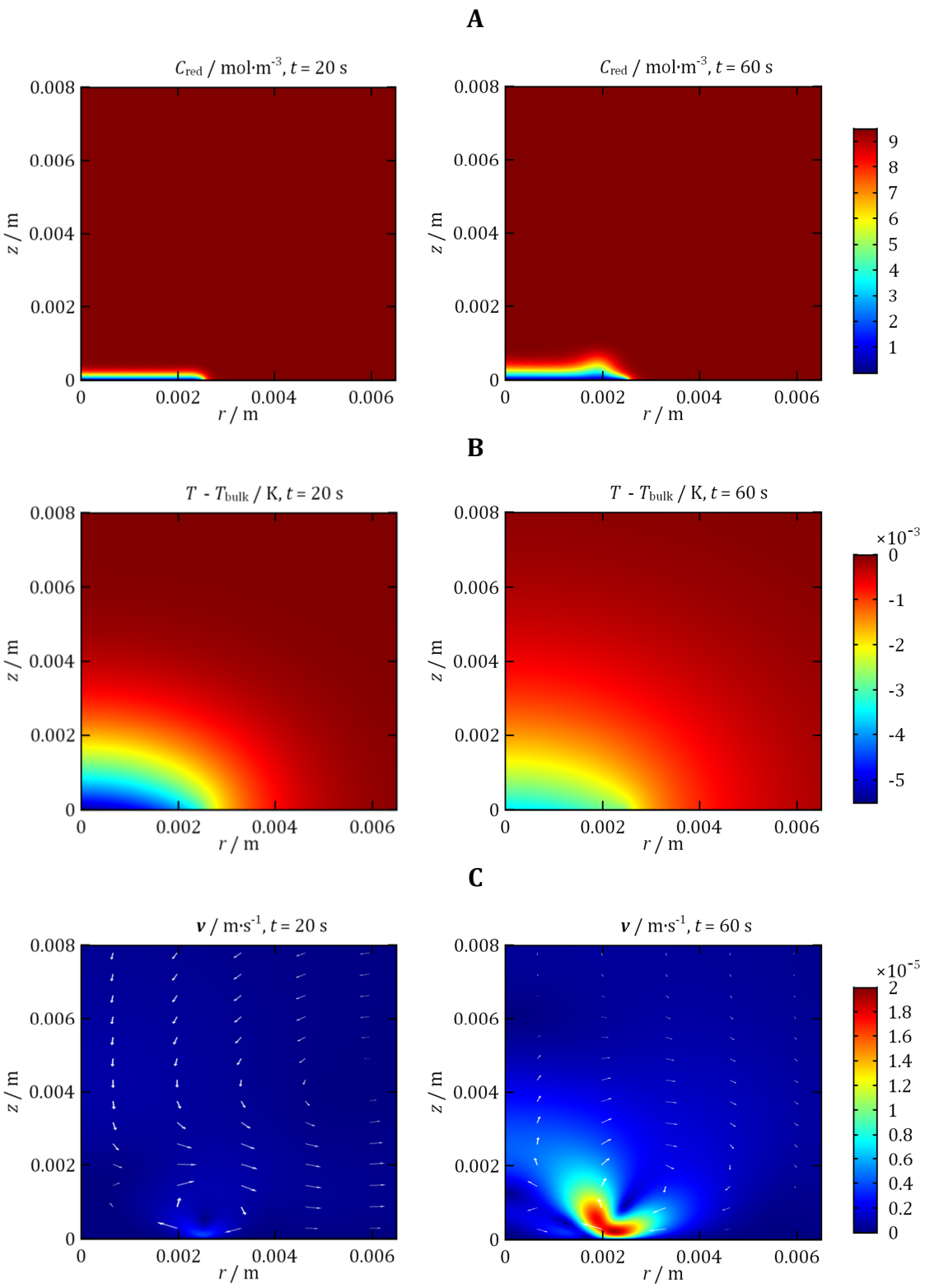


Figure A.5. C (**A**), T (**B**) and $\boldsymbol{v}$ profiles (**C**) at t = 20 and 60 s for a chronoamperometric oxidation of $[Fe(CN_6)]^{4-}$ at an electrode of radius r_e = 2.5 mm. The simulation includes both solutal and thermal convection and is performed with the experimentally measured ΔH [1], ΔH = 45.35 kJ·mol^{-1}. The length of the arrows representing the velocity vector is proportional to the natural logarithm of $|\boldsymbol{v}|$.

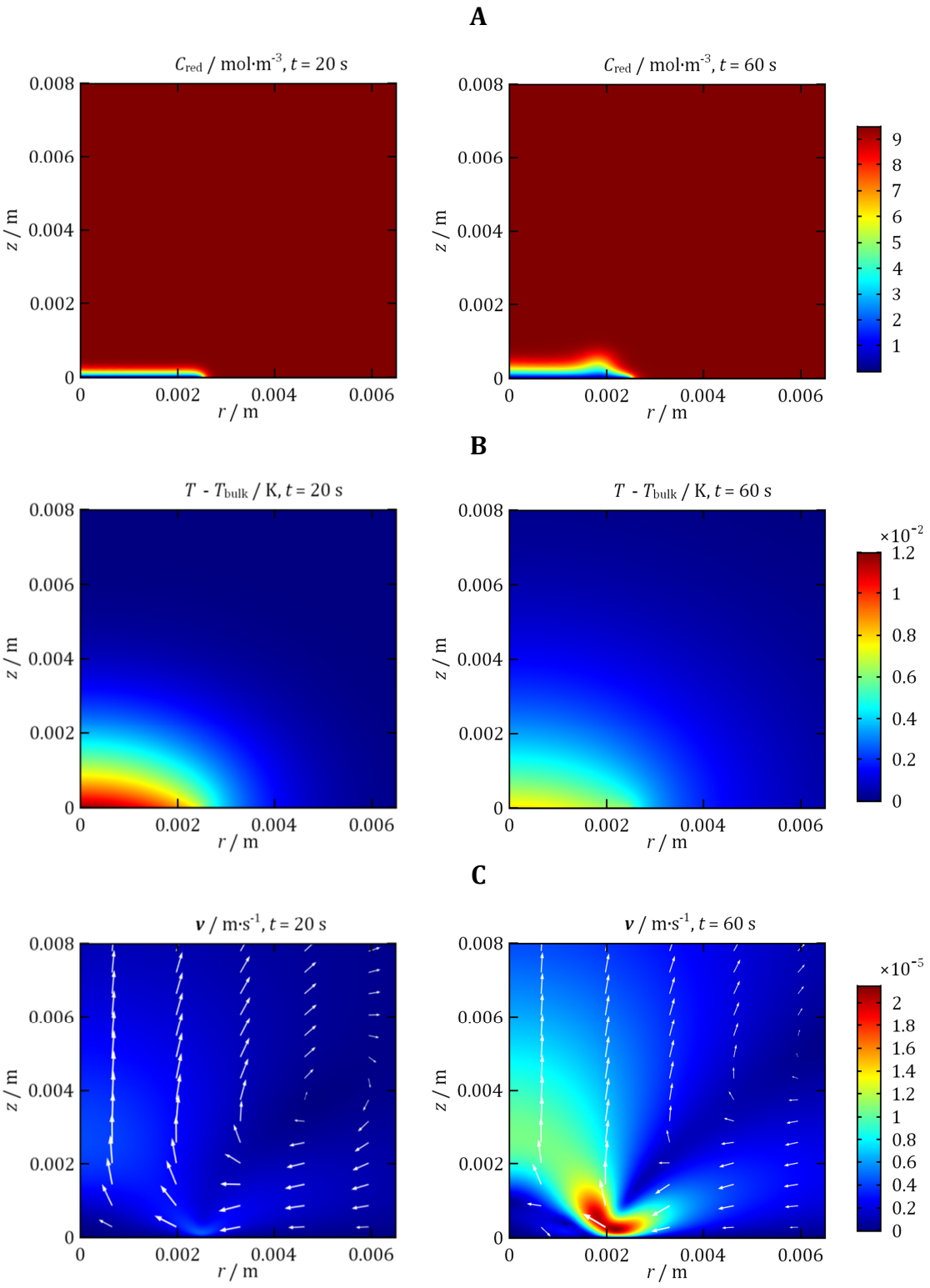


Figure A.6. C (**A**), T (**B**) and $\boldsymbol{v}$ profiles (**C**) at t = 20 and 60 s for a chronoamperometric oxidation of $[Fe(CN_6)]^{4-}$ at an electrode of radius r_e = 2.5 mm. The simulation takes both solutal and thermal convection into account and is performed with a limiting value of ΔH, ΔH = −100 kJ·mol^{-1}. The length of the arrows representing the velocity vector is proportional to the natural logarithm of $|\boldsymbol{v}|$.

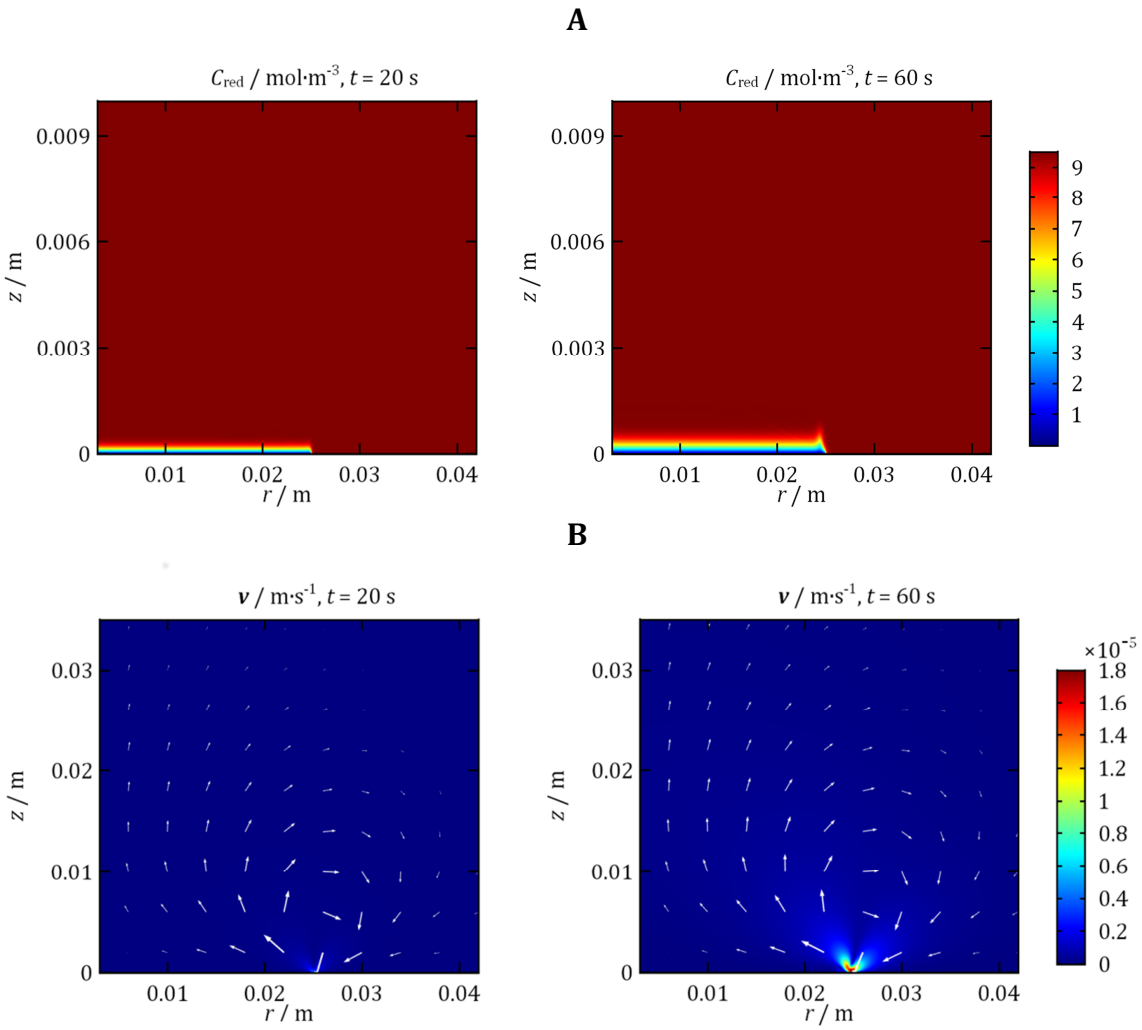
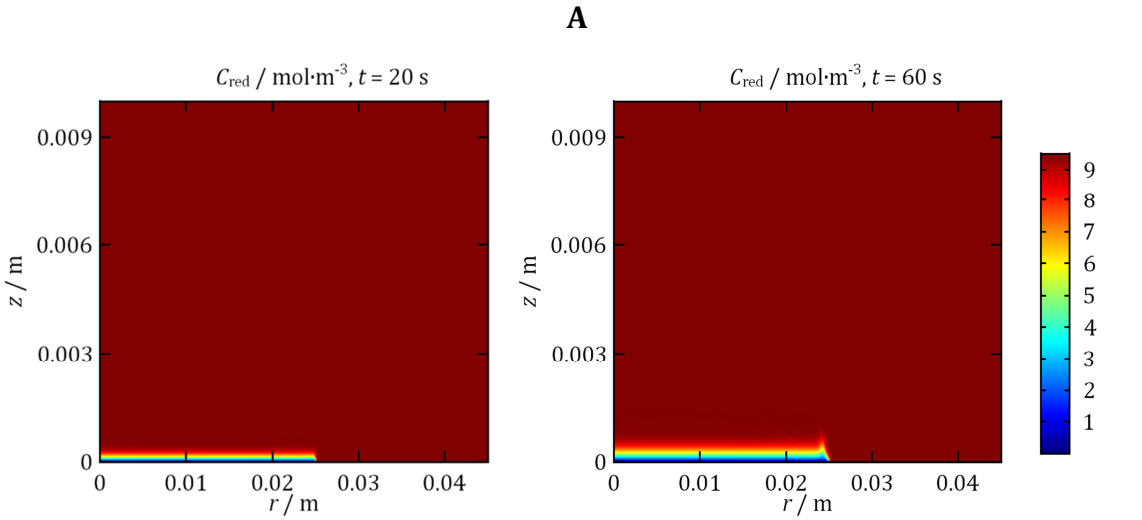


Figure A.7. Concentration (**A**) and velocity profiles (**B**) at t = 20 and 60 s for a chronoamperometric oxidation of $[Fe(CN_6)]^{4-}$ at an electrode of radius r_e = 25 mm. The simulation from which these plots are obtained includes diffusion and solute-driven convection only.



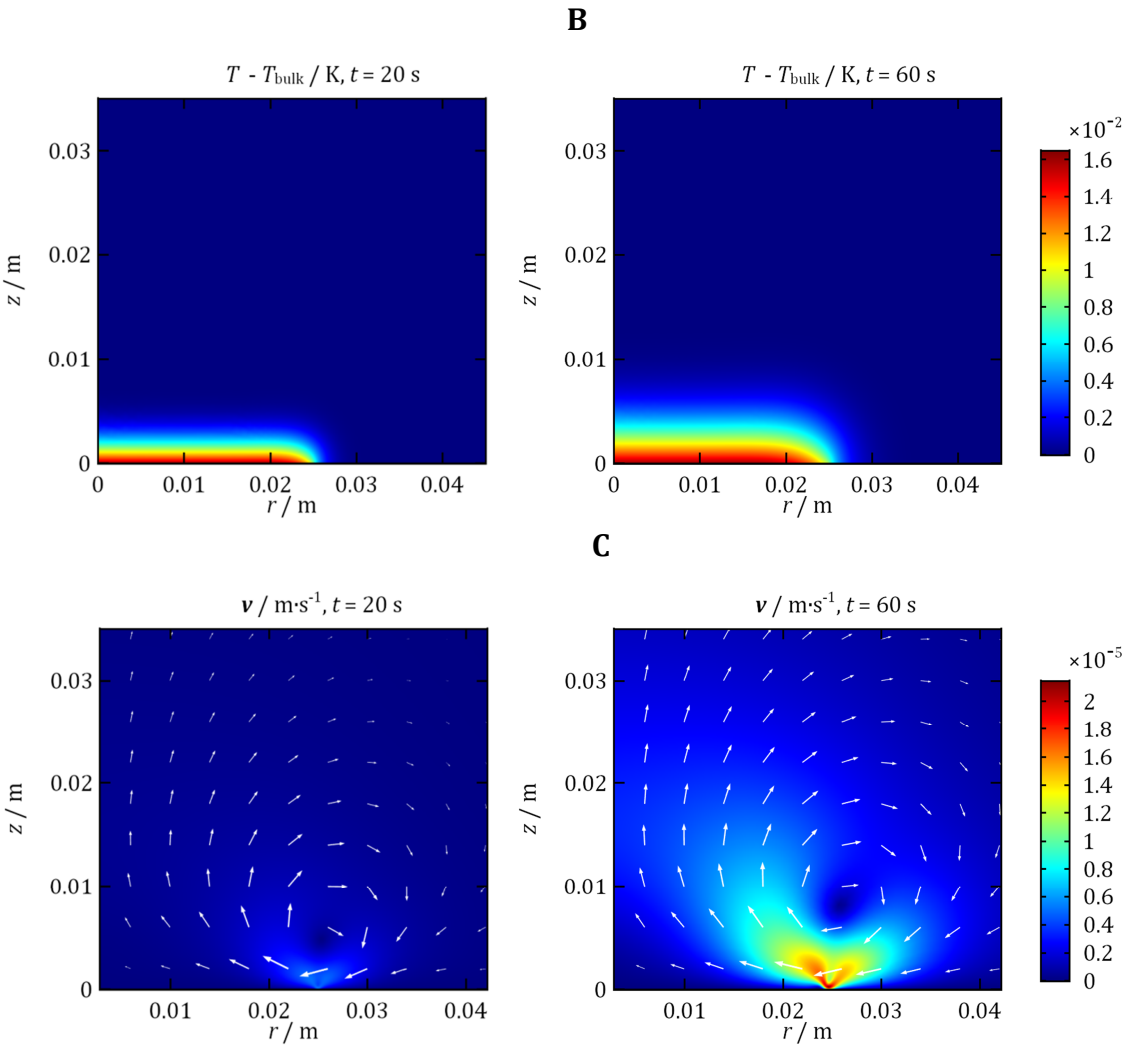


Figure A.8. Concentration (**A**), temperature (**B**) and velocity profiles (**C**) at t = 20 and 60 s for a chronoamperometric oxidation of $[Fe(CN_6)]^{4-}$ at an electrode of radius r_e = 25 mm. The simulation, which includes both solutal and thermal convection, is performed with a limiting value of the reaction enthalpy, ΔH = −100 kJ·mol^{-1}. The length of the arrows representing the velocity vector is proportional to the natural logarithm of $|\boldsymbol{v}|$.

A.2. Concentration, temperature and velocity profiles for simulations of cyclic voltammetry

The time-stepping and the spatial discretization of the governing equations were chosen in such a way that the simulated peak current predicted for the diffusion-only case was within 1% of the exact expression, Eq. (3.49).

Figures 8.9-8.18 show 'snapshots' of the concentration, temperature and velocity distributions for the various simulations of cyclic voltammetry discussed in the main text, taken at the vertex potential and at the end of the voltammetric scan.

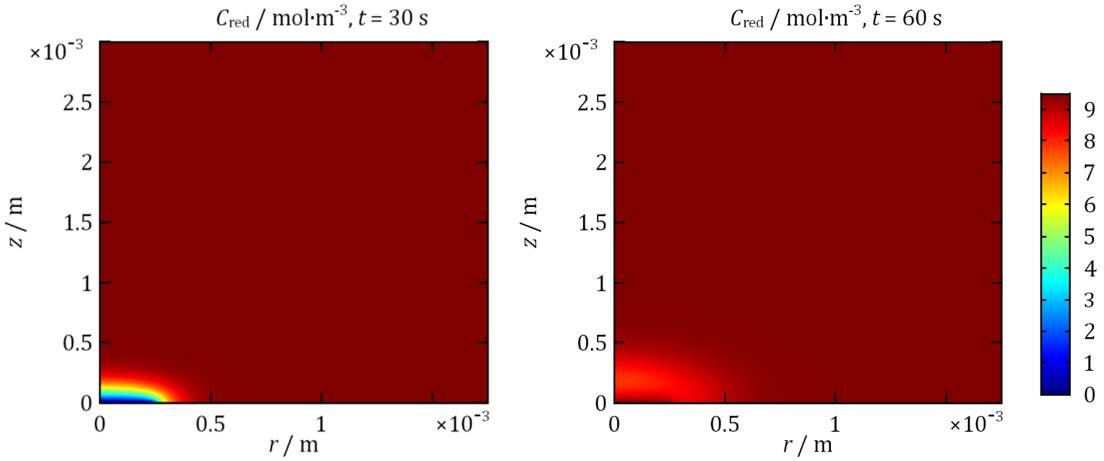
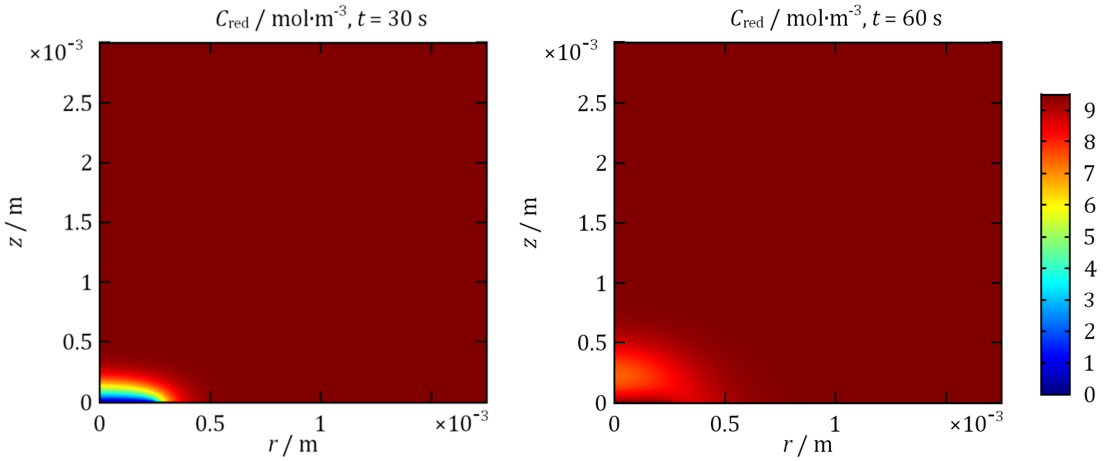


Figure A.9. Concentration profile at t = 30 and 60 s for a diffusion-only simulation of a cyclic voltammogram performed with a scan rate of $v = 33.7\ \mathrm{mV \cdot s^{-1}}$ at an electrode of radius r_e = 0.25 mm.

A



B

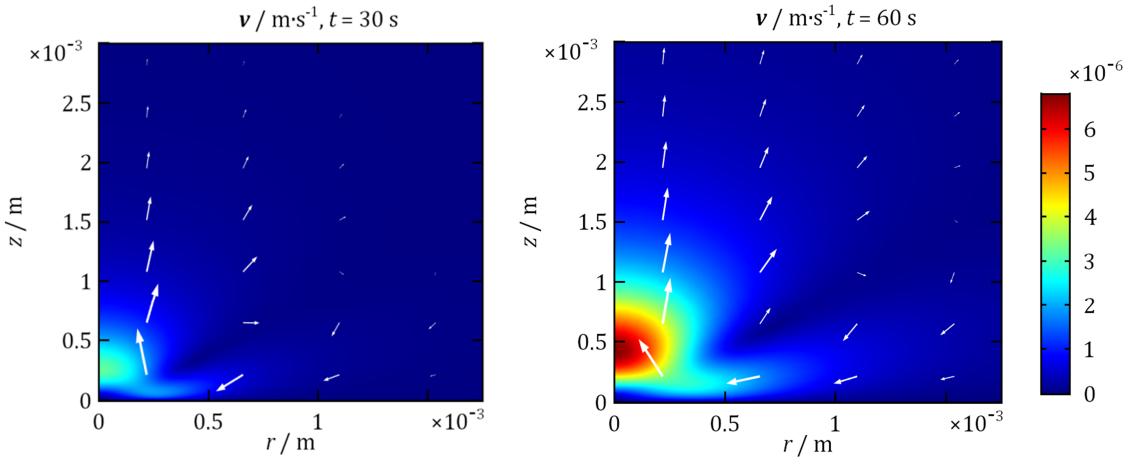
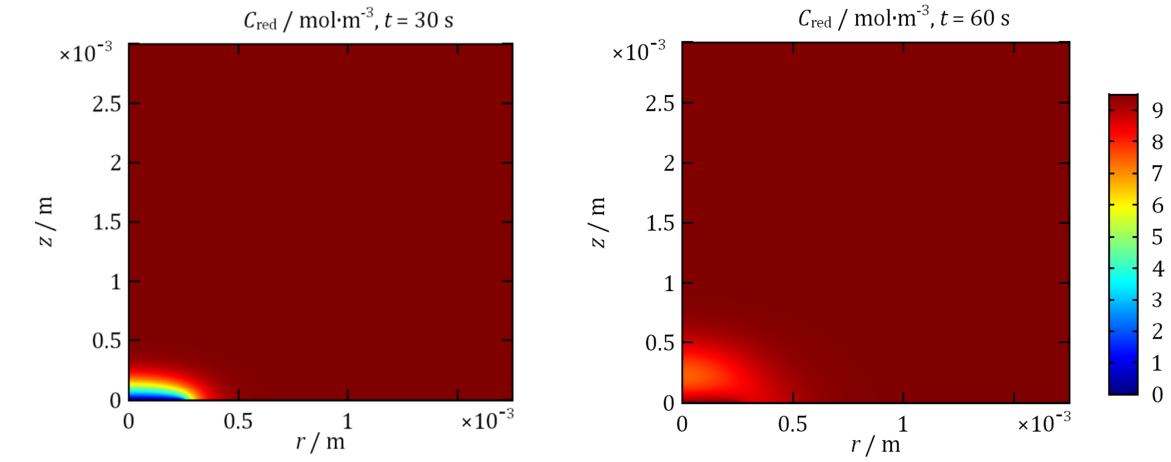
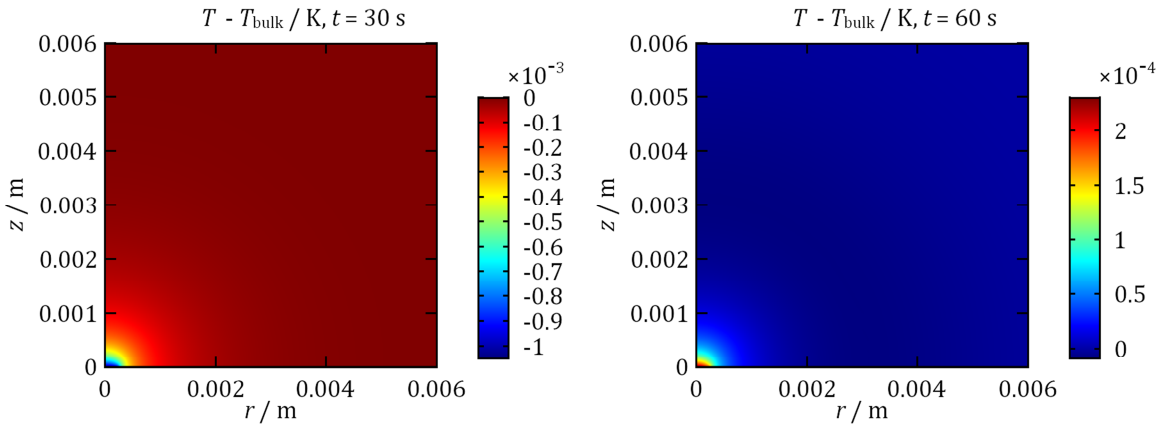


Figure A.10. Concentration (**A**) and velocity (**B**) profiles at t = 30 and 60 s for a simulation of a cyclic voltammogram with a scan rate of $v = 33.7\ \mathrm{mV \cdot s^{-1}}$ at an electrode of radius r_e = 0.25 mm. The simulation includes mass transport by diffusion and solute-driven convection.

A



B



C

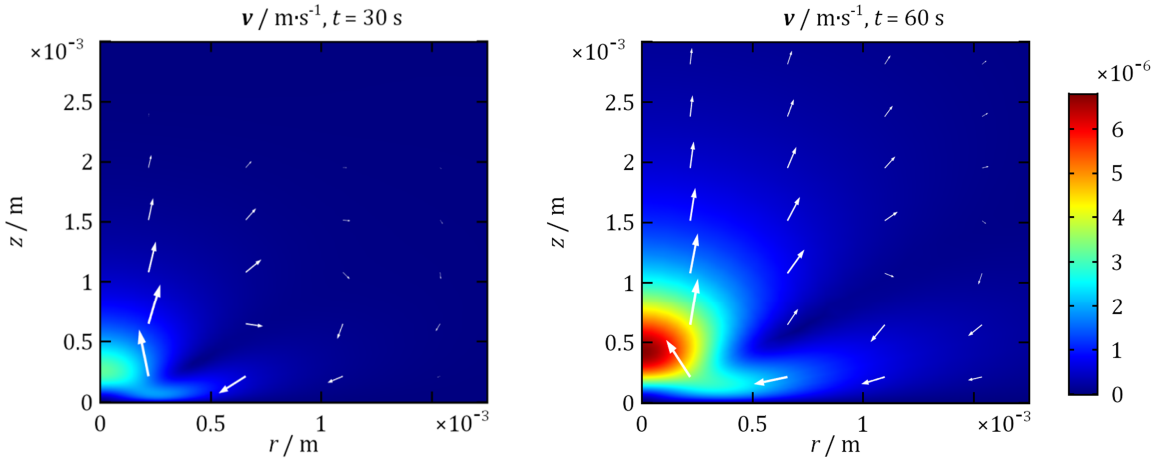
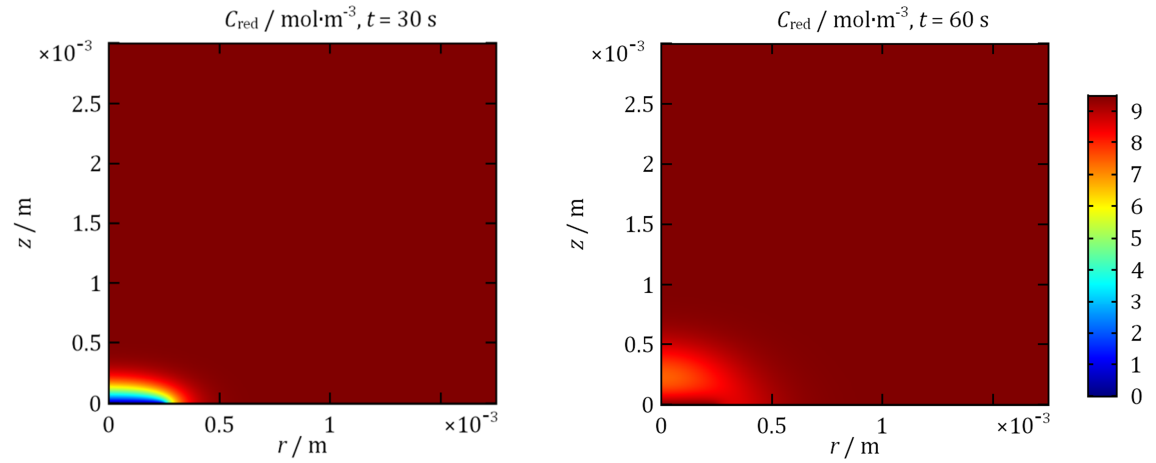


Figure A.11. Concentration (**A**), temperature (**B**) and velocity profiles (**C**) at t = 30 and 60 s for a simulation of a cyclic voltammogram with a scan rate of $v = 33.7\ \mathrm{mV \cdot s^{-1}}$ at an electrode of radius r_e = 0.25 mm. The simulation involves both solute-driven and thermal convection and is performed with the experimental value of the enthalpy change [1], ΔH = 45.35 kJ·mol^{-1}. The length of the arrows representing $\boldsymbol{v}$ in **C** is proportional to the natural logarithm of the absolute value of the velocity.

A



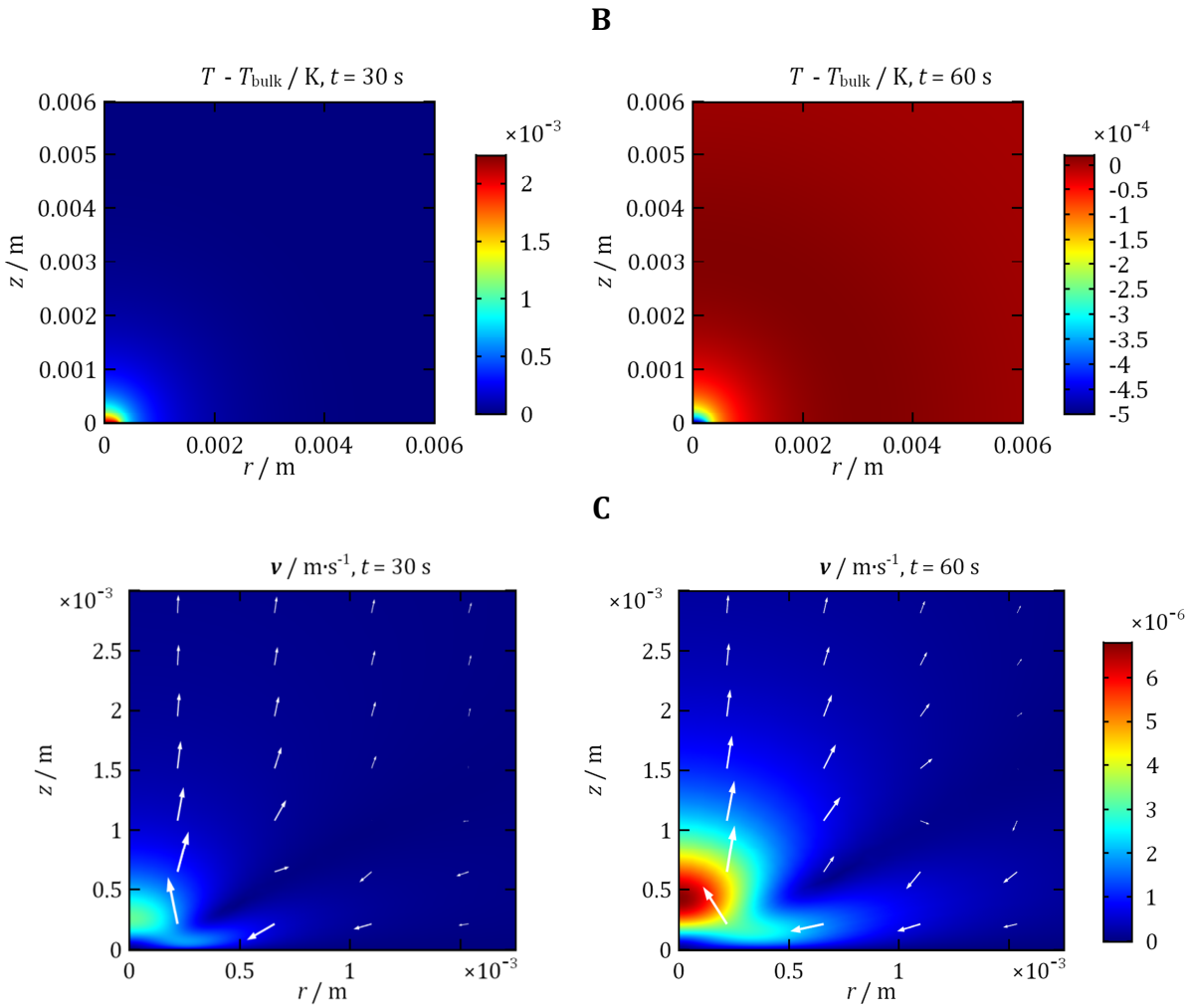


Figure A.12. Concentration (**A**), temperature (**B**) and velocity (**C**) profiles at t = 30 and 60 s for a simulation of a cyclic voltammogram performed with a scan rate of $v = 33.7\ \mathrm{mV \cdot s^{-1}}$ at an electrode of radius r_e = 0.25 mm. The simulation involves both solutal and thermal convection. The reaction enthalpy is set to a limiting value, $\Delta H = -100\ \mathrm{kJ \cdot mol^{-1}}$, that is opposite in sign to the experimentally measured one so as to maximize the effect of thermal convection. The length of the arrows representing $\boldsymbol{v}$ in **C** is proportional to the natural logarithm of the absolute value of the velocity.

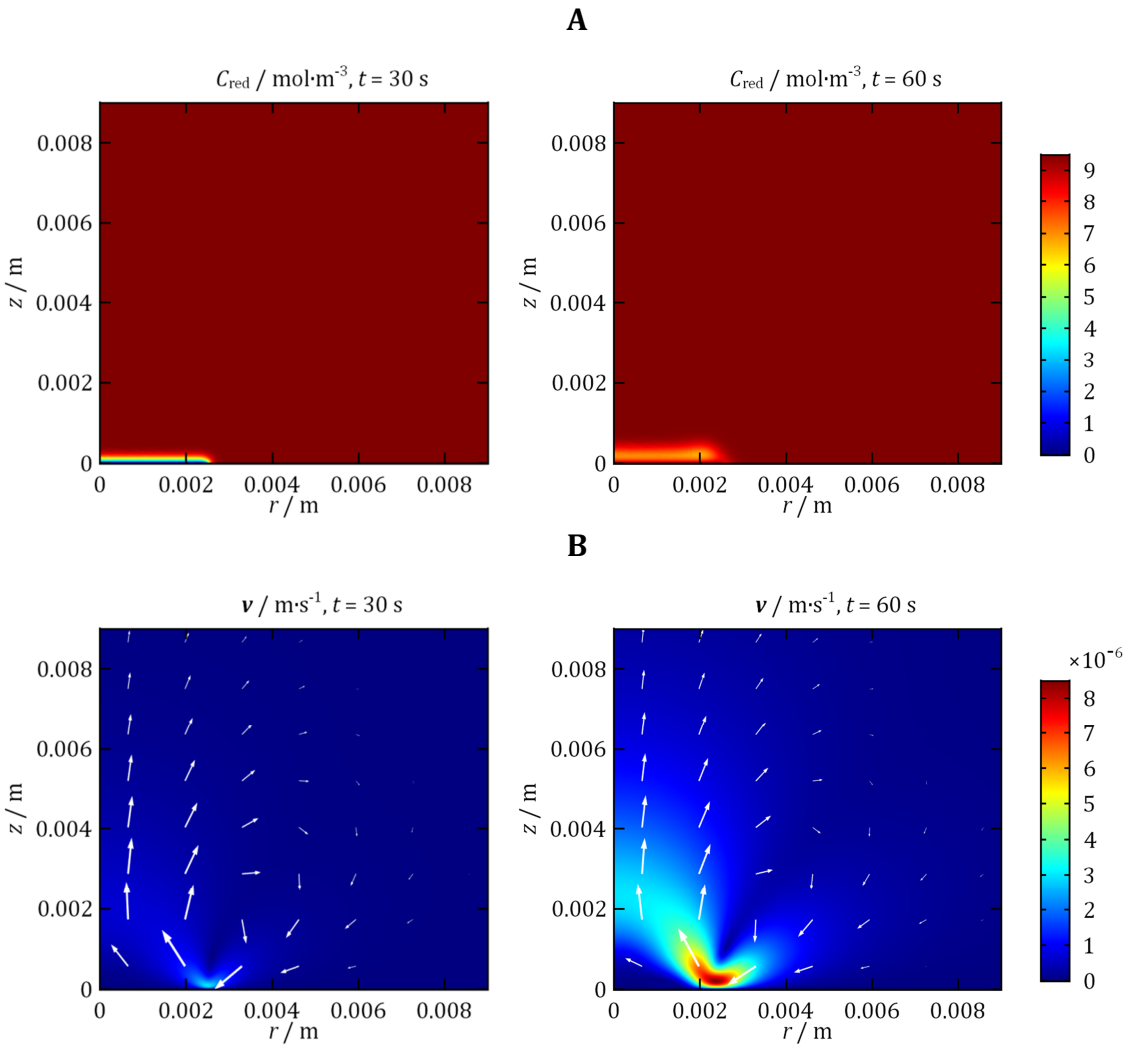


Figure A.13. Concentration (**A**) and velocity (**B**) profiles at t = 30 and 60 s for a simulation of a cyclic voltammogram performed with a scan rate of $v = 33.7\ \mathrm{mV \cdot s^{-1}}$ at an electrode of radius r_e = 2.5 mm. The simulation takes into account mass transport by diffusion and solute-driven free convection. The length of the arrows representing $\boldsymbol{v}$ in **B** is proportional to the natural logarithm of the absolute value of the velocity.

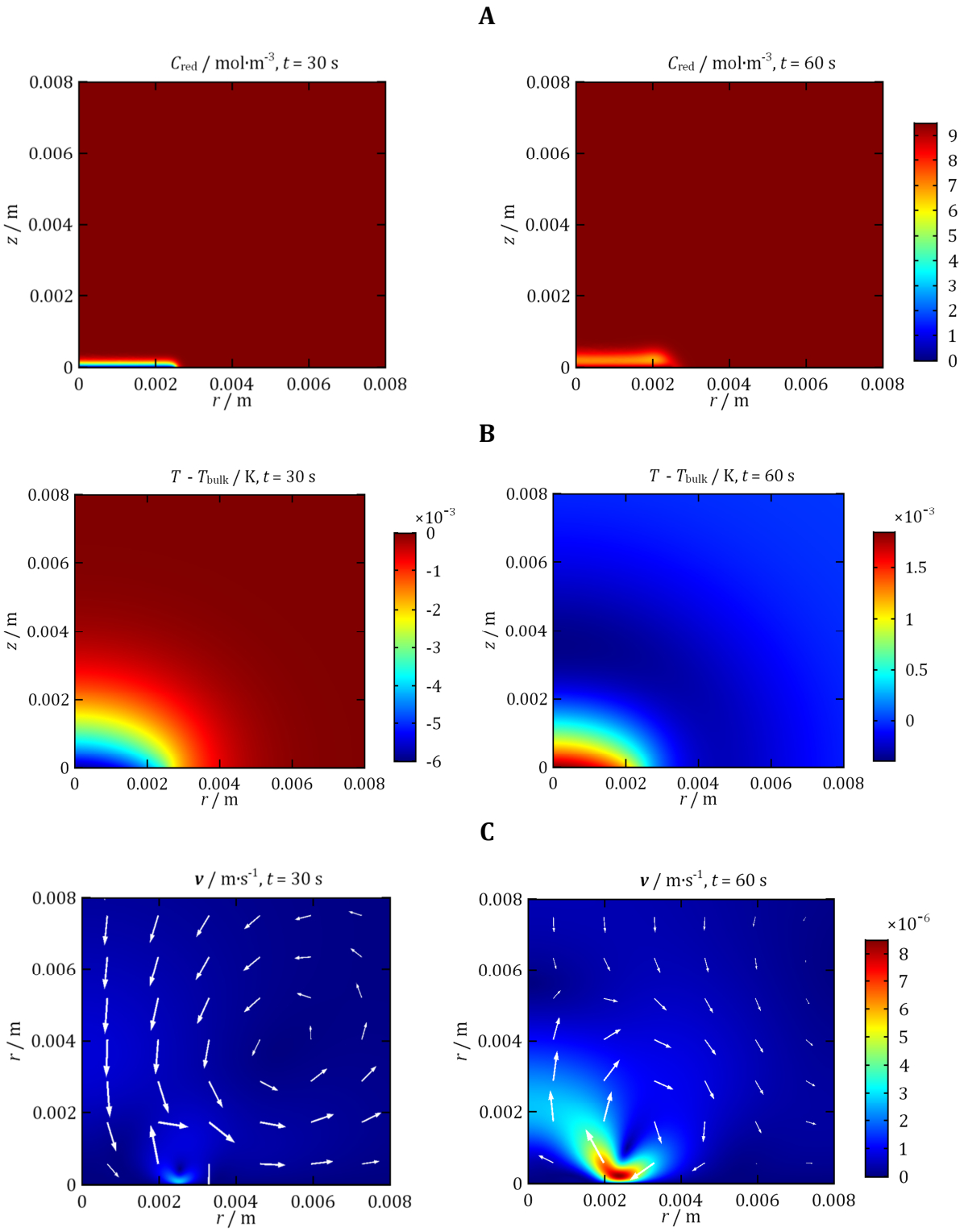


Figure A.14. C (**A**), T (**B**) and $\boldsymbol{v}$ (**C**) profiles at t = 30 and 60 s for a simulation of a CV with $v = 33.7\ \mathrm{mV \cdot s^{-1}}$ and r_e = 2.5 mm. The simulation, which involves solute-driven and reaction-induced thermal convection is performed with the experimental value of the enthalpy change [1], ΔH = 45.35 kJ·mol^{-1}.

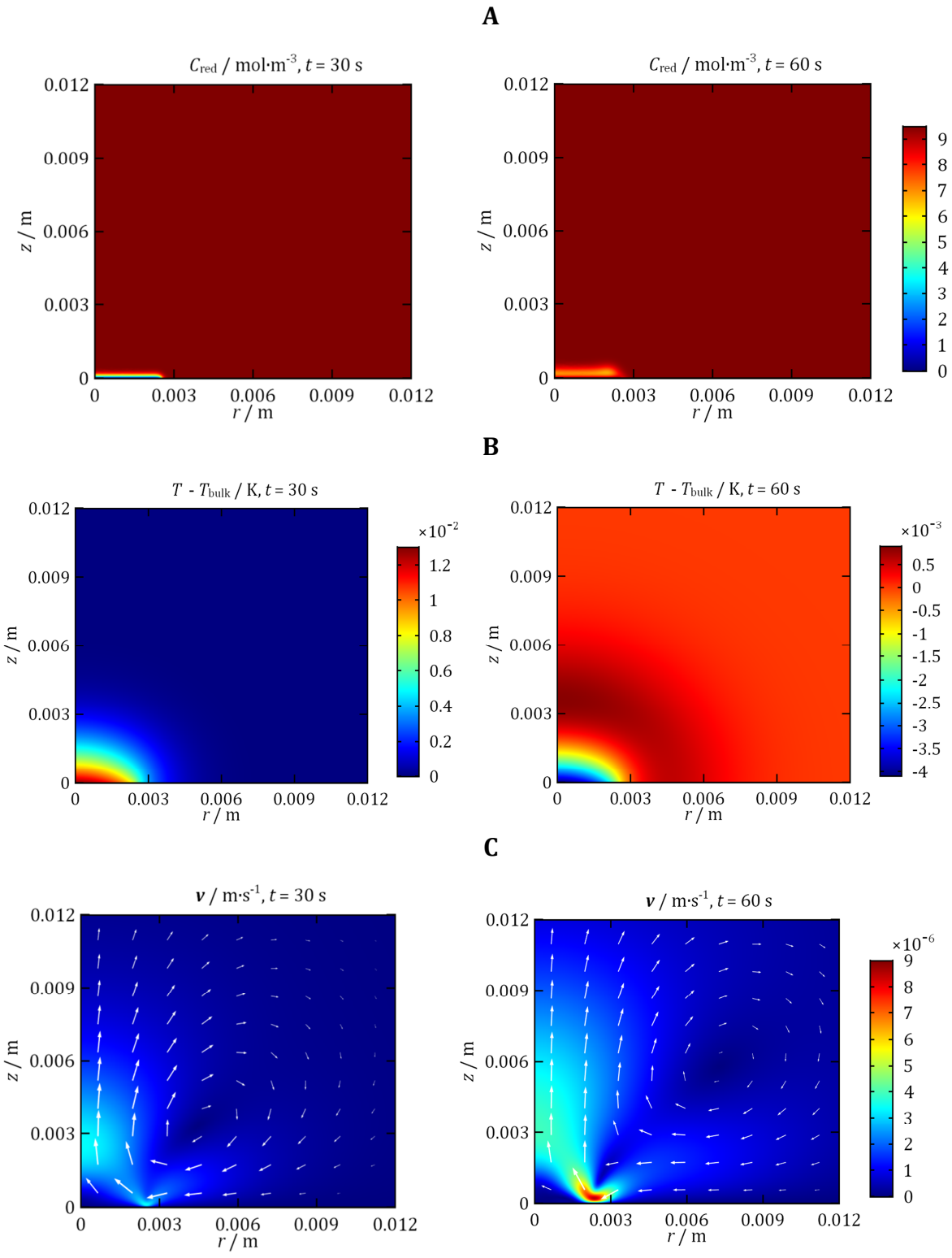


Figure A.15. C (**A**), T (**B**) and $\boldsymbol{v}$ (**C**) distributions at t = 30 and 60 s for a simulation of a CV with $v = 33.7\ \mathrm{mV \cdot s^{-1}}$ and r_e = 2.5 mm. The simulation includes both solutal and thermal convection; ΔH is set to a limiting value, $\Delta H = -100\ \mathrm{kJ \cdot mol^{-1}}$, and its sign is reversed with respect to the experimental value so as to maximize the effect of thermal convection; arrow length in **C** is proportional to $\ln(|\boldsymbol{v}|)$.

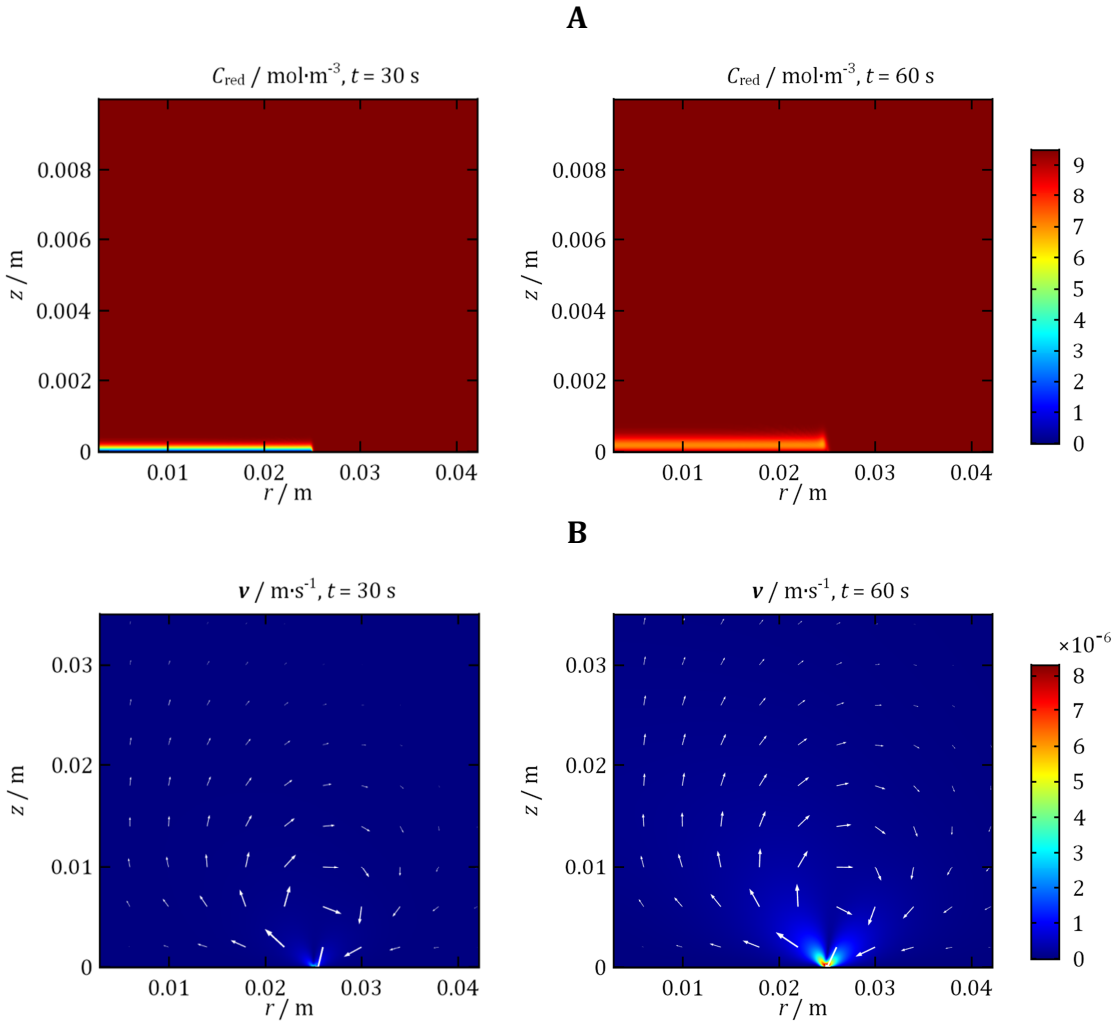
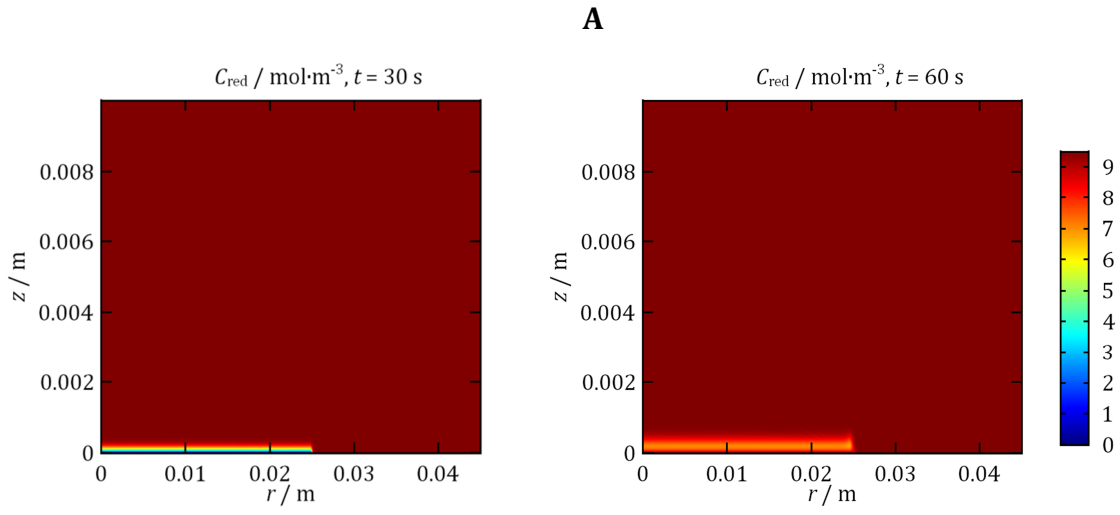


Figure A.16. Concentration profile at t = 30 and 60 s for a simulation of a cyclic voltammogram performed with a scan rate of $v = 33.7\ \mathrm{mV \cdot s^{-1}}$ at an electrode of radius r_e = 25 mm. The simulation involves mass transport by diffusion and solute-driven convection.



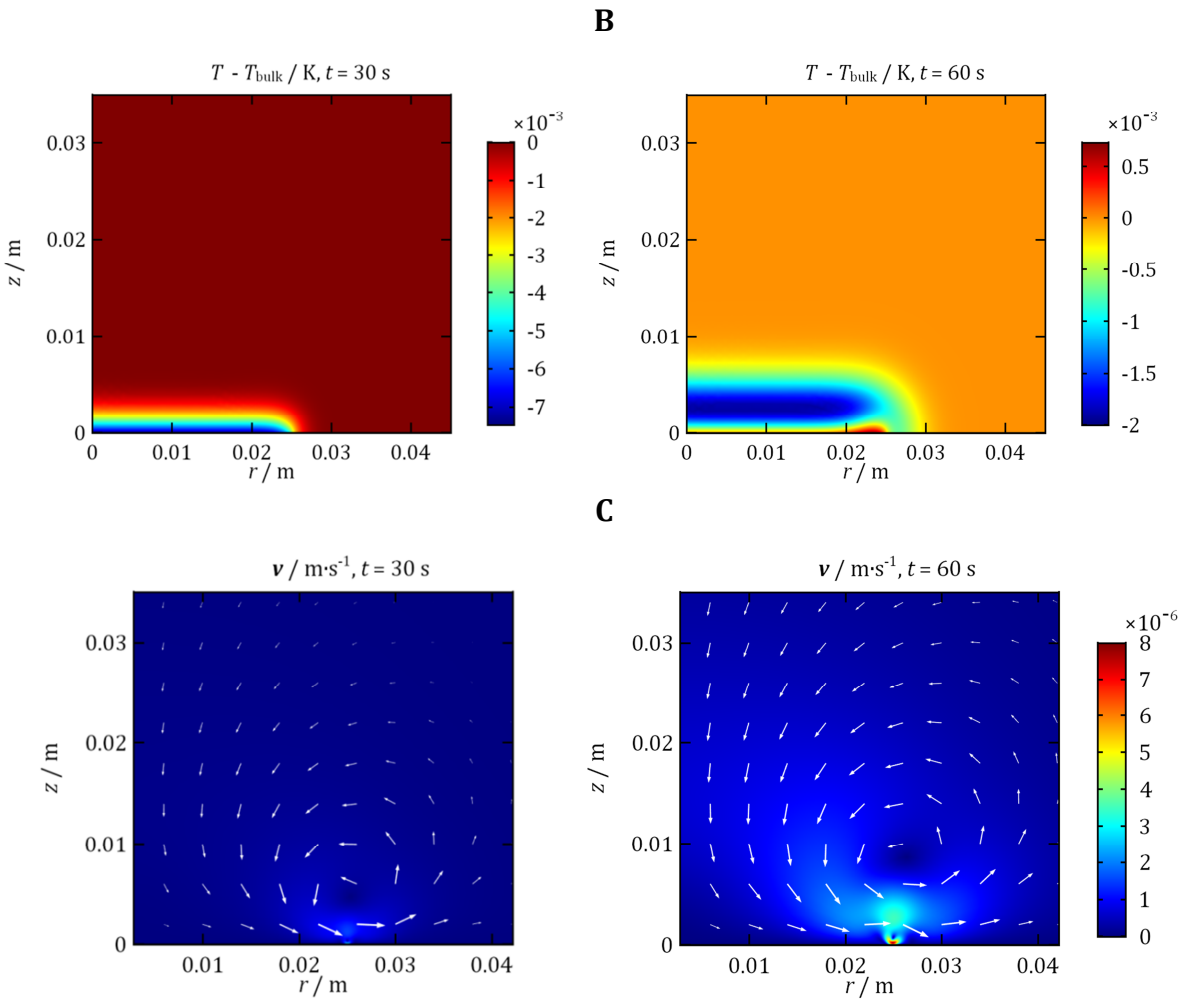
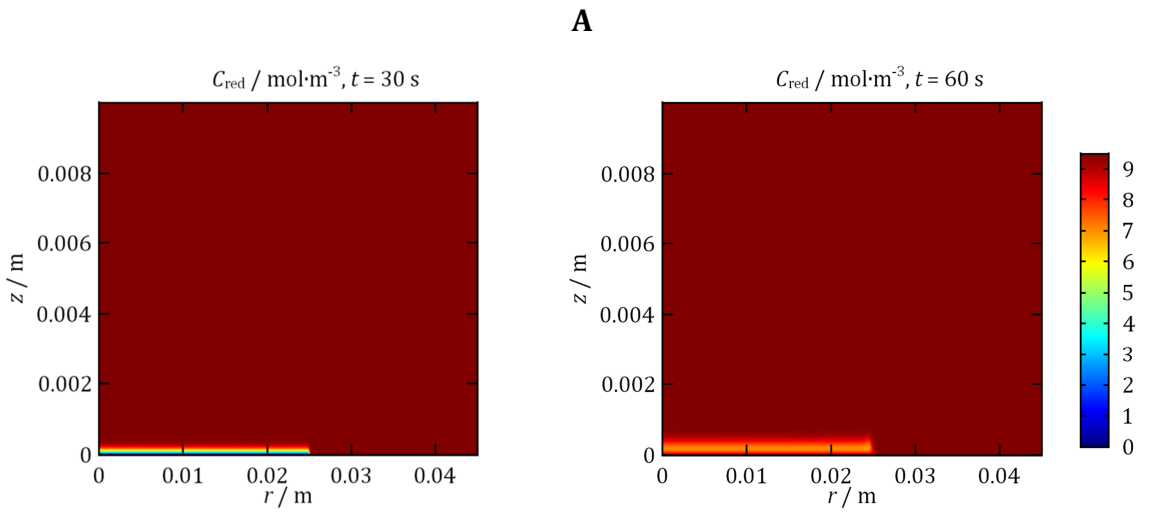


Figure A.17. Concentration (**A**), temperature (**B**) and velocity (**C**) profiles at t = 30 and 60 s for a simulation of a CV performed with a $v = 33.7\ \mathrm{mV \cdot s^{-1}}$ and r_e = 25 mm. The simulation involves both solute-driven and thermal convection and is performed with the experimental value of the enthalpy change [1], ΔH = 45.35 kJ·mol^{-1}.



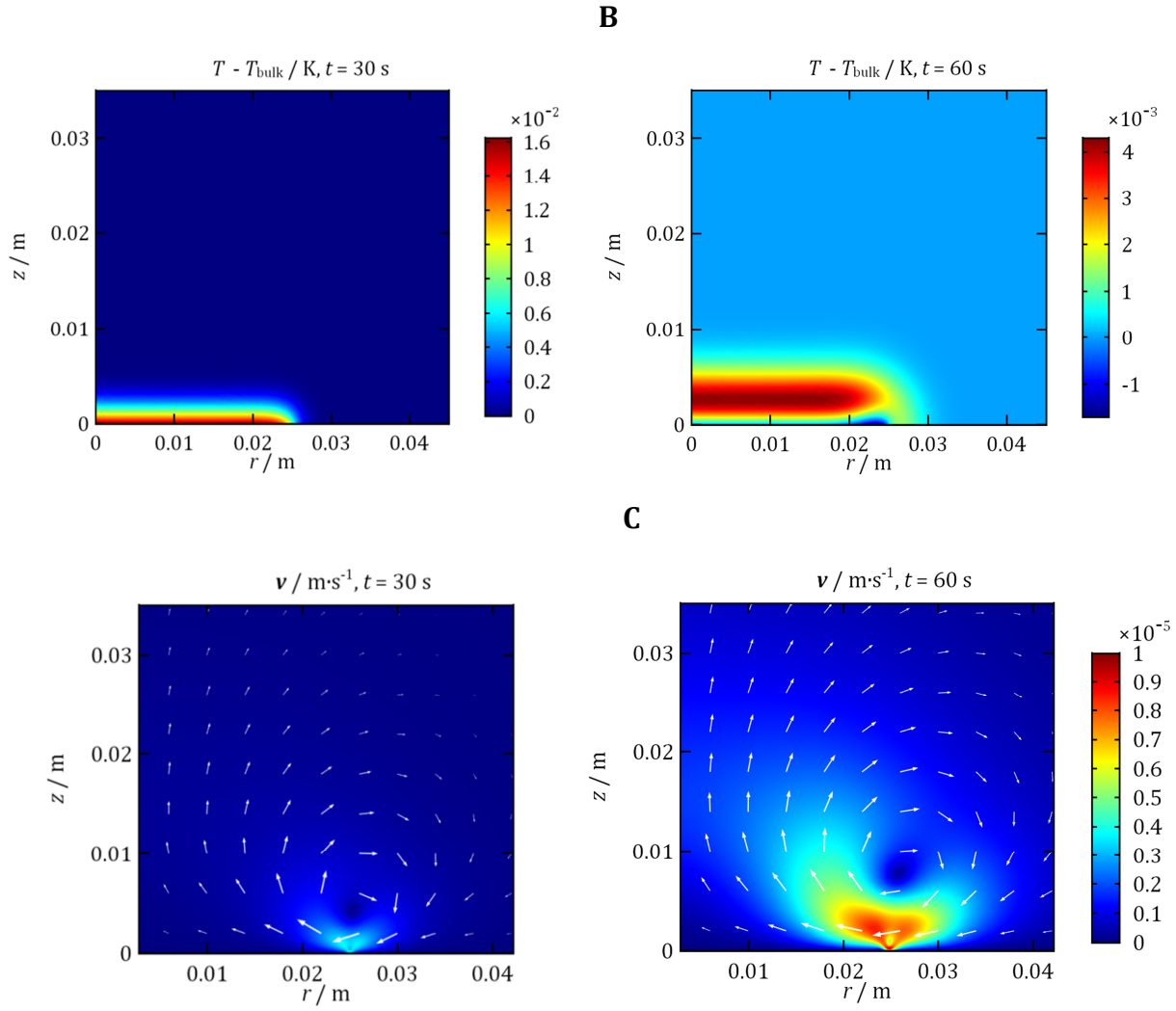


Figure A.18. Concentration (**A**), temperature (**B**) and velocity (**C**) profiles at t = 30 and 60 s for a simulation of a CV with $v = 33.7\ \mathrm{mV \cdot s^{-1}}$ and r_e = 25 mm. The simulation involves both solute-driven and reaction-induced thermal convection; the reaction enthalpy is set to a limiting value, $\Delta H = -100\ \mathrm{kJ \cdot mol^{-1}}$, that enhances the effect of thermal convection. The length of the arrows representing the velocity vector is proportional to the natural logarithm of $|\boldsymbol{v}|$.

A.3. Reference

[1] P. Boudeville, A. Tallec, Electrochemistry and Calorimetry Coupling: IV. Determination of Electrochemical Peltier Heat, Thermochim. Acta, 126 (1988) 221-234.

Appendix B: Additional Data for Chapter 5

B.1. Details on the simulations discussed in Chapter 5 and stability tests

This section provides additional information on the systems discussed in Chapter 5 in the form of plots of the temperature and velocity in the solution, in terms of both their volume-averages and 'snapshots' of their distributions.

Here, we also provide details on the stability of the observed flow patterns. As discussed in Chapter 5, our approach consists in two steps – first, we substitute the zero-flux condition at the top wall of the cylinder with Eq. (5.29) and obtain the stationary velocity and temperature distribution emerging in the modified problem. Then, we use other possible velocity, temperature and pressure distributions as initial conditions for the same simulation, thereby obtaining information about their stability in this system.

The numerical solution of the equations was sought numerically in COMSOL Multiphysics with a time-stepping algorithm with a variable step size. For most simulations at r_{cell} = 3 mm, the maximum step size was set to Δt_{max} = 3.5 s; the exception were the simulations performed in order to compare the stability of different flow patterns, where larger time steps were used, see below. For the simulations at r_{cell} = 8 mm we used Δt_{max} = 1 s in order to describe adequately the more complicated temporal evolution of the velocity profiles.

B.1.1 Simulations for r_{cell} = 3 mm

B.1.1.A. *Solution colder than substrate at t = 0 (ΔT > 0)*

Homogeneous BDD substrate

Figure B.1 and Figure B.2 complement the discussion of the properties of the two types of flow observed in systems with homogeneous BDD substrates from Chapter 5. In Figure B.1 we plot the volume-average temperature distribution for the pattern with clockwise motion in the simulated region. Figure B.2 provides plots of the average solution velocity and temperature against time, as well as 'snapshots' of their distributions at t = 100 s for the anticlockwise pattern. Comparing Figure B.1 and Figure B.2B, one can infer that only the flow with clockwise motion in the simulated region has a noticeable, albeit small effect on the overall heat transfer in the solution, bringing about a change of ~ 1% in $\Delta\tilde{T}_{av}$. The different extent of the influence of the two convective flow patterns is further illustrated by the comparison between 'snapshots' of the respective temperature profiles in Figure 5.2C and Figure B.2D – in the latter, T is approximately independent of r, as it would be in the conduction-only case.

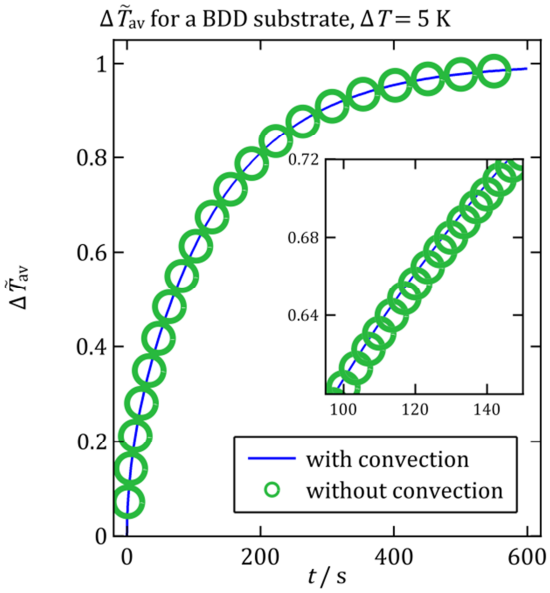


Figure B.1. $\Delta\tilde{T}_{av}$ vs t for a homogeneous BDD substrate for the flow pattern with upwelling at r = 0 (obtained by using linear elements for T). As the inset illustrates,

convection has an effect on the average temperature in the solution, although this reaches ~ 1% of $\Delta\tilde{T}_{av}$ at most.

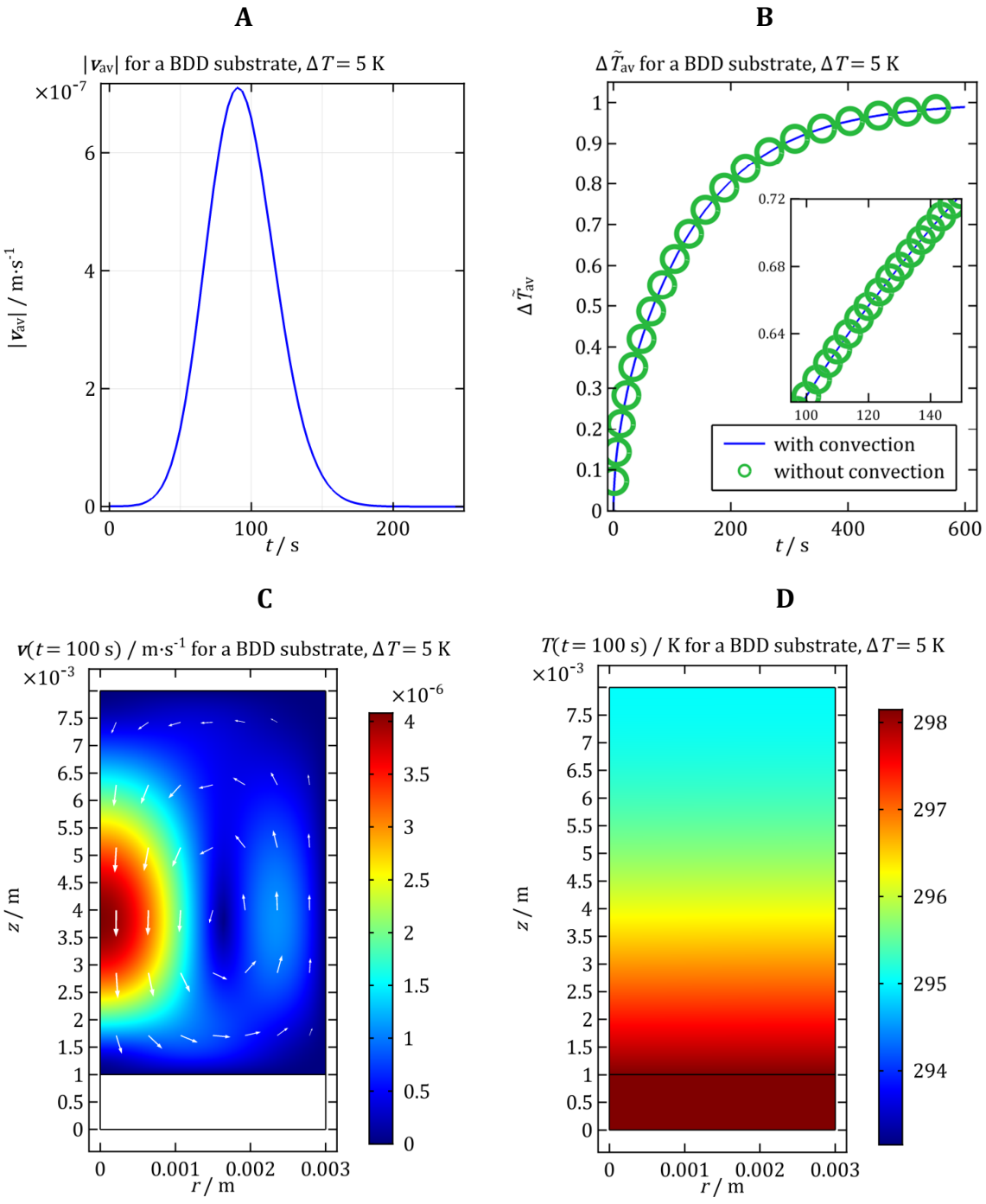


Figure B.2. Results for a homogeneous BDD substrate obtained from a simulation that uses quadratic elements for T: **A** – $|\boldsymbol{v}_{av}(t)|$; **B** – $\Delta\tilde{T}_{av}(t)$; **C** and **D** – 'snapshots' of $\boldsymbol{v}$ and T at t = 100 s, respectively. Note that the fluid moves downward at r = 0 in this case, in contrast with the flow pattern illustrated in Figure 5.2 and Figure B.1.

Stability tests

Cells having a fixed-temperature top wall rather than an insulated one were simulated using both linear and quadratic shape functions for the temperature. The simulations were performed in two runs for each setting – in the first run, the maximum step was set to $\Delta t_{\max} = 5$ s; in the second one, the maximum step was unrestricted. For the simulation using first-order shape functions, the first run was for $t \in [0\text{ s}, 160\text{ s}]$ and the second for $t \in [120\text{ s}, 300\text{ s}]$, whereas for the simulation using second-order shape functions, the runs were for $t \in [0\text{ s}, 180\text{ s}]$ and $t \in [165\text{ s}, 300\text{ s}]$.

The results for the volume-averaged velocity magnitude are plotted versus time in Figure B.3A and Figure B.4A for the two types of simulations. As the figures illustrate, the simulations for long and short times yield identical results for the period of overlap. In both cases, the obtained flow patterns are qualitatively identical to those for a thermally insulated cell – compare the snapshots of $\boldsymbol{v}$ in Figure B.3 and Figure B.4 with these in Figure 5.2 and Figure B.2, respectively. Notably, the plateau values of $|\boldsymbol{v}_{\text{av}}|$ are nearly identical for the two types of flow – 1.127 and 1.129×10^{-4} m·s^{-1} for the clockwise and anticlockwise, respectively; the corresponding temperature distributions are both strongly affected by convection. However, as we see in Figure B.3A and Figure B.4A, the flow pattern with upwelling at $r = 0$ reaches a stationary state quicker. Therefore, we can tentatively conclude that the faster development of one the two flows causes the difference of two orders of magnitude in intensity between them for a cell with insulated walls (Figure 2A vs. Figure B.2). The slower development of the flow with upwelling next to the side walls for the latter system means that by the time the flow pattern is established, the driving force for convection has already diminished significantly, hence the low velocity.

A further indication of the equal stability of the two flows is the fact that upon reverting from Eq. (5.29) back to a no-flux boundary condition, the convective rolls illustrated in Figure B.3-Figure B.4 maintain their direction before reaching a quiescent state.

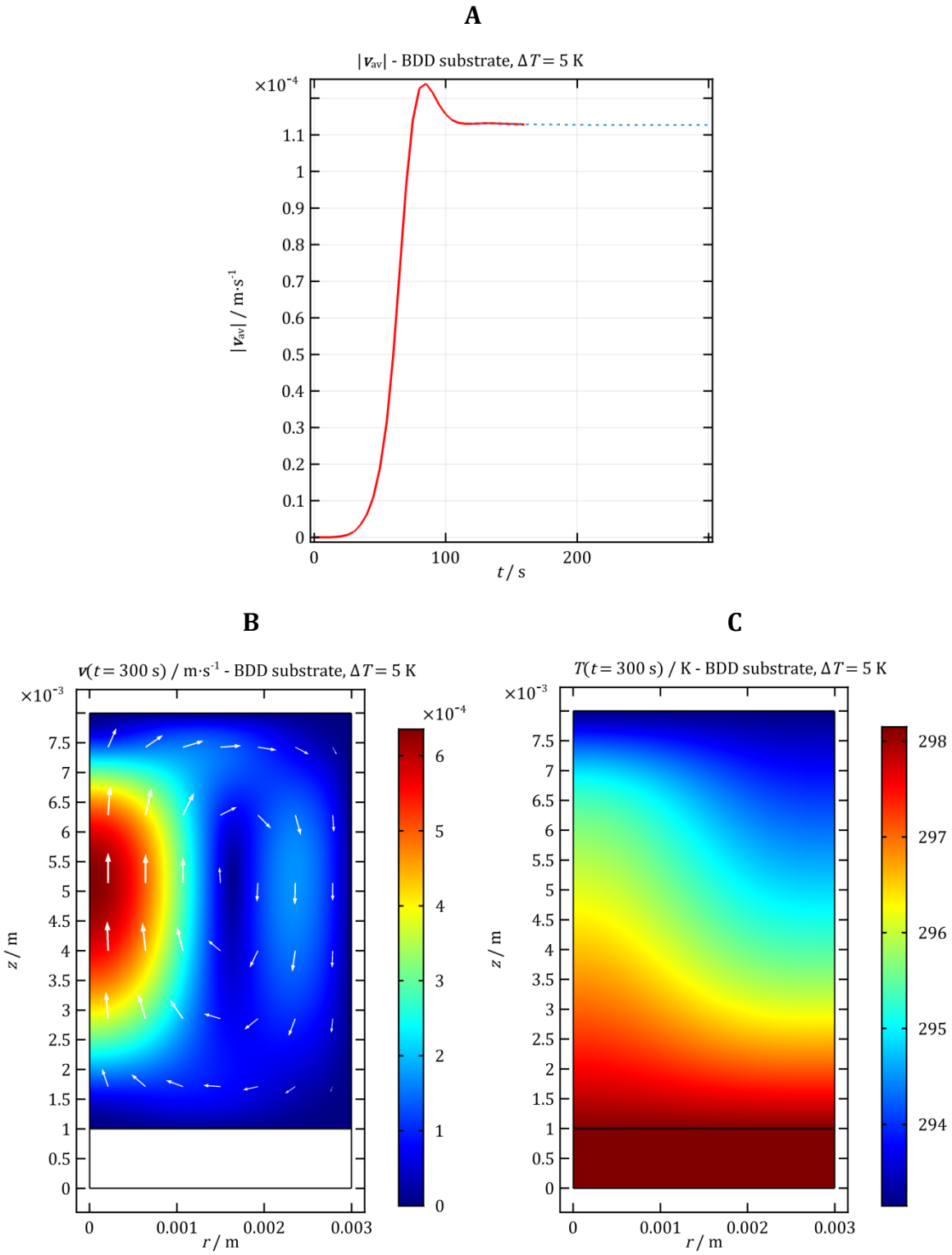


Figure B.3. Results for a simulation with a fixed temperature difference between the top and bottom cell walls. The substrate is made of BDD and linear elements are used for T. **A** – volume-averaged velocity magnitude. Solid line – simulation for short t (0-160 s), dashed line – simulation for long t (120-300 s). **B** – velocity distribution at t = 300 s, **C** – temperature distribution at t = 300 s.

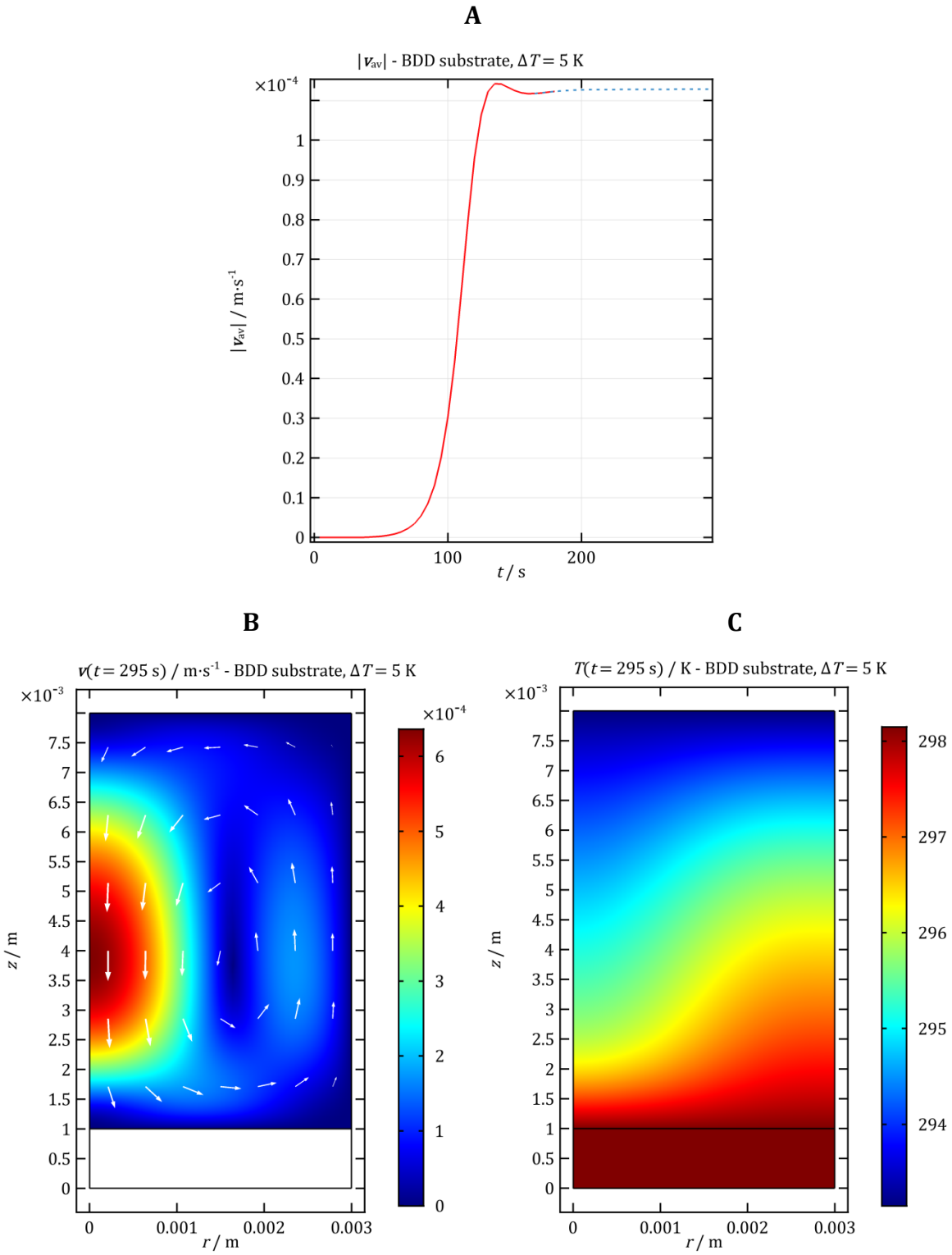


Figure B.4. Results for a simulation with a fixed temperature difference between the horizontal cell walls, The substrate is made of BDD and quadratic elements are used for *T*. **A** – volume-averaged velocity magnitude. Solid line – simulation for short *t* (0-180 s), dashed line – simulation for long *t* (165-300 s). **B** – velocity distribution at *t* = 295 s, **C** – temperature distribution at *t* = 295 s.

A simulation employing quadratic shape functions for T was run with the stationary distributions of T, $\boldsymbol{v}$ and p (at t_0 = 300 s) from the simulation using linear elements as initial conditions and vice versa (with t_0 = 295 s); the maximum time step was Δt_{max} = 5 s for both cases.

In both cases, the flow and temperature patterns from the initial condition remain unchanged throughout the simulated experiment. The average velocity relaxes from the initial condition to a stationary state within a time frame of ~ 30 s, as seen in Figure B.5A-B. Importantly, the simulations yield the same value of $|\boldsymbol{v}_{av}|$ as the one obtained for a stagnant fluid at t = 0, the only difference being the direction of flow. This suggests that the two stationary patterns are simply mirror images of each other and that the asymmetry between Figure B.3 and Figure B.4 is due to the different accuracy of the simulations employing linear and quadratic shape functions.

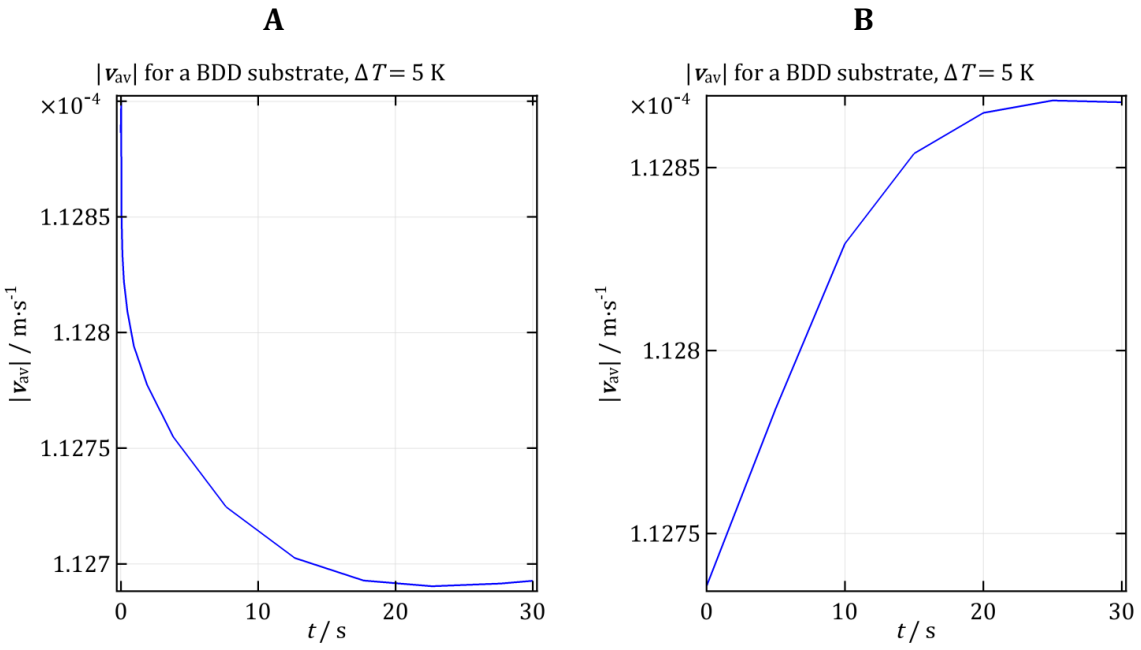
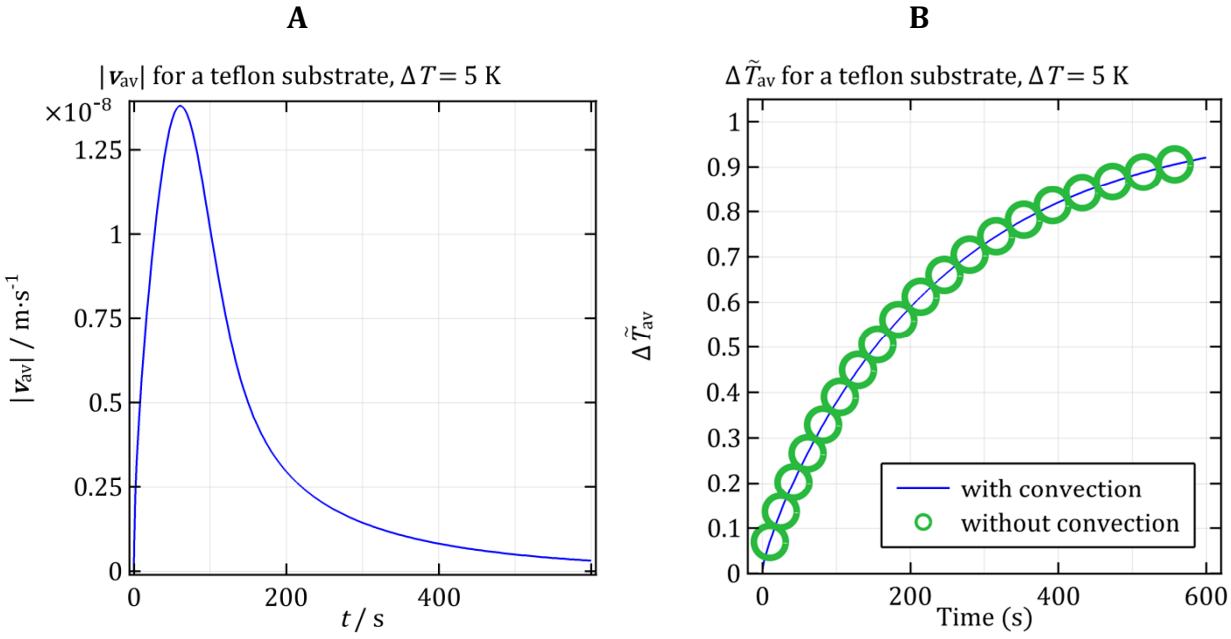


Figure B.5. $|\boldsymbol{v}_{av}(t)|$ for a system with a BDD substrate and a fixed temperature difference between the top and bottom walls: **A** – linear elements for T, initial condition for anticlockwise flow in the simulated region; **B** – quadratic elements for T, initial condition for clockwise flow.

Homogeneous teflon substrate

In this case, the velocity of the convective flows induced in the solution is negligible ($|\boldsymbol{v}_{\mathrm{av}}| \lesssim 10^{-8}$ m·s^{-1}), and our discretization of the governing equations is no longer suitable for its description, which causes the velocity distributions to exhibit high levels of numerical noise. Such low-intensity flows do not have a discernible influence on the temperature profile and would not contribute to mass transport; therefore we do not attempt to study their stability or find settings for the discretization that resolve them better. It is nonetheless worthy of note that, as with the homogeneous BDD substrate, employing linear and quadratic shape functions for T gives rise to two types of flow that differ in their direction and intensity (compare Figure B.6A and Figure B.7A). However, due to the low thermal conductivity of the substrate, the heat flux through its lower surface is not sufficiently intense to induce a strong perturbation in the solution density and a significant convective flow. For that reason, the overall heat transfer is essentially unperturbed by the flow, as demonstrated by the plots of $\Delta\tilde{T}_{\mathrm{av}}$ in Figure B.6C-Figure B.7C, and the temperature profile is approximately independent of r, as it would be in the absence of convection (Figure B.6B-C, Figure B.7B-C).



C

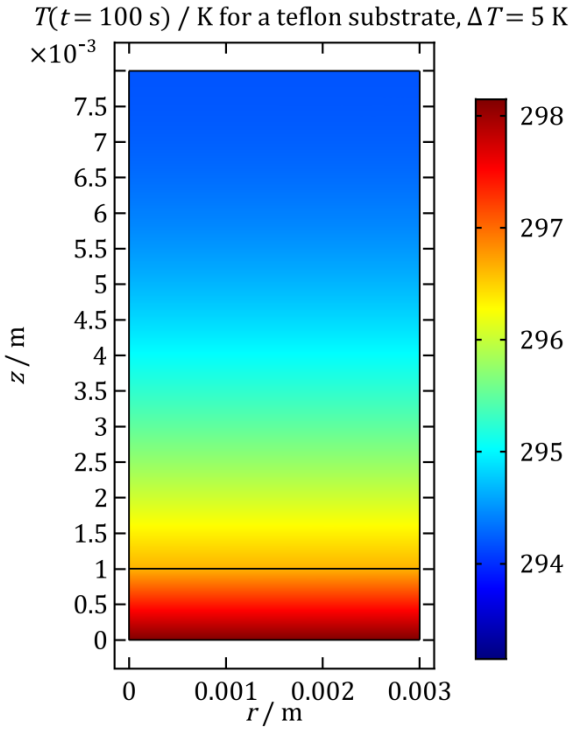
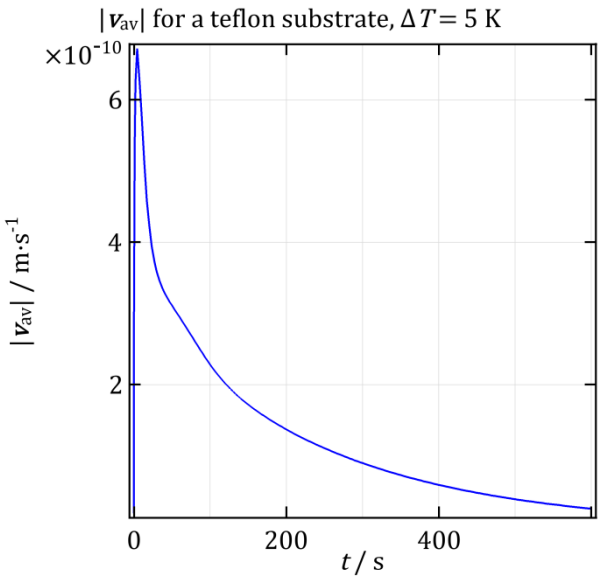
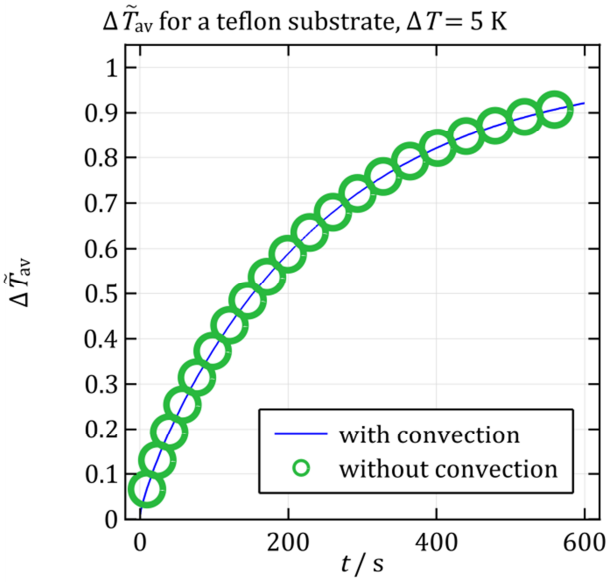


Figure B.6. Results for a cell with a homogeneous teflon substrate at its bottom, simulated using linear elements for T. **A** – volume-averaged velocity, $|\boldsymbol{v}_{av}(t)|$; **B** – volume-averaged dimensionless temperature difference, $\Delta\tilde{T}_{av}$; **C** – temperature distribution at t = 100 s.

A



B



C

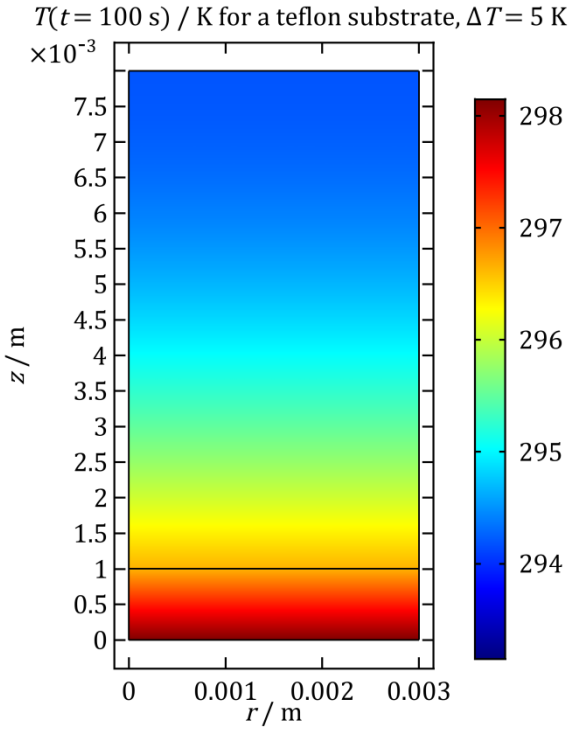


Figure B.7. Results for a cell with a homogeneous teflon substrate at its bottom, simulated using quadratic elements for T. **A** – volume-averaged velocity, $|\boldsymbol{v}_{av}(t)|$; **B** – volume-averaged dimensionless temperature difference, $\Delta\tilde{T}_{av}$; **C** – temperature distribution at t = 100 s.

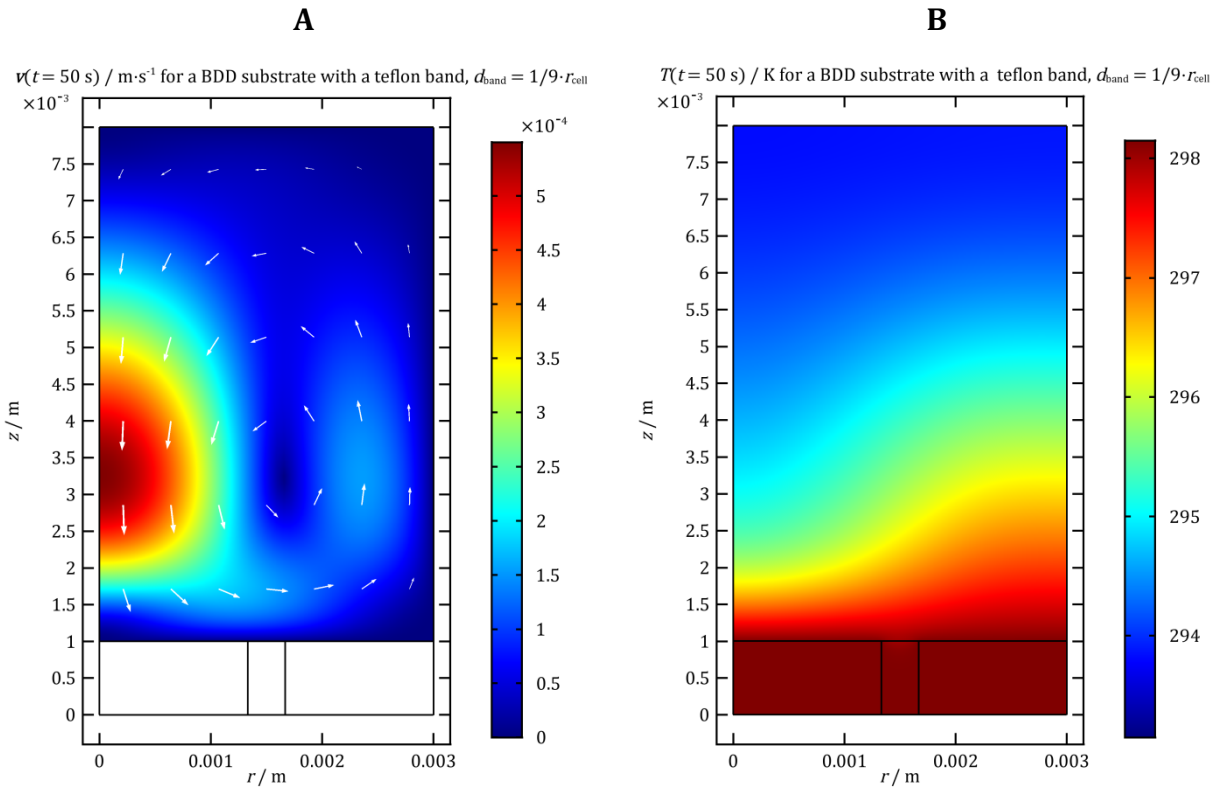
BDD substrates with teflon annular bands

In Figure B.8, we provide 'snapshots' of the velocity and temperature distributions for this configuration at the approximate moment in time when the average solution velocity reaches its peak value, complementing Figure 5.3 from Chapter 5.

Figure B.9 and Figure B.10 present the results from our studies with varying ΔT, depicting the volume-averaged dimensionless temperature difference and the volume-averaged velocity for the different substrates. As seen in Figure B.9, the difference between $\Delta\tilde{T}_{av}$ for the simulations involving convection and the conduction-only case is nearly zero at ΔT = 3 and 4 K, whereas for ΔT = 5 K, it reaches a maximum value of 2.5, 5.8 and 7.5% for d_{band}/r_{cell} = 1/27, 1/9 and 1/3,

respectively. Figure B.10 demonstrates that this qualitative difference in behaviour is brought about by a sharp increase in the average solution velocity.

For verification purposes, we ran simulations of BDD substrates with a teflon annular band employing quadratic shape functions for T, which yielded the same qualitative results as those using linear ones, but the maximum volume-averaged velocity was higher for the second-order polynomials, the variation being 4.2% for $d_{band}/r_{cell} = 1/27$, 0.3% for $d_{band}/r_{cell} = 1/9$ and 0.13% for $d_{band}/r_{cell} = 1/3$.



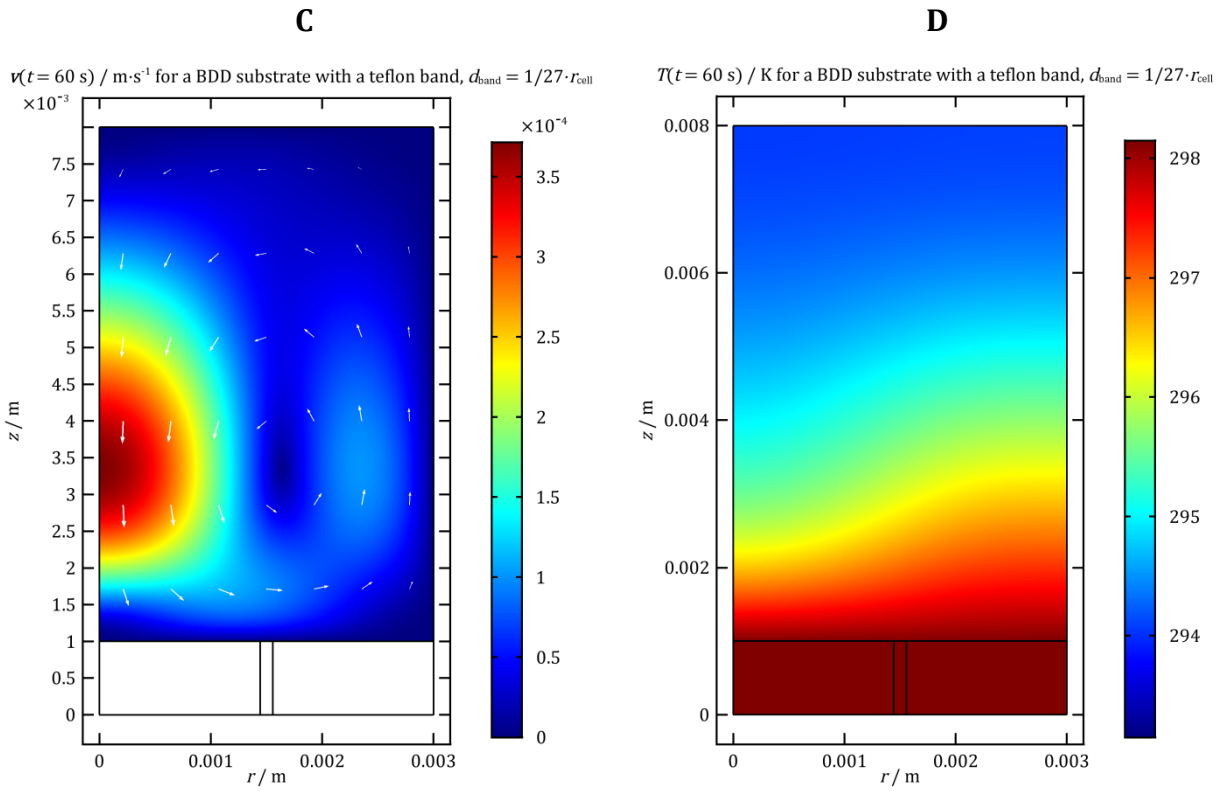
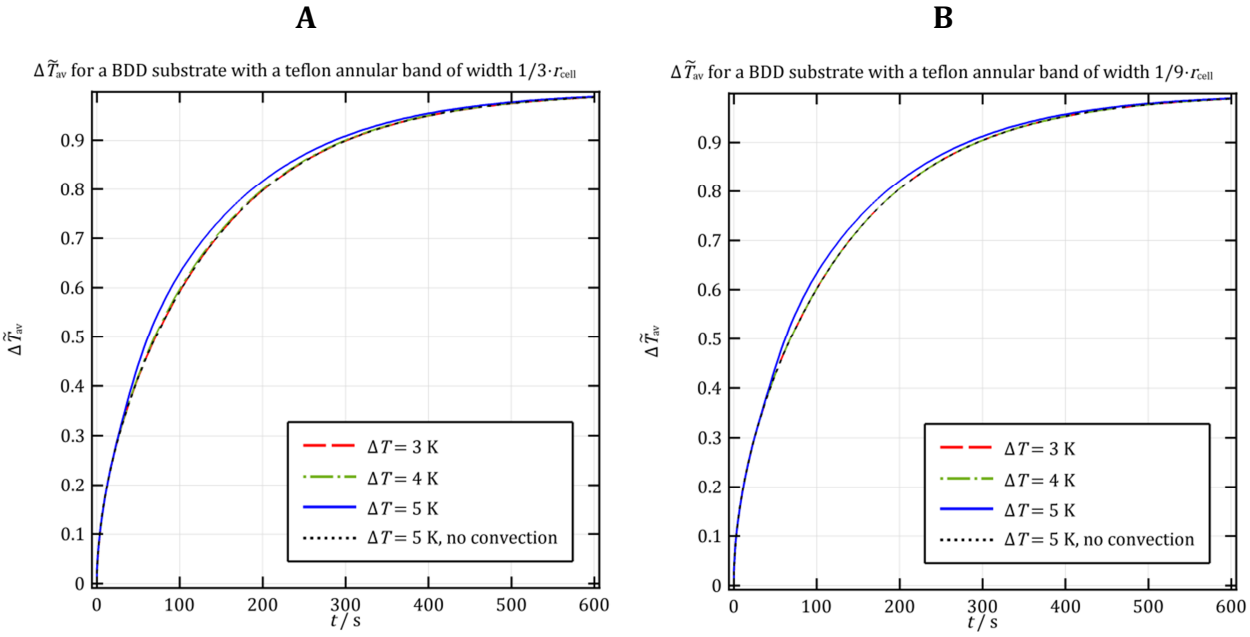


Figure B.8.Results for BDD substrates with a teflon annular band. **A**, **B** – velocity and temperature profiles at t = 50 s for d_{band}/r_{cell} = 1/9; **C**, **D** – $\boldsymbol{v}(t$ = 60 s), $T(t$ = 60 s), d_{band}/r_{cell} = 1/27.



C

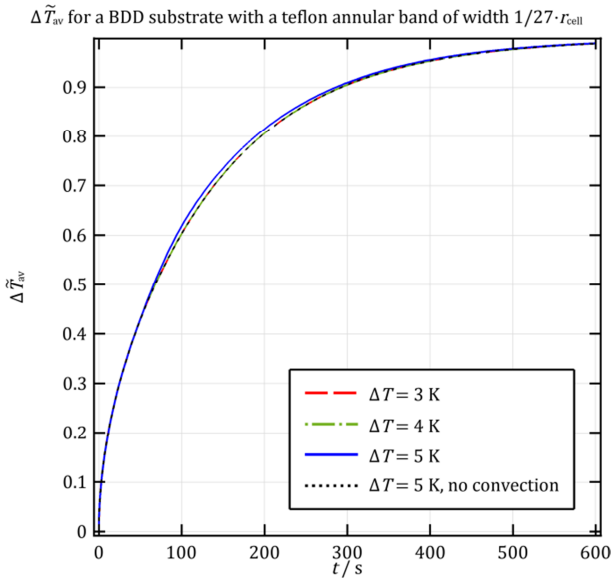
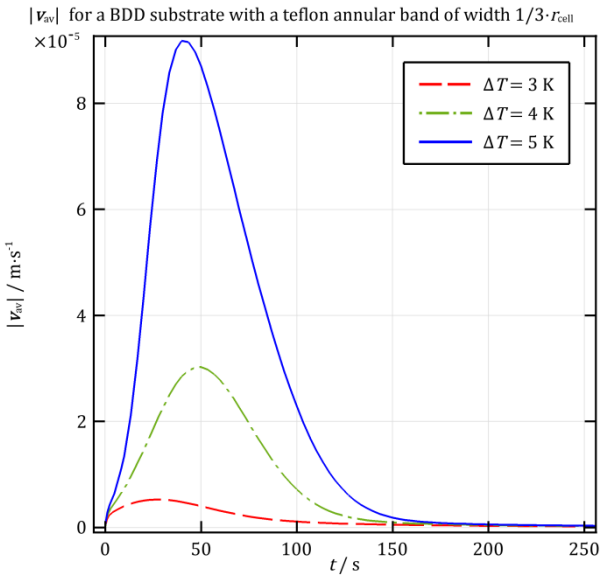
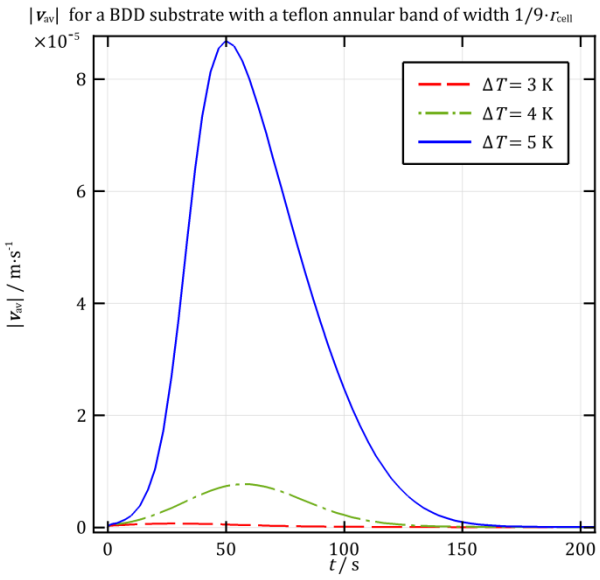


Figure B.9. $\Delta\tilde{T}_{av}(t)$ for BDD substrates with teflon annular bands of varying width, d_{band} equal to **A** – $r_{cell}/3$, **B** – $r_{cell}/9$, **C** – $r_{cell}/27$. The convective simulations are conducted at various values of the initial temperature difference ΔT, as per the legend, and compared with a simulation that accounts for conduction only.

A



B



C

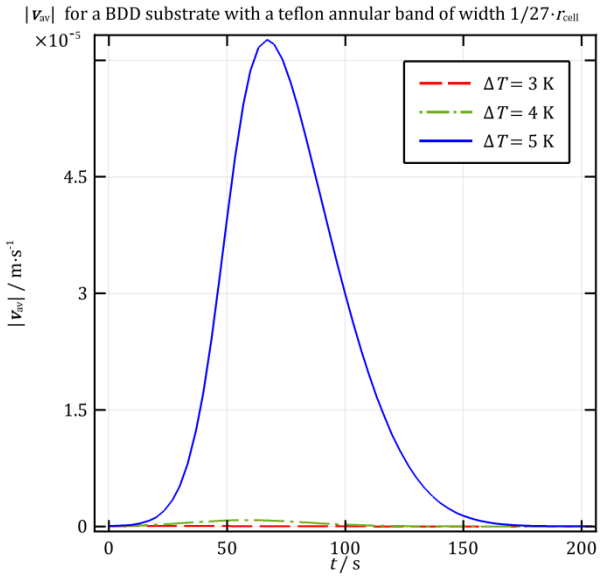


Figure B.10 $|\boldsymbol{v}_{av}(t)|$ for BDD substrates with teflon annular bands of varying width, d_{band}, equal to **A** – $r_{cell}/3$, **B** – $r_{cell}/9$, **C** – $r_{cell}/27$.

Stability tests

We performed a qualitative stability analysis of the flows observed for BDD substrates with teflon annular bands. To do this, we substituted the no-flux boundary condition at the top wall with Eq. (5.29), as we did for homogeneous BDD substrates.

The simulations were performed in two stages, the first having a maximum time step of 3.5 s, covering the period $t \in [0\text{ s}, 115\text{ s}]$. The second stage had an unrestricted maximum time step and was for the interval $[t_{in}, 300\text{ s}]$, where $t_{in} =$ 90.9 s, 89.8 s and 93.3 s for $d_{band}/r_{cell} = 1/3$, 1/9 and 1/27, respectively. As the plot of $|\boldsymbol{v}_{av}(t)|$ in Fig. B.11A shows, the results from the two stages are consistent with each other in the region of overlap. The flow patterns and the temperature profiles at the stationary state, shown in Fig. B.11B-C for $d_{band}/r_{cell} = 1/3$, are consistent with those obtained for a cell with thermally insulated walls in that the fluid moves downwards at the cylinder axis, compare with Figure 5.3.

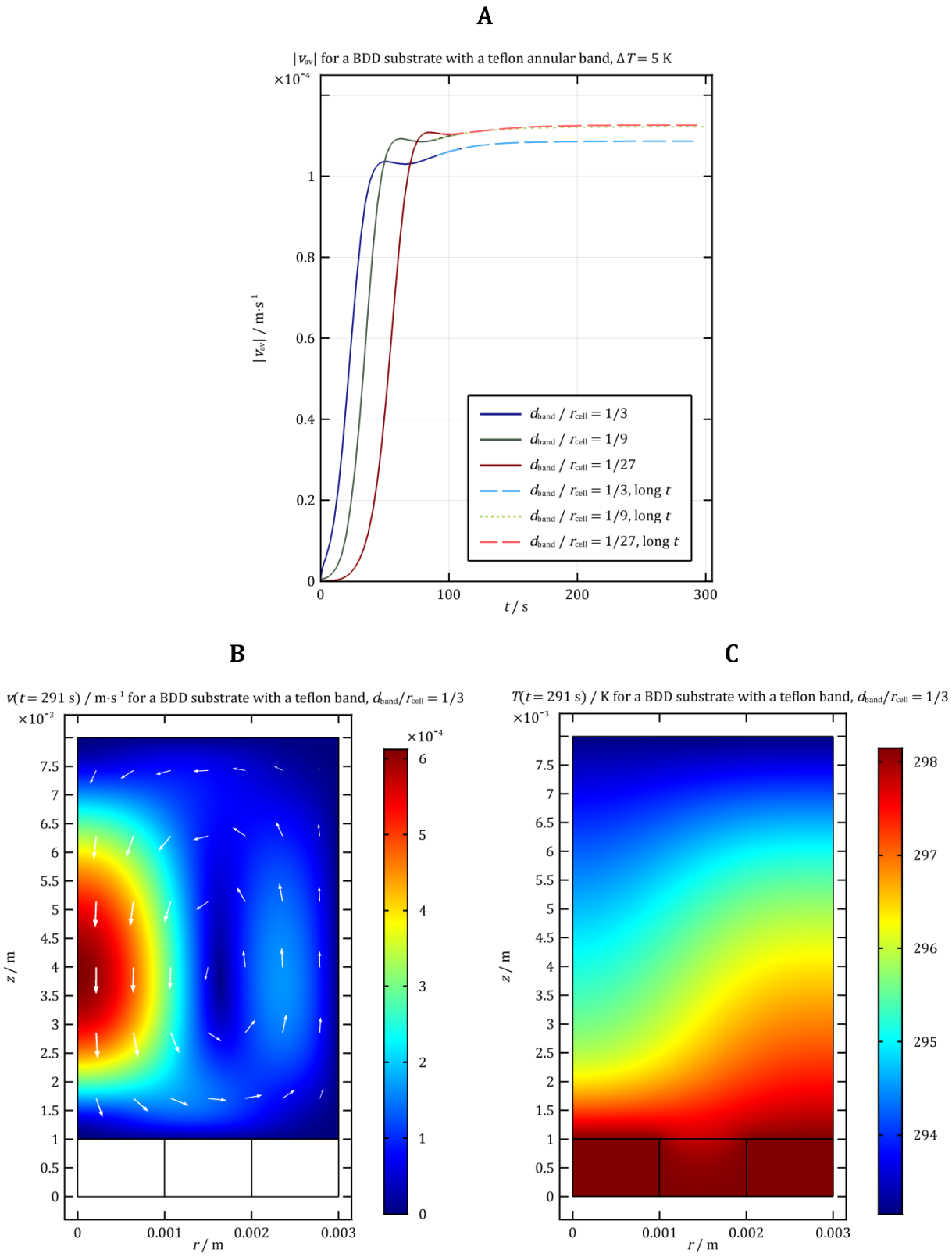


Figure B.11. Results for simulations with a fixed temperature difference between the top and bottom cell walls, The substrate is made of BDD and has a teflon annular band. **A** – volume-averaged velocity magnitude. Solid lines – simulations for short t, dashed/dotted lines – simulations for long t (see text for details). **B** and **C** – velocity and temperature distributions for d_{band}/r_{cell} = 1/3 at t = 291 s.

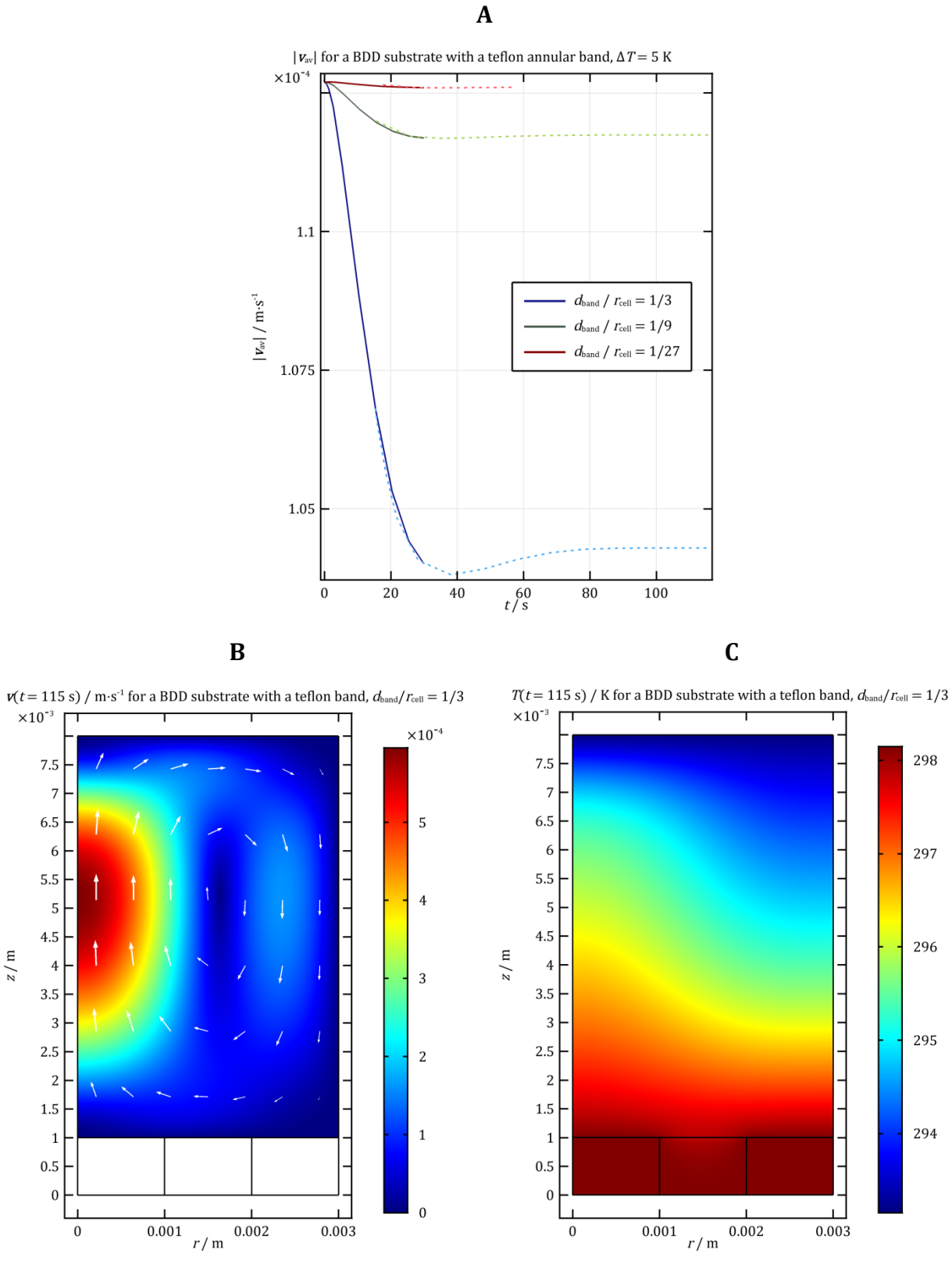


Figure B.12. Results for BDD substrates with teflon annular bands from simulations with a fixed temperature difference between the top and bottom cell walls. The initial conditions for $\boldsymbol{v}$, T^{L} and p correspond to upwelling in the cylinder centre and

are taken from the simulation of a homogeneous BDD substrate that uses linear elements for T. T^S is taken from the stationary prediction of the simulation of the same substrate with stagnant initial conditions. **A** – volume-averaged velocity magnitude. Solid lines – simulations for short t, dashed/dotted lines – simulations for long t (see text for details). **B** and **C** – velocity and temperature distributions for $d_{band}/r_{cell} = 1/3$ at $t = 115$ s.

We tested the stability of the observed flow pattern with upwelling at the side wall of the cylinder qualitatively by taking $\boldsymbol{v}$, T and p at the stationary state at $t \approx 300$ s as initial conditions, and reverting to a no-flux boundary condition at the top wall. This had no qualitative effect on the flow pattern apart from leading to a gradual decay and the eventual establishment of a quiescent equilibrium state, as in our other simulations of cells with thermally insulated walls.

As for homogeneous conductive substrates, we performed additional studies of the stability of the flow pattern in which there is upwelling instead of downflow at $r = 0$, i.e., the approximate mirror image of the one discussed above. To do this, we took the stationary velocity profile with clockwise motion in the simulated region from the simulation of a homogeneous BDD substrate with the boundary condition (5.29), as well as the stationary distributions of the pressure and the temperature of the liquid (all at $t \approx 300$ s). For T^S, we used the stationary distribution at $t \approx 300$ s for the respective d_{band} as obtained from the simulations of BDD substrates with teflon annular bands with initial conditions for stagnant solution. The simulations were run in two stages, the first one covering the temporal interval [0 s, 30 s] and having a maximum time step of 5 s. The second stage was for $t \in$ [15.39 s, 120 s], [15.658 s, 120 s] and [17.68 s, 65 s] for $d_{band}/r_{cell} = 1/3$, 1/9 and 1/27, respectively and had no restriction on the time step. The length of the simulated experiment was greater for the larger annular bands because of the longer characteristic time for attaining a stationary velocity profile (see Figure B.12A). The initial velocity and temperature distributions in the liquid were preserved qualitatively, as shown in Figure B.12B-C. This indicates that toroidal rolls with upwelling at $r = 0$ and $r = r_{cell}$ are

approximately equivalent in stability provided that driving force for convection is constant.

As an additional test of the stability of the flow pattern with upwelling at $r = 0$, which we did not observe for simulations with stagnant initial conditions, we ran simulations with the top boundary condition changed back to no-flux and using as initial conditions the distributions of $\boldsymbol{v}$, T and p at the stationary state as predicted by the simulations illustrated in Figure B.12. The flow patterns underwent complex evolution and the upwelling at $r = 0$ was not preserved. Thus, our data suggests that for BDD substrates with a teflon annular band, the roll with downward fluid motion at the cylinder axis is more stable under transient conditions than its approximate mirror image about $z = h_s$, even though the two are equivalent in stability under stationary conditions.

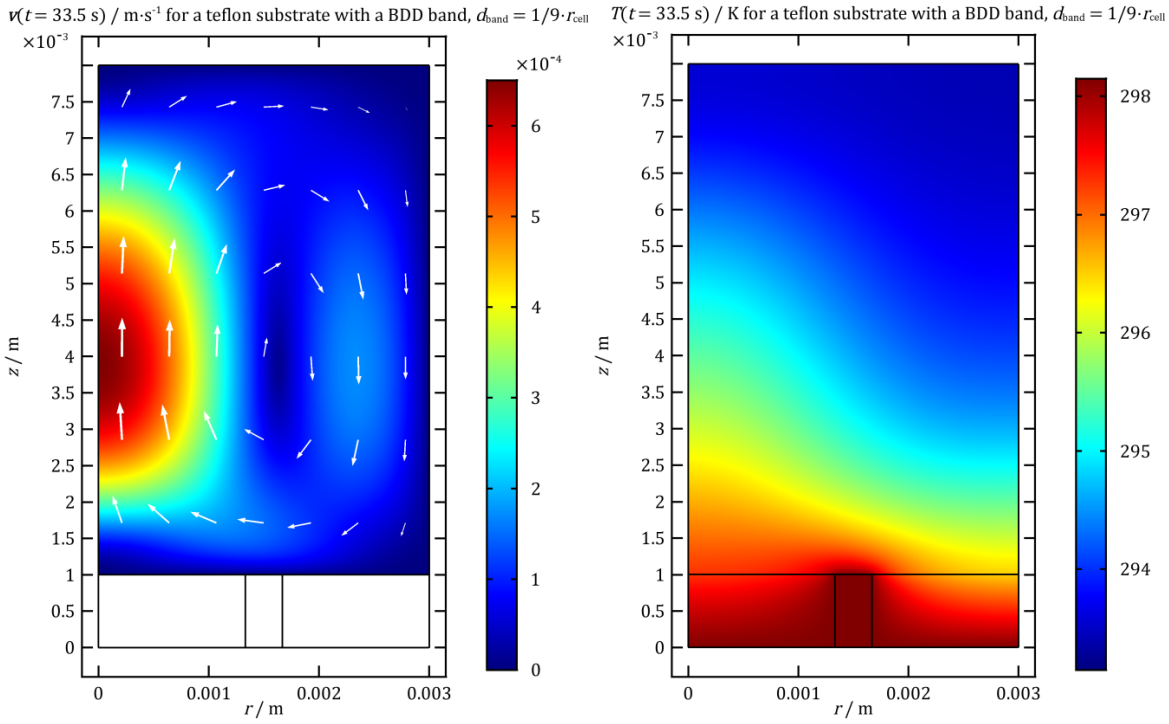
Teflon substrates with BDD annular bands

Figure B.13 shows 'snapshots' of $\boldsymbol{v}$ and T for model cells with insulated top and side walls in contact with teflon substrates with BDD annular bands. The plots in Fig. B.13A-D illustrate the velocity and temperature distribution for $d_{band}/r_{cell} = 1/9$ and $1/27$ at a moment of time chosen to be close to the peak of $|\boldsymbol{v}_{av}(t)|$ and thus complement Figure 5.4B-C.

In Figure B.14 and Figure B.15, we present $|\boldsymbol{v}_{av}(t)|$ and $\Delta\tilde{T}_{av}(t)$ for $d_{band}/r_{cell} = 1/9$ and $1/27$ at varying initial temperature differences. As in the case with $d_{band}/r_{cell} = 1/3$ (Figure 5.5 in Chapter 5), we see a sharp increase in the convective velocity that causes $\Delta\tilde{T}_{av}(t)$ to deviate significantly from the conduction-only case as ΔT is increased from 4 to 5 K. However, whereas for $d_{band}/r_{cell} = 1/3$, there is a discernible effect of convection on $\Delta\tilde{T}_{av}$ at $\Delta T = 4$ K, no such difference is seen for substrates with thinner conductive bands. This suggests that for $d_{band}/r_{cell} = 1/9$ and $1/27$, Ra_{cr} is higher than for $d_{band}/r_{cell} = 1/3$ and is between 1.9×10^4 and 2.4×10^4. At $\Delta T = 5$ K, the relative difference in $\Delta\tilde{T}_{av}$ between convective and purely conductive simulations involving no convection reaches a maximum value of 5.5%, 8.0% and 11.5% for $d_{band}/r_{cell} = 1/27$, $1/9$ and $1/3$, respectively.

For verification purposes, we performed simulations employing quadratic shape functions for T, as we did for the 'inverse' configuration. We arrived at identical results to the ones obtained using linear elements, again with minor differences in the numerical values, the variation in $|\boldsymbol{v}_{av}|_{max}$ being 0.5% for d_{band}/r_{cell} = 1/27, 1.1% for d_{band}/r_{cell} = 1/9 and 0.4% for d_{band}/r_{cell} = 1/3.

A **B**



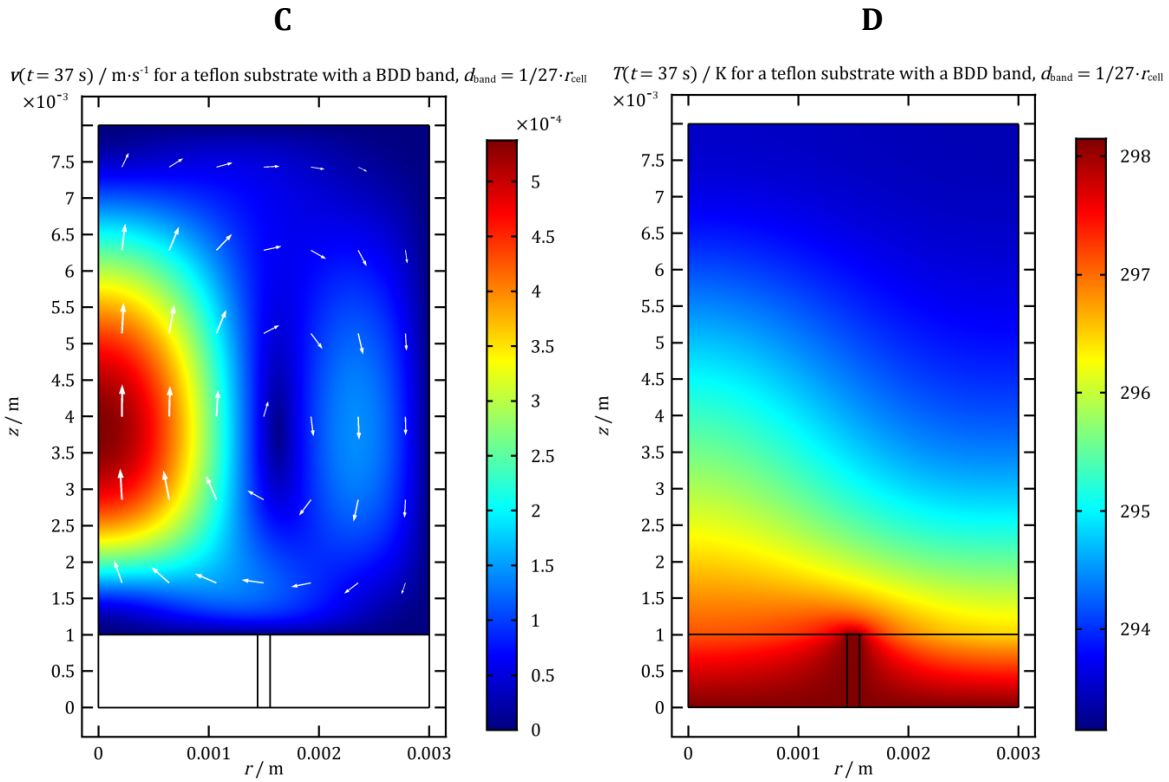


Figure B.13. Results for teflon substrates with BDD annular bands. **A**, **B** – velocity and temperature profiles at t = 33.5 s for d_{band}/r_{cell} = 1/9; **C**, **D** – $\boldsymbol{v}(t$ = 37 s), $T(t$ = 37 s), d_{band}/r_{cell} = 1/27.

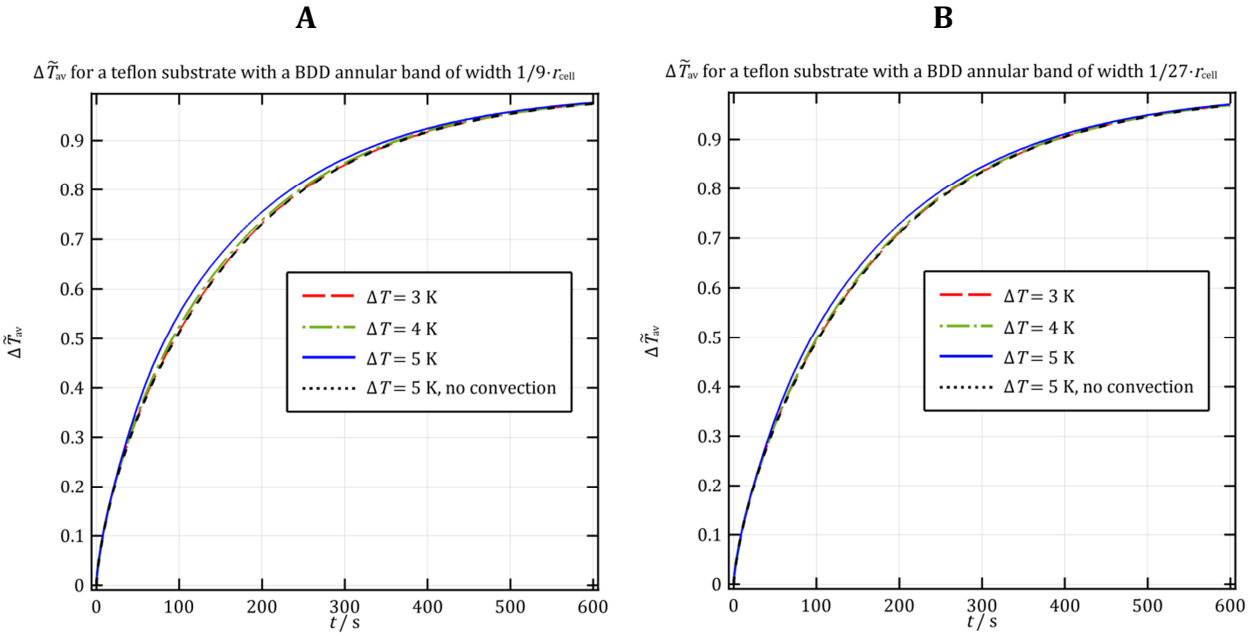


Figure B.14. $\Delta\tilde{T}_{av}(t)$ at varying initial temperature differences ΔT for teflon substrates with BDD annular bands of varying width, d_{band} equal to **A** – $r_{cell}/9$, **B** – $r_{cell}/27$.

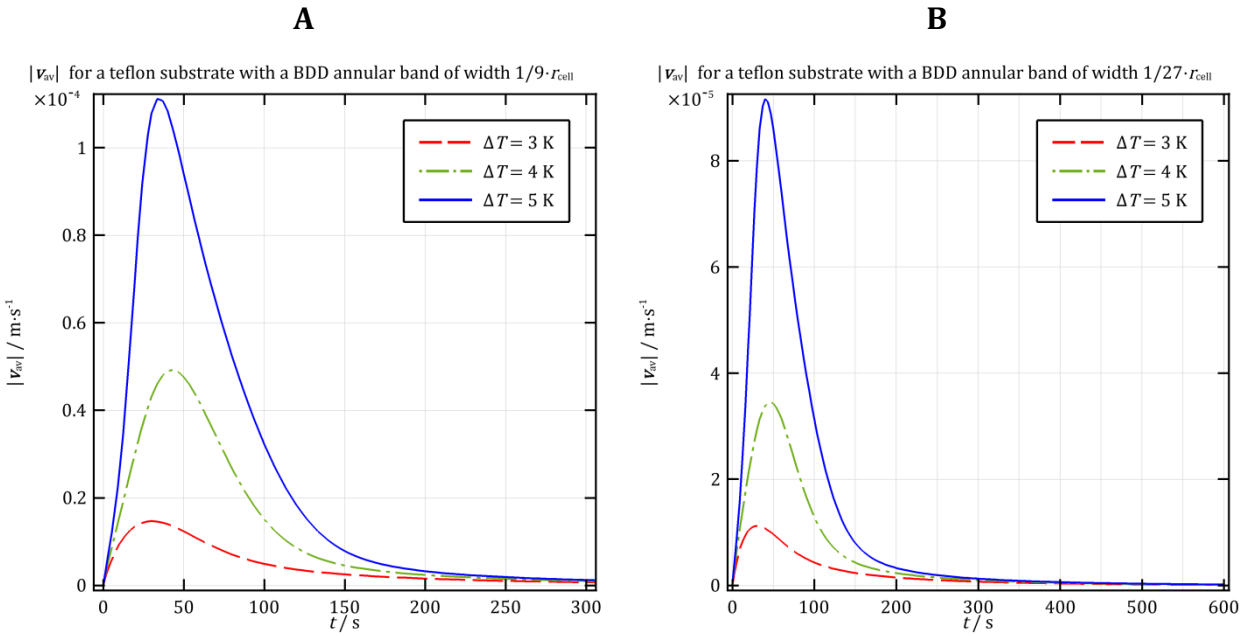


Figure B.15. $|\boldsymbol{v}_{av}|$ at varying initial temperature differences ΔT for teflon substrates with BDD annular bands of varying width, d_{band} equal to **A** – $r_{cell}/9$, **B** – $r_{cell}/27$.

Stability tests

Simulations of teflon substrates with BDD annular bands were also run with linear elements for T and the boundary condition (5.29) that permits a stationary state. As in the previous cases, the simulations were run with a restriction on the maximum time step (Δt_{max} = 3.5 s) at short t and with no restriction at long t. The simulated time periods were [0 s, 100 s] for the initial stage and [t_{in}, 300 s] for the latter one, where t_{in} = 79.1 s, 78.7 s and 75.7 s for $d_{band}/r_{cell} = 1/3$, 1/9 and 1/27, respectively. Figure B.16A presents the dependence of $|\boldsymbol{v}_{av}|$ on t for these cases and demonstrates that the simulations for long t agree with those for short t at the region of overlap. The stationary flow patterns and the temperature distributions, illustrated in Figure B.16B-C for $d_{band}/r_{cell} = 1/3$, are qualitatively identical to those observed in the case of a cell with thermally insulated walls, seen in Figure 5.4B-C.

By analogy with our treatment of the 'inverse' configuration, teflon substrates with BDD annular bands, we subjected the flow patterns with upwelling at r = 0 to a simple stability test. For that purpose, we set the boundary condition at the top cylinder wall back to that for thermal insulation and used the profiles $\boldsymbol{v}$, T and p at

the stationary state (as illustrated in Figure B.16) as initial conditions. The flow diminished in intensity as the solution temperature approached its equilibrium state but its direction remained unchanged.

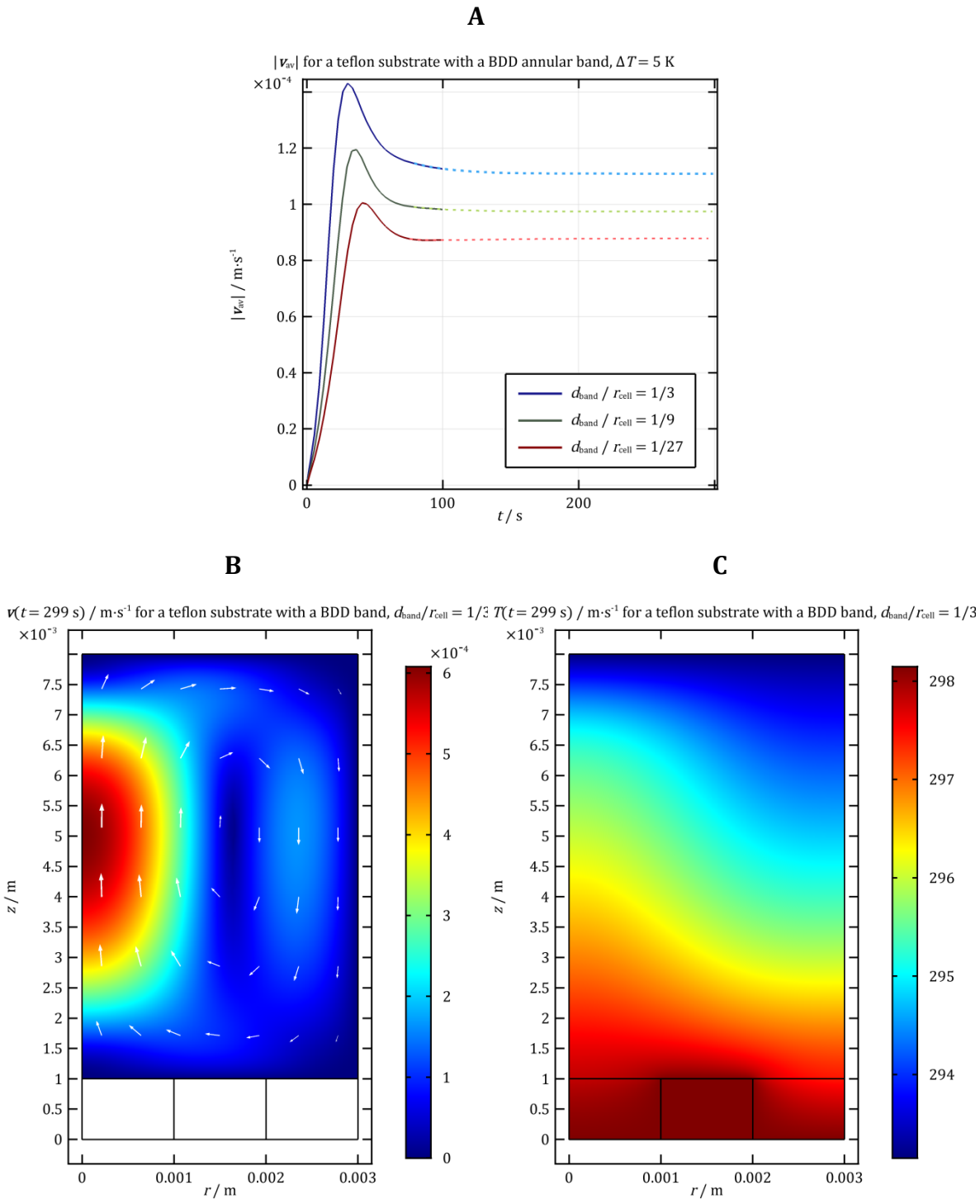


Figure B.16. Results for simulations with a fixed temperature difference between the top and bottom cell walls, The substrate is made of teflon and has a BDD annular band. **A** – volume-averaged velocity magnitude. Solid lines – simulations for short *t*,

dashed/dotted lines – simulations for long t (see text for details). **B** and **C** – velocity and temperature distributions for $d_{band}/r_{cell} = 1/3$ at $t = 299$ s.

As with the case of a homogeneous conductive substrate and a BDD substrate with a teflon annular band, we also tested whether a flow with the opposite direction would be stable. As initial conditions, we took the stationary profiles of $\boldsymbol{v}$, T and p in the liquid from a simulation of a BDD substrate that yields an anticlockwise flow in the simulated region (see Figure B.4) and the stationary temperature distribution in the solid (both at $t \approx 300$ s) from the simulations of the teflon substrates with the corresponding d_{band} and initial conditions for stagnant solution (seen in Figure B.16C for $d_{band} = 1/3 r_{cell}$). The simulations were run in two stages, the first one covering the interval [0 s, 100 s] with a maximum time step of 5 s. For the second stage, encompassing [80 s, 300 s], the time step was unconstrained. In all cases, the flow pattern and the form of the temperature profile of the liquid from the initial condition were preserved. Fig. B.17A illustrates that the system reached a steady state in ~ 200 s, the time scale necessary for the temperature of the substrate to evolve from the profile in the initial condition (Figure B.16C) to the stationary one for the present case (Fig. B.17C). Thus, as in the case of the 'inverse' configuration, the rolls with upwelling and downflow at $r = 0$ are both stable under boundary conditions that permit a stationary flow.

Again by analogy with the case of BDD substrates with teflon annular bands, we also changed the boundary condition back to that for a cell with insulated top and side walls and ran simulations with the stationary profiles of T, $\boldsymbol{v}$ and p from Figure B.17 as initial conditions. For this series of simulations, we observed that the flow pattern underwent multiple qualitative changes before eventually decaying, and that its direction (anticlockwise in the simulated region) was not preserved throughout its evolution. Thus, we can conclude that for teflon substrates with BDD annular bands under transient conditions, the flow pattern with upwelling at $r = 0$ is more stable than its approximate reflection with respect to $z = h_s$, despite the fact that the two are equivalent in stability under stationary conditions.

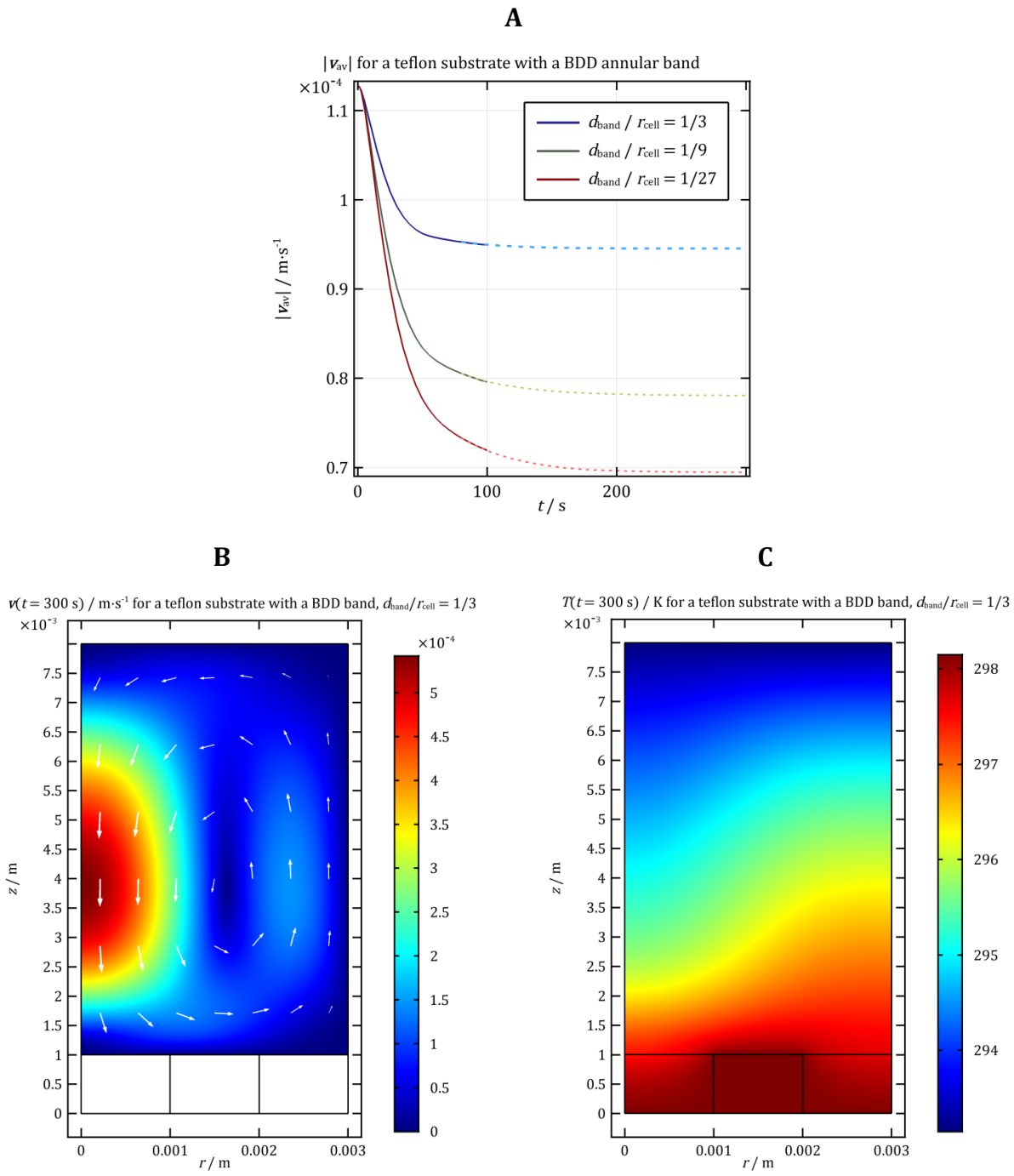
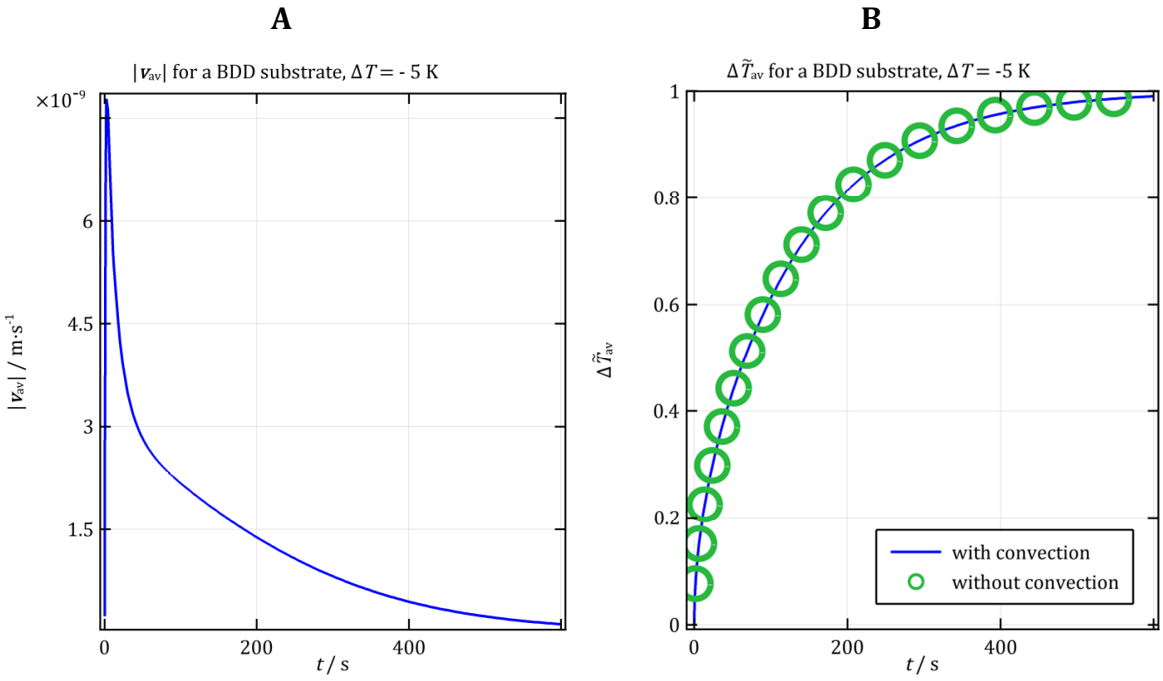


Figure B.17. Results for teflon substrates with BDD annular bands from simulations with a fixed temperature difference between the top and bottom walls. The initial conditions for $\boldsymbol{v}$, T^{L} and p correspond to upwelling at the side wall of the cylinder centre and are taken from the simulation of a homogeneous BDD substrate that uses quadratic elements for T. T^{S} is taken from the stationary prediction of the simulation of a teflon substrate with a BDD annular band with the respective value of d_{band} that employs stagnant initial conditions. **A** – volume-averaged velocity magnitude. Solid lines – simulations for short t, dashed/dotted lines – simulations for long t (see text for details). **B** and **C** – $\boldsymbol{v}$ and T distributions for $d_{\mathrm{band}}/r_{\mathrm{cell}} = 1/3$ at $t = 300$ s.

B.1.1.B. *Solution warmer than substrate at* $t = 0$ ($\Delta T < 0$)

Homogeneous BDD substrate

The maximum flow velocity for this case is of the order of $\sim 10^{-9}$ m·s^{-1}, independent of the order of elements used for T (Figs. B.18A, B.19A), thereby making convective heat transfer negligible, as seen in the temperature profile within the solution, as well as in $\Delta\tilde{T}_{av}(t)$, Figs. B.18B, D; B.19B-C. In this system, the solution temperature is expected to be stably stratified and observed flows are likely caused by numerical noise, as the fluctuations of $|\boldsymbol{v}|$ seen within the bulk of the liquid in Fig. B.18C suggest. Thus, we do not discuss the stability of these flows here.



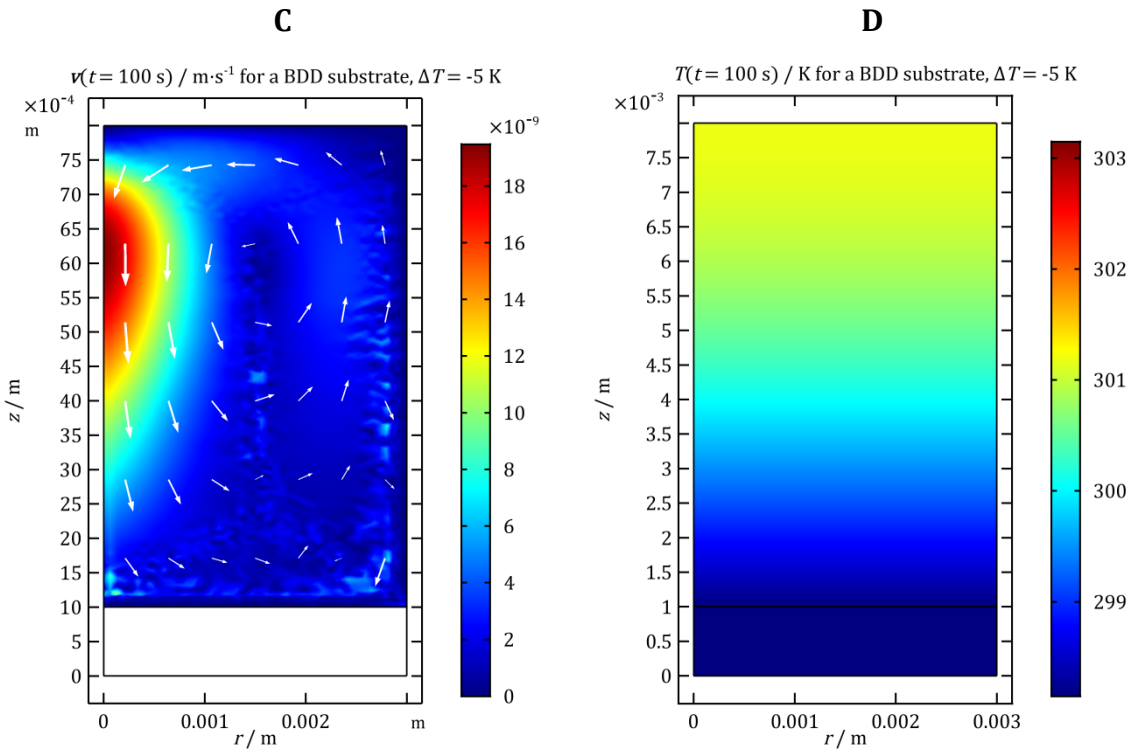
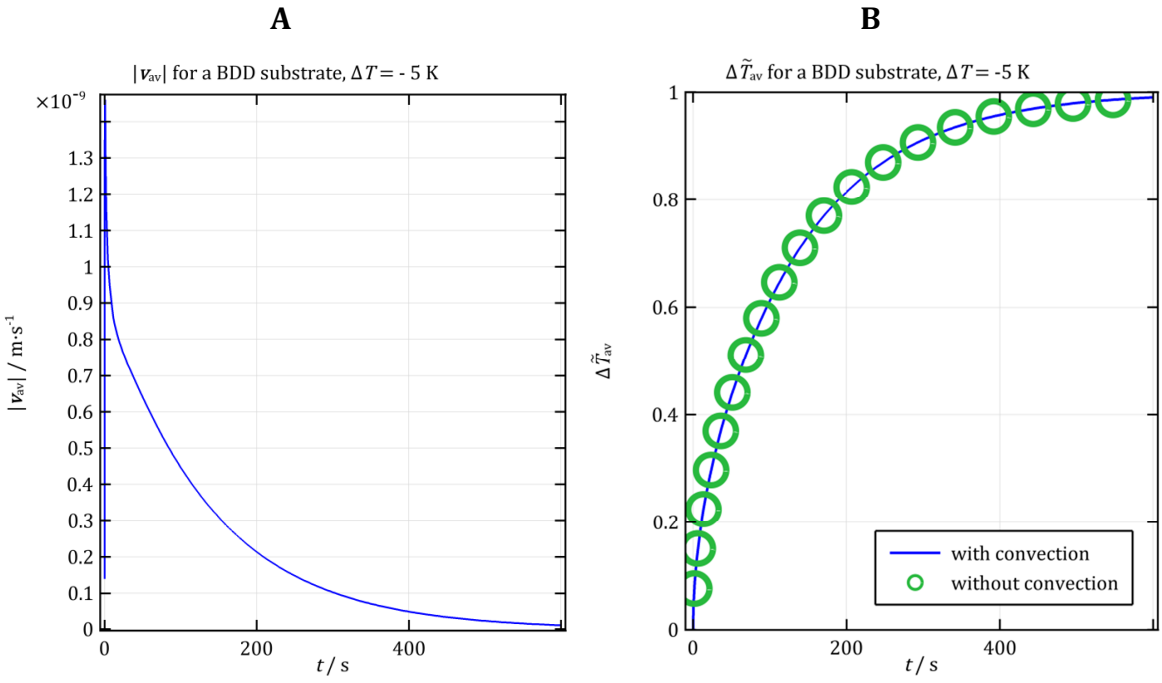


Figure B.18. Results for a homogeneous BDD substrate obtained from a simulation that uses linear elements for T; the solution is initially warmer than the substrate and $\Delta T = -5$ K. **A** – volume-averaged velocity magnitude vs. time; **B** – volume-averaged dimensionless temperature difference; **C** – 'snapshot' of T at t = 100 s.



C

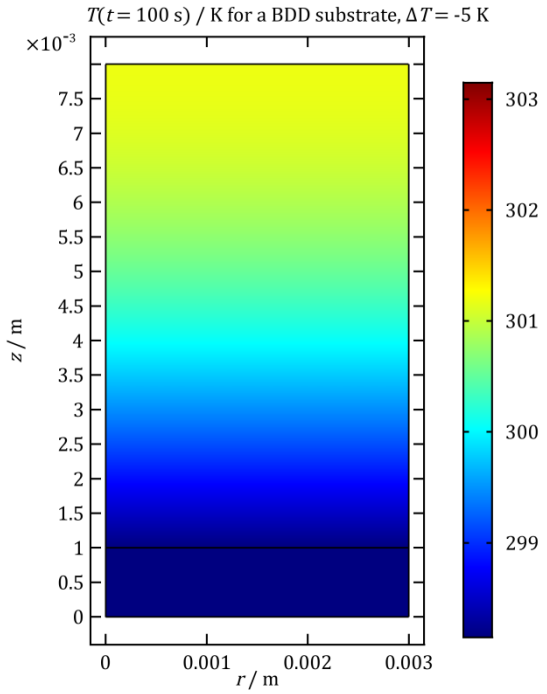


Figure B.19. Results for a homogeneous BDD substrate obtained from a simulation that uses quadratic elements for T; the solution is initially warmer than the substrate and $\Delta T = -5$ K. **A** – volume-averaged velocity magnitude vs. time; **B** – volume-averaged dimensionless temperature difference; **C** – 'snapshot' of T at $t = 100$ s.

Homogeneous teflon substrate

In this case, the average solution velocity is again negligible – it reaches a peak value of just 10^{-10} to 10^{-9} m·s^{-1}, depending on whether linear or quadratic elements are used, see Figs. B.20A and B.21A. The convective flow is again likely due to numerical noise and is not sufficiently intense to affect the heat transfer, as demonstrated by the plots of $\Delta\tilde{T}_{\mathrm{av}}$ versus t in Figs. B.20B and B.21B and the temperature profiles in Figs. B.20C and B.21C. As we are not interested in flows of such low velocity, we do not probe their stability here.

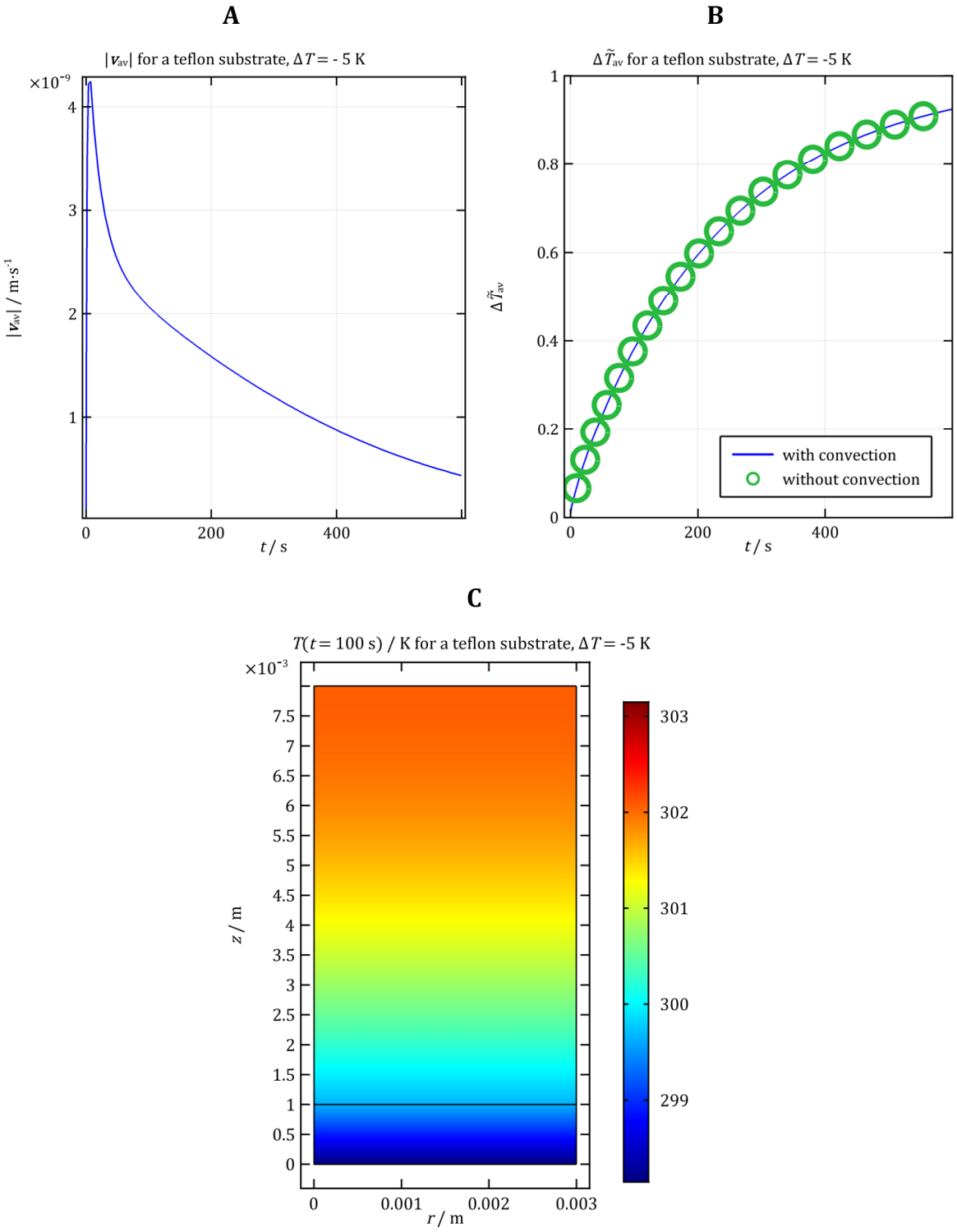


Figure B.20. Results for a homogeneous teflon substrate obtained from a simulation that uses linear elements for T; the solution is initially warmer than the substrate and $\Delta T = -5$ K. **A** – volume-averaged velocity magnitude vs. time; **B** – volume-averaged dimensionless temperature difference; **C** – 'snapshot' of T at $t = 100$ s.

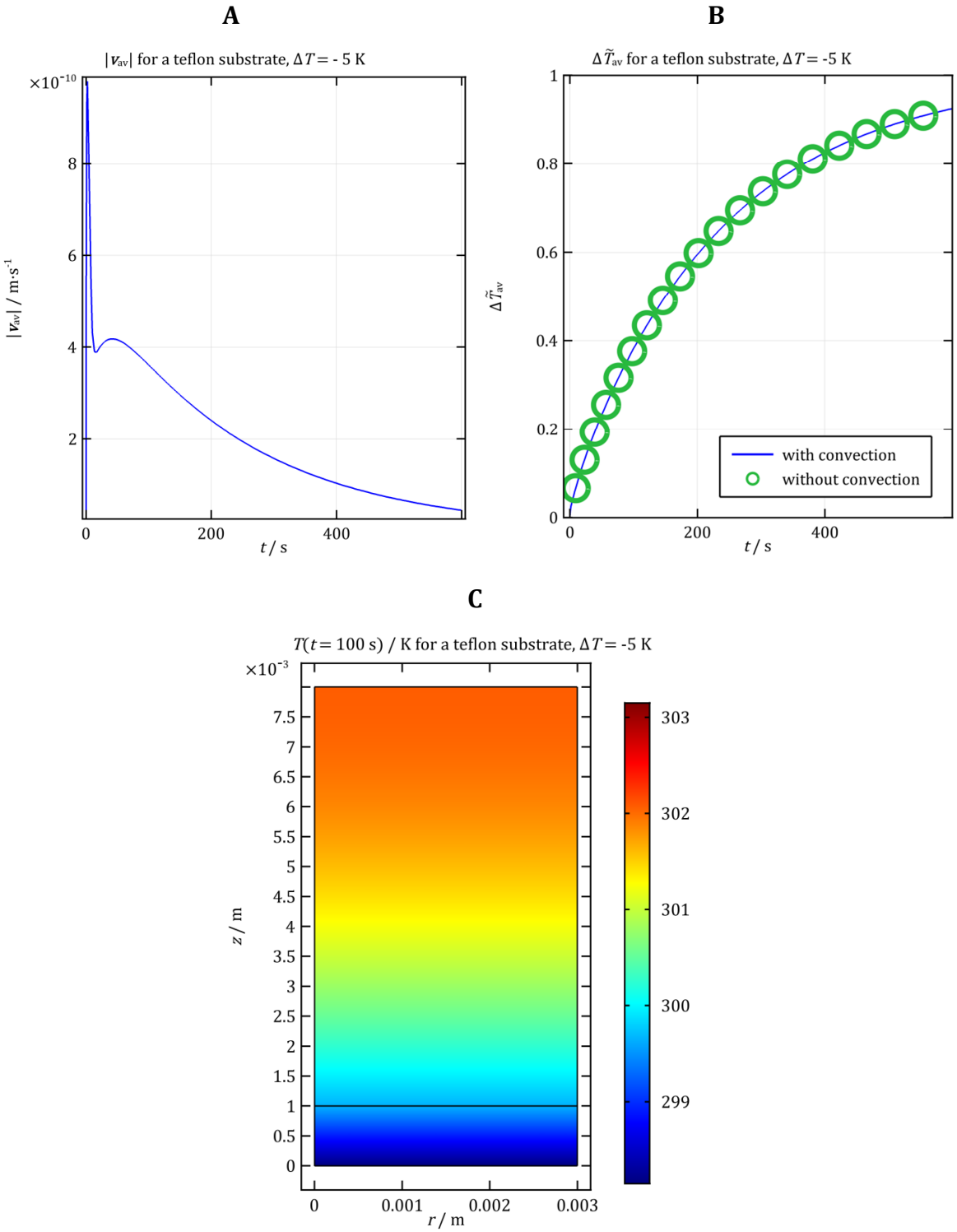


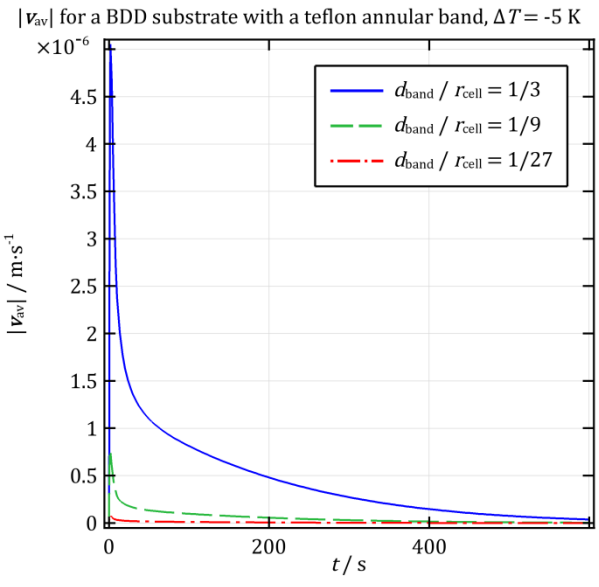
Figure B.21. Results for a homogeneous teflon substrate obtained from a simulation that uses quadratic elements for T; the solution is initially warmer than the substrate and $\Delta T = -5$ K. **A** – volume-averaged velocity magnitude vs. time; **B** – volume-averaged dimensionless temperature difference; **C** – 'snapshot' of T at t = 100 s.

BDD substrates with teflon annular bands

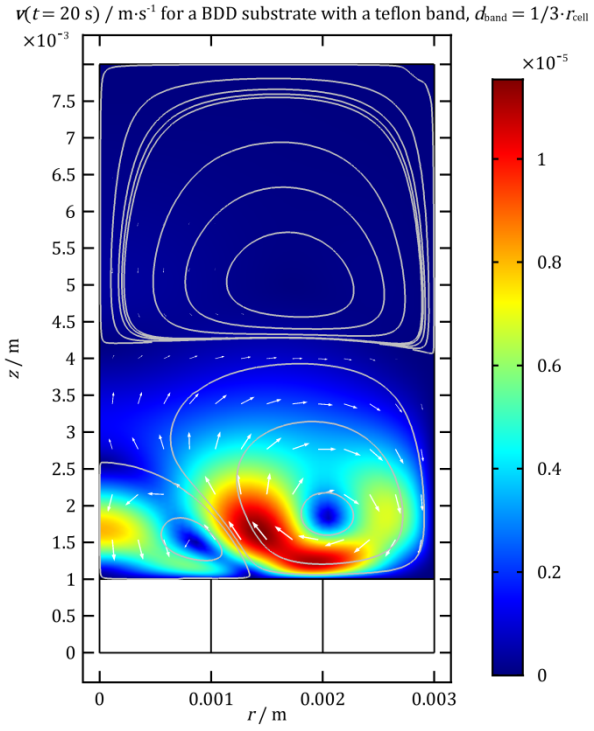
In Fig. B.22, we present the average velocity, as well as 'snapshots' of $\boldsymbol{v}$ and T for BDD substrates with teflon annular bands situated within cells with insulated side and top walls at $\Delta T = -5$ K. Notably, as Fig. B.22A illustrates, the intensity of the flow strongly depends on the width of the insulating annular band – the maximum velocity is 8.5×10^{-8} m·s^{-1} for $d_{band}/r_{cell} = 1/27$, 7.7×10^{-7} m·s^{-1} for $d_{band}/r_{cell} = 1/9$ and $5.1\text{x}10^{-6}$ m·s^{-1} for $d_{band}/r_{cell} = 1/3$. However, as seen in Figure B.23, for all of the studied values of d_{band}, the convective flow within the solution has no appreciable effect on the overall heat transfer within the solution. Although we also simulated systems with $\Delta T = -3$ and -4 K, we do not show results here since, unlike the case of $\Delta T > 0$, there is no threshold value of Ra, and $\Delta\tilde{T}_{av}$ remains unaffected for all $\Delta T < 0$.

For the purpose of verifying our results, we also performed the same simulations with quadratic elements for T. This led only to a quantitative difference in the observed toroidal rolls, namely an increase in $|\boldsymbol{v}_{av}|_{max}$ of 1.3%, 0.8% and 5.3% for $d_{band}/r_{cell} = 1/3$, 1/9 and 1/27, respectively. The variability of $|\boldsymbol{v}_{av}|_{max}$ with the element order is likely due to the different numerical accuracy of the two schemes. The comparatively large deviation for $d_{band} = 1/27 \cdot r_{cell}$ is unimportant as for such a thin band, the flows within the solution are negligible and contain high levels of noise.

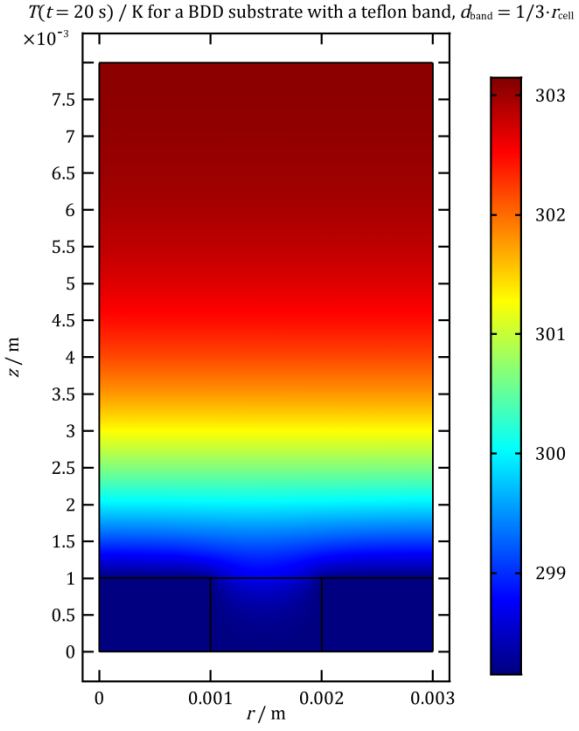
A



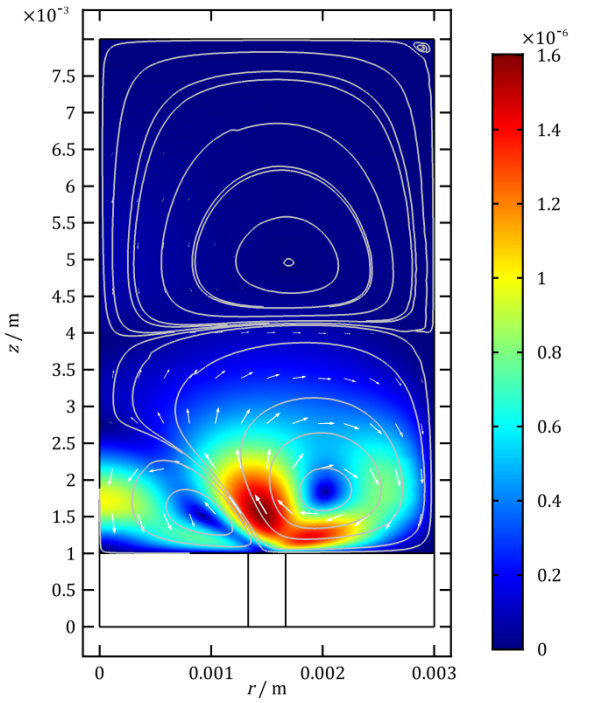
B


v(t = 20 s) / m·s-1 for a BDD substrate with a teflon band, dband = 1/3·rcell
×10-3
z / m
r / m
×10-5

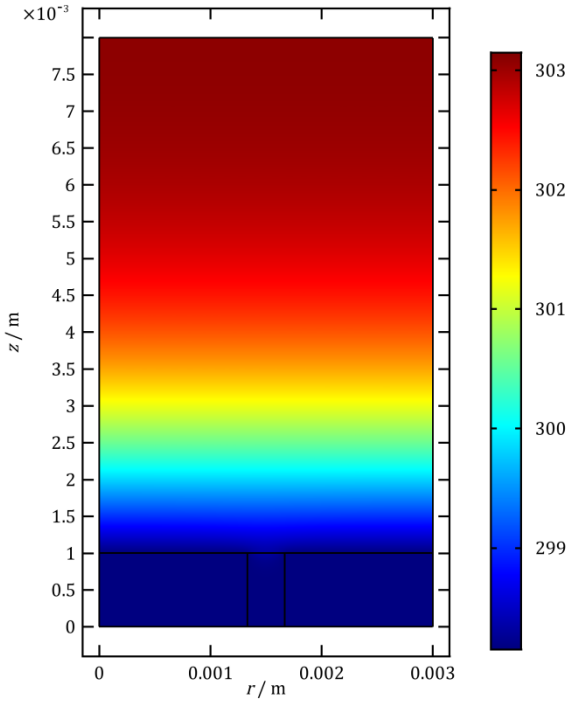
C


T(t = 20 s) / K for a BDD substrate with a teflon band, dband = 1/3·rcell
×10-3
z / m
r / m

D


v(t = 20 s) / m·s-1 for a BDD substrate with a teflon band, dband = 1/9·rcell
×10-3
z / m
r / m
×10-6

E


T(t = 20 s) / K for a BDD substrate with a teflon band, dband = 1/9·rcell
×10-3
z / m
r / m

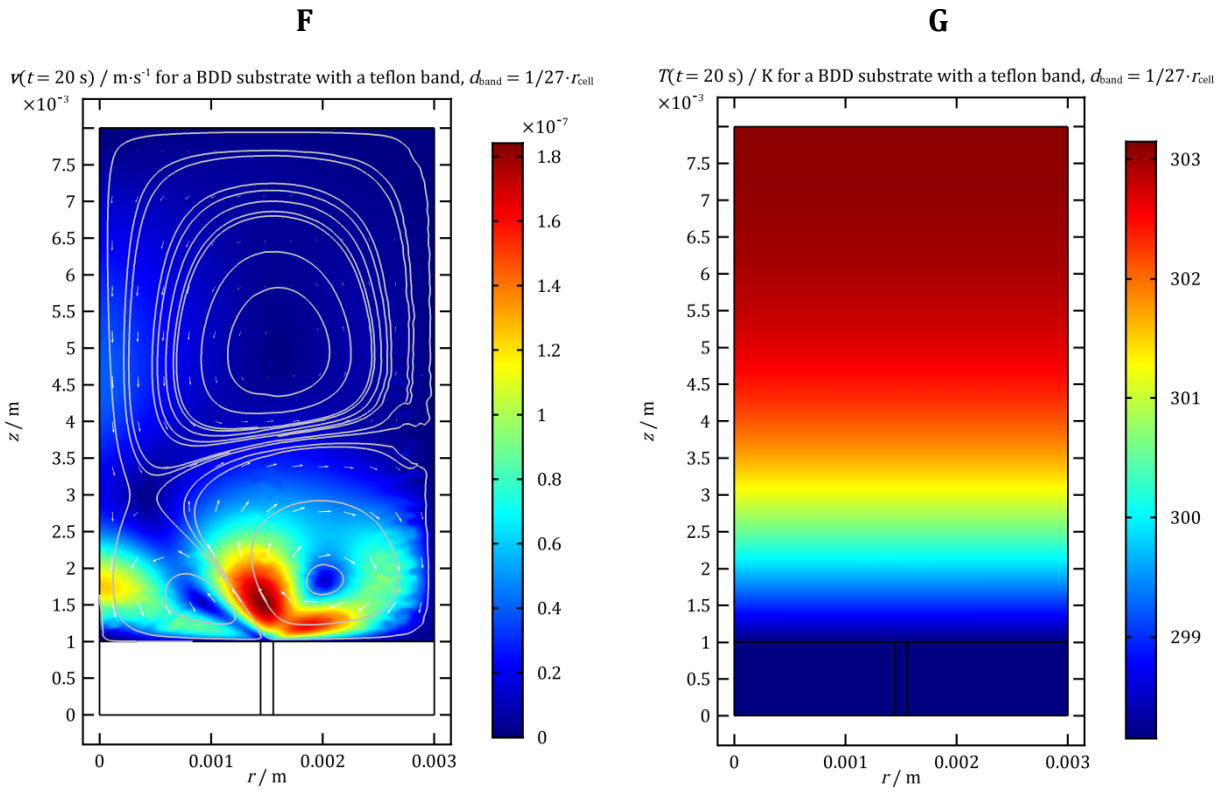


Figure B.22. Results for a BDD substrate with a teflon band for simulations in which the solution is initially warmer than the substrate (ΔT = −5 K). **A** – volume-averaged velocity magnitude. **B**, **D**, **F** – velocity distribution and streamlines illustrating the convective rolls for d_{band}/r_{cell} = 1/3, 1/9 and 1/27 taken at t = 20 s; **C**, **E** and **G** – $T(t = 20\ s)$ for d_{band}/r_{cell} = 1/3, 1/9 and 1/27.

Stability tests

We ran simulations with the boundary condition (5.29) to study the stationary state for a conducting substrate with an insulating band. The simulations cover a time period of 300 s for the three band widths studied elsewhere in the text – see Figure B.24 for a plot of the average velocity in the solution as a function of time. The velocity for bands of width $1/9{\cdot}r_{cell}$ and $1/27{\cdot}r_{cell}$ is of the order of 10^{-7} m·s^{-1} or below (see Figure B.24A), as is the case for a cell with insulated walls. These flows contain high levels of numerical noise and are not of interest for our study.

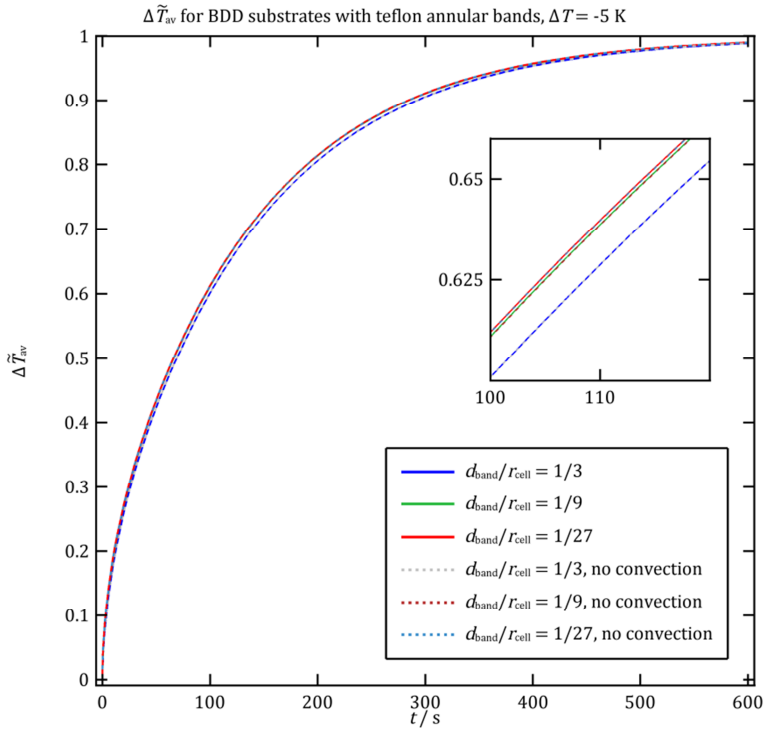


Figure B.23. $\Delta\tilde{T}_{av}(t)$ for convective simulations of BDD substrates with teflon annular bands (solid lines) compared against simulations involving no convection (dashed lines), $\Delta T = -5$ K.

In the stationary flow pattern for $d_{band} = 1/3 \cdot r_{cell}$, illustrated in Figure B.24B, the flow is identical to that seen in a cell with an insulated top wall (Fig. B.22B) – in the simulated region (see Figure 5.1), there is a clockwise main roll occupying the space between r_1 and r_{cell} along the radial coordinate and between $h_s + h_{cell}/2$ and $h_s + h_{cell}$ along the normal. As with a cell with thermally insulated walls (Fig. B.22B), there are two additional rolls – one in the region $r \in [0, r_1]$ and one that occupies the upper half of the cylinder. For both of them, the flow is much less intense than in the main roll, and is in the opposite direction.

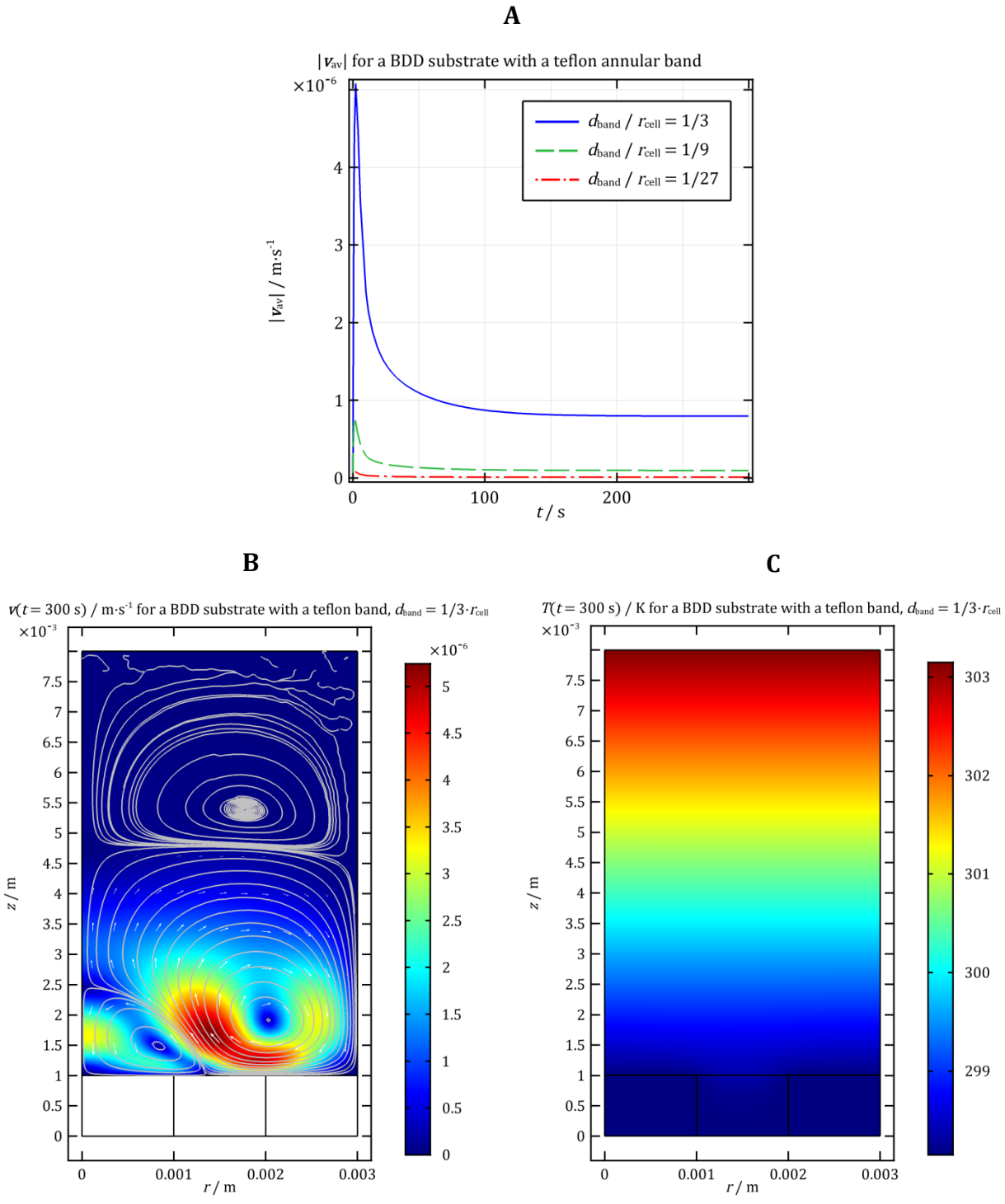


Figure B.24. Results for simulations with a fixed temperature difference between the top and bottom cell walls, The substrate, which is initially colder than the solution (ΔT = −5 K), is made of BDD and has a teflon annular band. **A** – volume-averaged velocity magnitude. **B** – $\boldsymbol{v}(t$ = 300 s) and streamlines and **C** –$T(t$ = 300 s) for d_{band}/r_{cell} = 1/3 at t = 300 s.

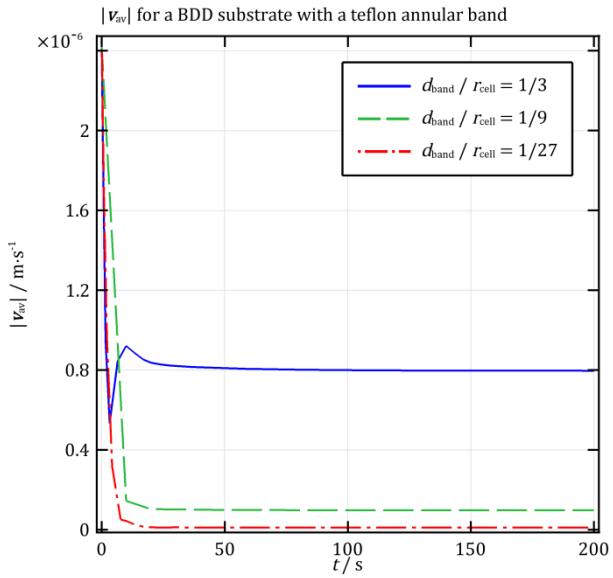


Figure B.25. Volume-averaged velocity magnitude $|\boldsymbol{v}_{\mathrm{av}}(t)|$ for BDD substrates with teflon annular bands from simulations with a fixed temperature difference of ΔT = –5 K between the bottom and top cell walls. The initial conditions for $\boldsymbol{v}$, T^{L} and p correspond to direction of the fluid motion in the rolls opposite to that obtained from simulations of the same substrate with an initial condition for a stagnant solution and $d_{\mathrm{band}}/r_{\mathrm{cell}}$ = 1/3 (see Figure B.24). T^{S} is taken from the stationary prediction of the simulation of a BDD substrate with a teflon annular band with the respective value of d_{band} that employs stagnant initial conditions. Note the drastic change in the average solution velocity – this corresponds to a reversal of the direction of flow and establishment of a pattern resembling the ones in Fig. B.22 and Figure B.24.

We tested whether a flow in which the direction of movement in the rolls is reversed with respect to Figure B.24B is stable for this system. To this end, we used the stationary distributions (taken at t = 300 s) of $\boldsymbol{v}$, T^{L} and p from a simulation of the 'inverse' configuration with $d_{\mathrm{band}}/r_{\mathrm{cell}}$ = 1/3 as initial conditions (see Figure B.28 below). For the temperature of the solid, we used the stationary distribution as calculated at t = 300 s for a conductive substrate with an insulating band (seen in Figure B.24C for $d_{\mathrm{band}}/r_{\mathrm{cell}}$ = 1/3). In contrast to the case with ΔT > 0, here the direction of the flow is reversed on a timescale of ~ 10 s and the pattern obtained

from simulations with an initially stagnant solution is restored. This is illustrated in Figure B.25, where the drop in the average velocity corresponds to the period when the intensity of fluid motion in the rolls drops before they reverse direction. Thus, we can conclude that for a teflon substrate with a BDD annular band at $\Delta T < 0$, the stability of the rolls is influenced by the direction of flow within them. The pattern in which the flow direction in all rolls is reversed with respect to the ones pictured in Figure B.24B, is unstable for this substrate, but, as we show below, it is stable for substrates possessing the 'inverse' structure.

Teflon substrates with BDD annular bands

Figure B.26 presents results for teflon substrates with BDD annular bands at $\Delta T = -5$ K, complementing Figure 5.6 from Chapter 5 by giving 'snapshots' of $\boldsymbol{v}$ and T for $d_{\text{band}} = 1/9$ and $1/27$ near the moment the average velocity reaches its peak value. In Figure B.27, by comparing with $\Delta\tilde{T}_{\text{av}}$ for purely conductive heat transfer, we show that, despite the considerable velocities within the solution ($\boldsymbol{v}_{\text{av}} \sim 10^{-6}$ m·s^{-1}), none of the flows have a significant influence on the solution temperature. As with the 'inverse' configuration, we also performed simulations at $\Delta T = -3$ and -4 K, but do not show results from them here since there is no qualitative difference with the case of $\Delta T = -5$ K.

To verify our results, we ran the same simulations with quadratic elements for T and observed no difference in the flow pattern. We did, however, observe small variations in $|\boldsymbol{v}_{\text{av}}|_{\text{max}}$ as in our other simulations of substrates with annular bands – increasing the shape function order led to an increase in peak height of 1.4% for $d_{\text{band}}/r_{\text{cell}} = 1/3$, and a decrease of 2.7% and 1.1% for $d_{\text{band}}/r_{\text{cell}} = 1/9$ and $1/27$, respectively.

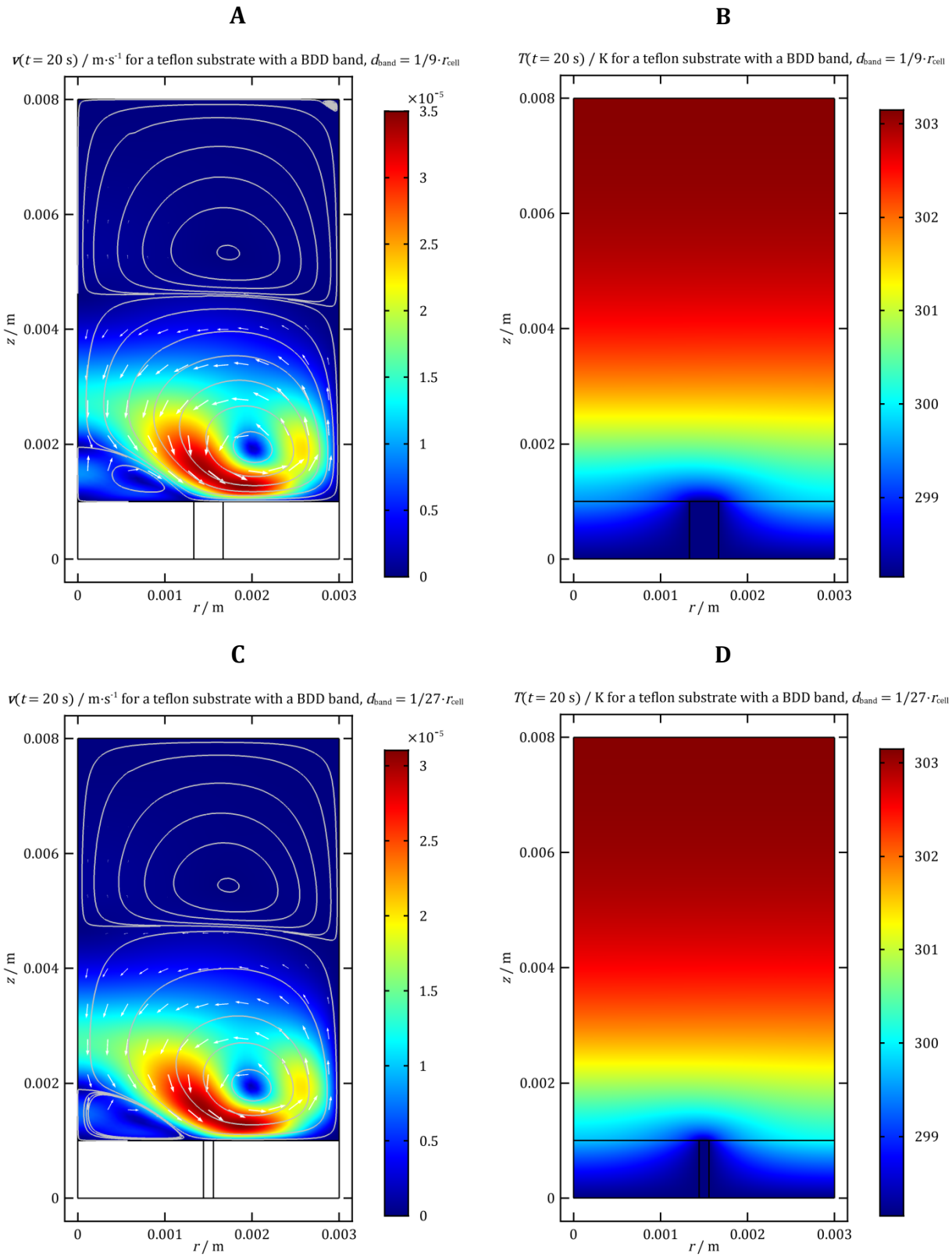


Figure B.26. Results for a teflon substrate with a BDD band, The solution is initially warmer than the substrate (ΔT = −5 K). **A** and **C** – velocity distributions and streamlines at t = 20 s for d_{band}/r_{cell} = 1/9 and d_{band}/r_{cell} = 1/27; **B** and **D** – $T(t$ = 20 s) for d_{band}/r_{cell} = 1/9 and d_{band}/r_{cell} = 1/27.

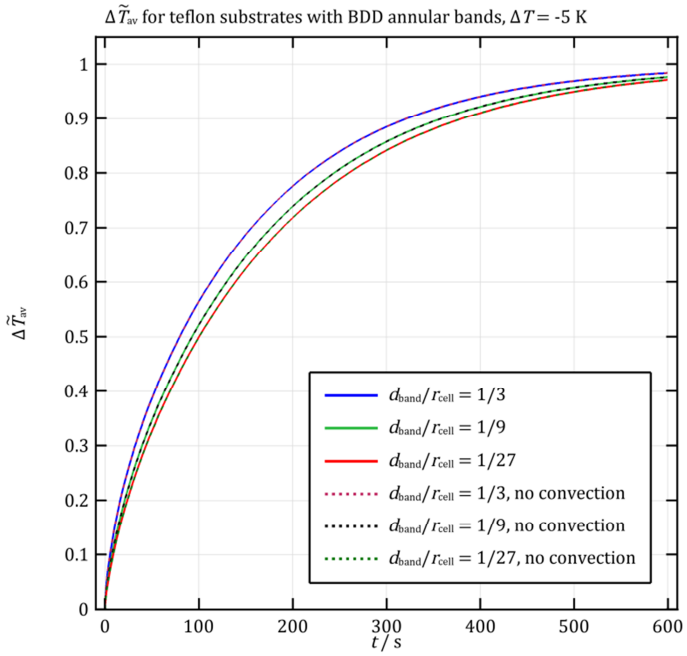


Figure B.27. $\Delta\tilde{T}_{av}(t)$ for convective simulations of teflon substrates with BDD annular bands (solid lines) compared against simulations involving no convection (dashed lines), $\Delta T = -5$ K.

Stability tests

In analogy with other configurations, we also studied the flow stability qualitatively by performing simulations with the fixed-temperature boundary condition (5.29) at the top wall rather than a condition for no normal heat flux. As illustrated in Figure B.28, in all cases, we observed flows with a stationary average velocity of the order of 10^{-6} m·s^{-1} and a velocity distribution with a main anticlockwise roll and secondary clockwise ones identical to those from the simulations of cells with thermally insulated top walls.

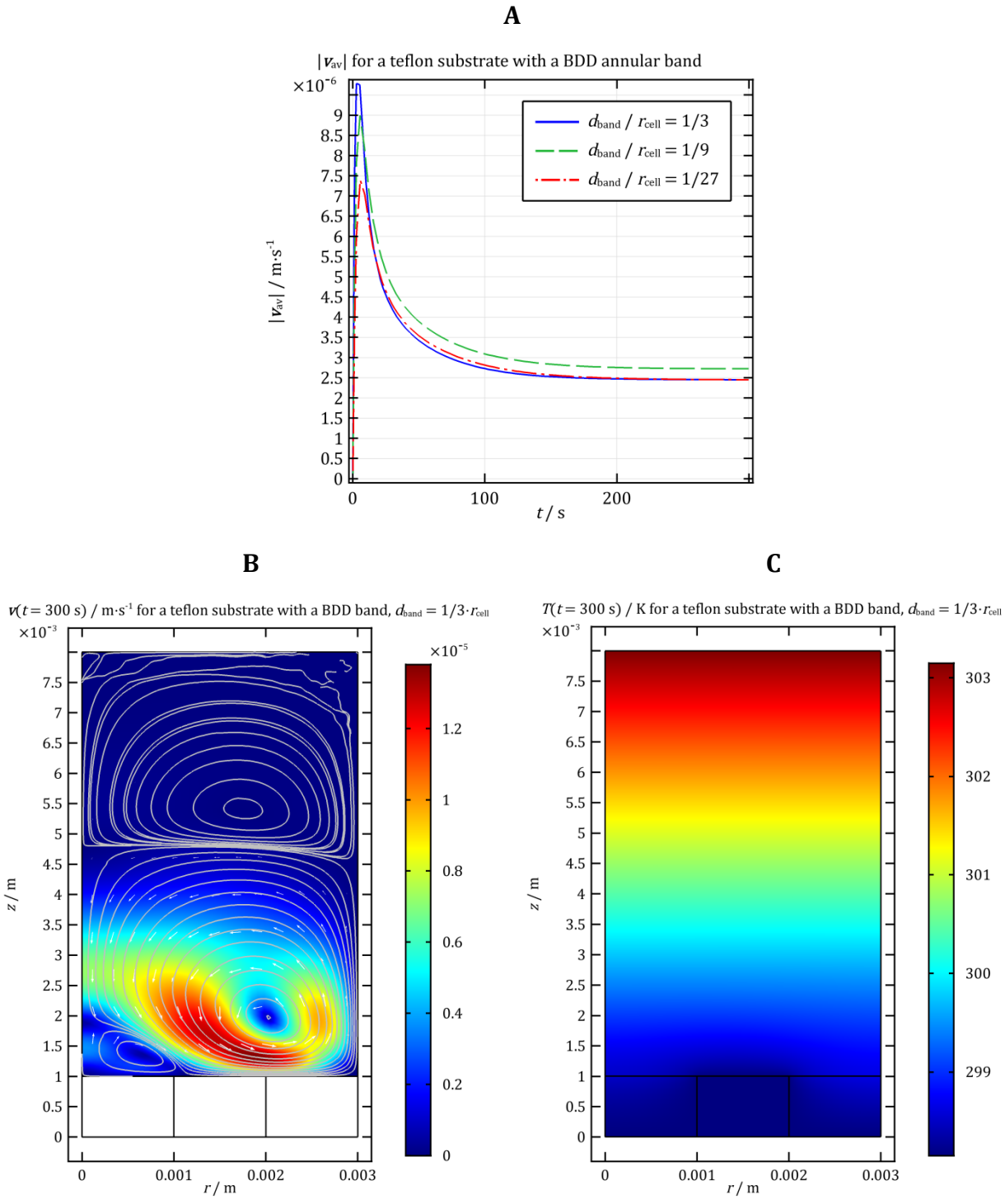


Figure B.28. Results for simulations with a fixed temperature difference between the top and bottom cell walls, The substrate, which is made of teflon and has a BDD annular band, is initially colder than the solution (ΔT = −5 K). **A** – volume-averaged velocity magnitude. **B** and **C** – velocity and temperature distributions for d_{band}/r_{cell} = 1/3 at t = 300 s.

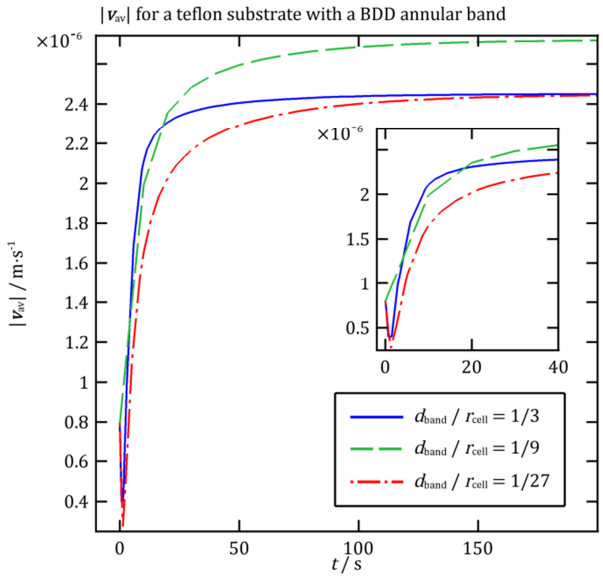


Figure B.29. Volume-averaged velocity magnitude $|\boldsymbol{v}_{av}(t)|$ for teflon substrates with BDD annular bands from simulations with a fixed temperature difference of ΔT = –5 K between the bottom and top walls. The initial conditions for $\boldsymbol{v}$, T^{L} and p correspond to direction of the fluid motion in the rolls opposite to that obtained from simulations of the same substrate with an initial condition for a stagnant solution. T^{S} is taken from the stationary prediction of the simulation of a teflon substrate with a BDD annular band with the respective width that employs stagnant initial conditions. Note the initial drop in the average solution velocity (inset) – this corresponds to a reversal of the direction of flow and a transition to a pattern resembling the ones in Figure B.26 and Figure B.28.

We tested the stability of a flow pattern in which the direction of movement within the rolls is reversed. To that end, we ran simulations with the stationary distributions of $\boldsymbol{v}$, T^{L} and p for the 'inverse' configuration at d_{band}/r_{cell} = 1/3 as initial conditions. For T^{S}, we employed the stationary profile for a teflon substrate with a BDD annular band with the same d_{band} as the studied substrate. In these simulations, the flow reverses direction with respect to the initial conditions over a time scale of ~ 10 s and reaches a stationary state analogous to that pictured in Figure B.28 over a period of ~ 100 s (see Figure B.29 for a plot of $|\boldsymbol{v}_{av}|$). From these results, we can conclude that the direction of flow within the convective rolls is an intrinsic feature

of the convective patterns that develop in cells containing teflon substrates with BDD annular bands, as is the case for the 'mirror' configuration.

B.1.2 **Simulations for r_{cell} = 8 mm**

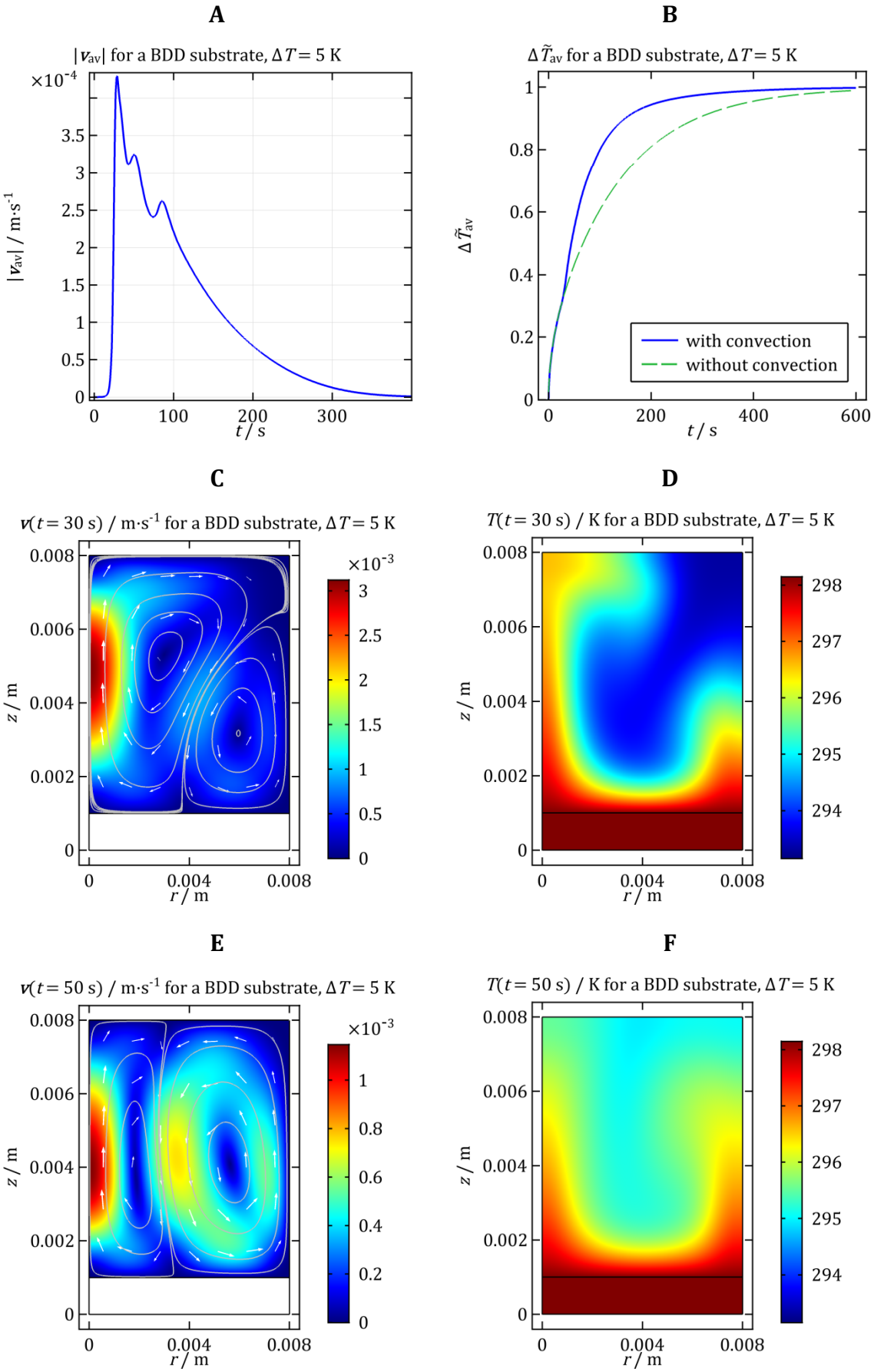
Due to the similarity with the discussion for the smaller cell, here we do not provide all details regarding the simulations of the larger cell. In particular, we only discuss the stability analysis of the flows for r_{cell} = 8 mm where it differs substantially from the previous case.

In all simulations of the cell with r_{cell} = 8 mm, we set the pressure difference $\Delta p = p - p_0 + \rho z|\boldsymbol{g}|$ at the point (r_{cell}, h_{s} + h_{cell}) to zero. This eliminates a contribution to the pressure that depends only on time and thus simplifies the numerical solution of the problem. As only the pressure gradient and not its absolute value matter for an incompressible fluid, this does not affect the physically meaningful quantities that are being solved for.

B.1.2.A. *Solution colder than substrate at t = 0 (ΔT > 0)*

BDD substrate

Figure B.30 illustrates the results for this system discussed in Chapter 5 with plots of $|\boldsymbol{v}_{\mathrm{av}}|$, $\Delta\tilde{T}_{\mathrm{av}}$. 'Snapshots' of the velocity and temperature at the vicinity of the three maxima in the volume-averaged velocity illustrate the main stages in the evolution of the flow.


A
|vav| for a BDD substrate, ΔT = 5 K
×10-4
3.5
3
2.5
2
1.5
1
0.5
0
|vav| / m·s-1
0
100
200
300
t / s
B
ΔT̃av for a BDD substrate, ΔT = 5 K
1
0.8
0.6
0.4
0.2
0
ΔT̃av
with convection
without convection
0
200
400
600
t / s
C
v(t = 30 s) / m·s-1 for a BDD substrate, ΔT = 5 K
0.008
0.006
0.004
0.002
0
z / m
×10-3
3
2.5
2
1.5
1
0.5
0
0
0.004
0.008
r / m
D
T(t = 30 s) / K for a BDD substrate, ΔT = 5 K
0.008
0.006
0.004
0.002
0
z / m
298
297
296
295
294
0
0.004
0.008
r / m
E
v(t = 50 s) / m·s-1 for a BDD substrate, ΔT = 5 K
0.008
0.006
0.004
0.002
0
z / m
×10-3
1
0.8
0.6
0.4
0.2
0
0
0.004
0.008
r / m
F
T(t = 50 s) / K for a BDD substrate, ΔT = 5 K
0.008
0.006
0.004
0.002
0
z / m
298
297
296
295
294
0
0.004
0.008
r / m

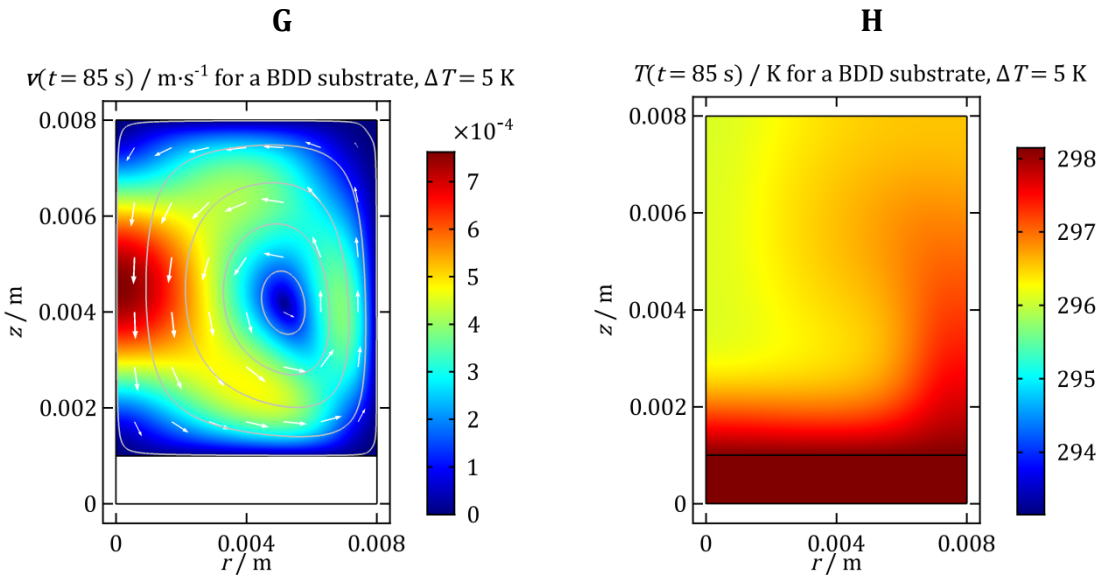


Figure B.30. Results for a BDD substrate situated at the bottom of a cell of radius 8 mm (linear elements for T). The solution is initially colder than the substrate (ΔT = 5 K). **A** – $|\boldsymbol{v}_{av}|$ vs. t; **B** – volume-averaged dimensionless $\Delta\tilde{T}_{av}$ vs. t; **C, E, G** – velocity distribution and streamlines illustrating the convective rolls taken at t = 30, 45 and 85 s; **D, F, H** – T at t = 30, 45 and 85 s.

Teflon substrate

Figure B.31 and Figure B.32 complement the discussion of our simulations of teflon substrates situated in cells with a radius of 8 mm. They represent the results obtained with linear and quadratic elements for T, respectively – note the difference in direction in the motion of the fluid, as well as the contrasting temperature distributions. For each case, the 'snapshots' of $\boldsymbol{v}$ and T are taken approximately at the moment of time corresponding to the main peak in the average solution velocity.

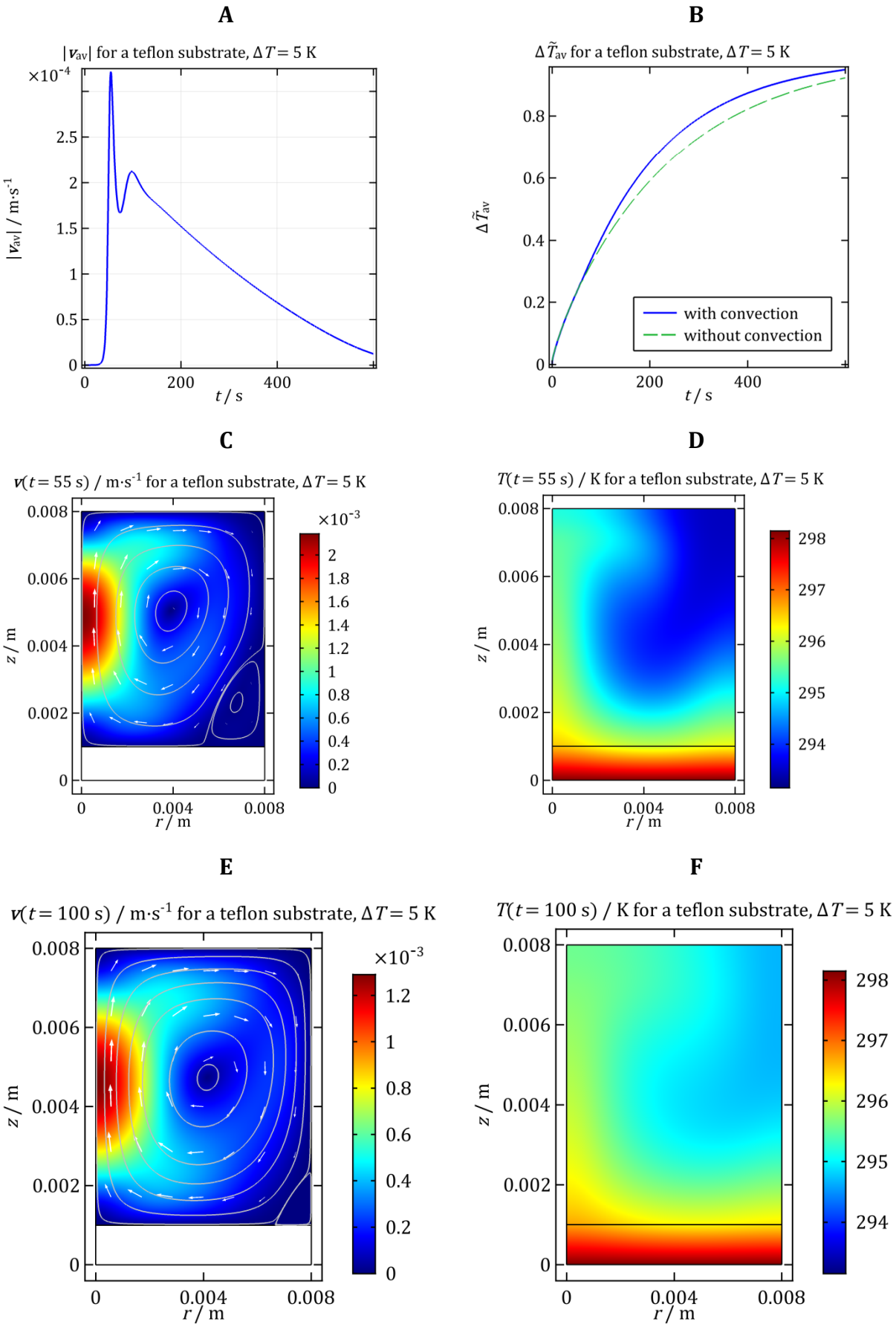


Figure B.31. Results for a teflon substrate situated at the bottom of a cell of radius 8 mm obtained using linear shape functions for T. The solution is initially colder than the substrate (ΔT = 5 K). **A** – $|\boldsymbol{v}_{av}|$ vs. t; **B** – $\Delta \tilde{T}_{av}$ vs. t; **C** and **E** – $\boldsymbol{v}$ and

streamlines illustrating the main and secondary convective rolls at t = 55 and 100 s; **D** and **F** – temperature distribution at t = 55 and 100 s.

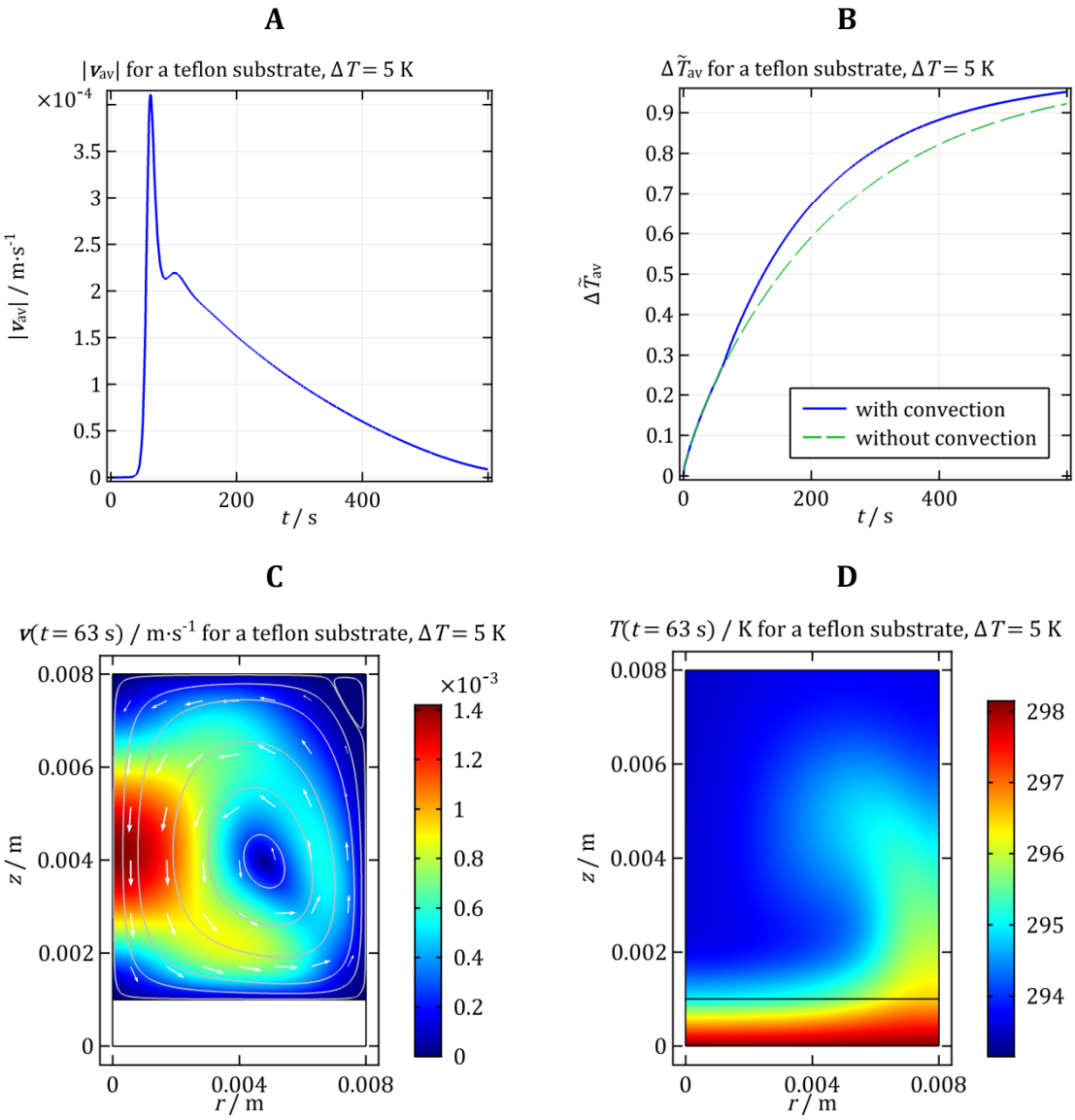


Figure B.32. Results for a teflon substrate situated at the bottom of a cell of radius 8 mm obtained using quadratic shape functions for T. The solution is initially colder than the substrate (ΔT = 5 K). **A** – $|\boldsymbol{v}_{av}|$ vs. t; **B** – volume-averaged dimensionless temperature difference $\Delta\tilde{T}_{av}$ vs. t; **C** – velocity distribution and streamlines illustrating the main and secondary convective rolls at t = 63 s; **D** – temperature distribution at t = 63 s.

BDD substrate with a teflon annular band

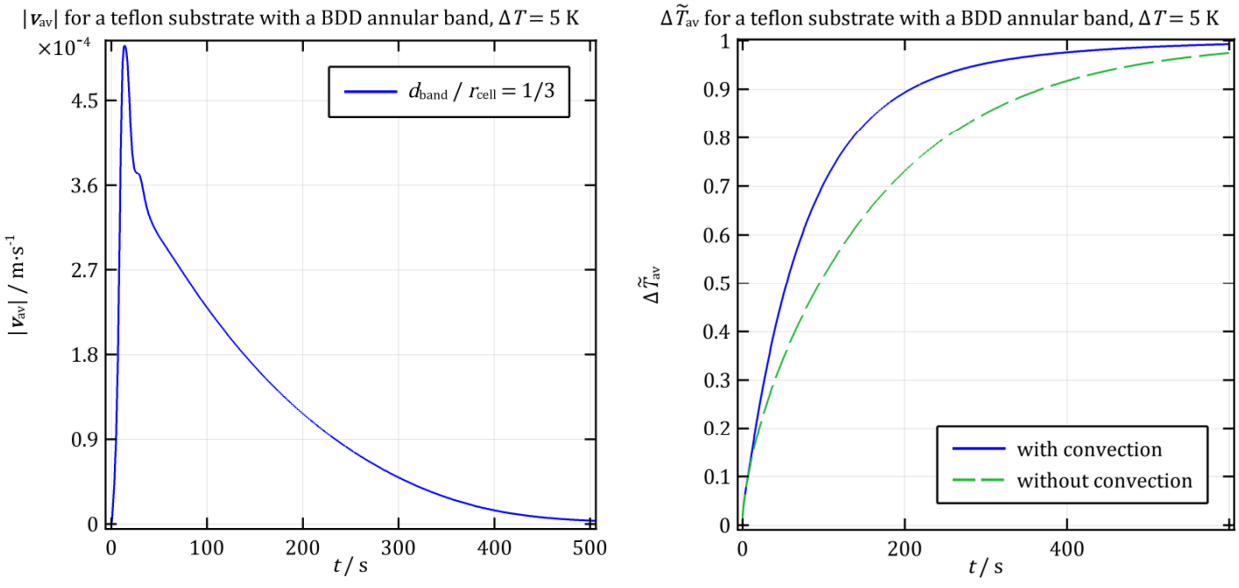
We studied the stability of the flows arising in this system using a methodology very similar to the one we described for substrates with the same structure situated at the bottom of cells with r_{cell} = 3 mm. The only point of difference was that to test the stability of the flow pattern with upwelling at r = 0, we used the velocity, temperature and pressure distributions obtained for long times from our simulation of a teflon substrate with a BDD annular band utilising the fixed-temperature boundary condition (5.29). As before, the initial condition for the temperature distribution within the solid substrate was taken from the steady-state limit of the simulation of a BDD substrate with a teflon annular band with a stagnant initial solution.

As we pointed out in Chapter 5, our tests indicate that for this system, the roll with direction of flow opposite to that illustrated in Figure 8C is unstable for an insulated cell, as is the case for r_{cell} = 3 mm.

Teflon substrate with a BDD annular band

Figure B.33 presents plots of $|\boldsymbol{v}_{av}|$, $\Delta\tilde{T}_{av}$ and 'snapshots' of the velocity and temperature for teflon substrates with BDD annular bands discussed in Chapter 5.

A **B**



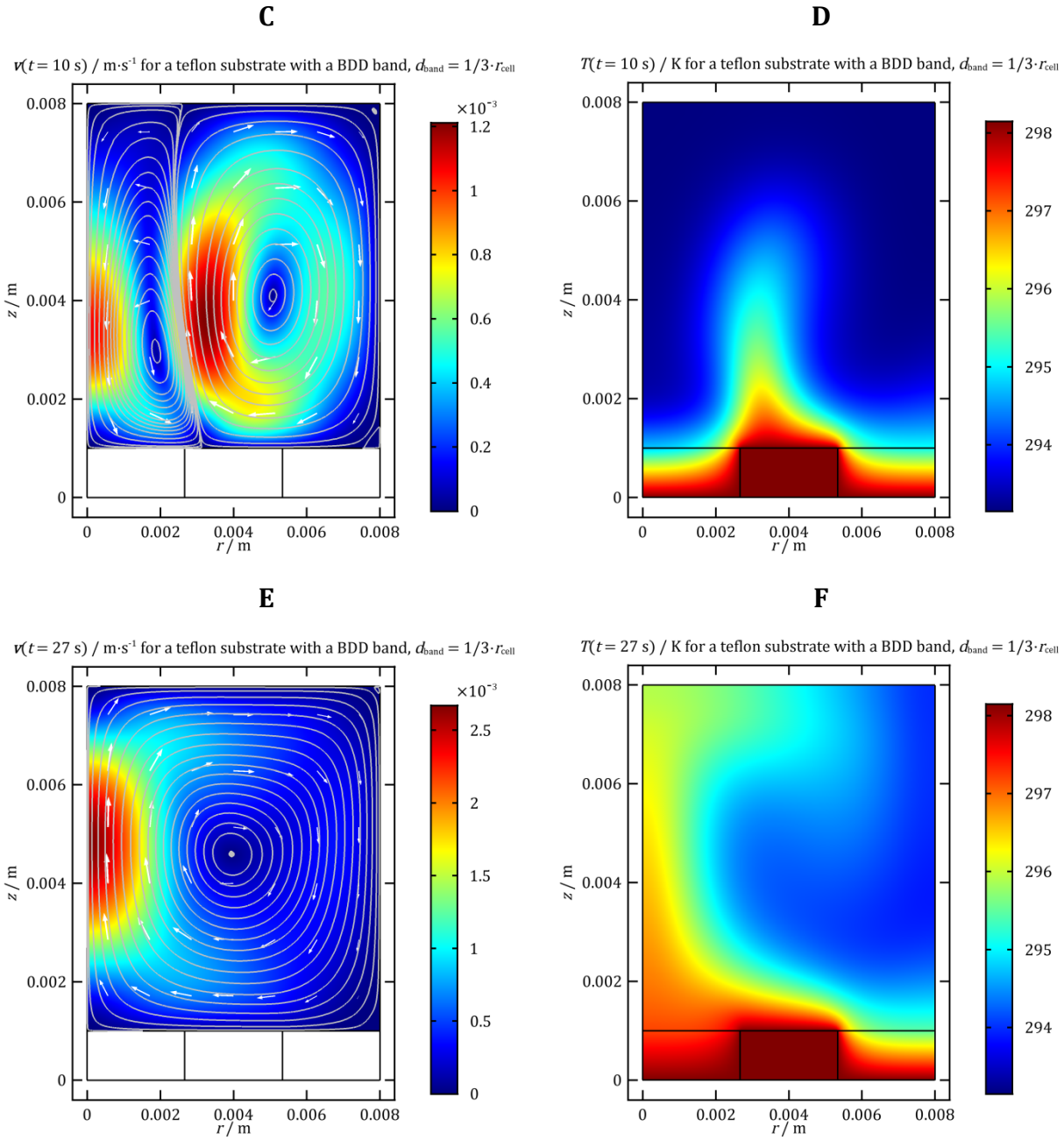


Figure B.33. Results for a teflon substrate with a BDD annular band (d_{band}/r_{cell} = 1/3) situated at the bottom of a cell of radius 8 mm. The solution is initially colder than the substrate (ΔT = 5 K). **A** – $|\boldsymbol{v}_{av}|$ vs. t; **B** – volume-averaged dimensionless $\Delta\tilde{T}_{av}$ vs. t; **C** – velocity distribution and streamlines illustrating the two convective rolls that arise in the system at t = 10 s, corresponding to the maximum in velocity; **D** – temperature distribution at t = 10 s, exhibiting a sharp maximum at $r \sim r_1$. **E**, **F** – illustrations of the convective flow that arises at long times and the temperature distribution corresponding to it.

We tested the stability of the flow in this system in the same way as we did for r_{cell} = 3 mm. As in the case of BDD substrates with teflon annular bands at r_{cell} = 8 mm, the only difference in our approach was that to establish whether the roll with direction opposite to that in Figure B.33 is stable, we used the steady-state distributions of $\boldsymbol{v}$, T^{L} and p obtained from the simulation of the 'inverse' configuration with Eq. (5.29) as the top boundary condition. For T^{S}, we used the distribution from the steady-state limit of the simulation of a teflon substrate with a BDD annular band and a stagnant initial solution.

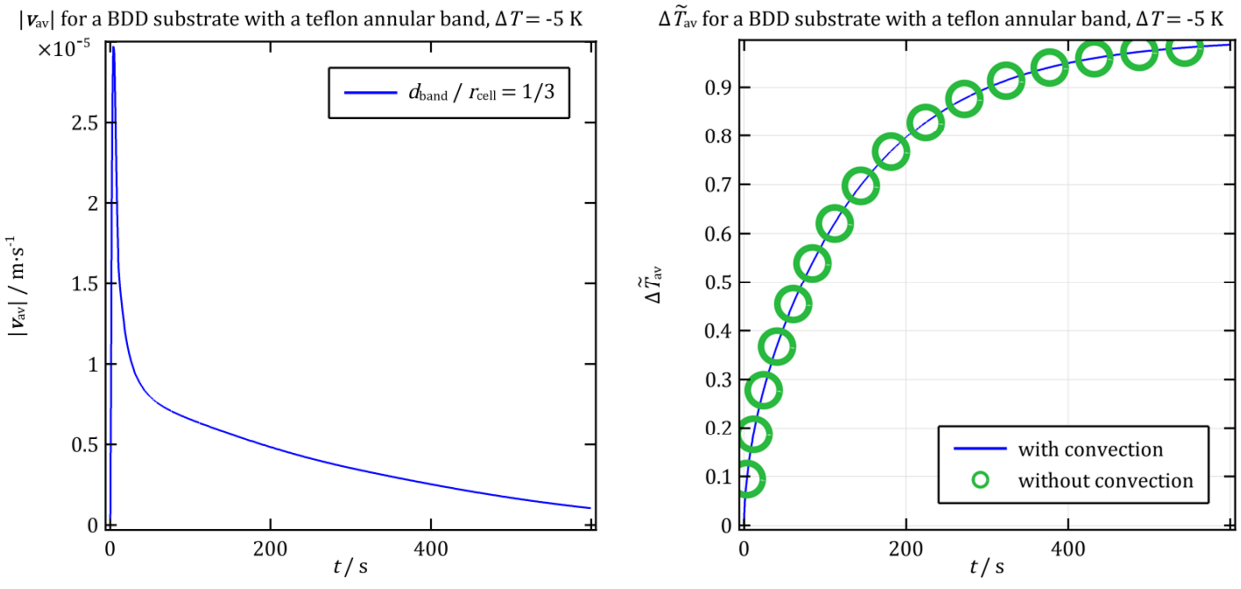
As we have noted in Chapter 5, these tests indicate that the roll with direction opposite to that shown in Figure B.33 is unstable, as is the case for r_{cell} = 3 mm.

B.1.2.B. *Solution warmer than substrate at t* = 0 (ΔT < 0)

BDD substrate with a teflon annular band

Figure B.34 illustrates the results for this system discussed in Chapter 5 with plots of $|\boldsymbol{v}_{av}|$, $\Delta\tilde{T}_{av}$ and 'snapshots' of the velocity and temperature. Comparison with Figure B.24 shows that the increase of r_{cell} leads to a considerable increase in $|\boldsymbol{v}_{av}|$, but no qualitative difference in the system's behaviour.

A **B**



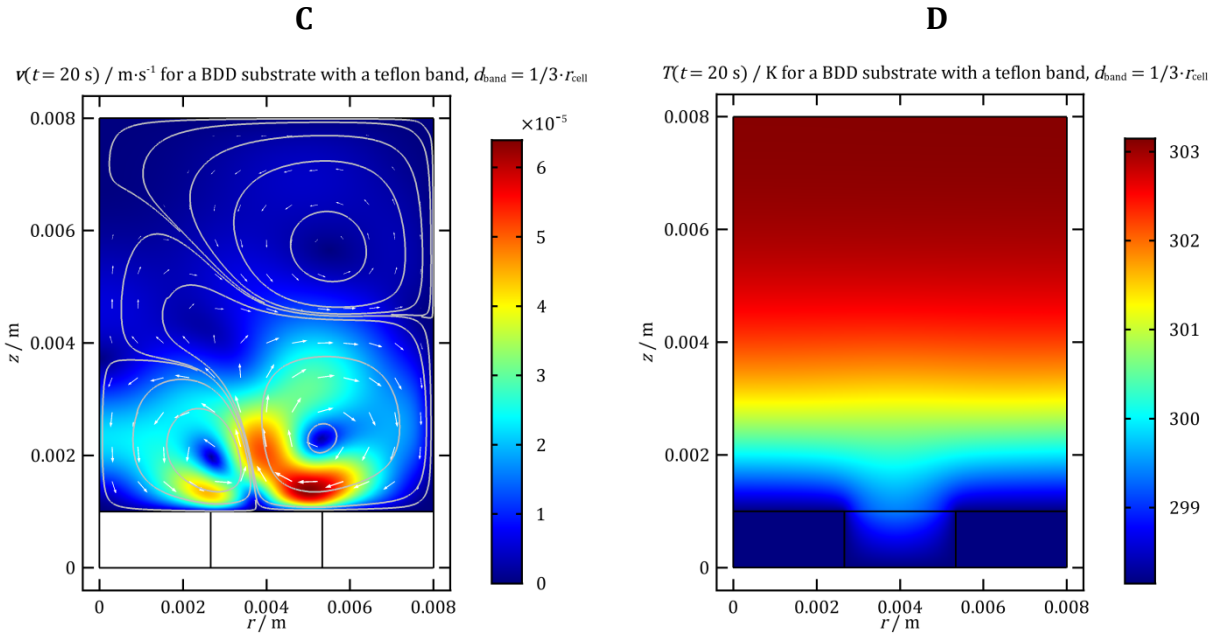


Figure B.34. Results for a BDD substrate with a teflon band (d_{band}/r_{cell} = 1/3) situated at the bottom of a cell of radius 8 mm. The solution is initially warmer than the substrate (ΔT = −5 K). **A** – $|\boldsymbol{v}_{av}|$ vs. t; **B** – volume-averaged dimensionless $\Delta\tilde{T}_{av}$ vs. t; **C** – velocity distribution and streamlines illustrating the convective rolls taken at t = 20 s; **D** – $T(t = 20\ \text{s})$.

Teflon substrate with a BDD annular band

Figure B.35 illustrates the results for this system discussed in Chapter 5 with plots of $|\boldsymbol{v}_{av}|$, $\Delta\tilde{T}_{av}$ and 'snapshots' of the velocity and temperature. As with the 'inverse' substrate structure, the analogy with the case of the smaller cell is complete, the only difference being the lower velocity magnitude for the latter – see Figure 5.6 for comparison.

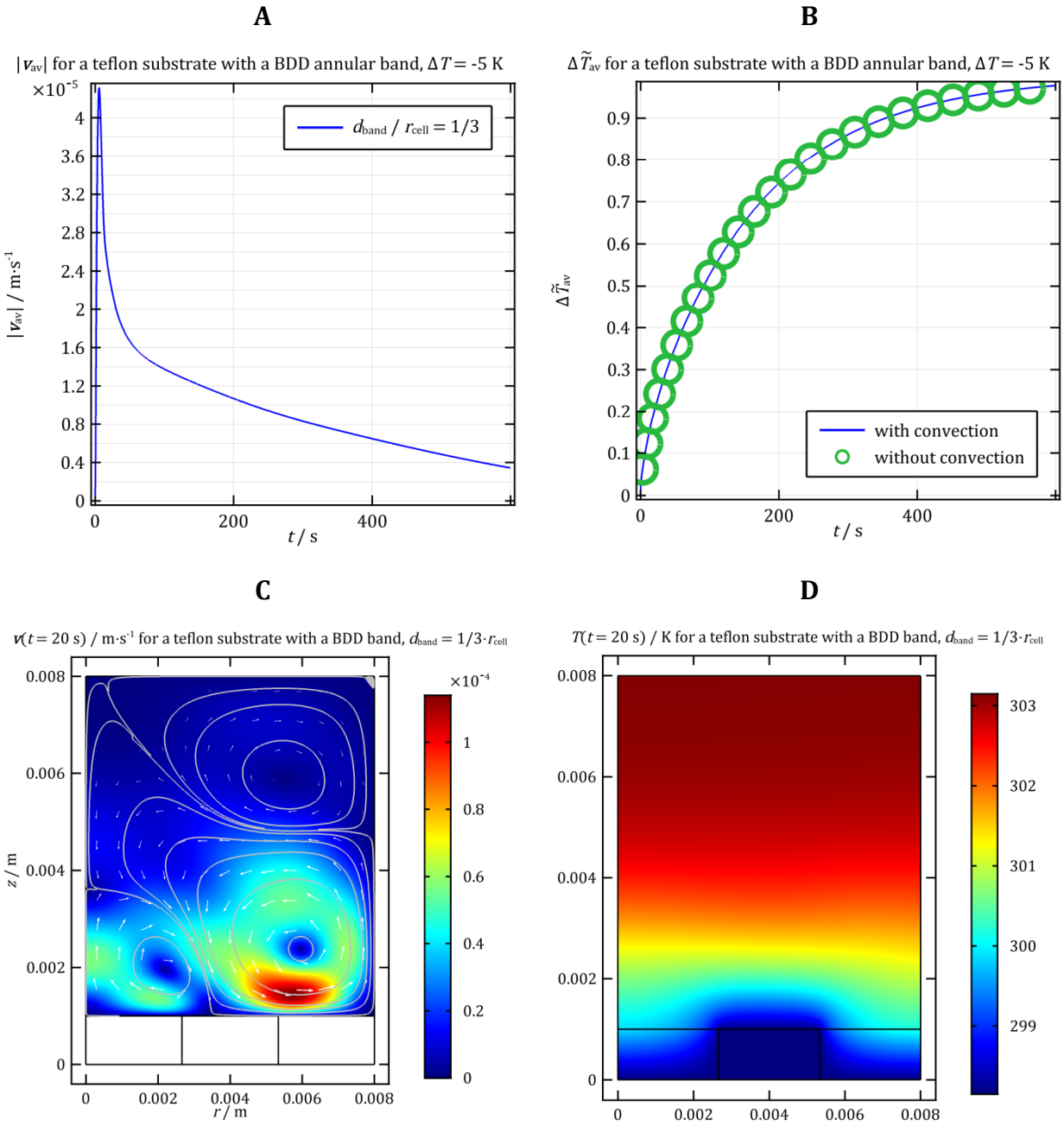


Figure B.35. Results for a teflon substrate with a BDD band (d_{band}/r_{cell} = 1/3) situated at the bottom of a cell of radius 8 mm. The solution is initially warmer than the substrate (ΔT = −5 K). **A** – $|\boldsymbol{v}_{av}|$ vs. t; **B** – volume-averaged dimensionless $\Delta\tilde{T}_{av}$ vs. t; **C** – velocity distribution and streamlines illustrating the convective rolls taken at t = 20 s; **D** – $T(t = 20\ s)$.

B.2. Meshing

The numerical solution of the governing equations via the finite element method requires the meshing of the simulated region of space. Along with the rest of the numerical procedure, this was implemented in COMSOL Multiphysics. For the liquid next to the boundaries with a no-slip condition, we employed COMSOL's 'boundary layer' mesh, which consists of a grid of quadrilaterals that expands in the direction normal to the interface; for the bulk liquid phase and the solid, we used a free triangular mesh. The settings we employed result in 11022 and 22058 elements in total for homogeneous substrates for r_{cell} = 3 and 8 mm, respectively. In the case of annular bands, we set the number of elements at the interface between the solution and the annular band ($z = h_s$, $r \in [r_1, r_1 + d_{band}]$) to 75 in order to guarantee that the velocity and temperature distributions in the vicinity of the band are adequately described. The total number of elements in the mesh was 17169 for d_{band}/r_{cell} = 1/3, 19947 for d_{band}/r_{cell} = 1/9, and 22325 for d_{band}/r_{cell} = 1/27 at r_{cell} = 3 mm; at r_{cell} = 8 mm and d_{band}/r_{cell} = 1/3, it is 27943.

Appendix C: Additional Data for Chapter 6

C.1. Details of the simulation procedure

For the density, thermal conductivity and heat capacity of glass, the approximate values ρ_{glass} = 2.2x10^3 kg·m^{-3}, κ_{glass} = 1.14 W·m^{-1}·K^{-1} and $C_{p\,\text{glass}}$ = 830 J·kg^{-1}·K^{-1} were used. The parameters of the liquid were taken at $T_{\text{solution }0}$ and calculated as follows: the density ρ_0^{L} and the thermal expansion coefficient α were computed from Eq. 16 in Ref. [1]; the heat capacity C_p^{L} is taken from Eq. 17 in the same reference; the viscosity η – from Eq. 15 in Ref. [2] and the heat conductivity κ – from Eq. 10 in Ref. [3]. For calculating the Marangoni number, the value of the temperature derivative of surface tension of water measured by Cini et al. [4] at 293.15 K, $\partial_T \gamma = -0.149\ \text{mN} \cdot \text{m}^{-1} \cdot \text{K}^{-1}$ was used.

The simulations of the heat transfer in the cell were conducted in COMSOL Multiphysics® 5.3. A free triangular mesh was used for the bulk of the fluid and the cell; the regions next to the no-slip surfaces and the liquid|gas interface were meshed with 5 boundary layers; the total number of mesh elements used was 15317. The temporal discretization was performed with a maximum time-step of 0.5 s. To ensure convergence had been achieved, the simulations were repeated with a finer mesh having 10 boundary layers next to the no-slip and the liquid|gas interfaces and consisting of 33690 elements; the maximum time step was reduced to 0.25 s. The results for $\Delta T_{\text{probe}} = T_{\text{thermostat}} - T_{\text{probe}}$ were compared between the two types of simulations and found to agree within 1.3% across the whole time domain of the study.

C.2. Assessment of the experimental significance of the perturbations in ΔT_{probe} at short times

The following analysis aims to determine whether the thermometer probe used in the experiments conducted here can measure the perturbations in ΔT_{probe} predicted by simulations with free-surface boundary conditions. To this end, the probe was subjected to an approximate square-wave temperature disturbance – after having been equilibrated with the surrounding air at $T \sim 295.3$ K, it was immersed in water with a temperature of $T \sim 297.9$ K. The probe's response was monitored and modelled as that of a first-order low-pass Butterworth filter with a cut-off frequency of 0.175 Hz, chosen so that filtering a square-pulse disturbance of similar amplitude, $T - T(t = 0) = 2.6 \cdot \eta(t - 5)\eta(20 - t)$, η being the Heaviside step function, yielded a result comparable to the experimental data (see Figure C.1).

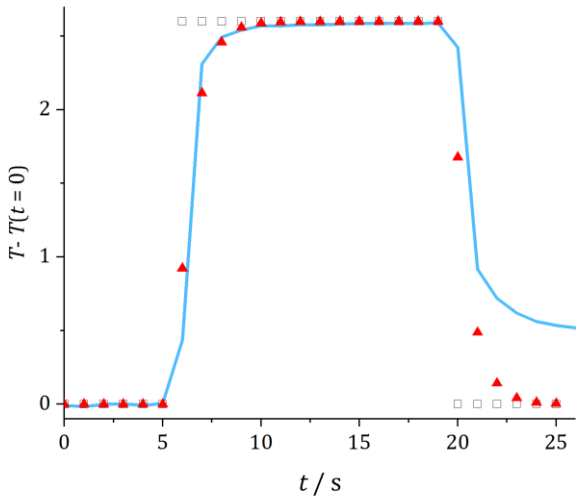


Figure C.1. Test of the response time of the thermometer probe. Solid line – recorded response of the sensor upon its immersion in water; squares – simulated square pulse; triangles – square wave filtered with a first-order low-pass Butterworth filter with a cut-off frequency of 0.175 Hz.

This filter was then used to process simulated data for $T_{\text{probe}} - T_{\text{solution 0}} = \Delta T - \Delta T_{\text{probe}}$ from simulations of sealed cells with radiative heat flux, free-surface

and no-slip boundary conditions and ΔT 1.3 and 1.8 K sampled with a frequency of 1 Hz; the results are plotted in Figure C.2.

As the figure, which deals with the same data as Figure 6.3B from the main text and Figure C.3B, indicates, the probe's response time would allow it to record disturbances of the magnitude of those predicted for ΔT_{probe} for free-surface conditions. Thus, the fact that such disturbances were not observed in the experimental data is a strong indication that a no-slip rather than a free surface boundary condition is appropriate for the studied system.

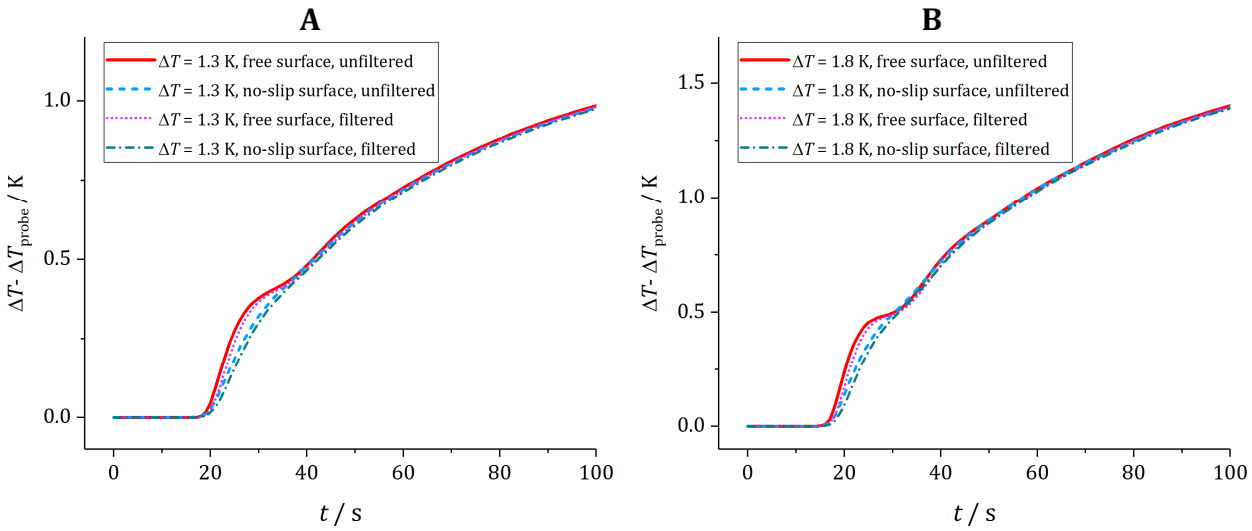


Figure C.2. Data for $T_{\text{probe}} - T_{\text{solution }0}$ at **A**) ΔT = 1.3 K and **B**) ΔT = 1.8 K from simulations with 1) no filtering and a free-surface boundary condition (solid lines) or a no-slip boundary condition (dashed lines); 2) data from free-surface (dotted lines) and no-slip (dash-dot lines) filtered with a first-order Butterworth filter with a cut-off frequency of 0.175 Hz. Although the filter induces a time-delay and alters the data, there is still a significant difference between the cases of free and no-slip hydrodynamic boundary conditions. This implies that the thermometer probe is capable of measuring such perturbations and, as fluctuations such as the ones seen here for the free-surface case are not seen experimentally, is an argument in favour of employing a no-slip boundary condition.

C.3. Data for simulations and experiments at ΔT = 1.8 K

Figure C.3 presents data from simulations and experiments at ΔT = 1.8 K; it is equivalent to Figure 6.3 from the main text but presents a case with a larger initial temperature difference.

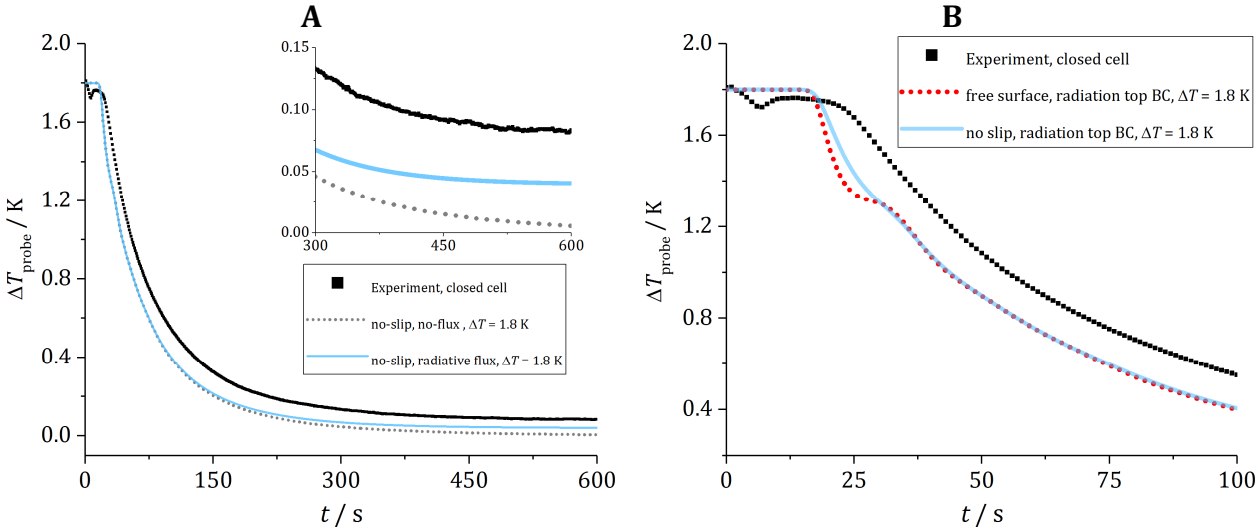


Figure C.3. Difference between the temperature of the thermostat and that at the measurement point ($\Delta T_{probe} = T_{thermostat} - T^{L}(r = 0, z = h_{liquid}/2 + d_{wall})$) as a function of time at an initial ΔT of 1.8 K. **A**. Comparison of experimental data (points) and simulations with a no-slip boundary having 1) a no-flux boundary condition (dashed line) and 2) a radiative heat flux condition at the liquid|air interface (solid line). Note that the simulation with a boundary condition for thermal insulation predicts that the solution temperature asymptotically tends towards $T_{thermostat}$, whereas the one with radiative heat flux predicts a temperature difference close to the experimentally observed one. **B**. Plot of the experimental data from **A** at short times and calculated values for simulations with radiative heat flux, 1) a no-slip hydrodynamic boundary condition (solid line) and 2) a free-surface one (dashed line).

Figure C.4 presents the evolution of the temperature and velocity fields for a simulation with free surface boundary conditions and radiative heat transfer at ΔT = 1.8 K. As discussed in the main text (Chapter 6), the greater driving force for

the convection yields a considerable difference in the observed flow – here, the intensity of the secondary roll that develops close to the cylinder axis is large enough to significantly perturb the temperature profile in the vicinity of the substrate, as seen in Figure C.4C. As in the case with a smaller initial temperature difference, the two convective cells merge at long times and thereafter a single roll occupies the whole volume of the liquid (Figure C.4D).

In simulations conducted with ΔT = 2.3, the secondary flow intensifies and $\Delta T_{\text{probe}}(t)$ goes through five inflections. In simulations with ΔT = 3 and 4 K, we observe that the vertically elongated secondary flows become considerably more pronounced and so does their influence on ΔT_{probe}, causing the simulated curve to have not just multiple inflections but also multiple extrema. As the experimentally measured T_{probe} does not possess such features, we restrict our discussion of the flow patterns to the case with $\Delta T \leq 2.3$ K in which the secondary convective cells have only a limited effect.

Moreover, we should note that we have observed convective flow patterns qualitatively similar to the predicted ones via monitoring the dissolution of a $KMnO_4$ crystal placed at the cell bottom; the initial temperature difference for these experiments was $\Delta T \approx 7$ K. We observed approximately radially symmetric flows with internal circulation within the cell but we do not made an attempt at their quantitative characterization or discuss them further due to the qualitative nature of the data.

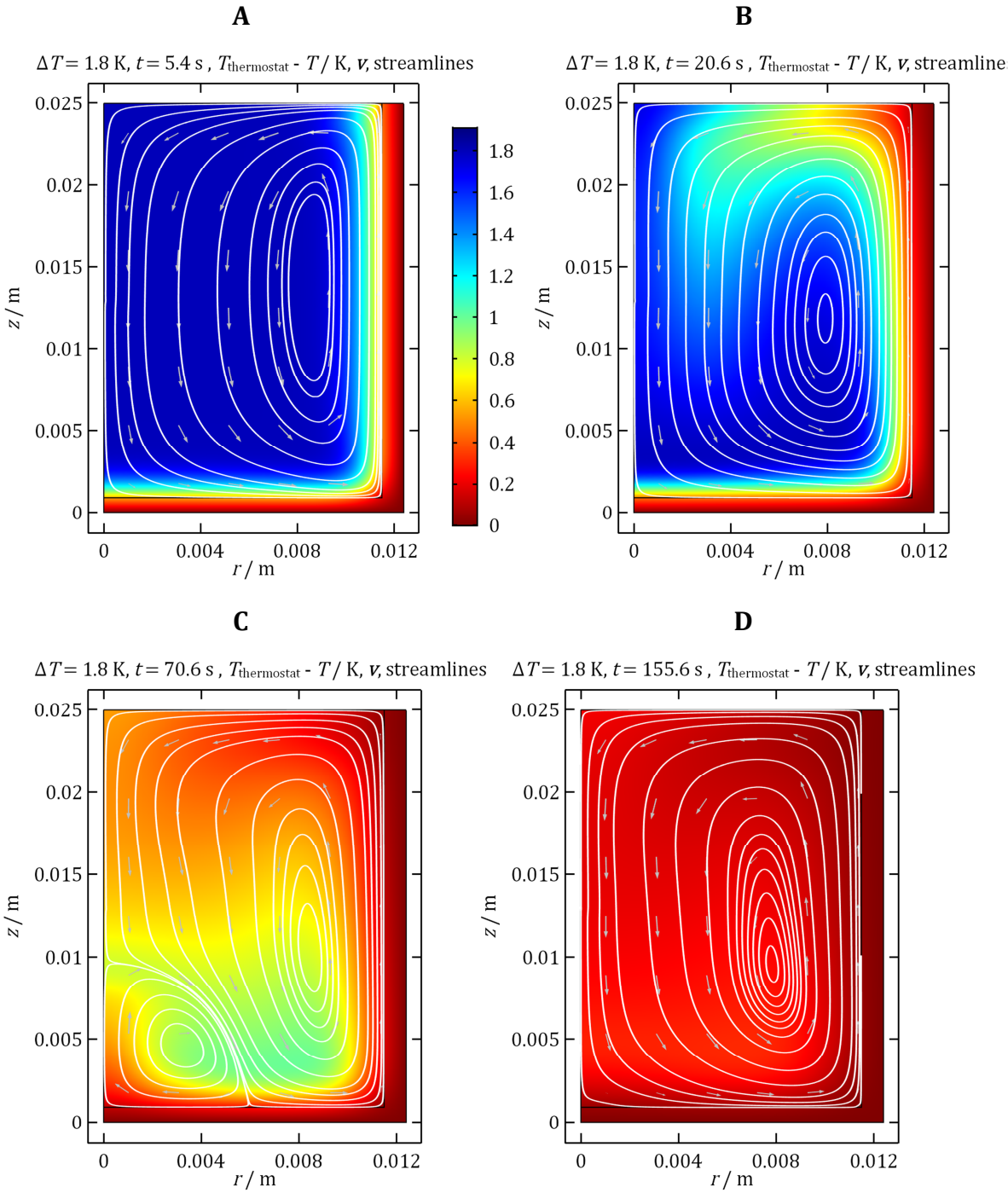
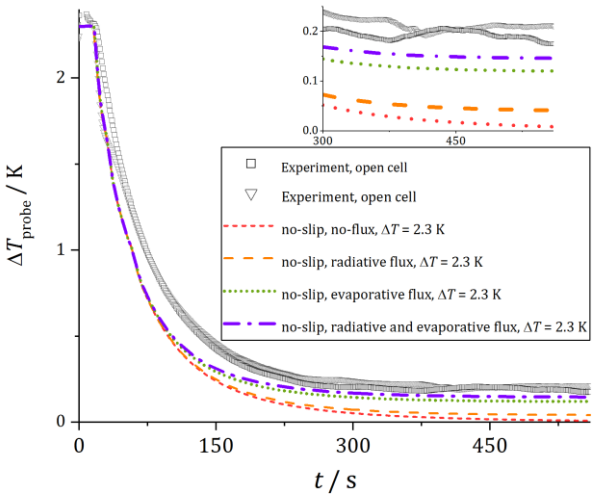


Figure C.4. Temperature distribution, streamlines and arrow plot of the velocity field for a simulation with a no-slip surface, a boundary condition for radiative heat transfer through the liquid|gas interface and ΔT = 1.8 K. In each plot, the length of the arrows is proportional to the local value of $|\boldsymbol{v}|$, but the proportionality constant varies between frames. Note that in this case the secondary roll that appears at the cylinder axis is of substantial intensity and perturbs the local temperature profile to a much greater degree than at ΔT = 1.3 K, compare **C** with Figure 6.4**C.**

C.4. Additional data simulations and experiments under open-cell conditions at ΔT = 2.3 K

Figure C.5 contains a comparison of the simulated ΔT_{probe} curves from Figure 6.5 in the main text with ones that involve no evaporative heat flux. As in Figure 6.3, where results for a closed cell are illustrated, a no-flux boundary condition at the liquid|gas interface yields ΔT_{probe} that tends towards zero at long times and a condition for radiative flux gives a long-time limit of 0.04 K. The inset in Figure C.5A demonstrates that the long-time temperature differences corresponding to both conditions are considerably smaller than the experimentally observed ones, suggesting that evaporation plays a significant role in this system. Figure C.5B presents the same data as Figure C.5A but focuses on the region of short times, showcasing the small maximum in ΔT_{probe} that simulations with an evaporative flux predict. Moreover, we see in Figure C.5B that both simulations with evaporation yield identical ΔT_{probe} at short times – this happens because the radiative heat flux only becomes important towards the end of the experiment when the temperature difference between the solution and the ambient air is at its largest.

A



B

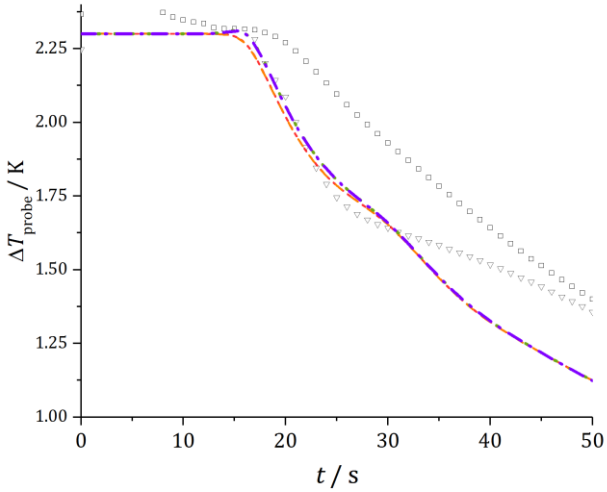


Figure C.5. Difference between the temperature of the thermostat and that at the measurement point ($\Delta T_{probe} = T_{thermostat} - T^{\llcorner}(r = 0, z = h_{liquid}/2 + d_{wall})$) as a function of time at an initial ΔT of 2.3 K. The two sets of points correspond to experimental measurements for a cell open to the environment. Points at short t are not shown as they deviate strongly from the trend because the thermometer probe is exposed to the air when the cell is placed in the water bath. The curves represent simulations with a no-slip surface and different thermal boundary conditions at the liquid|gas interface: 1) no flux (short-dashed line), 2) radiative heat flux (long–dashed line), 3) evaporative heat flux (dotted line) and 4) radiative and evaporative heat flux (dash-dot line). The simulation that includes both evaporative and radiative heat transfer is in closest agreement with the experimental data, which suggests that the model including these two mechanisms for heat exchange is the most adequate for an open cell.

C.5. Data on ΔT_{probe} for a cell immersed deeper in the water bath

Figure C.6 illustrates measurements for ΔT_{probe} conducted with a sealed cell of greater height that was positioned deeper within the water bath than for the other experiments discussed in Chapter 6 and Appendix C. The simulated curves correspond to no-slip hydrodynamic boundary conditions combined with either a

thermal insulation or a radiation condition at the liquid|gas interface. As discussed in the main text (Chapter 6), performing the experiment under such conditions leads to better agreement with simulations at long times, suggesting that contrary to the assumption of the model, the temperature distribution in the water bath is not homogeneous. However, the agreement between data for the smaller cell and our simulations is both sufficiently good for the purpose of this study and more relevant to the cell for nano-impacts, so we have not investigated the alternative experimental configuration in more detail.

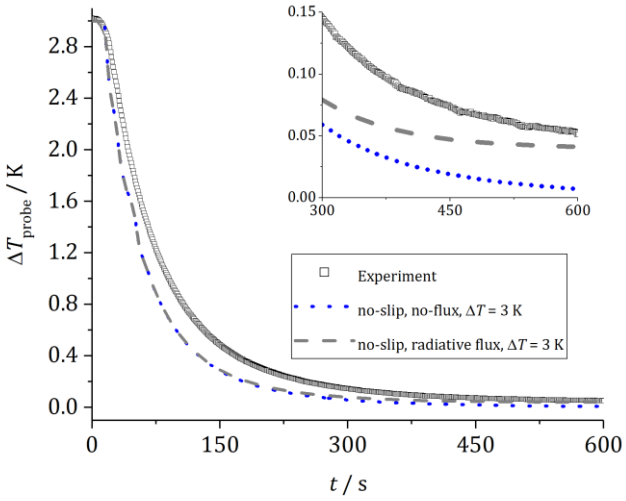


Figure C.6. Difference between the temperature of the thermostat and that at the measurement point ($\Delta T_{probe} = T_{thermostat} - T(r = 0, z = h_{liquid}/2 + d_{wall})$) as a function of time at an initial ΔT of 3 K. The curves are determined experimentally for a sealed cell fully immersed in the water bath (squares), simulations with a no-slip surface having 1) a no-flux boundary condition (dotted line) and 2) a boundary condition for radiative heat transfer (dashed line). Note that the simulation with a boundary condition for thermal insulation predicts that the solution temperature asymptotically tends towards $T_{thermostat}$, whereas the one with radiative heat flux predicts a temperature difference similar to the experimentally observed one.

C.6. Volume-averaged velocities of the observed flows

Figures C.7- C.8 present the volume-averaged velocity $|\boldsymbol{v}_{\mathrm{av}}|$ as defined by Eq. (6.13) for various simulations; for all of them, $|\boldsymbol{v}_{\mathrm{av}}|$ goes through a sharp maximum corresponding to the period of most intense flow before the temperature difference between the solution and the thermostat has diminished. The position and height of this peak depend on the initial temperature difference ΔT, as the comparison between simulations with ΔT = 1.3 (solid, dashed and dotted lines) and 1.8 K (dashdot line) in Figure C.7 shows. Moreover, it is visible from Figure C.7 that while a free-surface boundary condition leads to a higher maximum average velocity, this effect is minor – the latter condition yelds $|\boldsymbol{v}_{\mathrm{av}}|_{\mathrm{max}} = 8.0\times10^{-4}$ m·s^{-1} at ΔT = 1.3 K, which is close to the value of 7.7×10^{-4} m·s^{-1} for a no-slip surface at the same initial temperature difference. Furthermore, Figure C.7 illustrates that, crucially, if the heat flux through the liquid|gas interface is neglected, $|\boldsymbol{v}_{\mathrm{av}}|$ tends to zero at long times, reaching 7.5×10^{-6} m·s^{-1} at t_{exp} for a simulation with ΔT = 1.3 K – in this case, the system tends to a quiescent equilibrium state with a homogeneous temperature distribution. In contrast, in simulations with a radiative heat flux condition, the temperature distribution remains inhomogeneous even at long times, thus providing a driving force for convection and leading to an average velocity $|\boldsymbol{v}_{\mathrm{av}}|_{t\,=\,t_{\mathrm{exp}}} \approx 6.6\times10^{-5}$ and 6.5×10^{-5} m·s^{-1} for no-slip hydrodynamic boundary conditions at ΔT = 1.3 and 1.8 K, respectively. A likely explanation for the difference between the $|\boldsymbol{v}_{\mathrm{av}}|_{t\,=\,t_{\mathrm{exp}}}$ between simulations at different initial ΔT is that a true stationary state is not yet reached at the end of the simulated experiments, $t = t_{\mathrm{exp}}$.

The radiative heat flux only becomes important at long times when the difference between the ambient temperature and that of the liquid is larger. Thus, as the inset in Figure C.7 shows, the values of $|\boldsymbol{v}_{\mathrm{av}}|_{\mathrm{max}}$ for the simulations with no-slip conditions are nearly identical for no-flux and radiative flux conditions at the interface ($|\boldsymbol{v}_{\mathrm{av}}|_{\mathrm{max}}$ = 7.71 and 7.72×10^{-4} m·s^{-1}, respectively).

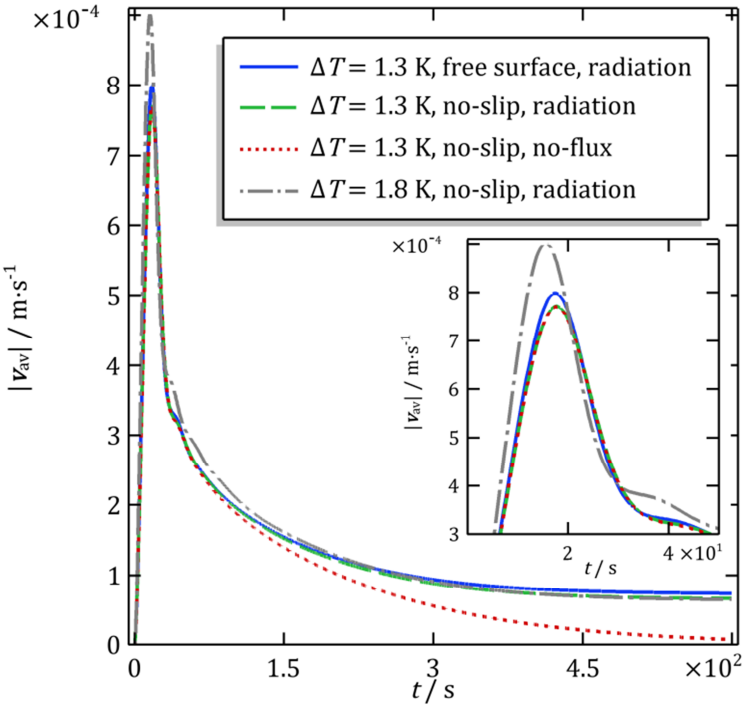


Figure C.7. Comparison of the volume-averaged velocity magnitude for four different simulations of closed-cell systems. Curves represent simulations with the following types of boundary conditions at the liquid|gas interface at ΔT = 1.3 K: solid – free-surface boundary and a radiation heat flux; dashed – no-slip and a radiation heat flux; dotted – no-slip surface and no heat flux. The dash-dot curve is for the case of ΔT = 1.8 K, a no-slip surface and a radiative heat flux and is given for comparison. Note that under conditions of thermal insulation, $|\boldsymbol{v}_{\mathrm{av}}|$ tends to zero at long times, whereas in the other simulations it tends to a positive constant value that is weakly influenced by the hydrodynamic boundary condition at the interface.

Figure C.8 presents results for $|\boldsymbol{v}_{\mathrm{av}}|$ for two simulations in which an approximation for the heat flux due to evaporation is included and for which ΔT = 2.3 K; they differ by the presence or absence of a radiative heat flux at the liquid|gas interface. The higher ΔT in these simulations leads to a higher maximum $|\boldsymbol{v}_{\mathrm{av}}|$ than in the cases illustrated in Figure C.7, $|\boldsymbol{v}_{\mathrm{av}}| \approx 1.01\times10^{-3}$ m·s^{-1}. Moreover, according to our approximate model, evaporation leads to a considerably stronger outward heat flux at the interface than radiation and thus in this case, the average velocity at $t = t_{\mathrm{exp}}$ is also higher than in Figure C.7. The evaporative flux at the interface leads to

$|\boldsymbol{v}_{\mathrm{av}}|_{t\,=\,t_{\mathrm{exp}}} \approx 1.5\times10^{-4}$ m·s^{-1}, whereas the combination of it and radiative flux yields 1.7×10^{-4} m·s^{-1}. As in the simulations without evaporation, the radiative heat flux only becomes important at long times, thus making the peak average velocities for the two cases illustrated in Figure C.8 identical to three significant digits.

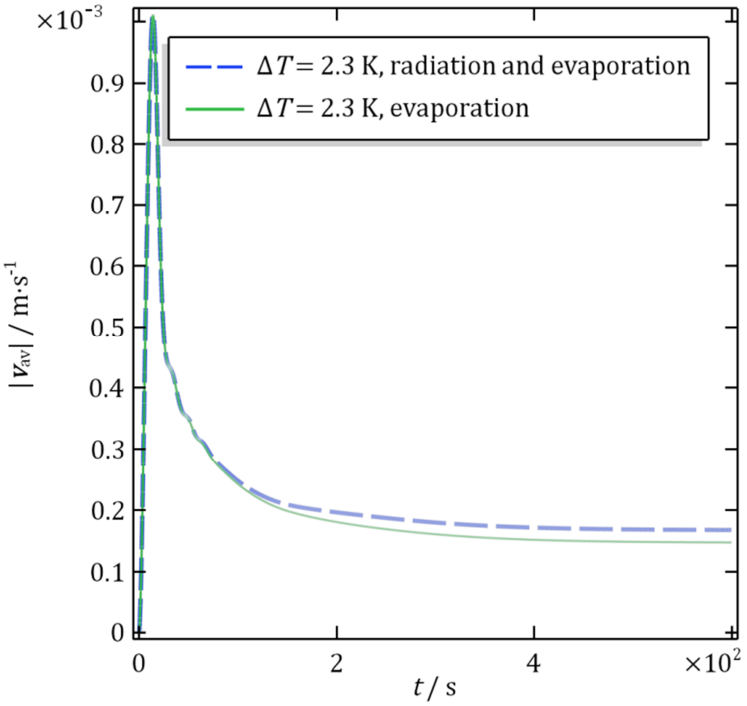


Figure C.8. Volume-averaged velocity magnitude for simulations with evaporation and a no-slip surface at ΔT = 2.3 K. The solid curve represents a model that includes only the heat flux due to evaporation, as given by Eq. (6.9) in the main text, while the dashed takes the radiative heat flux (6.8) into account as well. Note that the peak velocity is considerably higher than in Figure C.7 as a consequence of the larger initial temperature difference; furthermore, the stationary flow driven by evaporation has $|\boldsymbol{v}_{\mathrm{av}}|$ more than twice as high as the one caused by radiation alone.

C.7. Comparison of thermostating systems

The homemade thermostat system was first tested by changing the temperature of 10 mL H_2O from the room temperature to the one of study. Figure C.9 shows the temperature profiles of 10 mL H_2O that are being thermostated from 21.9 °C to 25.0 °C (A) and from 22.6 °C to 35 °C (B) by using the homemade thermostat system

(red curves) and the standard water bath (black curves); the accuracy of measurement was ± 0.1 °C. The plots demonstrate that it took around 5 min for the homemade system to increase the temperature of 10 mL solution from 21.9 °C to 25.0 °C (red curves in Figure C.9A) and 10 min from 22.6 °C to 35 °C. In contrast, for experiments with the conventional water bath, the thermostat took around 22 min to raise the temperature of the bath itself (containing 1 L of water) from 20 °C to 25 °C, and about 32 min from 25 °C to 35 °C, then 5 min to heat 10 mL solution from 21.9 °C to 25.0 °C and 3 min from 22.6 °C to 35.0 °C. For both systems, the maximum deviation between the local temperature and the desired value is ≈ ± 1 °C. The high efficiency and accuracy demonstrate that the homemade thermostat system has a good temperature control performance.

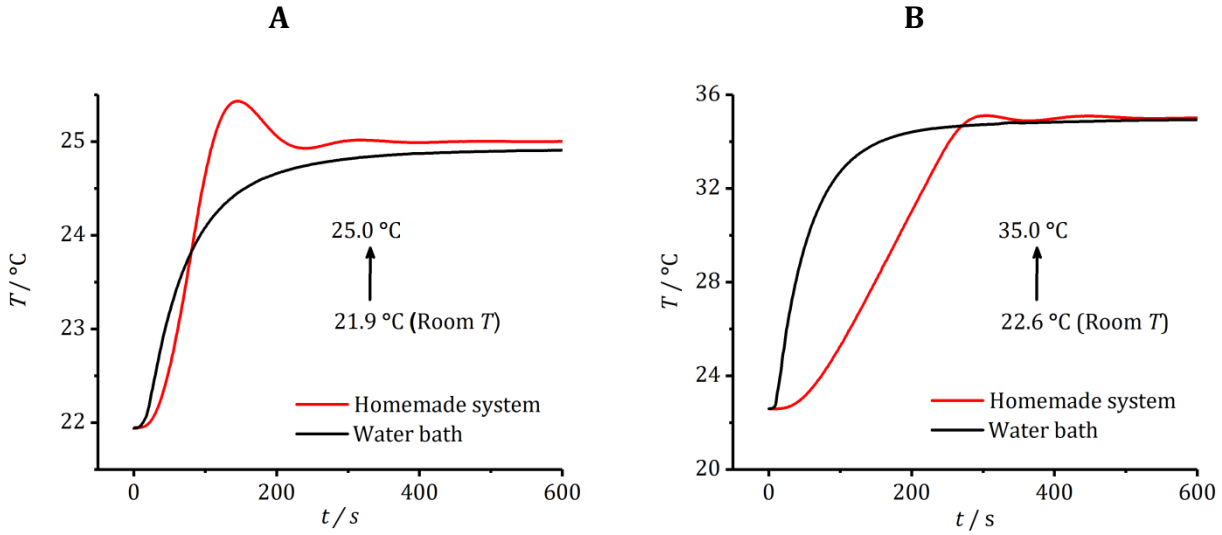


Figure C.9. Temperature profiles against time for the temperature of 10 mL H_2O being heated from room temperature 21.9 °C to 25.0°C (**A**) and from 22.6 °C to 35.0 °C (**B**) in the homemade system (red curves) and the conventional water bath (black curves).

C.8. References

[1] G.S. Kell, Density, Thermal Expansivity, and Compressibility of Liquid Water from 0° to 150°C: Correlations and Tables for Atmospheric Pressure and Saturation

Reviewed and Expressed on 1968 Temperature Scale, J. Chem. Eng. Data, 20 (1975) 97-105.

[2] J. Kestin, M. Sokolov, W.A. Wakeham, Viscosity of Liquid Water in the Range −8°C to 150°C, J. Phys. Chem. Ref. Data, 7 (1978) 941-948.

[3] C.A. Nieto de Castro, S.F.Y. Li, A. Nagashima, R.D. Trengove, W.A. Wakeham, Standard Reference Data for the Thermal Conductivity of Liquids, J. Phys. Chem. Ref. Data, 15 (1986) 1073-1086.

[4] R. Cini, G. Loglio, A. Ficalbi, Temperature Dependence of the Surface Tension of Water by the Equilibrium Ring Method, J. Colloid Interface Sci., 41 (1972) 287-297.

Appendix D: List of symbols and dimensionless criteria

D.1. List of symbols

a_i	activity of species 'i'
C_i	concentration of species 'i'
C_p	specific heat capacity at constant pressure
d	thickness of the turbulent boundary layer in Levich's model of turbulence
d_band	width of the annular band in Chapter 5
d_wall	wall thickness
D_i	diffusion coefficient of species 'i'
E	electrode potential
F	Faraday constant
$\boldsymbol{F}$	buoyancy force
$\boldsymbol{g}$	gravitational acceleration
G	Gibbs energy
h_cell	cell height
h_liquid	height of the liquid column in Chapter 6
h_s	substrate height
H	enthalpy
i	electrical current density
I	electrical current
$\boldsymbol{J}$	mass flux
l	characteristic length of turbulent eddies
L_diff	length scale for perturbation in the concentration profile
L_therm	length scale for perturbation in the temperature profile
M_i	molar mass of species 'i'
r	radial coordinate
r_1	position of the annular band in Chapter 5, $r_1 = (r_\mathrm{cell} - d_\mathrm{band})/2$
r_in	inner cell radius in Chapter 6
r_cell	cell radius
r_out	outer cell radius in Chapter 6
r_e	electrode radius
R	gas constant
p	pressure
t	time
S	entropy
T	temperature
$\Delta\tilde{T}_\mathrm{av}$	volume-averaged non-dimensional temperature difference
v	scan rate
v_i	partial molar volume of species 'i'
v_0	characteristic velocity
$\boldsymbol{v}$	fluid velocity
$\lvert\boldsymbol{v}_\mathrm{av}\rvert$	volume-averaged velocity magnitude
V	volume

W width of a vertical plate electrode
X^j quantity X pertaining to phase 'j', j = L (liquid), G (gas), C (cell), S (solid)
$\tilde{X}$ the quantity X nondimensionalized by a characteristic value
y normal coordinate
y_{lim} thickness of the 'true' diffusion layer in the model of Amatore et al.
z normal coordinate (cylindrical coordinates)
z_i charge of species 'i' nondimensionalized with the elementary charge
α thermal expansion coefficient
β densification coefficient
γ
- numerical constant in Chapter 2
- surface tension in Chapters 4 and 6

γ_i activity coefficient of species 'i'
δ thickness of the diffusion sub-layer in Levich's model of turbulence
δ_0 thickness of the viscous sub-layer in Levich's model of turbulence
$\tilde{\delta}$ thickness of the viscous sub-layer in the model of Amatore et al.
ε
- absolute dielectric permittivity in Chapter 1
- emissivity in Chapter 6

η dynamic viscosity
θ dimensionless electrode potential, $\theta = F{\cdot}(E - E_{\text{formal}})/(R{\cdot}T)$
κ thermal conductivity
μ chemical potential
ν kinematic viscosity
ρ density
σ
- dimensionless scan rate, $\sigma = Fr_e^2 v/\,(RTD_{\text{Red}})$ in Chapters 1 and 3
- Stefan-Boltzmann constant in Chapter 6

τ dimensionless time, $\tau = D_{\text{Red}}t/r_e^2$
χ thermal diffusivity
ϕ electrical potential

D.2. List of dimensionless criteria

$Br = \eta v_0^2/(\kappa\Delta T)$ Brinkman number – compares heat dissipation due to viscous friction and conduction

$Ca = \eta^{\text{L}} v_0/\gamma$ capillary number – compares capillary forces to viscous stress

$Gr = g\rho_0\ h^3 C_0(\partial\rho/\partial C)_{C=C_0}/\eta_0^2$ Grashof number - compares the importance of buoyancy forces and viscous forces

$M = v_0/c$ Mach number, in which c is the speed of sound in the medium

$Ma = |\partial_T\gamma|h_{\text{liquid}}|\Delta T|/(\eta_0\chi^{\text{L}})$ Marangoni number – compares surface tension gradients to viscous stresses

$N = \alpha\left|\frac{\Delta H}{\beta}\right|\sqrt{\frac{D_{\text{Red}}}{\rho c_p \kappa}}$ buoyancy ratio – compares the buoyancy forces induced by variations in concentration and temperature

$Pe_{\text{mass}} = |\boldsymbol{v}|r_e/D_{\text{Red}}$ Péclet number for mass transfer – compares the importance of mass transport due to convection and diffusion

$Pe_{\text{heat}} = \lvert\boldsymbol{v}\rvert r_{\text{e}}/\chi$	Péclet number for heat transfer – compares the importance of heat transport due to convection and conduction
$Pr = \eta_0/(\rho_0\chi_0)$	Prandtl number – compares the diffusivity of momentum to that of heat
$Re = \rho v_0 L/\eta$	Reynolds number, in which L is a characteristic length scale – compares the importance of inertial and viscous forces
$Ra = \alpha\rho_0 L^3\lvert\boldsymbol{g}\rvert\Delta T/(\eta_0\,\chi_0)$;	Rayleigh number – compares the importance of buoyancy forces and viscous forces
$Sc = \eta_0/(\rho_0 D)$	Schmidt number – compares the diffusivity of momentum to that of mass
$Sh = J/(WDC_0)$	Sherwood number, i.e., mass flux nondimensionalized with the characteristic diffusional mass flux